Wireless Indoor Localisation within the 5G Internet of Radio Light

A Thesis Submitted for the Degree of Doctor of

Philosophy by

Benjamin Charles Emmanuel
Meunier

Department of Electronic and Electrical Engineering,
Brunel University London

Abstract

Numerous applications can be enhanced by accurate and efficient indoor localisation using wireless sensor networks, however trade-offs often exist between these two parameters. In this thesis, real-world and simulation data is used to examine the hybrid millimeter wave and Visible Light Communications (VLC) architecture of the 5G Internet of Radio Light (IoRL) Horizon 2020 project. Consequently, relevant localisation challenges within Visible Light Positioning (VLP) and asynchronous sampling networks are identified, and more accurate and efficient solutions are developed.

Currently, VLP relies strongly on the assumed Lambertian properties of light sources. However, in practice, not all lights are Lambertian. To support the widespread deployment of VLC technology in numerous environments, measurements from non-Lambertian sources are analysed to provide new insights into the limitations of existing VLP techniques. Subsequently, a novel VLP calibration technique is proposed, and results indicate a 59% accuracy improvement against existing methods. This solution enables high accuracy centimetre level VLP to be achieved with non-Lambertian sources.

Asynchronous sampling of range-based measurements is known to impact localisation performance negatively. Various Asynchronous Sampling Localisation Techniques (ASLT) exist to mitigate these effects. While effective at improving positioning performance, the exact suitability of such solutions is not evident due to their additional processes, subsequent complexity, and increased costs. As such, extensive simulations are conducted to study the effectiveness of ASLT under variable sampling latencies, sensor measurement noise, and target trajectories. Findings highlight the computational demand of existing ASLT and motivate the development of a novel solution. The proposed Kalman Extrapolated Least Squares (KELS) method achieves optimal localisation performance with a significant energy reduction of over 50% when compared to current leading ASLT.

The work in this thesis demonstrates both the capability for high performance VLP from non-Lambertian sources as well as the potential for energy efficient localisation for sequentially sampled range measurements.

Acknowledgments

To my supervisor and friend Professor John Cosmas for choosing me to be a part of his team, for his support in technical knowledge as well as in life advice for me and my family, and finally for making this all possible by conceptualising and leading the 5G IoRL system. I further acknowledge and appreciate the financial support for the Internet of Radio Light (IoRL) project from Horizon 2020.

To my IoRL colleagues at Brunel Univeristy, Nawar Jawad and Kareem Ali for all the camaraderie and antics both at Brunel and abroad. Thank you for treating me like a brother and keeping moral high during the late night testing and last minute panics.

To Dr Tatiana Kalganova, for showing me how to successfully network and develop as a professional outside of my PhD. You were and always will be an inspiration and encouragement to me.

To those of the IoRL consortium, particularly at ISEP, for the amazing years of collaboration that made the IoRL project, and this thesis, possible.

To Mum, Dad, Tim, Olly, Janet, and Alec for moral support, taking the time to read every word and driving me on. I can only hope that the nights with drafts left open in your hands were those that left you well rested.

To my carefree and all loving dog, Brodie, for taking me on walks outdoors every day.

To Molly for her unyielding love, dedication, and patience. Thank you for being my rock.

Contents

Table of Figures

Table of Acronyms

Acronym	Meaning
3GPP	Third Generation Partnership Project
AOA	Angle of Arrival
AR	Augmented Reality
ASLT	Asynchronous Sampling Localisation Techniques
AWGN	Additive White Gaussian Noise
BD	Baseline Distance
BLE	Bluetooth Low Energy
BRE	Building Research Establishment
BS	Base-Station
BW	Bandwidth
CA	Constant Acceleration
CC	Constant Change
CH	Cluster Head
CHDCS	Cloud Home Data Centre Server
CMOS	Complementary Metal-Oxide Semiconductor
CNN	Convolutional Neural Network
COB	Chip on Board
CP	Calibration Parameters
CPU	Central Processing Unit
CV	Constant Velocity
DAS	Distributed Antenna System
DC	Direct Current
DE	Direct Extrapolation
DF	Data File
DHCP	Dynamic Host Configuration Protocol
DNCV	Discrete-time Nearly Constant Velocity
DOA	Direction of Arrival
DOS	Denial of Service
DRAN	Distributed Radio Access Network
eCPRI	Ethernet Ring with Common Public Radio Interface
EHF	Extremely High Frequency
EKF	Extended Kalman Filter
EM	Electromagnetic
EPC	Evolved Packet Core
EPLC	Estimation Period Latency Component
ERE	Extrapolated Range Error
FC	Fusion Centre
FD	Forwarding Device
FDM	Frequency Division Multiplexing
FMS	Follow Me Service
FOR	First Order Reflections
FOV	Field of View
FPGA	Field Programmable Gate Array
GNSS	Global Navigation Satellite Service
GPS	Global Positioning Service
HD	High Definition
HLC	Halo-Lens Compensation
HR	Halo Region
ID	Identification
IEEE	Institute of Electrical and Electronic Engineers
IF	Intermediate Frequency
IHIPG	Intelligent Home IP Gateway
IML	Inter-Measurement Latency
IMT	International Mobile Telecommunication
IMU	Inertial Measurement Unit
IoT	Internet of Things
IP	Internet Protocol
IPP	Indoor Positioning Protocol
IPS	Indoor Positioning System
IR	Infrared
ISM	Industrial, Scientific and Medical
ITU	International Telecommunications Union
KELS	Kalman Extrapolated Least Squares
KEWLS	Kalman Extrapolated Weighted Least Squares
KF	Kalman Filter
KPI	Key Performance Indicators
LB	Load Balancing
LBS	Location Based Services
LD	Location Database

LED	Light Emitting Diode
LIDAR	Light Detection and Ranging
LIG	Luminous Intensity Graph
LKF	Linear Kalman Filter
LOS	Line of Sight
LSC	Location Service Client
LSS	Least Squares Solution
LTE	Long-Term Evolution
MA	Measurement Augmentation
MAC	Medium Access Control
MDF	Mean Data File
MIMO	Multiple Input Multiple Output
MIoT	Massive Internet of Things
MISO	Multiple Input Single Output
MLa	Measurement Latency
MMTC	Massive Machine Type Communication
mmWave	Millimetre Wave
MNO	Mobile Network Operators
MPE	Mean Position Error
MRE	Mean Range Error
MSS	Multisource Streaming
MTPL	Motion to Photon Latency
NFV	Network Function Virtualisation
NFVO	Network Function Virtualisation Orchestrator
NLOS	Non-Line of Sight
NR	New Radio
ODBC	Open Database Connectivity
OFDM	Orthogonal Frequency Division Multiplexing
OOSM	Out of Sequence Measurements
PA	Path Angle
PCB	Printed Circuit Board
PD	Photodiode
PDCP	Packet Data Convergence Protocol
PE	Positioning Error
PHD	Probability Hypothesis Density
PL	Path Loss
RAN	Radio Access Network
RE	Range Error
RF	Radio Frequency
RFID	Radio Frequency Identification
RMSE	Root Mean Square Error
RRC	Remote Radio Control
RRLH	Remote Radio Light Head
RRLHC	Remote Radio Light Head Controller
RSS	Received Signal Strength
RSSI	Received Signal Strength Indicator
RTT	Round Trip Time
SDN	Software Defined Network
SHF	Super High Frequency
SMF	Sequential Measurement Fusion
SNR	Signal to Noise Ratio
SOR	Second Order Reflections
SQL	Structured Query Language
SRS	Sounding Reference Signals
SR-SCKF	Square Root - Sequential Cubature Kalman Filter
SUKF	Sequential Unscented Kalman Filter
TC	Time Corrected
TDM	Time Division Multiplexing
TDOA	Time Difference of Arrival
TIR	Total Internal Reflection
TM	Trademark
TOA	Time of Arrival
TOF	Time of Flight
TS	Taylor Series
TSWLS	Two Step Weighted Least Squares
TV	Television
TWR	Two Way Ranging
UAV	Unmanned Ariel Vehicle
UCP	Updated Calibration Parameters
UDN	Ultra-Dense Network
UE	User Equipment
UGV	Unmanned Ground Vehicle
UHD	Ultra-High Definition
UHF	Ultra-High Frequency
UKF	Unscented Kalman Filter
UT	Unscented Transform
UWB	Ultra-Wide Band
V2V	Vehicle to Vehicle
VLC	Visible Light Communications

VLP	Visible Light Positioning
VR	Virtual Reality
WI-FI	Wireless Fidelity
WLAN	Wireless Local Area Network
WLS	Weighted Least Squares
XR	Extended Reality

Table of Notations

$\boldsymbol{A}$	**Kalman Filter State Transition Matrix**
$\boldsymbol{A_{t_k,t_{k-1}}}$	Kalman Filter State Transition Matrix from Estimation Instant t_{k-1} to t_k
$\boldsymbol{A^i_{t^i_k}}$	Kalman Filter State Transition Matrix for the i'th Sensor During the k'th Sampling Period
$\boldsymbol{A^i_{synch}}$	Kalman Filter State Transition Matrix for the i'th Sensor to Synchronise the Estimate to the Estimation Instant
$\boldsymbol{A_r}$	The Effective Area of the Receivers' Photodiode
$\boldsymbol{Amp_i}$	Calibrated Amplitude of the Peak Applied to the Halo Region of the i'th VLC Source
$\boldsymbol{Arc\ Length}$	Length of the Arc Used to Define the Circular Target Trajectory
$\boldsymbol{\alpha}$	Free Space Constant Attenuation Factor
$\boldsymbol{\alpha^j}$	Free Space Constant Attenuation Factor for the j'th Multipath Component
$\boldsymbol{\alpha^i_{t_k}}$	Extrapolation Component for the i'th Sensor During the k'th Sampling Period
$\boldsymbol{a^x}$	Acceleration Component in the x-Axis
$\boldsymbol{a_{t_k}}$	Constant Acceleration Component
$\boldsymbol{a^i_{t^i_k,t^i_{k-1},t^i_{k-2}}}$	Measurement Acceleration for the i'th Sensor Across from the time of the k'th-2 to k'th Estimation Instant
$\boldsymbol{B}$	Kalman Filter Control Translation Matrix
$\boldsymbol{BW}$	Bandwidth
$\boldsymbol{\beta}$	Prior Knowledge of Sigma Point Distribution
$\boldsymbol{C_d}$	Diagonal Covariance Matrix of Noisy Distance Values
$\boldsymbol{C_n}$	Diagonal Covariance Matrix of Noisy TDOA Values
$\boldsymbol{C_{opt}}$	Optical Power Constant
$\boldsymbol{CP^i}$	Calibration Parameters for the i'th VLC Source
$\boldsymbol{CP}$	Array Of Calibration Parameters for All VLC Sources
$\boldsymbol{CDF^i_{x,y}}$	The Calibration Data File of RSS Measurements Collected at x, y Grid Coordinates from the i'th VLC Source
$\boldsymbol{c}$	The Speed of Light
$\boldsymbol{d}$	The True Distance
$\boldsymbol{d^i}$	The True Euclidian Distance Between the Target and the i'th Sensor
$\boldsymbol{\breve{d}^i}$	The Estimated Euclidian Distance Between the Target and the i'th Sensor Using an Initial Guess of the Target Coordinates
$\boldsymbol{\bar{d}}$	A Vector of True Euclidian Distances
$\boldsymbol{\bar{d}_{t_k}}$	A Vector of True Euclidian Distances Obtained during the k'th Sampling Period
$\boldsymbol{\hat{d}^i}$	The Noisy Euclidian Distance Estimate of the i'th Sensor
$\boldsymbol{d^i_{t^i_k}}$	The Euclidian Distance of the i'th Sensor obtained at the time of the i'th Sensors' Sampling Instant Within the k'th Sampling Period
$\boldsymbol{\hat{d}^i_{t^i_k}}$	The Euclidian Distance Estimate of the i'th Sensor obtained at the time of the i'th Sensors' Sampling Instant Within the k'th Sampling Period
$\boldsymbol{\Delta\hat{d}^i_{t^i_k,t^i_{k-1}}}$	The Change in Distance Measurements From the i'th Sensor Between Consecutive Sampling Instances
$\boldsymbol{\Delta\Delta\hat{d}^i_{t^i_k,t^i_{k-1},t^i_{k-2}}}$	The Rate of Change in Distance Measurements From the i'th Sensor Between Consecutive Sampling Instances
$\boldsymbol{\hat{d}^i_{t_k,est}}$	The Extrapolated Distance Measurement for the i'th Sensor at the Time of the k'th Sampling Instant
$\boldsymbol{\hat{d}^i_{t^i_k}}$**(B)**	The Euclidian Distance Estimate to Target B, of the i'th Sensor, Obtained at the i'th Sensor Sampling Instant Within the k'th Sampling Period
$\boldsymbol{\tilde{d}}$	A Vector Of Noisy Euclidian Distance Estimates
$\boldsymbol{\tilde{d}_{t_k}}$	A Vector Of Noisy Euclidian Distance Estimates Obtained During the k'th Sampling Period

$\boldsymbol{d_{x,y}^{i}}$	The True Euclidian Distance Between the i'th Sensor and Coordinate, $x, y, (z = 0)$
$\boldsymbol{\widehat{d}_{x,y}^{i}}$	The Noisy Euclidian Distance Estimate Between the i'th Sensor and Coordinate, $x, y, (z = 0)$
$\boldsymbol{d^{i,j}}$	The Difference in Euclidian Distances to the Target from Sensors i and j
$\boldsymbol{\widehat{d}^{i,j}}$	The Estimated Difference in Euclidian Distances to the Target from Sensors i and j
$\boldsymbol{d_{REF}}$	A Known Reference Distance
$\boldsymbol{D}$	A Diagonal Matrix of Noisy Distance Measurements
$\boldsymbol{D_{t_k}}$	A Diagonal Matrix of Noisy Distance Measurements Obtained During The k'th Sampling Instant
$\boldsymbol{D^{-}}$	The Minimum Euclidian Distance at Which the Halo Region Occurs
$\boldsymbol{D^{+}}$	The Maximum Euclidian Distance at Which the Halo Region Occurs
$\boldsymbol{D^{r}}$	The Range of Euclidian Distances Which Define the Halo Region
$\boldsymbol{D_{init}^{r}}$	The Initially Estimated Range Of Euclidian Distances Which Define The Halo Region
$\boldsymbol{\widehat{D}_{init}^{r}}$	The Exaggerated Estimated Range Of Euclidian Distances Which Define the Halo Region
$\boldsymbol{DF_{x,y}^{i}}$	The RSS Data File Corresponding To x, y Grid Coordinates obtained by the i'th VLC Source
$\boldsymbol{\delta}$	The Infinite Impulse Function (Delta Function)
$\boldsymbol{e_{t_k}^{-}}$	Priori Estimate Error
$\boldsymbol{e_{t_k}}$	Posterior Estimate Error
$\boldsymbol{\varepsilon_{x,y}^{R,i}}$	The Estimation Range Error Given Between the i'th VLC Source and $x, y, (z = 0)$ Coordinates
$\boldsymbol{\varepsilon_{\psi_{1/2}^{i},Sub^{i}}^{R,i}}$	The Average Range Error for the i'th VLC Source for specific SAHP And Subcarrier Data Values
$\boldsymbol{\varepsilon^{PE}}$	Position Estimation Error
$\boldsymbol{\varepsilon_{t_k}^{PE}}$	Position Estimation Error at the Time of the k'th Sampling Instant
$\boldsymbol{\varepsilon_{t_k,It}^{PE}}$	The It'th Iteration of the Position Estimation Error at the Time of the k'th Sampling Instant
$\boldsymbol{\hat{\varepsilon}_{t_k}^{MPE}}$	The Mean Positioning Error at the Time of the k'th Sampling Instant
$\boldsymbol{\varepsilon_{t_k^{i}}^{IML,i}}$	The IML Error Component of the i'th Sensor Measurement Obtained During the k'th Sampling Period
$\boldsymbol{\varepsilon_{t_k}^{R,i}}$	The Range Error from the i'th Sensor Measurement Obtained at the i'th Sensor Sampling Instant within the k'th Sampling Period.
$\boldsymbol{\varepsilon_{t_k}^{R,DE,i}}$	The Direct Extrapolation Range Error from the i'th Sensor Measurement Obtained at the i'th Sensor Sampling Instant within the k'th Sampling Period.
$\boldsymbol{f()}$	A Nonlinear Kalman Filter State Update Function
$\boldsymbol{F}$	An Acceleration Translation Matrix
$\boldsymbol{\widetilde{G}}$	Lambertian Model Gain Term
$\boldsymbol{\widehat{\widetilde{G}}}$	Estimate of the Lambertian Model Gain Term
$\boldsymbol{G_r(\psi)}$	Normalized Radiation Gain of the Transmitter With Respect to the Angle of Incidence
$\boldsymbol{G_i(\theta)}$	Normalized Incidence Gain Of The Transmitter With Respect To The Angle Of Radiation
$\boldsymbol{g(\theta)}$	Optical Concentrator Gain
$\boldsymbol{h}$	Nonlinear Measurement Function
$\boldsymbol{h^{i}}$	Nonlinear Measurement Function Relating to the i'th Sensor
$\boldsymbol{h^{i,1}}$	Nonlinear Measurement Function Relating to the First and i'th Sensors
$\boldsymbol{\widehat{h}}$	Height
$\boldsymbol{\widehat{h}_{i}}$	Height of the i'th VLC Source

$\widehat{\boldsymbol{h}}_{\boldsymbol{PD}}$	Height of the Photodiode
$\widehat{\boldsymbol{h}}_{\boldsymbol{g}}$	Height of the VLC Measurement Grid
$\boldsymbol{H}$	The Kalman Filter Measurement Translation Matrix
$\boldsymbol{H}(\boldsymbol{0})$	The LOS Channel
$\boldsymbol{H}_{\boldsymbol{i}}(\boldsymbol{0})$	The LOS Channel Model for the i'th VLC Source
$\boldsymbol{i}$	Index Variable
$\boldsymbol{It}$	Simulation Iteration Index
$\boldsymbol{I}$	An Identity Matrix
$\boldsymbol{I}_{\boldsymbol{4*4}}$	A Four by Four Identity Matrix
$\boldsymbol{j}$	Index Variable
$\boldsymbol{K}$	The Kalman Gain Matrix
$\boldsymbol{K}_{\boldsymbol{t_k}}$	The Kalman Gan Matrix at the Time of the k'th estimation Instant
$\boldsymbol{K}_{\boldsymbol{t_k^i}}$	The Kalman Gan Matrix computed at the i'th Sensor Sampling Instant within the k'th Sampling Period.
$\boldsymbol{k}$	Index of sampling periods and estimation instants
$\boldsymbol{k}_{\boldsymbol{max}}$	Maximum Number of Estimation Instants
$\boldsymbol{L}$	A Sigma Point Scaling Parameter
$\boldsymbol{LKF}^{\boldsymbol{i}}$	The Linear Kalman Filter Appointed to the i'th Sensor
$\mathbf{m}$	Meters
$\boldsymbol{m}$	Order of Lambertian Emission
$\boldsymbol{m}_{\boldsymbol{i}}$	Order of Lambertian Emission for the i'th VLC Source
$\widehat{\boldsymbol{m}}$	Estimated Order of Lambertian Emission
$\boldsymbol{M}$	Order of Lambertian Incidence
$\boldsymbol{MDF}_{\boldsymbol{x,y}}^{\boldsymbol{i}}$	Measurement Data File Of RSS Measurements Collected At x, y Grid Coordinates from the i'th VLC Source
$\widehat{\boldsymbol{n}}$	Number Of States
$\boldsymbol{n}$	Noise Component
$\boldsymbol{n}^{\boldsymbol{i}}$	Noise Component of the i'th Sensor
$\boldsymbol{n}_{\boldsymbol{t_k^i}}^{\boldsymbol{i}}$	Noise Component of the i'th Sensor the i'th Sensor Sampling Instant within the k'th Sampling Period
$\overline{\boldsymbol{n}}$	A Vector of Noise Components
$\overline{\boldsymbol{n}}_{\boldsymbol{t_k}}$	A Vector of Noise Components at the Time of the k'th Sampling Instant
$\boldsymbol{n}^{\boldsymbol{i,1}}$	TDOA Noise Component Between the First and i'th sensor
$\boldsymbol{N}$	Number Of Sensors / Anchor Nodes
$\boldsymbol{N}_{\boldsymbol{m}}$	Number Of Multipath Components
$\boldsymbol{N}_{\boldsymbol{0}}$	Power Spectral Density of Noise
$\boldsymbol{N}_{\boldsymbol{i}}$	Number Of Measurements Obtained for the i'th VLC Source
$\boldsymbol{N}_{\boldsymbol{UE}}$	Number Of UE Devices
$\boldsymbol{N}_{\boldsymbol{L}}$	Number Of Loops
$\boldsymbol{N}_{\boldsymbol{PE}}$	Number Of Position Estimations Calculated
$\boldsymbol{N}_{\boldsymbol{Iterations}}$	Number Of Iterations
$\boldsymbol{N}(\boldsymbol{\mu}, \boldsymbol{\sigma})$	A Normal Distribution with Mean μ and Standard Deviation σ
$\widehat{\boldsymbol{o}}$	The Dimension of The Measurement Vector
$\boldsymbol{\rho}(\boldsymbol{a}\|\boldsymbol{b})$	The Probability of a Given b
$\boldsymbol{P}$	Covariance Matrix of the State Estimate
$\boldsymbol{P}_{\boldsymbol{t_k}}^{-}$	Covariance of the Priori Estimation Derivations at the Time of the k'th Instant
$\boldsymbol{P}_{\boldsymbol{t_k}}^{\boldsymbol{i-}}$	Covariance of the Priori Estimation Derivations for the i'th Sensor Measurements at the Time of the k'th Estimation Instant
$\boldsymbol{P}_{\boldsymbol{t_k^i}}^{\boldsymbol{i-}}$	Covariance of the Priori Estimation Derivations for the i'th Sensor Measurements at the Time of the i'th Sensor Sampling Instant within the k'th Sampling Period

$\boldsymbol{P_{t_k}}$	Covariance of the Posterior Estimation Derivations at the Time of The k'th Estimation Instant
$\boldsymbol{P^{i}_{t_k}}$	Covariance of the Posterior Estimation Derivations of the i'th Sensor at the Time of the k'th Estimation Instant
$\boldsymbol{P^{\chi}_{t_k}}$	Covariance of the Posterior Estimation Derivations at the Time of the k'th Estimation Instant for the Propagated Sigma Points
$\boldsymbol{P^{zz}_{t_k}}$	Innovation Covariance at the Time of the k'th Estimation Instant
$\boldsymbol{P^{xz}_{t_k}}$	The Cross Covariance at the Time of the k'th Estimation Instant
$\boldsymbol{P_R}$	Received Signal Strength Indicator Value
$\boldsymbol{\widehat{P}_R}$	Estimate of the Received Signal Strength Indicator Value
$\boldsymbol{P_{R_i}}$	Received Signal Strength Indicator Value of the i'th VLC Source
$\boldsymbol{\overline{P}_R}$	Vector of Received Signal Strength Indicator Values
$\boldsymbol{P_{R_i,t_k}}$	Received Signal Strength Indicator Value of the i'th VLC Source at the k'th Estimation Instant
$\boldsymbol{\overline{P}_{R,t_k}}$	Vector Of Received Signal Strength Indicator Values Obtained during the k'th Sampling Period
$\boldsymbol{P^{x,y}_{R_i}}$	Received Signal Strength Power of the i'th VLC Source at $x, y, (z = 0)$ Coordinates
$\boldsymbol{P^{REF}_{R}}$	Reference RSS Measurement
$\boldsymbol{P^{REF}_{R_i}}$	Reference RSS Measurement for the i'th VLC Source
$\boldsymbol{P_T}$	Power Transmitted from a VLC Source
$\boldsymbol{P_{T_i}}$	Power Transmitted from the i'th VLC Source
$\boldsymbol{P^{+}_{i}}$	The i'th VLC Source RSSI Value at the Upper Bound of the Halo Region
$\boldsymbol{P^{-}_{i}}$	The i'th VLC Source RSSI Value at the Lower Bound of the Halo Region
$\boldsymbol{P^{r}_{i}}$	The i'th VLC Source RSSI Value Range Correlating to The Halo Region
$\boldsymbol{\psi}$	LOS Path Angle of Irradiance
$\boldsymbol{\psi_i}$	LOS Path Angle of Irradiance at the i'th VLC Source
$\boldsymbol{\psi_{1/2}}$	Semi-Angle at Half Power of a VLC Source
$\boldsymbol{\psi^{i}_{1/2}}$	Semi-Angle at Half Power of the i'th VLC Source
$\boldsymbol{\phi_i}$	Mapped RSSI Values for the i'th VLC Source
$\boldsymbol{Q}$	Kalman Filter Process Noise Covariance Matrix
$\boldsymbol{Q_{t_k}}$	Kalman Filter Process Noise Covariance Matrix at the k'th Estimation Instant
$\boldsymbol{Q_{t_k,t_{k-1}}}$	Kalman Filter Process Noise Covariance Matrix from the Time of the k'th -1 Estimation Instant To the Time of the k'th Estimation Instant
$\boldsymbol{Q_{t^i_k,t^i_{k-1}}}$	Kalman Filter Process Noise Covariance Matrix from the Time of the i'th sensors sampling instant within the k'th -1 Sampling Period to the i'th sensors sampling instant within the k'th Sampling Period
$\boldsymbol{Q^{i}_{t^i_k,t^i_{k-1}}}$	Kalman Filter Process Noise Covariance Matrix of the i'th sensors LKF from the Time of the i'th sensors sampling instant within the k'th -1 Sampling Period to the i'th sensors sampling instant within the k'th Sampling Period
$\boldsymbol{Q^{i}_{synch}}$	The i'th Sensors Kalman Filter Process Noise Covariance Matrix for Synchronizing Estimates to the next Estimation Instant
$\boldsymbol{q_a^{min}}$	Minimum Bound of Acceleration Noise Magnitude Value
$\boldsymbol{q_a^{max}}$	Maximum Bound of Acceleration Noise Magnitude Value
$\boldsymbol{q_a^{spacing}}$	Increment of Tried Acceleration Noise Magnitude Values
$\boldsymbol{R}$	Kalman Filter Measurement Noise Covariance Matrix
$\boldsymbol{R_{t_k}}$	Kalman Filter Measurement Noise Covariance Matrix at the Time of the k'th Estimation Instant
$\boldsymbol{R_{t^i_k}}$	Kalman Filter Measurement Noise Covariance Matrix of the Measurement Obtained from the i'th Sensor at the i'th Sensors Sampling Instant, Within the k'th Estimation Period

$\boldsymbol{R^{vlc}}$	Kalman Filter Measurement Noise Covariance Matrix of the VLC Position Estimate
$\boldsymbol{R^{mmw}}$	Kalman Filter Measurement Noise Covariance Matrix of the mmWave Position Estimate
$\boldsymbol{RDF^{i}}$	Reference Data File of RSS Measurements for the i'th VLC Source
$\boldsymbol{Rx}$	A Receiver
$\boldsymbol{Rx^{i}}$	Position of the i'th Receiver
$\boldsymbol{Rx^{i}_{mm}}$	Position of the i'th Millimeter Wave Receiver Antenna
$\boldsymbol{RRLH^{i}}$	Antenna Coordinates of the i'th RRLH
$\boldsymbol{RRLH}$	Array of RRLH Antenna Coordinates
$\boldsymbol{Radius}$	Radius of a Circle
$\boldsymbol{Radius_{max}}$	The Maximum Considered Radius of a Circle
$\boldsymbol{RMSE}$	Root Mean Square Error
$\boldsymbol{RMSE\left(\Delta t_m, \sigma_z, \theta_{path}, \sigma_a^2\right)}$	RMSE Acquired as a Result of the Given IML, Measurement Noise, Path Angle and Acceleration Noise Magnitude Value
$\boldsymbol{RMSE\%_{diff}}$	RMSE Percentage Difference
$\boldsymbol{r_{res}}$	Raw Resolution
$\boldsymbol{r_i}$	Horizontal Distance Between the Target and the i'th VLC Source
$\boldsymbol{r}$	Vector Of Horizontal Distances Between the Target and Each VLC Source
$\boldsymbol{rad}$	Radians
$\boldsymbol{s}$	A Signal
$\boldsymbol{S}$	Array Of Sensor Positions
$\boldsymbol{S^{i}}$	The i'th Sensor Position[1]
$\boldsymbol{S^{0}}$	The Position of the Target[2]
$\boldsymbol{S^{0}_{t_k}}$	The Targets' Position at the Time of the k'th Estimation Instant[1]
$\boldsymbol{S^{0}_{t_k^i}}$	The Targets' Position at the Time of the i''th Sensors Sampling Instant, Within the k'th Estimation Period[1]
$\boldsymbol{\widehat{S}^{0}_{t_k}}$	Estimate of the Targets Position at the Time of the k'th Sampling Instant
$\boldsymbol{\widehat{S}^{0}}$	Estimate of the Targets' Position[1]
$\boldsymbol{\widehat{S}^{0}_{vlc}}$	Estimate of the Targets' Position Produced Using VLC RSS Data[1]
$\boldsymbol{\widehat{S}^{0}_{mm}}$	Estimate of the Targets' Position Produced Using mmWave TDOA Data[1]
$\boldsymbol{\breve{S}^{0}}$	Initial Guess of the Targets' Position for the TDOA Taylor Series Solution[1]
$\boldsymbol{\delta S^{0}}$	Error in the Initial Guess of the Targets' Position Estimate for the TDOA Taylor Series Solution[1]
$\boldsymbol{\widehat{\delta S}^{0}}$	Estimated Error in the Initial Guess of the Targets' Position Estimate for the TDOA Taylor Series Solution[1]
$\boldsymbol{S_r}$	Slope Constant According To $G_r(\theta)$
$\boldsymbol{S_i}$	Slope Constant According To $G_i(\psi)$
$\boldsymbol{Sub}$	Subcarrier
$\boldsymbol{sub_i}$	The Optimal Subcarrier for the i'th VLC Source
$\boldsymbol{\sigma_x / \sigma_x^2}$	Standard Deviation / Variance of x-Axis Measurements
$\boldsymbol{\sigma_{x,vlc} / \sigma_{x,vlc}^2}$	Standard Deviation / Variance Of x-Axis Measurements Obtained from VLC Data
$\boldsymbol{\sigma_{y,vlc} / \sigma_{y,vlc}^2}$	Standard Deviation / Variance Of y-Axis Measurements Obtained from VLC Data
$\boldsymbol{\sigma_{x,mmw}}$	Standard Deviation of X-Axis Measurements Obtained from mmWave Data
$\boldsymbol{\sigma_{y,mmw}}$	Standard Deviation of Y-Axis Measurements Obtained from mmWave Data
$\boldsymbol{\sigma_a / \sigma_a^2}$	Standard Deviation / Variance Of Acceleration

[1] Sensor Coordinates may be given in either two or three dimensions.

[2] Target coordinates may be given in either two or three dimensions.

$\boldsymbol{\sigma_\tau}$	Standard Deviation of TOA Noise
$\boldsymbol{\sigma^2_{noise}}$	Total Noise Variance
$\boldsymbol{\sigma^2_{shot}}$	Shot Noise
$\boldsymbol{\sigma^2_{thermal}}$	Thermal Noise
$\boldsymbol{\sigma_a}$	Acceleration Noise Magnitude
$\boldsymbol{\widehat{\sigma}_a}$	Acceleration Noise Magnitude Considering IoRL Processing Latencies
$\boldsymbol{\breve{\sigma}_a}$	Acceleration Noise Magnitude Ignoring IoRL Processing Latencies
$\boldsymbol{\sigma_a(t_m, \sigma_z).}$	Optimal Acceleration Noise Magnitude According to A Specific IML And Measurement Noise Value
$\boldsymbol{\sigma_z}$	Standard Deviation of a (Distance) Measurement
$\boldsymbol{\sigma_d / \sigma_d^2}$	Standard Deviation / Variance of The Distance Estimate
$\boldsymbol{\sigma_V / \sigma_V^2}$	Standard Deviation / Variance of The Velocity Estimate
$\boldsymbol{\sigma^2_{\hat{d}^i_{t_k,est}}}$	Variance of the Extrapolated Pseudo Measurement $\hat{d}^i_{t_k,est}$
$\boldsymbol{t}$	Time
$\boldsymbol{t_k}$	Time at the k'th Estimation Instant
$\boldsymbol{t_k^i}$	Time at Which the i'th Sensor Obtains a Measurement Within the k'th Sampling Period
$\boldsymbol{t_{i,j}^{x,y}}$	Timestamp Pertaining To The j'th Measurement Obtained at (x, y) Coordinates from the i'th Source
$\boldsymbol{\Delta t}$	Delta Time
$\boldsymbol{\Delta t_m}$	Inter-Measurement Latency
$\Delta \boldsymbol{t_i}$	Measurement Latency Related to the Next Estimation Instant
$\boldsymbol{\Delta t_{i,k}}$	Measurement Latency Related to the Next Estimation Instant for the i'th Sensor
$\boldsymbol{\Delta t_s}$	Measurement Latency Related to the Previous Estimation Instant
$\boldsymbol{\theta}$	LOS Path Angle of Incidence
$\boldsymbol{\theta_i}$	LOS Path Angle of Incidence for the i'th Sensor
$\boldsymbol{\theta_{1/2}}$	Semi Angle at Half Power of the Photodiode
$\boldsymbol{\theta_{FOV}}$	Field Of View Angle
$\boldsymbol{\theta_{path}}$	Trajectory Path Angle
$\boldsymbol{\Delta T}$	Sampling Time Period
$\Delta \boldsymbol{T^i}$	Sampling Time Period of the i'th Sensor
$\boldsymbol{\Delta T^i_{t_k^i, t_{k-1}^i}}$	Sampling Time Period of the i'th Sensor Between Consecutive Sampling Periods
$\boldsymbol{\widehat{\Delta T}_L}$	Average Runtime of A Single Program Loop
$\boldsymbol{\Delta T_{N_L}}$	Recorded Runtime Over N_L Loops
$\boldsymbol{T(\theta)}$	Optical Filter Gain
$\boldsymbol{Tx}$	Transmitter Position
$\boldsymbol{Tx^i}$	Position of the i'th Transmitter
$\boldsymbol{Tx^i_{vlc}}$	Position of the i'th Transmitters' VLC source
$\boldsymbol{T_{EPLC}}$	Estimation Processing Latency Component

$\boldsymbol{\tau}$	Time Delay
$\boldsymbol{\tau_m}$	Round Trip Time Delay
$\boldsymbol{\tau^j}$	Time Delay of the j'th Multipath Component
$\boldsymbol{\tau^i}$	Time Delay of the i'th Multipath Component
$\boldsymbol{\tau_p}$	Known Processing Time of the Receiver
$\boldsymbol{\tau^i_{t_k}}$	TOA Between the Target and the i'th Sensor at the k'th Estimation Instant
$\boldsymbol{\hat{\tau}^i_{t_k}}$	TOA Estimate Between the Target and the i'th Sensor at the k'th Estimation Instant
$\boldsymbol{\tau^{i,j}}$	Time Difference of Arrival Between the Target and the i'th and j'th Sensors

$\hat{\tau}_{t_k}^{i,j}$	Time Difference of Arrival Between the i'th and j'th Sensor Measured at the k'th Estimation Instant
$\bar{\tau}_{t_k}$	Vector Of TDOA Measurements Obtained During the k'th Sampling Period
$\boldsymbol{u}$	Kalman Filter Control Input
$\boldsymbol{u}_{t_k}$	Kalman Filter Control Input at the k'th Instant
$\boldsymbol{U}$	RF Channel
$\boldsymbol{UCP}$	Array Of Updated Calibration Parameter Values for All VLC Sources
$\boldsymbol{UCP}^{\boldsymbol{i}}$	Updated Calibration Parameter Values for the i'th VLC Source
$\boldsymbol{v}$	Measurement Noise
$\boldsymbol{v}_{t_k}$	Measurement Noise at the k'th Estimation Instant
$\boldsymbol{v}_{t_k}^{i}$	Measurement Noise Attributed to the i'th Sensor at the k'th Estimation Instant
$\boldsymbol{v}_{t_k^i}^{i}$	Measurement Noise Attributed to the i'th Sensor obtained at the Time of the i'th Sensors Sampling Instant, Within the k'th Estimation Period
$\boldsymbol{v}_{t_k}^{mmw}$	mmWave TDOA Measurement Noise at the k'th Estimation Instant
$\boldsymbol{v}_{t_k}^{vlc}$	VLC RSS Measurement Noise at the k'th Estimation Instant
$\boldsymbol{v}^{\boldsymbol{x}}$	Velocity in the x-Axis
$\boldsymbol{v}^{\boldsymbol{y}}$	Velocity in the y-Axis
$\boldsymbol{v}_{t_k}^{x}$	Velocity in the x-Axis at the Time of the k'th Estimation Instant
$\boldsymbol{v}_{t_k}^{y}$	Velocity in the y-Axis at the Time of the k'th Estimation Instant
$\hat{\boldsymbol{v}}_{t_k}^{x}$	Estimated Velocity in the x-Axis at the Time of the k'th Estimation Instant
$\hat{\boldsymbol{v}}_{t_k}^{y}$	Estimated Velocity in the y-Axis at the Time of the k'th Estimation Instant
$\boldsymbol{V}$	Velocity Vector of the Target
$\boldsymbol{V}_{t_k}$	Velocity Vector of the Target During the k'th Sampling Period
$\boldsymbol{V}_{t_k^i,t_{k-1}^i}^{i}$	Measurement Displacement Velocity of the i'th Sensor From t_{k-1}^{i} To t_k^{i}
$\boldsymbol{W}$	WLS Weighting Matrix
$\boldsymbol{W}^{j,m}$	j'th Sigma Point Mean Weight
$\boldsymbol{W}^{j,c}$	j'th Sigma Point Covariance Weight
$\boldsymbol{w}$	Kalman Filter Process Noise
$\boldsymbol{w}_{t_k}$	Kalman Filter Process Noise at the k'th Sampling Instant
$\boldsymbol{w}_{t_k,t_{k-1}}$	Kalman Filter Process Noise from the time of the k'th-1 Estimation Instant to the k'th Estimation Instant
$\boldsymbol{\xi}_{\boldsymbol{i}}$	The i'th VLC Source Skew Factor
$\boldsymbol{x}$	X Coordinate or Axis
$\boldsymbol{x}^{\boldsymbol{i}}$	X Coordinate of the i'th Sensor
$\boldsymbol{x}^{\boldsymbol{0}}$	X Coordinate of the Target
$\hat{\boldsymbol{x}}^{\boldsymbol{0}}$	Estimated X Coordinate of the Target
$\boldsymbol{x}_{t_k}^{0}$	X Coordinate of the Target at the Time of the k'th Sampling Instant
$\boldsymbol{x}_{t_k^i}^{0}$	X Coordinate of the Target at the Time of the i'th Sensors Sampling Instant, Within the k'th Estimation Period
$\hat{\boldsymbol{x}}_{t_k}^{0}$	Estimated X Coordinate of the Target at the Time of the k'th Sampling Instant
$\bar{\boldsymbol{x}}^{\boldsymbol{0}}$	Initial Guess of Targets' X Coordinate for the Taylor Series Solution
$\boldsymbol{x}_{\boldsymbol{mm}}^{\boldsymbol{i}}$	X Coordinate of the i'th Sensors Millimeter Wave Antenna
$\boldsymbol{x}_{\boldsymbol{vlc}}^{\boldsymbol{i}}$	X Coordinate of the i'th Sensors VLC Source
$\boldsymbol{\delta x}^{\boldsymbol{0}}$	X Axis component of the Target Estimation Error
$\boldsymbol{X}$	State to be Determined
$\hat{\boldsymbol{X}}_{t_k}$	Estimate of the State to be Determined at the time of the k'th Estimation Instant
$\boldsymbol{X}_{t_k}$	State To Be Determined at the time of the k'th Estimation Instant
$\boldsymbol{\Delta X}_{t_k}$	Estimation Error of the State to Be Determined, at the Time of the k'th Estimation Instant

$\widehat{\Delta \boldsymbol{X}}_{t_k}$	Estimate of the Estimation Error for the State to Be Determined, at the Time of the k'th Estimation Instant
$\boldsymbol{X}_{t_k^i}$	State to Be Determined at the Time of the i'th Sensors Sampling Instant, Within the k'th Estimation Period
$\boldsymbol{X}_{t_k}^{\boldsymbol{i}}$	State to Be Determined for the i'th Sensors' LKF at the Time of the k'th Estimation Instant
$\boldsymbol{X}_{t_k^i}^{\boldsymbol{i}}$	State to Be Determined for the i'th Sensors' LKF at the Time of the i'th Sensors Sampling Instant, Within the k'th Estimation Period
$\widehat{\boldsymbol{X}}_{t_k}^{-}$	Prior State Estimate
$\widehat{\boldsymbol{X}}_{t_k^i}^{i-}$	Prior State Estimate For The I'th Sensor at Time of the k'th Sampling Instant
$\widehat{\boldsymbol{X}}_{t_k}$	Kalman Filter Posterior State Estimate at the Time of the k'th Estimation Instant
$\widehat{\boldsymbol{X}}_{\boldsymbol{shi}}$	Estimated Target State Obtained Through the Shi et al. Solution
$\widehat{\boldsymbol{X}}_{\boldsymbol{mod}}$	Estimated Target State Obtained Through Modified Shi et al. Solution
$\boldsymbol{\chi}$	Matrix of Sigma Vectors
$\boldsymbol{\chi}^{\boldsymbol{j}}$	The j'th Sigma Vector
$\boldsymbol{\chi}_{t_k}^{\boldsymbol{j}}$	The j'th Sigma Vector at the Time of the k'th Estimation Instant
$\boldsymbol{y}$	Y Coordinate or Axis
$\boldsymbol{y}^{\boldsymbol{i}}$	Y Coordinate of the i'th Sensor
$\boldsymbol{y}^{\boldsymbol{0}}$	Y Coordinate of the Target
$\widehat{\boldsymbol{y}}^{\boldsymbol{0}}$	Estimated Y Coordinate of the Target
$\boldsymbol{y}_{t_k}^{\boldsymbol{0}}$	Y Coordinate of the Target at the Time of the k'th Sampling Instant
$\boldsymbol{y}_{t_k^i}^{\boldsymbol{0}}$	Y Coordinate of the Target at the Time of the i'th Sensors Sampling Instant, Within the k'th Estimation Period
$\widehat{\boldsymbol{y}}_{t_k}^{\boldsymbol{0}}$	Estimated Y Coordinate of the Target at the Time of the k'th Sampling Instant
$\breve{\boldsymbol{y}}^{\boldsymbol{0}}$	Initial Guess of Targets' Y Coordinate for the Taylor Series Solution
$\boldsymbol{y}_{\boldsymbol{mm}}^{\boldsymbol{i}}$	Y Coordinate of the i'th Sensors Millimeter Wave Antenna
$\boldsymbol{y}_{\boldsymbol{vlc}}^{\boldsymbol{i}}$	Y Coordinate of the i'th Sensors VLC Source
$\boldsymbol{\delta y}^{\boldsymbol{0}}$	Y Axis component of the Target Estimation Error
$\boldsymbol{Y}$	Observed Signal
$\boldsymbol{\zeta}$	Sigma Point Spread Parameter
$\boldsymbol{z}^{\boldsymbol{i}}$	Z Coordinate of the i'th Sensor
$\boldsymbol{z}^{\boldsymbol{0}}$	Z Coordinate of the Target
$\widehat{\boldsymbol{z}}^{\boldsymbol{0}}$	Estimated Z Coordinate of the Target
$\breve{\boldsymbol{z}}^{\boldsymbol{0}}$	Initial Guess of Targets' Z Coordinate for the Taylor Series Solution
$\boldsymbol{z}_{\boldsymbol{mm}}^{\boldsymbol{i}}$	Z Coordinate of the i'th Sensors Millimeter Wave Antenna
$\boldsymbol{z}_{\boldsymbol{vlc}}^{\boldsymbol{i}}$	Z Coordinate of the i'th Sensors VLC Source
$\boldsymbol{\delta z}^{\boldsymbol{0}}$	Z Axis component of the Target Estimation Error
$\boldsymbol{z}$	Z Coordinate or Axis
$\boldsymbol{z}_{t_k}$	Measurement Vector at the k'th Estimation Instant
$\boldsymbol{z}_{t_k}^{\boldsymbol{i}}$	Measurement Obtained from the i'th Sensor, at the k'th Estimation Instant
$\boldsymbol{z}_{t_k^i}^{\boldsymbol{i}}$	Measurement Obtained from the i'th Sensor, at the Time of the i'th Sensors Sampling Instant, Within the k'th Estimation Period
$\boldsymbol{z}_{\boldsymbol{k}}^{\boldsymbol{mmw}}$	mmWave Measurement Vector at the k'th Estimation Instant
$\boldsymbol{z}_{t_k}^{\boldsymbol{vlc}}$	VLC Measurement Vector at the k'th Estimation Instant
$\mathbf{Z}_{t_k}^{\boldsymbol{j}}$	The j'th Propagated Sigma Vector
$\widehat{\boldsymbol{z}}_{t_k}$	Mean of the Transformed Observations

1 Introduction

1.1 Motivation

With the growing popularity of wirelessly connected devices, in all manner of fields and sectors, obtaining the exact position of a device presents a major potential advantage for a multitude of applications. The field of device localisation through wireless sensor networks, has introduced means to non-invasively track devices and subsequently those that carry them. This capability can be used to enrich user experiences within Virtual Reality (VR) applications and personal navigation, enhance industry performance through asset tracking and monitored delivery, and even autonomise drones and guide rockets into space. Within each of these applications the specifications, environments and networks present new challenges to overcome if growing demand is to be met.

Fortunately, the latest generation of networks referred to as 5th Generation (5G), like those before it, is set to bring in transformative radio access technologies. These will provide greater available bands of spectrum and New Radio (NR) transmission protocols as well as enhanced processing and network topologies such as Software Defined Networking (SDN) and Network Function Virtualization (NFV) which will enhance network flexibility. Employing the capabilities of such 5G networks is expected to greatly improve the accuracy, robustness, and computational efficiency of mobile device tracking.

This thesis comes as part of the Internet of Radio Light (IoRL) 5G project, a Horizon 2020 research program, aiming to establish a demonstrator for a 5G network within buildings. I, the author of this paper, joined the consortium six months into the project with a remit to research the Indoor Positioning System (IPS) and the various applications it could be used in.

Within this thesis, I present analysis of location data collected from the IoRL project measurement campaign. This data is then used to develop and evaluate a simulation model of the IoRL IPS. From the IPS modelling I identify points at which data is sampled asynchronously but to different degrees. By both assessing the effects of these asynchronous features and by considering existing solutions to the asynchronous problem, I propose a novel method in which to address the localisation challenges of asynchronous measurement sampling, while increasing the computational efficiency compared to existing solutions.

1.2 Thesis Contributions

1.2.1 Chapter 3

1. Experimental evaluation on the effects of centrally frosted Total Internal Reflection (TIR) lens characteristics on Visible Light Positioning (VLP) using 2D Received Signal Strength (RSS) trilateration techniques.
2. Proposed corrective calibration process for Visible Light Positioning (VLP) using 2D Received Signal Strength (RSS) trilateration for centrally frosted Total Internal Reflection (TIR) lenses (or those that emit a halo of increased intensity). Proven to decrease positioning error by 59% and 50% against applying datasheet values directly and using existing calibration techniques respectively.

1.2.2 Chapter 4

1. Simulated evaluation of a novel 5G localisation architecture involving the hybrid fusion of millimetre wave and VLP within the IoRL demonstration use case.

1.2.3 Chapter 5

1. Novel study into the effects of asynchronous sampling for range estimation and positioning in single sensor and multi-sensor systems respectively.
2. Comparative study on the effects of asynchronous sampling latency for non-linear localisation using both asynchronous and synchronous position estimation methods. Unlike existing studies this evaluation considers variable degrees of path non-linearity, sensor measurement noise and variable degrees of latency between consecutive sensor measurements.
3. Proposal and evaluation of adaptations to an existing asynchronous location estimator process for asynchronous sampling under nonlinear measurements.

1.2.4 Chapter 6

1. Proposal and study of a novel multisensor position estimation technique for sequentially asynchronous sampling and non-linear measurements. Simulations indicate the improved performance of the proposed estimation process against existing optimal estimators regarding both accuracy and computational demand for varying degrees of path non-linearity, sensor measurement noise and lack of sensor synchronisation.

1.3 Existing Publications

1.3.1 Peer Reviewed Journal Papers

1 Ali, Kareem, Cosmas, John, Zhang, Y., Zhang, H., Meunier, B., Jawad, N., Zhang, X., Shi, Lina, Gbadamosi, James, & Savov, A. (2021). Measurement Campaign on 5G Indoor millimeter Wave and Visible Light Communications Multi Component Carrier System.

2 Zhang, Y., Zhang, H., Cosmas, J., Jawad, N., Ali, K., Meunier, B., Kapovits, A., Huang, L.-K., Li, W., Shi, L., Zhang, X., Wang, J., Koffman, I., Robert, M., & Zarakovitis, C. C. (2020). Internet of radio and light: 5G building network radio and edge architecture. Intelligent and Converged Networks, 1(1), 37–57. https://doi.org/10.23919/icn.2020.0002

3 Shi, L., Shi, D., Zhang, X., Meunier, B., Zhang, H., Wang, Z., Vladimirescu, A., Li, W., Zhang, Y., Cosmas, J., Ali, K., Jawad, N., Zetik, R., Legale, E., Satta, M., Wang, J., & Song, J. (2020). 5G Internet of Radio Light Positioning System for Indoor Broadcasting Service. IEEE Transactions on Broadcasting, 66(2), 534–544. https://doi.org/10.1109/TBC.2020.2981755

1.3.2 Conference Proceedings

1. B. Meunier, J. Cosmas, N. Jawad and K. Ali, "Realising a new generation of 5G VR systems through Internet of Radio Light," 2020 IEEE International Symposium on Broadband Multimedia Systems and Broadcasting (BMSB), 2020, pp. 1-8, doi: 10.1109/BMSB49480.2020.9519726.
2. Meunier, B., & Cosmas, J. (2018). 5G Internet of Radio Light Virtual Reality System. IEEE International Symposium on Broadband Multimedia Systems and Broadcasting, BMSB. https://doi.org/10.1109/BMSB.2018.8436602
3. Cosmas, J., Meunier, B., Ali, K., Jawad, N., Salih, M., Meng, H. Y., Ganley, M., Gbadamosi, J., Savov, A., Hadad, Z., Globen, B., Gokmen, H., Malkos, S., Emre Cakan, M., Koumaras, H., Kourtis, M. A., Sakkas, C., Salomon, E., Avinoam, Y., … Kapovits, A. (2018a). A Scalable and License Free 5G Internet of Radio Light Architecture for Services in Homes Businesses. IEEE International Symposium on Broadband Multimedia Systems and Broadcasting, BMSB. https://doi.org/10.1109/BMSB.2018.8436938

1.3.3 Whitepaper Contributions

1. 5G PPP Technology Board. (2021). *Delivery of 5G Services to Indoors – the wireless wire challenge and solutions*. https://doi.org/10.5281/zenodo.4280750
2. 5GPPP, “AI and ML – Enablers for Beyond 5G Networks,” 2021, doi: 10.5281/zenodo.4299895.

2 Literature Review of Indoor Wireless Localisation

For decades, the ability to identify a person or devices' location indoors and outdoors accurately and reliably has been a key research area. Early civilisations used star constellations as reference points to determine their generalised orientations and enable navigation. Building on this fundamental need for surveying and navigation, the Global Positioning System (GPS) is a well-established Global Navigation Satellite System (GNSS) developed by the United States of America Department of Defence in 1973 [1]. The initial applications of GPS were limited for military and surveyors. In the present day though, GPS capabilities are found in almost all cars and mobile phones to provide navigational assistance to users.

In a digital era, as the number of network-connected devices increases rapidly [2] [3] and new applications arise, the public demand for greater performance of location-based services is met with increased density and urban or indoor communication challenges [4][5]. To address these matters, novel indoor positioning schemes and radio access technologies have been developed. From early positioning systems, which relied heavily on passive tracking techniques or invasive wearables [6][7] and were limited in deployment, the current widespread use of mobile devices and dense deployment of base stations has enabled new technologies and widespread implementation. Hybrid and adaptive position estimation techniques involving numerous technologies and sensors allow for modern localisation to improve accuracy by three to four orders of magnitude when compared to outdoor GPS [8].

This chapter presents a background to existing wireless indoor localisation methods. First, the preliminaries are introduced, covering the general concepts and processes involved in indoor wireless localisation and emphasising asynchronous data fusion for nonlinear systems. Secondly, comparisons and surveys of the latest research in relevant fields are given to highlight the current overview of existing systems. Thirdly, the Internet of Radio Light (IoRL) 5G Horizon 2020 system and related technologies are presented.

2.1 Introduction to Localisation Methods – Background and Preliminaries

Wireless localisation is neatly described by Jobs *et al.* [9] as the means of 'determining the position of a user/object by wireless signal'. Localisation has made great strides recently through advancements in, e.g., personal navigation where applications can provide estimates with centimetre to millimetre-levels of accuracy. Existing indoor localisation can be achieved through the combination of numerous wireless technologies with varying degrees of performance depending on the type of sensors available, algorithms implemented, and the application requirements. There is no single solution for all applications; hence various methods have been explored in the literature [8], [10]–[15]. While there

is a vast variety of possible technologies, processes, and overall positioning architectures, this section provides a generalised view of basic localisation schemes and the fundamental principles for context. To more easily evaluate the diversity of wireless localisation solutions, the following generalised framework is proposed wherein localisation systems are defined by four core components; Application, Sensor system(s), Data manipulation, and Output, as illustrated in Figure 2.1.

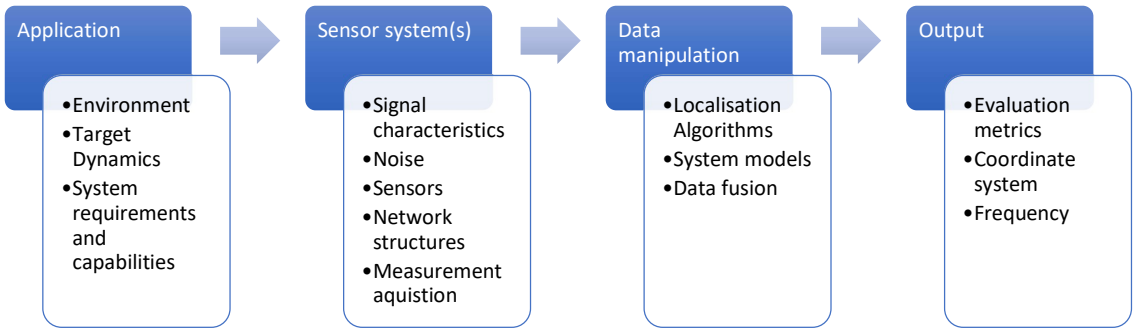

Figure 2.1 - Constituents of Location estimation processes

2.1.1 Application

Applications for indoor localisation continue to increase as the performance of indoor wireless sensor networks improve, and more smart devices are implemented within indoor environments. The recent expansion of the Internet of Things (IoT) devices [2], [16] influenced this greatly. Literature continues to expand on potential sectors in which position information can be utilised to improve the performance of existing systems or create new practices altogether. Key sectors where location data can be beneficial include transport, emergency responders, health, personal assistance, commercial, industrial and military. Examples of such systems are guidance for drones [17] and vehicles [18], enabling emergency responders to identify a 'person in need' [19], personal navigation [20], multisensory XR [21], automated tours [22], shopping navigation [23], and automation in smart factories [24].

While the core function of any location estimation system is to provide a user or device with an estimate of their position in space according to a given reference frame, the requirements and challenges that arise are not consistent due to the broad range of applications. These parameters influence the appropriate technologies and systems to implement.

Firstly, the type or number of targets to be localised in either 2D or 3D space can have significant implications on the system design. Dynamic targets present greater difficulty [25] when compared to static targets and have more stringent requirements, especially if the target movement is fast and complex to define. Active tracking systems describe a solution in which the target carries electronic sensor devices that can provide tracking data to the system [12], [26], [27]. Alternatively,

Passive tracking solutions lack these devices and must rely only on external systems. Depending on the application, a system designer may be limited to a specific setup and may need to consider portable power supplies.

Secondly, one must consider the system's environment regarding potential interference from existing signal congestion and potential multipath or blockages from physical obstacles. The environment may be dynamic, describing the nature of moving obstacles such as people or reflective surfaces. Additionally, systems may be limited by sensor coverage therefore the dimension of the environment must be considered. Moreover, the medium of the environment may impact the performance of a system and additional considerations must be made, where a target may need to be tracked underwater [28], in space or harsh climate conditions. This is important when regarding wireless signal propagation characteristics where atmospheric absorption may impact the system [29]–[34].

Finally, various applications demand different levels of performance with regard to precision, computation costs, estimation frequency, estimation latency and reliability.

In summary, the requirements and available solutions of a positioning service are heavily dependent upon the application, the metrics of which will be reviewed in later sections. Within this thesis, the consideration is limited to the scope of the IoRL project and the 5G applications laid out by both the IoRL consortium and Third Generation Partnership Project (3GPP) standardising body. In this respect, this thesis focuses on active multi-sensor[3] wireless indoor tracking of a single mobile device both in 2D and 3D space. Various IoRL project use cases within this setting are provided throughout the thesis and discussed in greater detail further in this chapter.

The following section provides preliminary information on existing sensor systems, technologies, and Indoor Positioning Systems (IPS) for context and background to the work presented in later chapters.

2.1.2 Sensor Systems

One principle that remains definite throughout any wireless localisation scheme is the use of sensors to obtain wireless signal characteristics. By acquiring these signal characteristics, it is possible to infer physical parameters and, consequently, estimate the target's potential location. Different signal characteristics are explored in literature. However, four standard identifiers, Received Signal Strength (RSS) [19], [35]–[38], Time of Arrival (TOA) [19], [39]–[45], Time Difference of Arrival (TDOA)[46]–[52] and Angle of Arrival (AOA) [19], [53]–[57], are discussed throughout this thesis. While AOA is not

[3] Multi-sensor system refers to a collaborative system of multiple sensors as opposed to a single-sensor system

directly applied within this body of work, it is discussed briefly for context as a prominent feature of wireless localisation.

2.1.2.1 Signal Characteristics for Active Systems

For wireless localisation to be performed, signal characteristics must be extracted from transmitted waveforms as they propagate through, and are affected by, an environment. From the resulting signal properties, it is possible to infer details of the environment and the location of the emitter or receiver. Signal characteristics are obtained through wireless communication between receivers and transmitters, which are types of sensors in this case. With such a multitude of different sensors and signal properties available, this section does not intend to explore the various types of sensors but, more specifically, the key signal properties that are commonly exploited in wireless localisation. A brief discussion regarding signal propagation is given to make sense of the following sensor systems and signal characteristics.

A signal is known to be subjected to noise $n(t)$ through a wireless channel, where t denotes time. Typically for ease of analysis, one may consider the channel to be an Additive White Gaussian Noise (AWGN) channel, where the noise component is AWGN with a two-sided spectral density $N_0/2$. An observed signal $Y(t)$ is then expressed as [58]:

$$Y(t) = s(t) + n(t). \tag{2.1}$$

Where s is the signal at time t. Throughout wireless propagation, a signal will undergo an assumed constant attenuation (α) and delay (τ). Therefore, the RF channel (U) between the transmitter and receiver can be modelled by [58]:

$$U(t) = \alpha\delta(t - \tau). \tag{2.2}$$

The received signal is then given by [58]:

$$\begin{aligned} Y(t) &= s(t) \otimes U(t) + n(t) \\ &= \alpha s(t - \tau) + n(t). \end{aligned} \tag{2.3}$$

Observing the propagation of signals as rays emitted from a transmitter, those rays that reach the receiver may do so through a direct path known as Line of Sight (LOS) or through varying paths that involve reflections from walls and other signals scattering objects. These reflected paths are referred to as the multipath components of a multipath system. To specify further, multipath signals can be registered by the number or 'order' of surface reflections encountered. Given that different objects

have different signal attenuation parameters regarding reflectivity and scattering [58]. Therefore, rays will arrive at the receiver with varying arrival times and signal powers. The obtained signal at the receiver is then the combination of all the paths that reach the receiver with their respective levels of attenuation and delay. The multipath channel with N_m multipath components is then modelled in the time domain as [59]:

$$U(t) = \sum_{j=1}^{N_m} \alpha^j \delta\left(t - \tau^j\right). \tag{2.4}$$

Here α^j and τ^j denote the attenuation and delay of the $j'th$ path, respectively. The received signal is therefore given by [59]:

$$Y(t) = s(t) \otimes U(t) + n(t) \; = \sum_{j=1}^{N_m} \alpha^j s\left(t - \tau^j\right) + n(t). \tag{2.5}$$

In multipath-rich environments, the LOS path can be challenging to distinguish from interfering multipath components; however, depending on the level of attenuation suffered by reflections or longer propagation paths, multipath components may not be as prominent. If the LOS path is not available, possibly due to obstruction, the situation is regarded as a Non-LOS (NLOS) system. In these cases, only multipath components are received. Figure 2.2 illustrates the concept of LOS and NLOS scenarios between a Transmitter (Tx) and a Receiver (Rx), as well as First Order Reflections (FOR) and Second-Order Reflections (SOR).

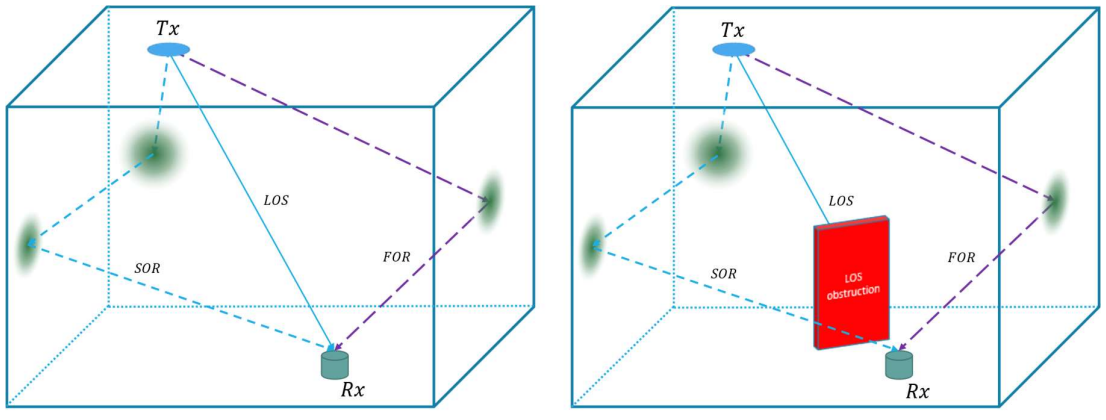

Figure 2.2 – LOS and NLOS environments with multipath components

In this thesis, the primary focus is on the use of LOS technologies as LOS signals are, for the purposes of the thesis, always considered to be obtained. However, the potential effects of multipath components are discussed and evaluated in parallel throughout.

2.1.2.1.1 Received Signal Strength (RSS)

The Received Signal Strength (RSS) of a signal obtained at a receiver is a simple, cheap and effective solution to calculate the distance between a transmitter and receiver. RSS principle relies on a known level of signal attenuation over a given distance [12], established by channel models that parameterise the Path Loss (PL) relative to the distance travelled. Many path loss models exist for different environments and technologies, each of which contain varying model parameters, values of parameters and mathematical functions [60][58]. RSS methods are widely adopted since very few, if any, adaptations must be made to systems to measure the received power of a signal. Here, the key signal characteristic is the attenuation factor α, as described in (2.2). A challenge for RSS based localisation is that a high number of environmental and system factors affect the channel and as a result the path loss, making the solutions very site specific [61][62] and prone to fluctuations. Challenges from randomly moving users or dynamic environments causes variable changes in the effects of signal attenuation, creating variability in the measured and modelled signal strengths [15]. Due to the nature of signal decay, RSS solutions are not viable for long distance ranging. It should also be noted that the RSS specifies the received signal power strength typically in decibel-milliWatts (dBm) or milliWatts (mW) as opposed to the Received Signal Strength Indicator (RSSI) which is a relative measure of the RSS with arbitrary units [15].

2.1.2.1.2 Time of Arrival (TOA)

The Time of Arrival (TOA) or 'Time of Flight' (TOF) of a signal describes the propagation time of a signal (τ), between the source and receiver. Using the measured time delay information and the known speed of the transmitted signal, it is possible to infer the distance travelled by the signal using (2.6) [53]. In (2.6), d denotes the distance of the signal path between the transmitter and receiver, τ represents the time delay between when the source is emitted and when the source is received as in (2.2), while c signifies the speed of the transmitted signal, this is commonly the speed of light for signals within the EM spectrum or the speed of sound for acoustic solutions.

$$d = \tau * c. \tag{2.6}$$

Due to the speeds of transmitted signals, the time resolution of TOA systems must be extremely small. Nanosecond-level timing synchronization is required for sub-meter accuracy [19]. Not only do TOA solutions require extremely high system clock speeds but synchronisation between the transmitter

and receiver must be equally as strict [61]–[63]. Since the hardware required to achieve the accurate time synchronisation and resolution required, TOA systems are considerably more complex and expensive to implement than RSS solutions. Atomic clocks are implemented on GPS satellites to maintain such high levels of timing accuracy.

Two-Way Ranging (TWR) [19][62], [64] methods measure the roundtrip propagation time to eliminate the need for tight clock synchronisation between both the receiver and transmitter. However, these methods require that the target and wireless system are both transceivers. The process involves emitting a signal from one node to another; the initial receiver then returns the signal directly back. The distance can be computed with prior knowledge of the computation time at the first receiving node through the following equation [64]:

$$d = \left(\frac{\tau_m - \tau_p}{2}\right) * c. \tag{2.7}$$

Here τ_m denotes the total measured Round-Trip Time (RTT) and τ_p represents the known processing time of the initial receiver.

Despite shadowing and obstruction being natural issues to TOA, it doesn't face the same concerns as RSS regarding free space losses [65]. The primary source of error within TOA systems is the timing errors, brought about by lack of synchronisation and LOS identification errors from poor timing resolution and multipath components [66].

2.1.2.1.3 Time Difference of Arrival (TDOA)

Time Difference of Arrival (TDOA) works similarly to TOA; however, TDOA determines the distance to a target using the difference in received propagation times between two signals [12]. This can be implemented in two ways, as illustrated in Figure 2.3, where the solid line signifies clock synchronisation between two sensors. While the need for tight system synchronisation is still apparent, this eliminates the need for more complicated synchronisation between transmitters and receivers [4], [63], [67]. Due to the subtractive nature of the process, the minimal number of sensors required for TDOA solutions is one greater than TOA or RSS due to the additional reference sensor necessary to form a substantial set of equations.

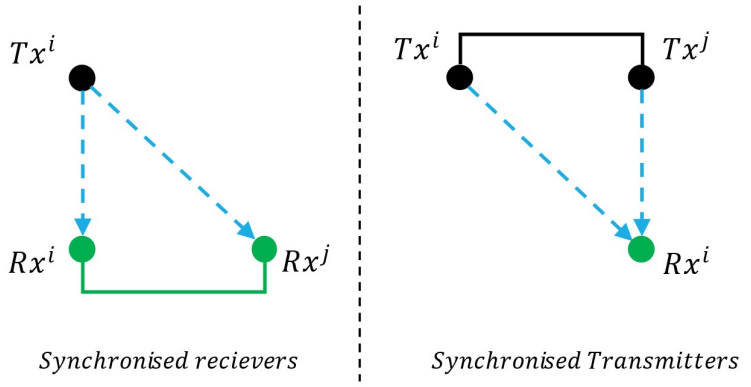

Figure 2.3 - TDOA technique with modified synchronised arrangements a) Synchronised receivers b) Synchronised transmitters

Once the TOAs have been received, the time difference between them [68] $(\tau^{i,j})$ is given as the TDOA. This forms a hyperbola on which the target lies.

$$d^{i,j} = \tau^{i,j} * c = (\tau^i - \tau^j) * c \tag{2.8}$$

Obtaining the TOA of a signal for both TOA and TDOA processes is achieved by one of two main approaches, correlation methods [21], [66], [67], [69] and energy detection [70]–[72]. It is important to stress the high time resolution required to obtain an accurate time estimate and, secondly, to distinguish the LOS path from multipath components. The receiver's ability to distinguish close multipath components and improve accuracy is dependent on the bandwidth [24], [52], [53], [62], [67], [73], [74].

2.1.2.1.4 Angle of Arrival (AOA)

The Angle of Arrival (AOA) solution uses a received signal to obtain the angle between the receiver and the target. This provides a bearing that is more accurately referred to as the Direction of Arrival (DOA). The benefit of the AOA approach is that only two receivers are needed to locate a target using the intersection of two path angles [75].

The AOA is inferred from the incoming signal using an array of antennas. Typically, the difference in phase or time of the signal at individual antenna elements can be used to infer the direction from which the signal arrived [61]. Alternatively, beam searching methods can be employed to detect the AOA [76]. Although AOA can provide accurate estimation when the transmitter-receiver distance is small, it use of antenna arrays requires more complex hardware [77] and careful calibration than RSS, TOA and TDOA techniques [67]. The accuracy deteriorates with increases in the transmitter-receiver distance [75]. A slight error in the angle of arrival calculation translates into a more significant

error in the actual location estimation [4] [8]. For a further exposé on AOA solutions, the reader is referred to Obeidat *et al*. [67] and the references therein.

2.1.3 Position Estimation Techniques

Given the reader's current understanding of the signal characteristics that can be utilised in a wireless sensor network, this section is intended to introduce the processes through which these signal characteristics can be used to estimate the position of a target device. Throughout this thesis, the mobile device to be located is referred to as the '*Target'*. In contrast*,* the sensors in fixed locations are referred to as the '*Sensors*', '*Base stations'*, '*Nodes*' or '*Anchors'* interchangeably.

2.1.3.1 Traditional Position Estimation Techniques

2.1.3.1.1 Proximity-based Localisation

When a mobile device is within the known coverage area of an anchor node, the mobile device's location can be associated with the coverage region of the connected anchor [14], [63]. For multisensor systems the target is co-located with the antenna that provides the strongest signal [61]. Fundamentally, proximity localisation provides the system with a generalised user location relative to the coverage area of a single antenna. Combining this with a more accurate RSS can minimise the region of estimated position [63]. While this solution is simple to implement, the accuracy is limited to that of the anchor's coverage [78]; more extensive coverage areas increase the uncertainty of this method. Therefore, densely populated networks of sensor nodes provide greater resolution.

2.1.3.1.2 Dead Reckoning

Dead reckoning is achieved with Inertial Measurement Units (IMUs) which are promising due to their compact size and cheap cost [79], [80]. Position estimates are calculated through the integration of acceleration measurements from accelerometers to obtain velocity and double integration to get displacement [5], [12]. IMUs can provide highly accurate localisation with high sampling rates in the order of thousands per second [12], [81]. A problem arises whereby errors arising from the double integration accumulate, and over time these grow to be very large. This leads to the position estimates 'drifting'. For this reason, Dead Reckoning often incorporates a secondary location estimate solution to repeatedly correct for the build-up of drift [5][63], [82].

2.1.3.1.3 Vision Analysis

Vision analysis is the process of using cameras as sensors to infer the user position from images. More specifically, the process identifies markers such as points, lines, spheres and angles within the images

[83] to relate the camera's position in world space. There are many different types of image-based systems; however, a distinction is made between fixed and mobile camera systems [4]. Fixed camera systems observe and locate a target within a designated Field of View (FOV) of the cameras used, whereas, in mobile camera systems, the target is equipped with a camera that uses images of the surroundings to locate itself. The latter is discussed further in this thesis. For a more comprehensive review, the reader is referred to Y. Wu *et al.* [83].

2.1.3.1.4 Scene Analysis – Fingerprinting

The principle of scene analysis relies on mapping the characteristics of signals within an environment, such that a reference database of unique 'fingerprints' is formed [21], [84]. The database is created during an offline stage and often requires surveying a large enough area with many data points to model the environment appropriately. During online measurements, the comparison using pattern matching techniques, between obtained measurements and the database infers the user position [85], [86]. Generally, having more data points recorded allows for a higher resolution in the online comparison phase [87], [88]. Due to the need to map individual areas, scene analysis is a highly site-specific approach. Furthermore, slight changes in the environment require repeated resurveying [89], [90], and the method is susceptible to dynamic noises [61], [72], [90].

2.1.3.1.5 Triangulation

Triangulation is the principle of attaining location estimated by forming triangles between the known coordinates of anchor nodes and the target. Triangulation has two subbranches, Angulation and Lateration that refer to the use of range-based or angle-based measurements.

2.1.3.1.5.1 Lateration

By determining a signal's TOA, RSS or TDOA, the distance between anchor nodes and a target can be estimated. These distances form a set of equations that define the geometric relationship of positions. Geometrically, the anchor nodes can be considered the centre points of circles (or the surface of the spheres) with radii equivalent to the length of the respective distance measurements obtained. The target may lie anywhere along the circumference of these circles (or spheres). Therefore, for 2D and 3D systems, the target's position is determined by the intersection of the circles or spheres, respectively. For 2D systems with two equations and 3D systems with three equations, the system is underdetermined. Therefore, an ambiguity arises as there can be multiple possible solutions. To obtain a unique solution, a 2D system requires a set of three equations, and 3D systems require a set of four equations. In practice, range estimations are subject to noise, and the desired point of

intersection is no longer apparent, as illustrated in Figure 2.4 for a 2D system. To overcome this level of uncertainty, the state of the target is given by the closest point of intersection.

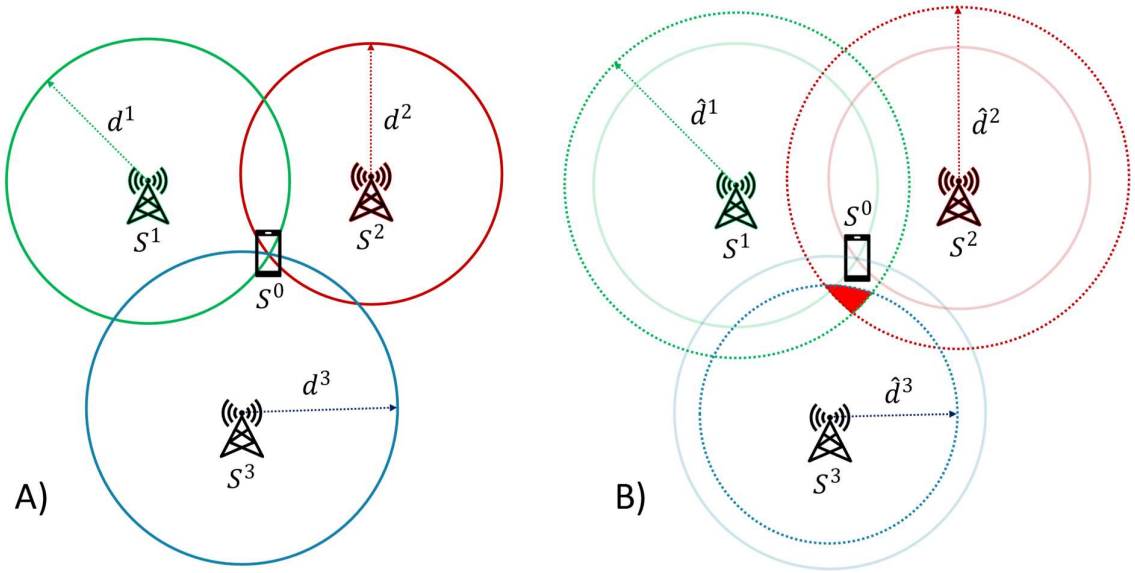

Figure 2.4 – 2D Trilateration and Errors for noiseless and noisy measurements A) Noiseless distance measurements with clear intersection locating the target device. B) Noisy distance measurements, indicated by dotted lines, produce position estimation errors and regions of uncertainty.

The Least Squares Solution

A standard approach to determining the multilateration solution involves applying the Least Squares solution (LSS). Taking an algebraic approach as presented in Norrdine *et al.* [91], one can consider a 2D system with N sensors observing a single target. The position of the sensors and target are given by $S^i = \left[x^i, y^i\right]^T$ for $i = (0, 1, \cdots, N)$ where $i = 0$ represents the target. The $i'th$ sensor $(i > 0)$ obtains a noisy range estimate $\left(\hat{d}^i\right)$ between itself and the target, given as the sum of the true distance (d^i) and the noise component (n^i) considered to be additive white Gaussian noise,

$$\hat{d}^i = d^i + n^i. \tag{2.9}$$

For general discussion, these noisy distance measurements and true distances are collated into $\tilde{d} = \left[\hat{d}^1, \hat{d}^2, \cdots, \hat{d}^N\right]^T$ and $\bar{d} = [d^1, d^2, \cdots, d^N]^T$ respectively, which gives:

$$\tilde{d} = \bar{d} + \bar{n}. \tag{2.10}$$

Here $\bar{n}$ is modelled as a zero-mean Gaussian random vector with diagonal covariance matrix C_d. Taking (2.9), d^i can be represented as [92]:

$$d^i = \left\|S^0 - S^i\right\| = \sqrt{(x^0 - x^i)^2 + (y^0 - y^i)^2}. \tag{2.11}$$

Therefore, substitution of (2.11) into (2.9) before re-arranging and squaring both sides as in C. H. Park & Chang [93] gives:

$$\begin{aligned}(x^0)^2 + (y^0)^2 - 2x^0x^i - 2x^0x^i \\ = \left(\hat{d}^i\right)^2 - \left(x^i\right)^2 - \left(y^i\right)^2 - 2\hat{d}^i n^i + \left(n^i\right)^2\end{aligned} \tag{2.12}$$

Applying the measurements obtained from the other $N-1$ sensors, in the same manner, defines a set of quadratic equations where the solution is the target coordinates. Under a sufficiently small noise assumption one can ignore the second-order noise terms [44][93][94]. The solution is given in the following matrix form [91]:

$$G\hat{\vartheta} = \hat{b} + e. \tag{2.13}$$

Here $e = D\bar{n}$ such that the complete representation is:

$$\begin{aligned}\begin{bmatrix} -2x^1 & -2y^1 & 1 \\ \vdots & \vdots & \vdots \\ -2x^N & -2y^N & 1 \end{bmatrix} \begin{bmatrix} x^0 \\ y^0 \\ (x^0)^2 + (y^0)^2 \end{bmatrix} \\ = \begin{bmatrix} \left(\hat{d}^1\right)^2 - (x^1)^2 - (y^1)^2 \\ \vdots \\ \left(\hat{d}^N\right)^2 - (x^N)^2 - (y^N)^2 \end{bmatrix} - 2\begin{bmatrix} \hat{d}^1 & 0 & 0 \\ \vdots & \ddots & \vdots \\ 0 & 0 & \hat{d}^N \end{bmatrix} \begin{bmatrix} n^1 \\ \vdots \\ n^N \end{bmatrix}.\end{aligned} \tag{2.14}$$

Ignoring the error e, the solution $\hat{\vartheta}$ is therefore given by the LSS [91] as:

$$\hat{\vartheta} = (G^T G)^{-1} G^T \hat{b}. \tag{2.15}$$

In cases where the measurement noises are uncorrelated with one another and have different uncertainties the solution is determined using the Weighted Least Squares (WLS) [91] solution,

$$\hat{\vartheta} = (G^T W^{-1} G)^{-1} G^T W^{-1} \hat{b}. \tag{2.16}$$

Where the weighting matrix W is given by the covariance of the random errors [68],

$$W = DC_d D. \tag{2.17}$$

Errors within the LSS multilateration solution result from the dependence on the accuracy of the ranging process [95]. Inaccurate range estimates hinder the identification of a unique intersection

point or even of any intersection at all. Additionally, one must be careful in the distribution of sensors due to the potential for flip ambiguity [94][96][97], which occurs when there are multiple potential intersections. This is typical in 3D systems where sensors are distributed across a flat ceiling in a rectangular arrangement. The common height leads to possible ambiguities in estimations which can be resolved by moving or adding a sensor at a different height or on the same plane but not on the circle formed by the position of the other sensors [17], [98], [99].

Hyperbolic Lateration

For TDOA measurements, the process is altered to reflect that the measurements obtained represent the difference between a single sensor's distance to the target and a reference sensor's distance to the target. Each TDOA measurement forms a hyperboloid of possible target positions where the two respective sensors are the foci [46]. As opposed to a sphere or a circle, the intersection of the hyperbolas presents the target. For N Anchor nodes within a system, there exists $(N-1)$ TDOA measurement equations [48].

Consider the same scenario given above for the circular/spherical multilateration technique where the first sensor $i = 1$ is taken to be the reference sensor and a 3D space is considered such that $S^i = \left[x^i, y^i, z^i\right]^T$ for $i = (0, 1, \cdots, N)$. The time difference between two sensors is given by $\tau^{i,1}$ for $i = (2, \cdots, N)$, which is converted to a distance using the propagation speed of the signal, typically the speed of light ($3* 10^8$ m/s) for Electro-Magnetic (EM) waves. From (2.11) a single TDOA measurement can be represented as follows [100]:

$$\begin{aligned}\hat{d}^{i,1} = \ & (d^i + n^i) - (d^1 + n^1) \\ & = \sqrt{(x^0 - x^i)^2 + (y^0 - y^i)^2 + (z^0 - z^i)^2} \\ & - \sqrt{(x^0 - x^1)^2 + (y^0 - y^1)^2 + (z^0 - z^1)^2} + \ n^{i,1}.\end{aligned} \tag{2.18}$$

In which $n^{i,1}$ represents the combination of both individual zero mean Gaussian white noise components n^i and n^1. The $(N-1)$ TDOA measurements define a set of non-linear hyperbolic equations, the solution of which gives the 3D coordinates of the target. For general discussion, these measurements are compiled as in (2.10) where $\tilde{d} = \left[\ \hat{d}^{2,1}, \hat{d}^{3,1}, \cdots, \hat{d}^{N,1}\right]^T$ and $\bar{n}$ is modelled as a zero-mean Gaussian random vector with diagonal covariance matrix C_n. Typically, due to the computation required, these solutions are first linearised and then solved by specific algorithms such as the Chan algorithm [101] and the Taylor Series [52], [100], [102]. The Taylor Series (TS) solution relies heavily on the suitability of the initial guess [100], and iterative steps can be computationally intensive. The

Chan solution requires general prior knowledge of the position to eliminate the ambiguous result that occurs from the square root process [52]. The Chan solution is also shown to be less effective than other solutions in near-field scenarios, meaning the target is close to the sensors [101][48]. In comparative studies [100][52], the Taylor Series solution shows an improved response due to ambiguous results in the Chan solution.

Taylor Series (TS) Solutions

The TS method linearises the set of non-linear hyperbolic equations by applying the Taylor-series expansion. Using an initial guess, an iterative method is then applied to solve the system of linear equations by determining the local linear LSS. For each measurement set the actual position of the target $S^0 = [x^0, y^0, z^0]^T$ is related to the initial guess $\check{S}^0 = [\check{x}^0, \check{y}^0, \check{z}^0]^T$ by errors in each coordinate $\delta S^0 = [\delta x^0, \delta y^0, \delta z^0]^T$ as:

$$S^0 = \check{S}^0 + \delta S^0. \tag{2.19}$$

One can denote the non-linear hyperbolic function given in (2.18) as a function of $\check{S}^0, S^i$ and S^1, denoted as $h^{i,1}(\check{S}^0, S^i, S^1)$. This function is expanded using the Taylor series using the initial estimate values $\check{S}^0$ and retaining only the first two terms [52].

$$\hat{d}^{i,1} \approx h^{i,1}\left(\check{S}^0, S^i, S^1\right) + a^{i,1}\delta x^0 + a^{i,2}\delta y^0 + a^{i,3}\delta z^0 + n^{i,1}. \tag{2.20}$$

In which,

$$a^{i,1} = \left.\frac{\partial h^{i,1}}{\partial x}\right|_{\check{x}^0,\check{y}^0,\check{z}^0} = \frac{x^1 - \check{x}^0}{\check{d}^1} - \frac{x^i - \check{x}^0}{\check{d}^i},$$

$$a^{i,2} = \left.\frac{\partial h^{i,1}}{\partial y}\right|_{\check{x}^0,\check{y}^0,\check{z}^0} = \frac{y^1 - \check{y}^0}{\check{d}^1} - \frac{y^i - \check{y}^0}{\check{d}^i}, \tag{2.21}$$

$$a^{i,3} = \left.\frac{\partial h^{i,1}}{\partial z}\right|_{\check{x}^0,\check{y}^0,\check{z}^0} = \frac{z^1 - \check{z}^0}{\check{d}^1} - \frac{z^i - \check{z}^0}{\check{d}^i},$$

where $\check{d}^i$ and $\check{d}^1$ are calculated using (2.11) where the target coordinates are given by the initial guess values of $\check{S}^0$. Then (2.20) can be rewritten as [52]:

$$G * \delta S^0 = D + \bar{n}. \tag{2.22}$$

Here,

$$G = \begin{bmatrix} a^{2,1} & a^{2,2} & a^{2,3} \\ \vdots & \vdots & \vdots \\ a^{N,1} & a^{N,2} & a^{N,3} \end{bmatrix}, D = \left[\hat{d}^{2,1} - h^{2,1}, \cdots, \hat{d}^{N,1} - h^{N,1}\right]^T,$$

and

$$\bar{n} = [n^{2,1}, \cdots, n^{N,1}]^T. \tag{2.23}$$

The LSS of (2.22) is given by (2.24):

$$\widehat{\delta S}^0 = (G^T G)^{-1} G^T D, \tag{2.24}$$

The initial guess $\check{S}^0$ is updated using (2.19) where an estimate of the coordinate errors $\left(\widehat{\delta S}^0\right)$ is estimated from (2.24). This process can be repeated to improve the response, as the results converge on a local solution.

2.1.3.1.5.2 Angulation

Angulation uses the intersection of measured angles, or 'bearings' obtained as AOA measurements between the target and known anchor positions to identify the target position [103]. This principle relies on the trigonometric properties of right-angled triangles where angle-side-angle measurements are sufficient to fully determine any triangle [76]. Using the known distance between anchors, only two transmitters and their AOA measurements are required to resolve the target location in 2D space [95]. In practical settings, due to measurement errors, the lines formed by multiple bearings may not intersect at a singular point [103] and therefore require best fit methods. Triangulation over large distances is highly sensitive to errors in the AOA measurements [8][61] [95].

2.1.3.1.6 Summary of Position Estimation Techniques

From the discussion above the suitability of positioning methods, these can be seen to be strongly dependant on the type of data available [95] and the application. For example, proximity based solutions are not suitable for providing high accuracy and scene analysis is not appropriate for dynamic environments. Obtained AOA measurements are suited to triangulation methods and RSS are fitting for proximity detection. These factors should be considered when establishing a wireless indoor positioning system.

The solutions presented so far provide valuable means to estimate the target position; however, more advanced filtering techniques can be applied to combine datasets and improve the

tracking performance of dynamic targets. These filtering processes are introduced in the following section.

2.1.3.2 Sensor Fusion and Tracking Filters

Sensor fusion, or synonymously *data fusion*, is well defined by Hall *et al.* [104] as techniques to

'*Combine data from multiple sensors, and related information from associated databases, to achieve improved accuracies and more specific inferences than could be achieved by the use of a single sensor alone.*'

In this respect this thesis refers particularly to multisensor fusion for state estimation, in which the state to be estimated is typically the target's position and relative data such as velocity or acceleration.

Each of the solutions and signal characteristics reviewed in Sections 2.1.2.1 and 2.1.3 have shown to have both advantages and disadvantages [8]. By combining two or more complimentary systems together, these shortcomings can be mitigated [105]. Where a single technique may lead to an erroneous result or fail to provide an estimate altogether, through fusion of additional data, the system can either improve or sustain a response. From an energy perspective, data fusion can be employed to reduce the number of redundant transmissions [106] and ambiguities. In general combining data from various sensors provides a means to enhance reliability, improve accuracy, and increase energy efficiency [107][108][109][106].

In particular, the sensor fusion considered throughout is achieved using the well-known Kalman Filters which were presented by R. E Kalman in 1960 [110]. Particle filters – another method for data fusion, involve iterative resampling of large quantities of data and are therefore not computationally efficient [111][108][80][112][113]. Due to the emphasis throughout this thesis on energy efficiency, Particle filters are not considered further. Additionally multi-target tracking techniques, such as Probability Density Hypothesis (PDH) filters, are not considered due to the focus throughout this thesis on localisation of a single target. For more details on these filtering processes the readers are referred to Elfring *et al.* [114] and Liu *et al.* [115], [116] respectively.

The following section introduces the Linear Kalman Filter (LKF) and its non-linear variants; the Extended Kalman Filter (EKF) and the Unscented Kalman Filter (UKF) for target tracking applications. This entails the operation of the filtering processes with insight into common system models and the tuning parameters.

2.1.3.2.1 Kalman Filters

The Kalman Filter (KF) describes a recursive solution to discrete data linear filtering. Since being introduced, the KF has become a standard approach for optimal estimation, owing to its fast recursive nature, efficiency, and robustness [117]. Many variations of the KF have been proposed and some have become well established, however, in this thesis the three main types are discussed: The Linear Kalman filter, the Extended Kalman filter and the Unscented Kalman Filter.

The KF provides many uses from smoothing and reducing noise [118]–[121], predictive tracking [7], [122]–[125], and data fusion [106], [108], [126]–[129].

Due to its versatility and numerous benefits, the KF has found applications within the fields of orbit calculation, signal noise reduction, and GPS [117].

From a high-level perspective, the KF can be seen as a feedback control system comprised of two stages, The prediction stage, and the update stage. In the prediction stage, the KF draws a prediction of the state at the next discrete time point, using a given model in the form of a linear state transition matrix, subsequently, this increments the filter in the time domain. The prediction is then compared, in the update step, with measurements using a weighting factor, established by the uncertainties of the prediction and measurements. The measurement that is applied can be considered the system feedback. The output is then returned to the prediction stage to repeat the process for the subsequent time step.

2.1.3.2.1.1 The Linear Kalman Filter

The Linear Kalman Filter (LKF) is the simplest form of the KF. This is an optimal linear estimator following the principles of Bayesian filter theories to estimate the state $X_{t_k} \in \mathbb{R}^{\hat{n}}$ of a discrete-time process controlled by the linear stochastic difference equation [120],

$$X_{t_k} = AX_{t_{k-1}} + Bu_{t_k} + w_{t_{k-1}}. \tag{2.25}$$

Where subscript t_k describes the adjoined value being related to the time of the k'th sampling instant. With a measurement $z_{t_k} \in \mathbb{R}^{\hat{o}}$ given by the following observation equation [130]:

$$z_{t_k} = HX_{t_k} + v_{t_k}. \tag{2.26}$$

Both $w_{t_{k-1}}$ and v_{t_k} respectively represent the process and measurement noise. These random variables are assumed to be normally distributed with zero mean, white noise and independent of one

another. The process noise and measurement noise are defined by their respective covariance matrices Q and R Such that [120]:

$$E(w) = 0, cov(w) = E(ww^T) = Q, \qquad \rho(w) \sim N(0, Q), \tag{2.27}$$

$$E(v) = 0, cov(v) = E(vv^T) = R, \qquad \rho(v) \sim N(0, R). \tag{2.28}$$

A is an $\hat{n}$ x $\hat{n}$ state transition matrix that relates the state at the previous time step (t_{k-1}) to the state at the current time step t_k. B is an $\hat{n}$ x l matrix relating an optional control input $u \in \mathbb{R}^l$ to the state. The measurement translation matrix H maps the state to the measurement z_{t_k}.

To distinguish the state at points within the process one may define $\hat{X}_{t_k}^-$ to be the prior state estimate, derived from the state transition matrix at time t_{k-1}, and $\hat{X}_{t_k}$ as the posterior state estimate, established by combining the measurements at interval t_k. From this, the priori and a posteriori estimate errors can be given as [82]:

$$e_{t_k}^- = X_{t_k} - \hat{X}_{t_k}^-, \tag{2.29}$$

$$e_{t_k} = X_{t_k} - \hat{X}_{t_k}. \tag{2.30}$$

The covariances of the a priori and a posteriori estimation deviations are defined by [121]:

$$P_{t_k}^- = E\left[e_{t_k}^- e_{t_k}^{-T}\right], \tag{2.31}$$

$$P_{t_k} = E\left[e_{t_k} {e_{t_k}}^T\right]. \tag{2.32}$$

Derivation of the KF equations aim to find an equation to calculate the a posteriori state estimate $\hat{X}_{t_k}$ as a linear combination of the a priori state estimate $\hat{X}_{t_k}^-$ and a weighted difference between an observation and a prediction of the measurement $\left(H\hat{X}_{t_k}^-\right)$ as given by [121]:

$$\hat{X}_{t_k} = \hat{X}_{t_k}^- + K\left(z_{t_k} - H\hat{X}_{t_k}^-\right). \tag{2.33}$$

The 'innovation' or residual $(z_{t_k} - H\hat{X}_{t_k}^-)$ describes the difference between the received measurement and the predicted measurement at the instant t_k. The Kalman gain, denoted by K, is an $\hat{n}$ x $\hat{o}$ matrix that determines the degree to which the innovation is combined with the a priori state estimate. Derivations of the Kalman gain involve equations which are provided in Maybeck & Siouris, and Welch & Bishop [120], [131] but ultimately the result is:

$$K_{t_k} = P_{t_k}^- H^T \left(HP_{t_k}^- H^T + R\right)^{-1}. \tag{2.34}$$

Notably from (2.34) as the measurement noise covariance R tends to zero, the value of K increases and weights the innovation more, thereby leaning the a posteriori state estimate towards the measurement [120]:

$$\lim_{R_{t_k}\to 0} K_{t_k} = H^{-1}. \tag{2.35}$$

Conversely, as the a priori process noise covariance matrix $P_{t_k}^-$ decreases, the Kalman gain reduces the weights of the innovation [120]:

$$\lim_{P_{t_k}^-\to 0} K_{t_k} = 0. \tag{2.36}$$

It is important to highlight this behaviour since the response of the filter is highly dependent on the weights of Q and R [132], [133]. These weights influence the Kalman gain and therefore determine the level to which the output agrees with the prediction or measurement.

Following *Bayesian theory,* (2.33) stems from the probability of the a priori estimate conditioned on all prior measurements. The a posteriori state estimate represents the mean of the state distribution, which is distributed normally if (2.27) and (2.28) are met, while the posteriori estimates error covariance matrix P_{t_k} reflects the variance of the state distribution [82], [120].

$$E\left[X_{t_k}\right] = \hat{X}_{t_k},$$
$$E\left[\left(X_{t_k} - \hat{X}_{t_k}\right)\left(X_{t_k} - \hat{X}_{t_k}\right)^T\right] = P_{t_k},$$

Therefore, (2.37)

$$\therefore \rho\left(X_{t_k}|z_{t_k}\right) \sim N\left(E\left[X_{t_k}\right], E\left[\left(X_{t_k} - \hat{X}_{t_k}\right)\left(X_{t_k} - \hat{X}_{t_k}\right)^T\right]\right)$$
$$= N\left(\hat{X}_{t_k}, P_{t_k}\right).$$

The resultant LKF equations are given by:

Prediction stage		**Update stage**	
$\hat{X}_{t_k}^- = A\hat{X}_{t_{k-1}} + Bu_{t_k}$	(2.38)	$K_{t_k} = P_{t_k}^- H^T\left(HP_{t_k}^- H^T + R\right)^{-1}$	(2.40)
$P_{t_k}^- = AP_{t_{k-1}}A^T + Q$	(2.39)	$\hat{X}_{t_k} = \hat{X}_{t_k}^- + K_{t_k}(z_{t_k} - H\hat{X}_{t_k}^-)$	(2.41)
		$P_{t_k} = \left(I - K_{t_k}H\right)P_{t_k}^-$	(2.42)

The KF under linear process and measurements functions and with noise which follows a Gaussian distribution is the optimal theoretical solution [108]. Nevertheless, these conditions are

rarely met in practical settings, yet under slight deviations the KF is robust enough to make reasonable estimations. For inherently non-linear process and measurement relationships non-linear variations of the Linear Kalman filter, namely the EKF and UKF have been established.

2.1.3.2.1.2 The Extended Kalman Filter (EKF)

The EKF approach attempts to linearise the estimate around a current state estimate using the first-order derivatives of the measurement and process functions [117]. By computing the Jacobians at each time step it is possible to locally linearise the non-linear function, in a process that is somewhat similar to the Taylor series. The process to be estimated is like that of the LKF, though, described by a non-linear stochastic difference equation given by [120]:

$$X_{t_k} = f\left(X_{t_{k-1}}, u_{t_k}, w_{t_{k-1}}\right), \tag{2.43}$$

And with a non-linear measurement function given by [120]:

$$z_{t_k} = h\left(X_{t_k}, v_{t_k}\right). \tag{2.44}$$

All variables are equivalent to those described in the LKF section however f represents the non-linear function that relates the previous time step t_{k-1} to the current time step t_k. The non-linear relationship between the state X_{t_k} and the measurement z_{t_k} is described by h. As with the LKF, the EKF equations follow the same prediction and update structure. While the EKF has found applications in robot localisation [108], [134] and IMU fusion [80] the process requires the iterative re-computation of Jacobian matrices, and this is not computationally efficient [82][108]. Additionally, the EKF relies heavily on a suitable initial estimate for linearisation and that the degree of local non-linearity of the functions being approximated is not too great. Results can be shown to deviate if the non-linearity of the system is too great [135][111] [82].

2.1.3.2.1.3 The Unscented Kalman Filter (UKF)

The UKF uses the framework of the LKF but applies the Unscented Transform (UT), leading to a definite sampling approach as opposed to a random sampling strategy. These sample points are referred to as sigma points, and while the number can vary depending on the strategy adopted the most common is to use $2\hat{n} + 1$ symmetrical sampling. Where $\hat{n}$ represents the dimension of the state to be estimated.

The Unscented Transform (UT) is a solution for calculating the statistics of a random variable after being transformed non-linearly [111]**.** The premise of the UKF is to use weighted sigma points to capture the mean and covariance of the original distribution. These points then maintain Gaussian distributions through non-linear functions up to the second order of non-linearity [108], [111], [136], [137]. The sigma points are chosen deterministically; used to map the Gaussian distribution; they are then non-linearly transformed; and finally used to reform a Gaussian distribution. Similar approaches to represent states through sampling has been proposed where the sampling points are selected differently regarding their number, weights, and values [137]. The process of the UKF is detailed below:

Generating sigma points

Firstly, the sigma points are deterministically defined as a matrix χ of $2\hat{n}+1$ sigma vectors χ^j [136]:

$$\chi_{t_{k-1}}^{0} = X_{t_{k-1}}, \tag{2.45}$$

$$\chi_{t_{k-1}}^{j} = X_{t_{k-1}} + \left(\sqrt{(\hat{n}+\lambda)P_{t_{k-1}}}\right)_{t_{k-1}}^{T}, \qquad (j = 1, \cdots, \hat{n}) \tag{2.46}$$

$$\chi_{t_{k-1}}^{j+\hat{n}} = X_{t_{k-1}} - \left(\sqrt{(\hat{n}+\lambda)P_{t_{k-1}}}\right)_{t_{k-1}}^{T}. \qquad (j = 1, \cdots, \hat{n}) \tag{2.47}$$

The corresponding sigma weights are appointed as follows where the superscript m denotes the mean weights and the superscript c is a covariance weight [111]:

$$W^{0,m} = \lambda/(\lambda+\hat{n}), \tag{2.48}$$

$$W^{j,m} = 1/\big(2(\lambda+\hat{n})\big), \qquad (j = 1, \cdots, 2\hat{n}) \tag{2.49}$$

$$W^{0,c} = W^{0,m} + (1-\zeta^2+\beta), \tag{2.50}$$

$$W^{j,c} = 1/\big(2(\lambda+\hat{n})\big). \qquad (j = 1, \cdots, 2\hat{n}) \tag{2.51}$$

The scaling parameter λ is determined as in (2.52) [111]:

$$\lambda = \zeta^2(L + \hat{n}) - \hat{n}. \tag{2.52}$$

Where ζ determines the spread of sigma points around the mean $X_{t_{k-1}}$, usually applied as a small positive value. L is another scaling parameter, often set to zero and β incorporates prior knowledge of the distribution of $X_{t_{k-1}}$ ($\beta = 2$ is optimal for Gaussian distributions) [138]. Following the same KF structure of prediction and update stages, the UKF prediction involves propagating the set of sigma vectors through the non-linear measurement function.

Prediction:

The set of sigma vectors are propagated through the non-linear process function f and subsequently incremented in time [136].

$$\chi_{t_k}^j = f\left(\chi_{t_{k-1}}^j\right), \qquad (j = 0, \cdots, 2\hat{n}) \tag{2.53}$$

The mean and covariance of the time updated distribution $\chi_{t_k}^j$ are approximated by using the weighted sample mean and covariance of the propagated sigma points, respectively [136].

$$\hat{X}_{t_k}^- = \sum_{j=0}^{2\hat{n}} W^{j,m} \chi_{t_k}^j, \tag{2.54}$$

$$P_{t_k}^- = \sum_{j=0}^{2\hat{n}} W^{j,c} \left(\chi_{t_k}^j - \hat{X}_{t_k}^-\right)\left(\chi_{t_k}^j - \hat{X}_{t_k}^-\right)^T + Q_{t_{k-1}}. \tag{2.55}$$

Measurement update:

The propagated sigma vectors are then transformed through the non-linear measurement function h [136].

$$\mathrm{Z}_{t_k}^j = h\left(\chi_{t_k}^j\right) \tag{2.56}$$

The mean and covariance (innovation covariance) of the resulting transformed observations are given in (2.57) and (2.59) [136].

$$\hat{z}_{t_k} = \sum_{j=0}^{2\hat{n}} W^{j,m} \mathrm{Z}_{t_k}^j, \tag{2.57}$$

$$P_{t_k}^{zz} = \sum_{j=0}^{2\hat{n}} W^{j,c} \left(\mathrm{Z}_{t_k}^j - \hat{z}_{t_k}\right)\left(\mathrm{Z}_{t_k}^j - \hat{z}_{t_k}\right)^T + R. \tag{2.58}$$

The cross covariance between $\hat{z}_{t_k}$ and $\hat{X}_{t_k}^-$ is then given by [136]:

$$P_{t_k}^{xz} = \sum_{j=0}^{2\hat{n}} W^{j,c}\left(\chi_{t_k}^j - \hat{X}_{t_k}^-\right)\left(\mathrm{Z}_{t_k}^j - \hat{z}_{t_k}\right)^T. \tag{2.59}$$

The Kalman gain is computed by using the innovation and cross-covariance matrices [136]:

$$K_{t_k} = P_{t_k}^{xz}(P_{t_k}^{zz})^{-1}. \tag{2.60}$$

The resulting state estimate and covariance are calculated by the Kalman gain of the innovation between the propagated estimated prediction ($\hat{z}_{t_k}$) and the measurement (z_{t_k}) and are given by [136]:

$$\hat{X}_{t_k} = \hat{X}_{t_k}^- + K_{t_k}\left(z_{t_k} - \hat{z}_{t_k}\right), \tag{2.61}$$

$$P_{t_k} = P_{t_k}^{\gamma} - K_{t_k}P_{t_k}^{zz}K_{t_k}^T. \tag{2.62}$$

Again, in the same manner as the EKF, the UKF requires re-computation of the weighted sigma points through each iteration of the filter and the UKF and EKF have the same order of computations [111], [138]. While the UKF doesn't require Jacobian matrices to be computed [111], simulations indicate the UTs require more computation time [137]. However, the UKF is considerably more stable than the EKF, as the non-linearisation can be more extreme and does not depend greatly on an initial estimate. In General, the UKF is considered superior to the EKF in both theory and in practical applications [117], [137], [139], [140].

2.1.3.2.1.4 Kalman Filters for Sensor Fusion

From the formulations above, the KF and variations are useful and lightweight tools for prediction of state estimates where the combination of provided predictions and measurements reduces the noise within the response. Notably, for instances where measurements are missing, estimations can be generated using the prediction stage independently, thus increasing the robustness of the response.

The KF processes described previously highlight how the KF efficiently fuses state estimates from the prediction and measurements. The same approach can be applied to effectively fuse numerous measurements together. This can be accomplished using homogenous or non-homogenous

sensor measurements, the latter approach simply requires a sensor specific measurement translation matrix H or measurement function h. Sensor fusion using the KF can be approached in one of two ways; multiple sensor values can be mixed in the observation model or sensors can be used as estimation inputs and others can be applied in the update [130]. The latter approach lacks the smoothing contributed by the applied motion model.

2.1.3.2.1.5 Tracking System Models

Within the context of tracking, the prediction step is generally a linear transformation while the update step is defined by a measurement model that is either linearly or non-linearly related to the state. The chosen model used by a KF is crucial for good performance and, while deviations are to be expected in practical use cases, a model should reflect the true system dynamics as best as possible. Various models, both in discrete and continuous time representations have been proposed and explored throughout literature for use in target tracking people with varying degrees of success [25]. Throughout this thesis, the focus is on tracking applications, therefore, the following popular models, namely the Constant Velocity (CV) [132], [133], [141] and Constant Acceleration (CA) [124], [141] models are explored.

Constant Velocity (CV)

The CV model, as the name suggests, describes a target travelling at a constant velocity. Therefore, the state transition matrix A, within the LKF equations given in (2.38) is presented in (2.63) for a second order system in one dimension, in the absence of a control input matrix (u_{t_k}). The term 'second order' refers to where only the position and velocities are included in the state in Cartesian form. Such that the state to be estimated is of the form $X = [x, v^x]^T$, which represent the targets x-coordinate and velocity in the x-axis (v^x) in terms of Cartesian coordinates. As (2.63) states, for each timestep, the Cartesian coordinates are incremented by the product of the estimated velocity component at magnitude of the time-step Δt [142]:

$$\begin{bmatrix} x \\ v^x \end{bmatrix} = \begin{bmatrix} 1 & \Delta t \\ 0 & 1 \end{bmatrix} \begin{bmatrix} x \\ v^x \end{bmatrix}. \tag{2.63}$$

A 2D or 3D representation can be simply obtained by the inclusion additional dimension parameters.

Constant Acceleration (CA)

Alternatively, KF designers may wish to opt for the CA model, in which the state is defined by a third order system such that the acceleration components in all dimensions are to be estimated in addition

to the velocity and position components. Therefore, the state to be estimated is given by $X = [x, v^x, a^x]^T$ where a^x denotes the acceleration components in the x-axis. Following the kinematic equations for displacement under constant acceleration one can obtain the following 2D matrix representation of (2.38) with no control input u_{t_k} [141]:

$$\begin{bmatrix} x \\ v^x \\ a^x \end{bmatrix} = \begin{bmatrix} 1 & \Delta t & \Delta t^2/2 \\ 0 & 1 & \Delta t \\ 0 & 0 & 1 \end{bmatrix} \begin{bmatrix} x \\ v^x \\ a^x \end{bmatrix}. \tag{2.64}$$

Similarly, to the CV model, a 2D or 3D representation can be simply obtained by the inclusion of additional dimension parameters.

2.1.3.2.1.6 System Identification

From the relationship defined in (2.34) and evaluated in (2.35) and (2.36) the values of the process noise and measurement noise covariance matrices have an evidently strong influence on the filter performance, and are generally considered to be the tuning parameters of the KF. Small Q values produce small gains that lead to good measurement noise reduction but reduce the filters response to measurements and thus lead to large latency during manoeuvres or potential divergence [117], [132], [133], [143]. The values and structures applied should be considered to provide the optimal description of the relationship between state variables as well as descriptions of the level of noise in either the measurements or the level to which the model correctly describes the system dynamics at any given instant. The process of determining the appropriate structures and noise values is referred to as system identification. In many cases, it is important for a filter designer to avoid overfitting the noise parameters to function optimally only under highly specific settings. Doing so reduces flexibility in the system and may lead to greater errors when the system is exposed to other settings.

The measurement noise covariance matrix R can be determined through evaluating offline measurements to determine the standard deviations in each variable [120]. For a second order one-dimensional system, where the received observation is the targets Cartesian x coordinate, the measurement translation matrix and measurement covariance matrix are typically given by [133][141]:

$$H = \begin{bmatrix} 1 & 0 \end{bmatrix}, \text{ and } R = \begin{bmatrix} \sigma_x^2 \end{bmatrix}, \tag{2.65}$$

Where the σ_x^2 denotes the variance of the single x-axis measurements. The measurement model given in (2.65) also assumes independent noise parameters are completely independent.

The process noise covariance matrix (Q) is less trivial to determine, and throughout the literature there has been no fully established method for deriving it, therefore, KF designers must perform system identification with careful regard not to perform overfitting of a system. This often includes tedious trial and error to determine a reasonable optimum for the given application. Several structures for the process noise covariance matrices have been derived for CV and CA models to describe the relationship between the state parameters. However, each still requires the identification of an additional scaling value to describe the model uncertainty. Various motion models are considered in Li & Jilkov [25] and derivations for the discrete-time motion model and continuous-time motion models are given along with their respective noise covariance matrices. Three process noise covariance matrices are explored and evaluated in Saho & Masugi [144].

Throughout this thesis only discrete time KFs are explored, therefore, to discretise the noise term, the highest order term is taken to be constant throughout the duration of each sampling period but different and uncorrelated for each sampling period [145].

For the second order CV model presented in Section 0 the commonly used Discrete-time Nearly Constant Velocity model (DNCV) [25] [144][142][137] uses a process noise covariance matrix that describes a random acceleration to account for small deviations in velocity. For the tracking applications expanded on throughout this thesis, the target is not influenced by any known input, hence, the control input u_{t_k} is omitted. Therefore, the discrete time dynamic model in the presence of noise and under no control input is given by [132]:

$$X_{t_k} = AX_{t_{k-1}} + w_{t_{k-1}}.$$

For the DNCV scenario, the dynamics are considered to have a small constant acceleration component a_k between time instants t_k and t_{k-1}, that is normally distributed with zero mean and standard deviation σ_a, therefore, $a_k = N(0, \sigma_a^2)$. The acceleration component is related to the state by the acceleration translation matrix, F, such that [25]:

$$X_{t_k} = AX_{t_{k-1}} + Fa_{t_{k-1}}. \tag{2.66}$$

For a second order, one-dimension DNCV model one can apply standard kinematics equations with the CV matrices presented previously but include the constant acceleration as a component of the noise term such that:

$$\begin{bmatrix} x \\ v^x \end{bmatrix} = \begin{bmatrix} 1 & \Delta t \\ 0 & 1 \end{bmatrix} \begin{bmatrix} x \\ v^x \end{bmatrix} + \begin{bmatrix} \Delta t^2/2 \\ \Delta t \end{bmatrix} a_{t_{k-1}} \tag{2.67}$$

From here, one can ascertain the covariance matrix of the process noise component as follows [25]:

$$w_k = F a_{t_{k-1}}$$

$$\begin{aligned} Q = Var\left(w_{t_{k-1}}\right) = E\left[w_{t_{k-1}} w_{t_{k-1}}^T\right] = E\left[F a_{t_{k-1}} a_{t_{k-1}}^T F^T\right] = \\ FE\left[a_{t_{k-1}} a_{t_{k-1}}^T\right] F^T = F\sigma_a^2 F^T = FF^T\sigma_a^2, \end{aligned} \tag{2.68}$$

Therefore,

$$Q = \begin{bmatrix} \Delta t^4/4 & \Delta t^3/2 \\ \Delta t^3/2 & \Delta t^2 \end{bmatrix} \sigma_a^2.$$

As for the CA model, the simplest noise model is referred to as the white noise acceleration model [25], which assumes the target's acceleration is a completely independent process and only differs from the DNCV model in that the noise component is greater. The Wiener-process acceleration model assumes the acceleration to process with independent increments. The same mathematical approach can be applied to the third-order process, however, the white process noise component is considered as a discrete-time Weiner process [145] and referred to as the Weiner- sequence acceleration model in Li & Jilkov [25]. Hence A and $w_{t_{k-1}}$ are given by [143]:

$$A = \begin{bmatrix} 1 & \Delta t & \Delta t^2/2 \\ 0 & 1 & \Delta t \\ 0 & 0 & 1 \end{bmatrix}, w_{t_{k-1}} = F a_{t_{k-1}} = \begin{bmatrix} \Delta t^2/2 \\ \Delta t \\ 1 \end{bmatrix} a_{t_{k-1}}. \tag{2.69}$$

Therefore, following the same approach taken in (2.68) one can posit the process noise covariance matrix Q to be [25][143]:

$$w_{t_{k-1}} = F a_{t_{k-1}},$$

$$\begin{aligned} Q = Var\left(w_{t_{k-1}}\right) = E\left[w_{t_{k-1}} w_{t_{k-1}}^T\right] = E\left[F a_{t_{k-1}} a_{t_{k-1}}^T F^T\right] = FE\left[a_{t_{k-1}} a_{t_{k-1}}^T\right] F^T \\ = F\sigma_a^2 F^T = FF^T\sigma_a^2, \end{aligned} \tag{2.70}$$

Therefore,

$$Q = \begin{bmatrix} \Delta t^4/4 & \Delta t^3/2 & \Delta t^2/2 \\ \Delta t^3/2 & \Delta t^2 & \Delta t \\ \Delta t^2/2 & \Delta t & 1 \end{bmatrix} \sigma_a^2.$$

Generally, The noise covariance matrices are assumed to be constant throughout filter operation, as indicated by the lack of the time associated subscript t_k in equations (2.39) and (2.40). For systems where the Q and R are in fact constant, the estimates covariance matrix and Kalman gain will converge to constant and stable values [120].

Throughout this sub-section, the process of advanced filter techniques, namely the linear and non-linear KFs have been presented for use within target tracking applications. Observations have been made regarding the KF's ability to reduce noise in measurements, perform predictions, and fuse multiple datasets, which is exploited throughout this thesis. Notably, the process and measurement noise covariance matrices act as tuning parameters that dictate the KF's response.

2.1.4 Review of Existing Indoor Localisation Systems

This section concludes the four-stage description of localisation systems illustrated in Figure 2.1, wherein the output of the system is a product of all the design parameters considered within the application, sensors, and processes discussed above.

This section initially discusses the evaluation criteria of specifically indoor positioning systems using wireless sensor networks for people or mobile device tracking. A summary of existing relevant systems is then presented to provide context to the performance of existing systems and highlight the range of techniques. This summary is by no means exhaustive, therefore, for more particular details the reader is encouraged to consider the following literature. Kozlowski *et al.* [107] and Deak *et al.* [27] provide insightful details of localisation from the sensor and device perspectives respectively. Xiao *et al.* [90] considers a broader catalogue-based approach to existing systems, while Y. Gu *et al.* [86] focuses more on localisation within the context of personal networks.

2.1.4.1 Evaluation Metrics

Various existing surveys [4], [8], [12], [15], [27], [61], [63], [67], [75], [86], [90] and literature [107], [146] propose performance metrics for the systems they evaluate. In general, similar metrics are expressed across most studies, however, the diversity in performance metrics typically arises from contextually biased papers while others may group parameters differently. The selection of metrics presented is selected to best reflect those across the various literatures explored.

2.1.4.1.1 Accuracy & Precision

Arguably, the most valuable localisation metric, the accuracy of a system is commonly determined as the average Euclidian distance between the estimated location of the target and the true location of the target in 2D or 3D space. The precision, defined as the success probability of position estimations with respect to predefined accuracy, Gu *et al.* [86] considers how consistently the system works by revealing the variability in performance. However, there is a trade-off between these and other characteristics where a compromise between "suitable" accuracy and other metrics is needed.

2.1.4.1.2 Reliability / Fault Tolerance

In general, an indoor localisation solution is constructed with numerous components in which sources of error may occur. These errors may affect both the accuracy and the likelihood that an estimate is generated. Observing the system at the sensor level, Deak *et al.* [27] discusses how all sensors obtain measurements with some degree of noise. These errors may be inherent in the sensing modality, the environment, introduced during the sensors manufacture or stem from other factors such as pushing for energy efficiency. These factors can contribute towards either a noisy measurement or, more drastically, a sensor being unable to provide any measurement at all. Furthermore, the way in which a system processes or considers data within a system can impact both the response and the likelihood a position estimate is generated. Some solutions, such as the LSS are less effective under higher noise due to small noise assumptions or the potential for ambiguities. Moreover, hybrid solutions or network structures are better equipped to generate estimates when a sensor fails.

2.1.4.1.3 Energy Efficiency

With devices becoming more automated and mobile, localisation of battery-operated devices is in growing demand. In turn, energy efficiency incurs lower running costs, increased active lifetime for battery powered devices and reduces the environmental impact. Typically, a system implemented under stricter performance requirements is subjected to trade-offs in energy efficiency, as the system requires further complexity to achieve the desired output.

2.1.4.1.4 Latency

The latency of an indoor positioning system can be used to describe both the frequency of the estimates provided and the overall estimation latency, which is the length of time taken for an estimate to be obtained by the device from the instant the position estimate is obtained. Both elements are crucial in real-time tracking applications and are heavily related to the sampling rate of

sensors, computation time, and transmission protocols [86]. The latency is an important factor which can affect the response time of applications and suitability for highly dynamic targets.

2.1.4.1.5 Scalability

As expressed by Liu *et al.* [61]**,** the scalability of a system can be regarded in terms of geography or density. The geography describes the area or volume of coverage that systems can provide. This is typically related to the observable range of the individual sensors and the potential requirement for collocation from a specific number of sensors. The dimensionality of an IPS, such that it can describe a target in 2D or 3D space is also an important consideration. The density describes the number of objects a system can locate within a given period. The more devices a system can serve at one time the more desirable the system may be.

2.1.4.1.6 Complexity

Demanding improved performance or functionality from a system naturally incurs the need for increased complexity with regards to managing increased data and carrying out a greater number of tasks. The complexity of a system can be attributed to hardware, software, and operation factors [61]**.** The more widely regarded in literature is the software or computational complexity of a system, which relates to the processes and algorithms used. This directly effects energy constraints on less powerful and mobile devices where less intensive processing is desirable. Due to the difficulty in defining the analytic complexity of the processes involved in location estimation, the computation time of the process is generally considered. The hardware and operation factors can be attributed to complex deployment and maintenance, especially if a solution requires lots of prior information for calibration. Counter-intuitively, a system may be more complex to operate due to a simplified or limited system. One such example is where a system relies on the targets orientation to be limited during use. This is less intuitive to use and, therefore, more complex from a user perspective.

2.1.4.1.7 Cost

The cost of a system is strongly influenced by the complexity of the application, which in turn dictates the type and number of sensors required. The cost of a positioning system can be considered within the following subsets: monetary, time, space, weight, and energy [61]. The contributing factors lie in the hardware, infrastructure, installation, and maintenance [90]**.** The most direct costing is the financial costings required by each of the four factors. Time costs refer to the efforts of operation required in installation and maintenance [86]**.** The space and weight costs of the device and infrastructure hardware describe the form factors limitations and mobility of a system. These

considerations may affect the installation and maintenance. Energy cost is primarily related to the maintenance and lifetime of a system or device. Notably, a system can benefit from reduced costings if it exploits existing infrastructure or hardware.

2.1.4.2 Established Systems

As discussed throughout this chapter, wireless spatial localisation systems can be categorised by the signal characteristics measured by the sensors (AOA, TOA, TDOA, RSS) and the process applied (triangulation, fingerprinting etc.). To highlight the diversity of these solutions within various approaches, the explored solutions are catalogued by the physical layer in which they operate. i.e., the wireless technology used to communicate with the mobile or static devices. To further limit the scope of this study, the solutions considered in this section are constrained to active systems, characterised by the solutions need to have electronic devices situated on the target, that actively utilise data from anchors. Alternatively, passive systems consider less invasive methods in which the target is tracked without the need for any worn, carried, or embedded electronic devices.

The technologies considered within this overview are sound, optical, and radio frequency (RF) signals. Satellite navigation [147], magnetic signals [148] [149], Inertial Measurement Units (IMU) [150], and image-based [23] [151] [152] localisation solutions are omitted from the following discussion as these solutions are either not commonly used for indoor localisation or do not consider the signal characteristics discussed in earlier chapters.

2.1.4.2.1 Sound

2.1.4.2.1.1 Acoustic

Acoustic signal-based localization leverages the ubiquitous microphone sensors in smart-phones to capture acoustic signals emitted by sound sources. Established solutions such as Beep [153], Whistle [154] and Echotag [155], are shown to achieve high localization of 3 ft, <20 cm and 1 cm accuracies employing TOA, TDOA multilateration, and fingerprinting methods. However, due to the smart-phone microphone sampling rate and filter limitations only audible band acoustic signals (<20 KHz) can provide accurate estimations. To avoid potentially uncomfortable noise pollution the power must be restricted which requires more complex low power signal detection methods [15].

2.1.4.2.1.2 Ultrasonic

Ultrasonic signals within the frequency band 2 MHz to approximately 15 MHz have been proven to provide centimetre level accuracy indoor localisation for multiple targets simultaneously at low energy costs [15]. Typical examples of established systems are Active Bats [156], CRICKET [31], and Dolphin

[157]. Each of these employ TOA multilateration for localisation. The Active Bat solution requires a wearable tag and is received by a ceiling mounted array of receivers [86]. Wearables are small and exhibit a lifetime of 15 months while achieving an impressive 50 estimations per second [27]. CRICKET couples' ultrasonic signals with RF signals for synchronisation, and while achieving high accuracy around 6 cm, however, it suffers from the inherent narrowband disadvantage [90]. Due to short propagation distances the Active Bats solution relies on densely and accurately positioned ceiling sensors, which are not convenient or scalable [27], while CRICKET increases power consumption to synchronise the RF and ultrasound data. Ultrasonic signals are susceptible to humidity and temperature changes, therefore, temperature sensors are often required for ultrasonic systems to accommodate for potential fluctuations [15]. Gu *et al.* [86] also reports that noise from 'jangling metal objects' and 'crisp packets' can affect performance.

2.1.4.2.2 Optical

2.1.4.2.2.1 Infrared

Typically, the Infrared (IR) system described in literature is the Active Badge solution which provides no more than symbolic location information of a wearable within a given room of a building. While the lifecycle of the wearable is over half a year, results are only obtained every 15 seconds [86]. More promising commercial solutions, such as VR tracking for the HTC VIVE have shown promising results with millimetre-level accuracy through various experimental studies [158][81]. While IR technology is promising, with accuracies within the millimeter scale, the response is reported to be affected by fluorescent lighting and direct sunlight [27] [159].

2.1.4.2.2.2 Visible Light

Visible Light Communication (VLC) is an emerging technology for high-speed data transfer [15] that uses visible light between 400 and 800 THz, modulated and emitted primarily by Light Emitting Diodes (LEDs) which are widely deployed and make VLC technology a highly cost effective and scalable solution [63]. Existing systems such as Elipson [160] and Luxapose [151] have indicated centimetre level accuracies, however, due to the Lambertian nature of light emission most solutions are often limited to 2D solutions or require additional technologies and more complex algorithms to achieve 3D estimates. A more in-depth evaluation of Visible Light Positioning (VLP) is presented further in this literature review.

2.1.4.2.3 Radio Frequency

The radio frequency band is, by a considerable margin, the most explored technology for wireless localisation solutions, owing to its accessibility, long range transmission, and easy detectability [146].

2.1.4.2.3.1 Wi-Fi

Wi-Fi is the name of popular wireless networking technology. Wi-Fi operates within the RF bands of 2.5 GHz for IEEE 802.11b, IEEE 802.11 g, and IEEE802.11n, and in 5 GHz for IEEE 802.11a. A key advantage to Wi-Fi systems is that much of the infrastructure already exists and increasing numbers of IoT devices are available. Early implementations of Wi-Fi based approaches such as RADAR [161], [162] exhibit poor localisation performance of several meters due to multipath fading, reflections, and obstructions affecting radio wave propagation. Recent systems such as Wi-FiNet [163] achieves a RMSE of 28 cm by applying a Convolutional Neural Network (CNN) for fingerprinting. While Wi-FiNet and similar systems, compared by Hernandez *et al.* [163], are promising, their performance significantly degrades when considering dynamic targets or locations that are different to the training data.

2.1.4.2.3.2 Bluetooth

Bluetooth solutions are built on the IEEE 802.15.1 standard for intended use within short range wireless Device to Device (D2D) communication. More recent Bluetooth Low Energy (BLE) provides a highly energy efficient and longer communication range of 70 - 100 m compared to previous systems [15]. Examples of current systems include the iBeacons from Apple and Eddystone from Google which use RSS to determine if a user is within certain discrete metre-level ranges. To account for variations in measurements, estimates are produced every one second while sampling is carried out every 50 ms [67]. While signal properties are similar to WiFi, Fingerprinting methods have been applied with BLE to make use of portability and lower power consumption of Bluetooth beacons, [164] where results show similar meter level accuracies to that of Wi-Fi.

2.1.4.2.3.3 Zigbee

ZigBee arrived as a specification based on the IEEE 802.15.4 standard which offers long distance D2D transmission in a wireless mesh network [67]. It uses the 868 MHz band in Europe, 915 MHz bands in the USA and Australia, and 2.4 GHz in other regions. With a focus on low cost, low data rate, and energy efficient personal area networks [15], ZigBee fingerprinting solutions such as ZIL [165], present competitive accuracies to Wi-Fi based solutions while being far more energy efficient. Regardless,

Zigbee technology is not widely adopted into many consumer devices, therefore, making it less explored than similar Bluetooth technology.

2.1.4.2.3.4 Radio Frequency Identification (RFID)

Radio Frequency Identification (RFID) is primarily intended for transferring and storing data using electromagnetic transmission from a transmitter to any RF compatible circuit [15]**.** RFID is a tag-based technology that is categorised as either active or passive. The RFID tags operate within the Ultra-High Frequency (UHF) and microwave frequency bands. Active RFIDs are powered by a local source to periodically transmit their ID over hundreds of meters of range, whereas passive RFID systems require no power source but, consequently, have a much more limited communication range (a couple of meters). SpotOn [166] presents an RSS triangulation-based RFID approach which, due to poor accuracy of 3 m, is proposed for low accuracy applications such as lighting control. More recently, Chong Wang *et al.* [26] presents an RFID solution utilising a ceiling-mounted matrix array with spacings of 1 foot between nodes. The solution achieves better accuracies of 1.5 ft and 0.78 ft in the x and y axes respectively. Generally, RFID solutions are not widely integrated into consumer devices. Additionally, due to the limited capability of passive RFID tags implementing multiple access mechanisms to avoid interference is non-trivial [167].

2.1.4.2.3.5 Ultra-Wide Band (UWB)

Ultra-Wide Band (UWB) is described as a radio wave whose fractional bandwidth is greater than 20% or at least 500 MHz [90]. Ultrashort pulses (i.e., nanoseconds) are transmitted over large bandwidth in the frequency range from 3.1 to 10.6 GHz using a very low duty cycle, which results in reduced power consumption [15]. The pulses make UWB signal's much easier to filter out from multipath components, providing accurate identification of a signals time delay component [15]. Additionally, the difference in radio spectrum and type of signal used, makes UWB more resilient to interference from other RF signals while the lower frequencies are better suited to penetrate materials including walls [61] Ubisense is a UWB system which uses TDOA and AOA to detect a wearable tags location. This system exhibits very high accuracy and precision, approximately 15 cm for 95% of the estimations [27]. Warehouse experimentation conducted in Ruiz & Granja [168] compares Ubisense, to two other commercial UWB time based location solutions (BeSpoon and Decawave), the study indicates the superior performance of the Decawave system, which uses TWR TOA or TDOA. However, UWB signals do suffer interference from metallic and liquid materials. Additionally, the short communication range, of approximately less than 10 m, limits UWB applications to exceptionally dense networks [90].

2.1.4.3 Localisation Discussion

The systems described above highlight the variability in performance of Indoor Positioning Systems owing to the respectively applied technology and processes. For RF frequencies, the UWB solutions exhibit superior performance due the use of high signal bandwidth which enables high time resolution for time-based measurements. Notably hybrid solutions present improved performance compared to single technology systems. With regards to the evaluation of indoor positioning within this thesis, high accuracy and reliability are evidently critical for modern application demands. The trade-off however is typically additional Energy, Complexity and Cost, which are each important factors to consider. Moreover Energy, Complexity and Cost are reflected in the latency of a solution therefore this thesis evaluates the accuracy, reliability, and latency of Indoor localisation solutions. Furthermore, the positioning system evaluated throughout this body of work concentrates on the localisation of a single UE device within a restricted environment, therefore the scalability of the solution is not greatly considered.

2.2 Localisation in Asynchronous Sensor Networks

In literature, sensor systems are often assumed to be synchronous, in that certain processes within a network occur at the exact same time. In practice, maintaining perfect synchronisation across an entire network is rather difficult and costly. When handling sensor data and performing data fusion to generate location estimates, asynchronous behaviour can negatively affect the performance of an Indoor Positioning System (IPS). Due to the complexity of sensor networks, there are several different ways in which a network of sensors can be regarded as asynchronous.

Within this section, network topologies are first introduced due to the differentiation of applied fusion methods and datatypes. Potential asynchronous features of wireless sensor networks are then discussed, before the challenges are presented and existing solutions are reviewed.

2.2.1 Network Architectures

When considering data fusion, it is important to consider the type of data to be fused and where in the network the network the fusion occurs. The component that conducts the fusion process is referred to as the *fusion centre* (FC).

The simplest network structure is a *centralised network* [169], [170] where all raw data from independent sensors is transmitted to a single fusion centre. This system is considered optimal in the sense that it obtains all available data to establish the best output. However, with all data being transmitted to a singular node, the bandwidth of a system is a considerable constraint, additionally

the processing required to be performed for all targets within a system increases the computational demand of the fusion centre [171].

To alleviate the bandwidth and processing burden, a *distributed* architecture considers a system of sensors, each established with their own processing capabilities. Localisation is then able to be performed throughout the network as sensors share their state estimates and act as fusion centres. A distributed network is additionally more robust to failures as there is no single dependant node [172], [173]. Sensor fusion within a distributed network considers the fusion of state estimates, referred to as 'tracks', from various sensors. In this regard, distributed fusion is synonymous with 'Track-Track' fusion and 'state fusion'. This type of architecture is, however, more complicated than centralised fusion [174].

While a distributed network presents many added benefits, the complexity is amplified in larger networks. Furthermore, the requirement to embed each sensor with the means to directly estimate the target state is not always feasible or economical. Additionally, long distance communications pose potential difficulties in ensuring communication channels and timings. A proposed improvement is the development of a *decentralised network* or '*clustered network'* [173], [175] where the system is divided into various groups of sensors. Each group is considered part of a cluster and all sensors within a cluster communicate to a single fusion centre or 'Cluster Head' (CH), in a centralised manner. Various CHs are then able to communicate among themselves, sharing their local estimates in a distributed sense to perform state fusion.

2.2.2 Types and Causes of Asynchronous Systems

For a generalised overview, the following section introduces types of asynchronous components within a system. This list is by no means exhaustive and it should be noted that within a system there could be many possible causes for asynchronous localisation to occur.

2.2.2.1 Asynchronous Clocks

A system can be regarded as asynchronous if the communicating wireless nodes suffer unknown clock offsets or frequencies. In this respect, communicating devices are all considered to have their own 'local time' and, therefore, are asynchronous to one another. The challenges presented by such an asynchronous nature are primarily limited only to time-based measurements, where the delay of the signal is required to be measured at high accuracies, yet the differences between sensors local times obscures the registration of time delay. The effect of such a system is variable on whether the system is considered in either the uplink or the downlink.

2.2.2.1.1 Uplink

Within an uplink scenario, a transmitting target device emits a signal periodically within its own local time frame. This signal is received by listening sensors and TOA measurements are generated, which are affected by their own local time features. The resulting fusion of these results can be considered as noisy measurements of a singular transmission. Solutions presented in Xie *et al.* [176] and Li *et al.* [177] utilise a displacement estimate to eliminate the clock offsets. This requires each node to perform TDOA between its own consecutive measurements.

2.2.2.1.2 Downlink

Within a downlink scenario, where each device clock has its own local time, each signal is transmitted from a respective sensor at a slightly different instant in global time. Not only does this scenario suffer the effects of temporal misalignment in a time-based measurement but, additionally introduces potential for spatial misalignment for all manner of range-based measurements. In a dynamic scenario each measurement acquired at different timepoints represents the relationship between the respective anchor and the target at a slightly different target position. The outcome of such a downlink scenario equates to asynchronous sampling of sensors and is considered further in the following sections.

2.2.2.2 Asynchronous Sampling

Within some systems, sensor devices may obtain measurements of the target at different timepoints. Often this occurs due to the use of non-homogenous sensors where the sampling rates are incoherent. A typical example considers the use of IMU devices, known for their extremely high sampling rates, coupled with a slower system such as radar [178] or image detection. Alternatively, sampling rates may be simply misaligned as in the case of asynchronous clocks discussed above in Section 2.2.2.1. Regardless of the contributing factors, the outcome of asynchronous sampling is a set of measurements describing the state of the target at different points in time. Within a dynamic target tracking application, such spatial misalignments can lead to positioning errors if ignored.

2.2.2.2.1 Sequential Sampling

In a more specific case, the sampling rates and the period between individual sensor observations can be considered equivalent, such that the sensors are purposely sampled sequentially. Such a system can be established due to the use of multiplexing protocols such as Time-division-Multiplexing (TDM), deterministic scheduling, or contention-based protocols [36] between nodes in a network. In these cases, the approach is considered to avoid interference between communications.

TDM is a multiplexing protocol that considers transmission of unique datasets among different devices across a single frequency channel by allocating distinct timeslots within a transmission frame for each device. As a result, each device communicates with the target sequentially. In a similar fashion, Deterministic scheduling and contention-based protocols reduce the bandwidth requirements and energy waste by allocating distinct communication periods for each device.

2.2.2.3 Packet Delays – Asynchronous Reception of Data

Wireless sensor networks may succumb to communication delays of data packets due to the individual internal processing speeds of nodes, buffers at nodes, required re-transmission of faulty or non-received data, or due to variable lengths of transmission paths [179]–[181]. While these delays may lead to simply delayed retrieval, depending on the extent to which the data is delayed, more recent data may have already been acquired since. In such a case the data is regarded as an Out-of-Sequence Measurement (OOSM) and must be handled accordingly. The simplest approach is to ignore OOSM [106], [170], [182] however this is not optimal with regards to utilising all available data. Alternative approaches consider re-transmission of delayed or lost data which can then be re-applied using Kalman filter techniques [106], [173], [180], [182], [183]. Communication delays of sensors are not considered throughout this thesis therefore all measurements are considered to be obtained in sequence.

2.2.2.3.1 Asynchronous Systems Considered in this Thesis

Throughout this thesis the term sequential sampling is explored for a system in which all clocks are assumed to be perfectly synchronised with one another, all sampling rates are equivalent and packet delays are negligible, therefore, the data arrival sequence at the fusion centre is equivalent to the measurement acquisition at the sensors in the time domain and is referred to as in-sequence measurements. To this end, the rest of this section evaluates existing data fusion techniques for location estimation under asynchronous sampling. We first consider asynchronous fusion of linear ITU measurements and then non-linear measurements.

2.2.3 Linear Solutions for State Estimation Under Asynchronous Sampling

Linear solutions describe the scenario where the sensor measurements to be fused at the FC are linear to the state to be determined, typically this describes the targets coordinates in two or three dimensions and the velocity components along each axis. Within a centralised network, a single sensor can be assumed to either directly measure the target's position or velocity, or contain the necessary processing capabilities to do so. Alternatively, these linear measurement sets can be obtained in a

distributed network where track measurements are obtained and, therefore, require fusion. For any of the previously mentioned causes of asynchronous sampling, linear measurements of the state may be obtained asynchronously.

2.2.3.1 Linear Tracking Scenario

Throughout this section the following system is considered to give context to the individual causes and complications of such asynchronously sampled systems. A singular target node is travelling through a network of N sensors and is described by the following discrete-time linear system [169]:

$$X_{t_k} = A_{t_k,t_{k-1}} X_{t_{k-1}} + w_{t_k,t_{k-1}}. \tag{2.71}$$

Here X_{t_k} describes the state of the target at time of the $k'th$ sampling instant (t_k), $A_{t_k,t_{k-1}}$ is the state transition matrix from estimation instant t_{k-1} to t_k and $w_{t_k,t_{k-1}}$ is the system noise which is assumed to be white Gaussian distributed with zero mean and covariance $Q_{t_k,t_{k-1}}$. A fusion centre is tasked with periodically combining the observations of all N sensors received within the estimation period $\Delta T = t_k - t_{k-1}$. During ΔT, each sensor delivers a single observation of the state with the measurement equation given by [169]:

$$z^i_{t^i_k} = H X_{t^i_k} + v^i_{t^i_k}. \tag{2.72}$$

In which H is the measurement translation matrix, assumed to be constant throughout and equivalent between the sensors. The measurement noise $v^i_{t^i_k}$ is assumed to be white Gaussian with zero mean with covariance matrix $R_{t^i_k}$ and t^i_k is the time point the $i'th$ observation relates to within the sampling period $(t_k, t_{k-1}]$. For simplicity, one can consider the order of the sensor numbers to correlate to the order of measurement acquisition at the sensors and at the fusion centre such that $t_{k-1} < t^1_k < t^2_k \cdots < t^i_k \cdots < t^N_k < t_k$.

2.2.3.2 Sequential State Fusion

The optimal solution for asynchronous data fusion is to sequentially process sensor measurements relative to the time they are obtained at the sensors. Research in Zhang, Chen, *et al.* [173] presents a Sequential Measurement Fusion (SMF) structure through consecutive Kalman filtering. Within a given estimation interval ΔT, as a measurement $z^i_{t^i_k}$ is received, the respective timestamp t^i_k is used to predict the state of the target at the instant. The solution is then updated using the measurement

received, and this process is repeated for all N sensor measurements, before a final prediction step is executed to obtain the state estimate at the required estimation instant t_k. The sequential process also provides an elegant solution in cases where no measurements are available. The solution simply considers a single prediction step over the estimation interval.

2.2.3.3 Batch Fusion Approach - Measurement Augmentation (MA)

Yanyan *et al.* [181] presented a centralised batch fusion algorithm for asynchronous sensor systems, in which asynchronous measurements are synchronised in the time domain according to the dynamic model of the target. The solution is applicable for an arbitrary number of sensors and respective sampling rates. In general, the method requires the timestamps of datapoints to re-organise the measurements according to their acquisition time. The approach then considers the backwards state transition matrix to relate individual measurements to the state of the target at the timepoint they were taken. In effect the solution, aptly referred to as Measurement Augmentation (MA), augments asynchronous measurements to generate a set of pseudo-measurements with a common fusion instant. Consequently, the solution results in the computation of high-order inverse matrices and correlates the pseudo-measurements generated with the process noise. In later works Hu *et al.* extends the concept of MA to distributed networks [184].

Ironically, the SMF and MA approaches have been proven to be equivalent to one another in papers that claim the processing of each method to be superior. Zhang *et al.* [173] demonstrates that the precision of both techniques is equivalent and through the definition of computational complexity being the number of multiplications and divisions in the required algorithms, the complexity of MA is greater than SMF [182]. Zhang further explains how the procedures for MA and SMF are effectively equivalent. The SMF, however, distributes the required processing throughout the estimation period leading to lower computational complexity.

While additional linear techniques such as multiscale theory, multirate filter banks, and distributed fusion approaches are described in literature [170], [185]–[187], the interest of this thesis lies in the case of asynchronous sampling of non-linear measurements. More specifically, distributed fusion is concerned with fusion of state estimates and is therefore inherently a linear measurement fusion problem. The author of this thesis, declares that to the best of their knowledge these principles are not currently applied to the case of non-linear measurements and, therefore, are outside the scope of this thesis.

2.2.4 Nonlinear Solutions for State Estimation with Asynchronous Data

Throughout this thesis localisation is considered for asynchronously sampled range measurements which are non-linearly related to the target state. The following section discusses existing techniques to appropriately fuse non-linear and asynchronously sampled data.

2.2.4.1 Optimal Nonlinear Sequential Measurement Fusion (SMF)

Zhang *et al.* [188] build on previous linear SMF research with the use of the Unscented Transform (UT) to address non-linear data. The solution follows the same premise as the optimal sequential fusion for linear methods, however, applying a UKF process for every measurement. This entails the prediction and measurement fusion for each sensor measurement as it is obtained by the FC.

Various studies employing a sequential non-linear KF consider a generalised asynchronous sampling scenario where measurements are obtained sequentially but with random communication delays. As a result, the process noise covariance matrix $Q_{t_k^i, t_k^{i-1}}$ of the UKF is given as a function of the variable latency between measurements, which is dependent on the communication and sampling. As such, the process noise is the sum of deterministic and stochastic components. The deterministic part, as with constant sampling cases, can be derived through offline experimentation. The stochastic component is unknown and variable and, therefore, more complex to determine.

To accommodate for this stochastic component of noise and its potential to diverge the filter over time, Yang *et al.* [129] [126] and Zhu *et al.* [189] implement a fading factor within the process noise to compensate for the unmodelled stochastic process noise component. The proposed approach requires dual deterministic sampling which further increases the computational demand. Zhang *et al.* [36] considering the same process however with a Sequential Cubature Kalman Filter (SR-SCKF) in place of a SUKF, assume the stochastic component of the process noise to be a uniformly distributed random variable, on the intuition that it is simpler to approximate a region of values rather than exact solutions.

The use of sequential non-linear KFs presents a simple tracking solution for asynchronous sampling, however, the papers considered fail to describe the computational demand of such processes, and as one can infer from the repeated use of non-linear KFs, this presents increases in the computational demand.

2.2.4.2 Nonlinear Measurement Augmentation

In a very specific case, Jeon *et al.* [174] derives a form of non-linear MA process using the Unscented Transform (UT). The study focuses specifically on the application of non-linear trajectory models within an interacting multiple model study. Due to the computational cost of the MA processes

already being greater in comparison to the SUKF, this approach is not considered further within the thesis.

2.2.4.3 Least Squares Batch Solutions Assuming a Constant Velocity

In the pursuit of less computationally intensive solutions to the asynchronous challenge, one may consider a variety of solutions in which simpler LSSs are considered. Examples of existing work is discussed below.

In very early work Blair *et al.* [178] employed a linear LSS technique to compress multiple high rate optical sensor measurements into a single measurement, synchronous with lower rate radar data. The two datasets are then able to be fused together as a single synchronous measurement. The approach relies on the assumption that the target has a constant velocity during the estimation interval [170]

While considering the biases of sensors producing both range and bearing estimates Pu *et al.* [190] presents a new non-linear LSS formulation for asynchronous multi-sensor target tracking, by assuming a nearly-constant velocity model. For a single sensor, the proposed method highlights the challenge of estimating the azimuth bias and target velocity due to the ambiguities in the solution. These ambiguities are resolved using multiple sensors, as there is only a single common velocity component. Simulated results are promising against KF solutions.

Additionally, Shi *et al.* [44] adopt a multilateration process proposing the use of a modified Two-Step Weighted LSS (TSWLS) solution for a sequential TDMA scenario with dynamic sensor nodes that have both positioning error and asynchronous clocks. Shi *et al.* suggests that the minor time differences between transmissions renders the target speed observable, and thus, attempts to jointly estimate the target velocity and position under the approximation of a CV model.

2.2.4.4 Extrapolation

An interesting use case in which sensor data is often asynchronous is in the use of high rate IMU data coupled with slower sampling sensors such as cameras, Radar and Light Detection and Ranging (LIDAR) systems. To compensate for temporal or spatial misalignments, extrapolation methods have been applied to effectively augment received measurements and synchronise datapoints.

Geneva *et al.*[191]. considers a scenario where measurements provided by sensors do not align with the timepoints of the graphical nodes used for localisation. While adding a new node that corresponds to the asynchronous measurements is possible, minimising the number of nodes within the graph-based localisation approach is preferable for memory usage. The approach considers a simple linear interpolation or extrapolation under a CV model assumption between consecutive

sensor measurements to obtain the measurement at the nearest corresponding graphical node time point.

Guo *et al.* [192] considers the online EKF fusion of IMU measurements and images obtained by Complementary Metal-Oxide Semiconductor (CMOS) rolling shutter cameras that suffer time misalignment due to asynchronous clocks. The rolling shutter cameras additionally represent a challenge as each pixel row of the camera is read sequentially, therefore, individual measurements of features within the pixel rows will relate to individual camera poses (position and orientation). While an ideal solution would model the pose corresponding to each pixel row this solution is not computationally viable. The proposed solution exploits the targets given trajectory model to interpolate between camera poses to align pixel data. For similar fusion of rolling shutter cameras and IMU data, Patron-Perez *et al.* [193] employs spline based interpolation as opposed to linear interpolation.

2.2.4.5 Asynchronous Systems Summary

Within later chapters of this thesis asynchronous sampling of non-linear measurements is encountered and therefore, applicable localisation techniques for asynchronous sampling have been presented from existing literature. Sequential non-linear filters, such as the SUKF, present an optimal format but dictate the need for repeated non-linear transforms which present potential increased computational demand. While complexity is discussed in the literature, it is not formally evaluated. Linear assumptions which are presented, offer a promising approach to reduce computational burden but rely on small noise assumptions of LSS and on constant velocity assumptions over the estimation period. Additionally, across each of the discussed studies, a singular estimation period ΔT and fixed measurement noise is considered for either a line, fixed circle, or fixed square target trajectory. This provides no insight into the effectiveness of the solutions in a wider context. Extrapolation methods typically consider pose (linear) extrapolations or IMU measurements and to the best of the author of this thesis's knowledge are not evaluated for range measurements alone.

The remainder of the chapter introduces the IoRL system within the context of 5G networks and presents relevant localisation technologies that are considered throughout this thesis.

2.3 5G Network Technologies (Introduction to 5G)

As described in Tadayoni *et al.* [194], the development of mobile technologies is considered in three different ways; through commercialised terms of 'generations', International Mobile Telecommunication (IMT) standards outlined by the International Telecommunications Union (ITU)

or, standards and releases which are provided by standardising bodies such as the Institute of Electrical and Electronics Engineers (IEEE) or Third Generation Partnership Project (3GPP). Throughout this thesis, the commercial term 'Generations' is considered for clarity as these align somewhat with the releases and standards presented by 3GPP, which are referred to throughout.

The Fifth Generation, referred to as 5G, of mobile networks is set to tackle the drastic expansion of mobile data traffic observed over the last decade [195]. This trend is predicted to continue as demands for higher transmission speeds, lower latencies, increasing connectivity, and expectations of mobile services persists.

Beyond the sheer numbers of devices and the demands for high quality of service from wireless communications, new industry sectors and services such as Massive Internet of Things (MIoT), Massive Machine Type Communication (MMTC), Vehicle-to-Vehicle (V2V), and Vehicle-to-Everything (V2X) have emerged that are influencing the way in which wireless communications are implemented. Within the 3GPP service requirements, outlined in Release 16 [196], the revolutionary approach to 5G networks is highlighted. This is highly focused on the flexibility of such a system to support varying industry verticals, services traffic loads, and communities. Therefore, the 5G architecture must be adaptable to provide simultaneous support for multiple combinations of reliability, latency, throughput, and positioning.

Throughput is expected to increase with one to tens of Gbps [197], [198], [199] data rates proposed to support new services within Virtual Reality (VR), Augmented Reality (AR), and Ultra-High-Definition (UHD) TV. While flexibility within 5G service levels suggests a variety of latency demands, time sensitive applications such as remote control and factory automation dictate stringent latency requirements on 5G Key Performance Indicators (KPI) for very low end-to-end latency of 1 – 10 ms [200], [201]. Additionally, with MIoT the device density is expected to increase from a typical 4G connection density of 2,000 devices per square kilometre to upward of a million devices per square kilometre [201]. Therefore, highly reliable connectivity and significant improvements in resource efficiency will be necessary.

2.3.1 Localisation Within 5G

As part of the expectations of 5G networks, wireless localisation of mobile terminals within indoor and outdoor environments is expected to be provided with varying degrees of performance to satisfy individual levels of services and requirements. The 3GPP, a critical standardising body for the release of new network services, have defined KPI for 5G localisation throughout a series of releases. During the initial 5G packet, referred to as Release 15, KPI details presented in TS22.261 V15 *Annex B* [202] describe localisation use cases within four groups of sectors; Automotive, Transport, logistics & IoT,

Health and wellness & smart cities, and Media & Entertainment. In these groups, outdoor positioning accuracies are outlined as <0.3 m, <0.3 m, 1-10 m and 0.3 cm – 1 m respectively. Indoor localisation within these groups is detailed as 'also needed' [202]. Within Release 16, further enhancements and specifications towards localisation KPI are outlined in TS22.261 V16 [196] relating KPI to relative Service Levels coordinated with the needs of industry as specified in TS22.104 V16 *Section 5.7* [200]. The Service Levels described consider a variety of industrial use cases with varied performance metrics pertaining to horizontal and vertical accuracies within 95 % confidence levels, the availability of the positioning service within the environment, positioning latency, the environment and target velocity. Most notably, the most stringent indoor positioning requirements pertain to 'inbound logistics for manufacturing' [200] at Service Level 7 which dictates horizontal and vertical accuracies under 20 cm with 99 % confidence and a latency of 1 second at a potential target velocity of 30 km/h. Further location requirements specified within Release 16 TS22.261 V16 *Section 7.3.2.2* [196] describe energy efficient positioning services for battery operated devices in use cases such as asset tracking. Therefore, 5G systems should implement support for positioning at lower accuracies (3-10 m) outlined in Service Layer 1 for twelve years using a maximum of 1800mWh of battery power under the assumption of multiple position estimates per hour.

Example use cases of positioning within 5G networks are provided in TS22.261 V16 [196] and discuss factory floor requirements to locate assets and dynamic objects such as forklifts. Positioning can also be considered for autonomous guidance and V2X for both UAV and Unmanned Ground Vehicles (UGV), where accurate and reliable real-time positioning data is critical to ensure safety.

In summary, due to the plethora of existing connected devices and parties involved, both user and industry, the needs of future networks are diverse. This is evident in the contrast of ultra-low latency and high data throughput communication, with low energy and long battery life demands.

2.3.2 5G Solutions

Previous 'Generations' of networks have expanded on existing functionalities and delivered enhanced system performance through the employment of novel communication techniques, new radio access and larger bandwidth [194] [203]. In much the same way, for 5G networks to meet the demands of users, the research, development, and use of multiple new technologies must be considered and combined. Such new technologies as massive Multiple Input Multiple Output (MIMO), ultra-dense network (UDN), millimetre Wave (mmWave) communication, and device-to-device (D2D) communication are deemed key enablers of 5G technologies.

To achieve these stringent system demands, 5G networks are set to enhance both the Radio Access Networks (RAN) and Networking Solutions. Regarding RAN, newly accessible unlicensed

spectrum at higher frequencies and with larger available bandwidths enables greater speeds and capacity of networks. Higher frequencies have much shorter wavelengths, facilitating the use of smaller antenna form factors and thereby the development of antenna arrays. Subsequently, the development of smaller antenna arrays provides a means for Massive MIMO technology where multiple independently controlled antennas are simultaneously active. While spatial division multiplexing allows different data streams to occupy the same frequencies at the same time [204]. Through controlled shaping of the signals, the waveforms emitted from the antennas can be summed up constructively to achieve higher efficiency, increased Signal-to-Noise Ratio (SNR) and focused reception. Alternatively, this premise can be reversed to intentionally form deconstructive interference elsewhere [205]. This beam forming produces concentrated transmission paths which counteract the path losses of higher frequency bands. 5G networks, due to the higher attenuation characteristics of employed signals, are utilising dense deployment of smaller local cells to accommodate the harsh connectivity requirements in densely populated environments.

Beyond radio access and novel transmission methods, the flexibility required of 5G networks necessitates the development of adaptable network architectures capable of redirecting data, dependant on data traffic, user needs, and energy constraints. network slicing, Network Function Virtualisation (NFV) Edge computing and Software Defined Networking (SDN) are some among the expected networking improvements expected within 5G systems.

2.3.3 The IoRL System

This thesis forms part of the Internet of Radio Light (IoRL) Horizon 2020 system and, therefore, the indoor localisation evaluated within this thesis is explored and takes into account the scope of the IoRL system. The following section introduces the proposed structure, technologies, applications and indoor positioning system of the IoRL project in hopes of better understanding the type of indoor localisation parameters and requirements dictated by the various applications as discussed in Section 2.1.1.

Remark 1 - The IoRL project is a research project and, therefore, variations to the proposal and use cases are natural over the course of the project. The following review and summary are considered an overview for the readers understanding. Relevant changes that are regarded to affect the Indoor Positioning System (IPS) are documented throughout the thesis and will, in fact, lead to the development of the 5th and 6th chapter of this thesis.

2.3.3.1 Overview

The IoRL system [206] presents a novel network architecture for use within buildings, with applications in homes, supermarkets [207], museums, and public transport services [208]. The IoRL system offers a low interference and high security solution for sub 1ms latencies, 10 cm positioning accuracy and 10GBps data rates; achieved through the integration of Wireless Local Area Networks (WLAN), Millimetre Waves (mmWave), Visible Light Communications (VLC), and Software Defined Networking (SDN). The overall concept architecture is presented in Figure 2.5 (a simpler adaptation of that found in Cosmas, Zhang, *et al.* [206]) .

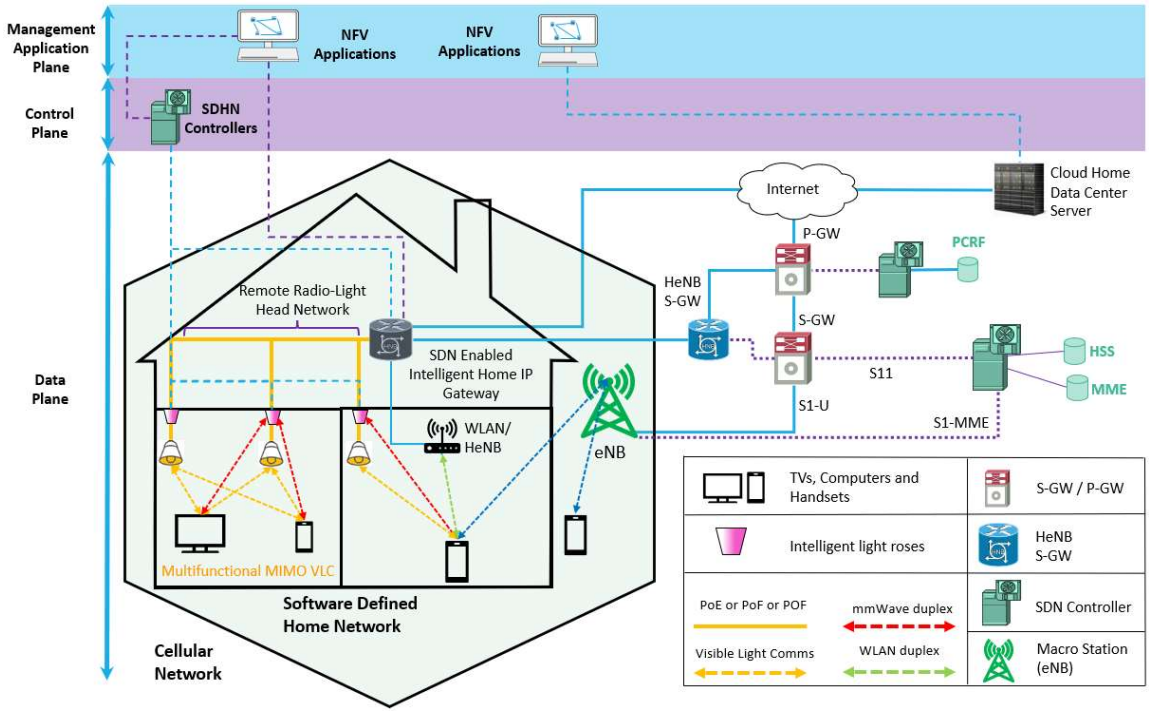

Figure 2.5 - IoRL Architecture

Due to the demand for wireless indoor networks and the inability to adequately penetrate building materials, existing home networks commonly deploy a single router access point to propagate data internally using RF signals. The drawbacks of such existing systems are a lack of coverage and the use of low frequencies that provide inadequate Quality of Service (QoS), especially for the requirements of future networks. The IoRL system increases coverage within buildings via deployment of numerous mmWave and VLC transceivers throughout existing lighting systems.

A great number of benefits can be drawn from the intuitive application of multiple high speed network transmitters located within existing light roses. These access points are referred to as the

Remote Radio Light Heads (RRLH's) and fulfil the obvious need to locate the VLC transmission points within light modules. Moreover, light roses provide ideal coverage for LOS technologies, and have existing conduits which would reduce installation costs. The application of multiple technologies located in multiple RRLHs in each room present an opportunity for high quality indoor localisation through triangulation. This configuration also offers both flexibility for Multiple Input Multiple Output (MIMO) diversity by transmission of the same data through multiple RRLHs for reliability or MIMO multiplexing, where different sets of data can be transmitted through different technologies or antennas, thereby increasing throughput. The IoRL system focuses on a Multiple Input Single Output (MISO) diversity proposal in the downlink and Single Input Multiple Output (SIMO) diversity in the uplink to increase coverage in the likely event of receiver occlusion from one of more RRLHs [207]. In instances where VLC and mmWave antennas are occluded, Multi-Source streaming is utilised to ensure the availability of a lower capacity WLAN connection for undisrupted connectivity [207]. Additionally, the hybrid use of high frequency LOS technologies such as mmWave and VLC benefits from frequency reuse, increased bandwidth, and unlicensed spectrum that provide improved data rates and security. Security is increased, as network attackers are unable to interact with the network as they are unable to connect to LOS technologies without being directly inside the building. The Distributed Antenna System (DAS) configuration reduces data propagation distances and is expected to greatly reduce network latencies.

2.3.3.2 IoRL System Architecture

The system architecture is considered in four layers; Service, Network Function Virtualisation (NFV), Software Defined Network (SDN) and Access as illustrated in Figure 2.6 [209].

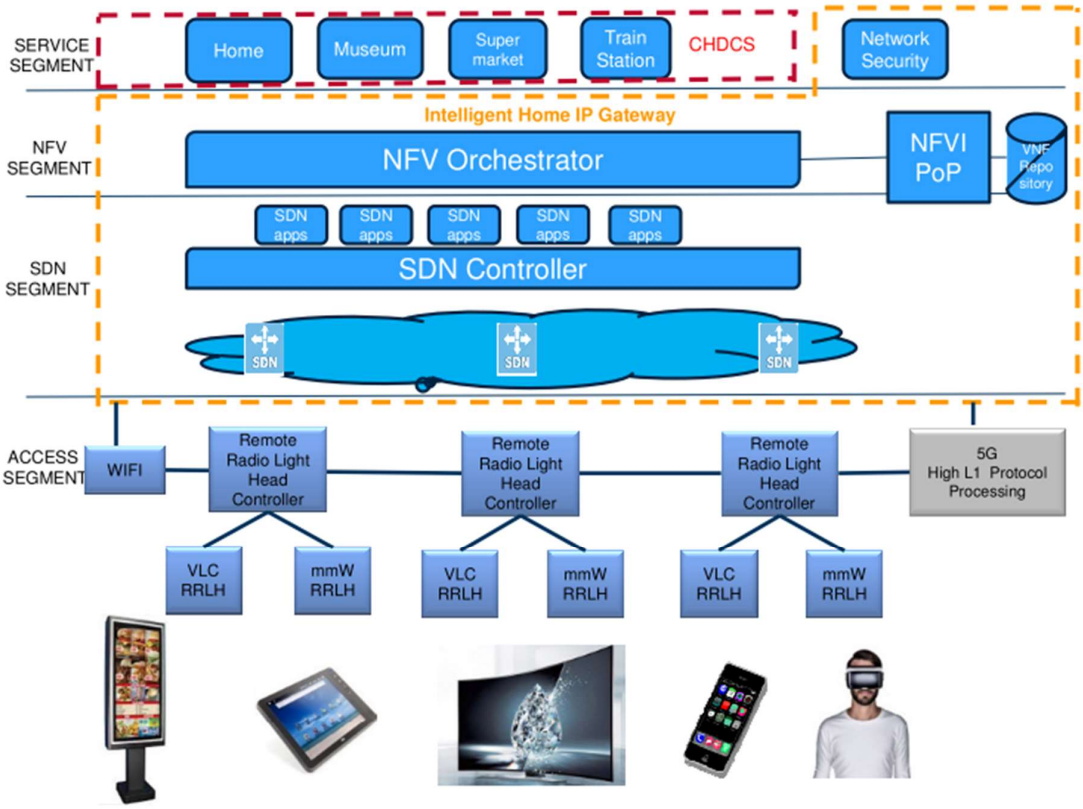

Figure 2.6 - IoRL Layer Architecture

This structure can be considered 'akin to a radio-light home eNodeB suitable for single building network rather than an Evolved Packet Core (EPC) suitable for a whole country' [210].

The Service layer runs server-side applications for streaming audio-video, receiving and storing results on databases and monitoring security etc. from a multi-core Cloud Home Data Centre Server (CHDCS). Additionally, the service layer manages mobile apps from User Equipment (UE) i.e. smart phones, tablet PCs, VR headsets and HDTVs.

At the front-end the Access layer consists of a series of RRLH transceivers situated within the light roses in each room of a building. Each RRLH consists of a single VLC LED source connected to a VLC frequency modulation module and a mmWave antenna system connected to a mmWave RF duplex module. These are powered through the existing lighting infrastructure and arranged to minimise the overall form factors of the ceiling light. This configuration provides only a VLC downlink channel and both an uplink and downlink mmWave channel. The RRLH Controller (RRLHC) is developed on a Field programmable Gate Arrays (FPGA) and drives a total of four RRLHs transmitting an identical transmission block sub-frame. This produces a MISO downlink path and a MISO uplink path for the

given coverage area, which is typically a room or floor area of a building. Each RRLHC is connected in series through a 10 Gbps Ethernet Ring with Common Public Radio Interface (eCPRI) between rooms in a building, like the common electric lighting connections found in homes. A 10 MHz reference clock signal is generated locally and sent to each mmWave RRLH module for use in 5G synchronisation. Each RRLHC houses two lower Layer 1 processors, the first generates an Intermediate Frequency (IF) signal to drive the VLC MISO modules using a splitter and the second that generates an Intermediate Frequency (IF) signal to drive or be driven by mmWave RF Duplex modules using a RF splitter [209]. The ethernet ring also connects a single WI-FI access point to provide a guaranteed connection in cases of LOS signal occlusion from both mmWave and VLC. A singular Distributed Radio Access Network (DRAN) acts as the upper layer-1 processors connected in the ethernet loop. The final component within the ethernet ring is the layer-2 and 3 5G protocol processor that handles the 5G Medium Access Control (MAC) layer and Remote Radio Control (RRC) respectively in a single remote server unit. Together, these components produce the IoRL Radio Access Network (RAN).

The IoRL RAN achieves connection to the internet through a central server or multi-core computer which acts as an Intelligent Home IP Gateway (IHIPG). The IHIPG has connections to the internet, Mobile Network Operators (MNO) and e/gNB and routes data according to application and user needs through the means of Software Defined Networking (SDN) and Network Function Virtualisation (NFV

The NFV layer, contained within the IHIPG is comprised of the Network Function Virtualization Orchestrator (NFVO). This is the top-level management entity of the IHIPG domain and invokes different Virtual Network Functions (VNFs) required for an IHIPG to facilitate local access and deep packet inspection, mobility management, and network security functions. The concepts of NFV and parallel processing pipeline are beneficial to distribute the complex processing required to the IHIPG, thereby, reducing the form factors of the RRLHs [209] [211].

Various use cases are presented in Cosmas, Meunier, *et al.* and Cosmas, Zhang, *et al.* [206]–[209] for the IoRL system and further VNFs are specified for each of the various demo sites of the IoRL project in Cosmas *et al.*[211] and are summarised in Table 2.1.

Table 2.1 - Summary of Proposed IoRL VNFs

VNF	Scenario provided	Summary	Location data required?
Load Balancing (LB)	General	Monitors incoming/outgoing traffic of the RAN and determines the need for transmission through the mmWave/VLC or Wi-Fi Access points.	No
Multisource Streaming (MSS)	General	Simultaneous use of Wi-Fi and mmWave/VLC transmission for downloading media at various resolutions to improve reliability.	No
Proxy servers	General	Managing content and mapping protocols to enable media continuation throughout the house	Yes
Security Monitoring	General	Various preventative measures to reduce potential malicious network attacks such as Rogue Dynamic Host Configuration Protocol (DHCP) servers, Eavesdropping and Denial of Service (DoS).	Potentially
4k/8k streaming	Home	Utilising the 5G high throughput expected from mmWave and VLC transmission to deliver high resolution content to remote displays.	No
VR Multiplayer	Home	Streaming high resolution and ultralow latency VR media between networked users for multiplayer interactivity	No
Follow me Service (FMS)	Home	Streaming video to televisions in rooms in which the smart phone user is located as they move.	Yes
AR overlay	Train	Overlay Virtual models to aid in identification of hardware requiring maintenance.	Yes
Monitoring workforce	Train	Locating maintenance workers for monitoring, safety and evacuation.	Yes
360 remote tourisms	Commercial	Streaming 360 camera content directly to remote VR users for a shared experience.	No

The SDN Layer contains the SDN Forwarding Device (FD) that routes IP packets between the 5G Layer-2/3 Protocol Processors and the internet or 5G network interfaces connected to the SDN Controller. The delivery is managed for different destinations, such as internet, mobile network, Wi-Fi, and different RRLHC's of the IoRL RAN, based on the type of traffic categorised by different network entities and applications [210] [209]. An overview of SDN access and handover procedures between indoor and outdoor connections to the internet or mobile networks using the IoRL network is provided in Cosmas *et al.* [210]. A complete overview of the IoRL architecture is provided in Figure 2.7.

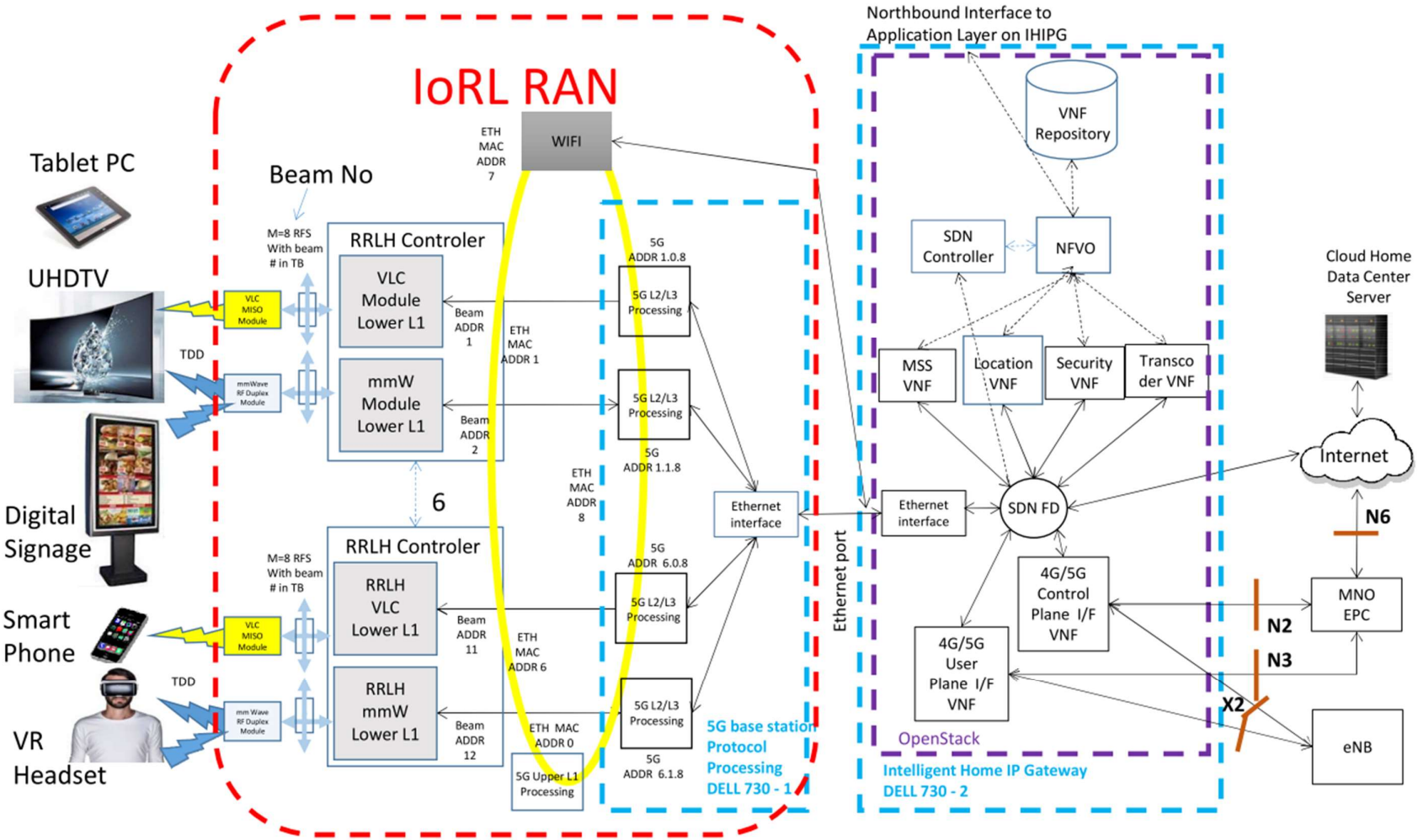

Figure 2.7 - Complete overview of the IoRL system architecture

2.3.3.3 The IoRL Indoor Positioning System (IPS)

The importance of the IoRL IPS is highlighted by the extent of potential services outlined within Table 2.1 that may benefit from available location data. The IoRL Indoor Positioning Protocol (IPP) is discussed in Zhang *et al.* [212]. A summary is given within this thesis to help the reader understand the existing protocols, components, and transactions of data within the IoRL network. These will be implemented later for testing and evaluating the performance of the IoRL IPS and its capability in fulfilling the potential location-based services.

2.3.3.3.1 IoRL IPS Overview

The IoRL IPS is constructed from four key components: the Location Service Client (LSC), the Location Database (LD), the Location Server (LS), and the RRLH Controller (RRLHC). The LSC is a software application contained within either the UE or CHDCS. The functionality of the application requires access to location data to provide services such as indoor navigation, monitoring, follow-me-TV, and more. The RRLHC is responsible for attaining the relevant measurement parameters. For the mmWave uplink channel, Sounding Reference Signals (SRS) are transmitted by the UE, and received by the RRLHs. The Time of Arrival (TOA) of the SRS are subsequently calculated by the RRLHC. These measurements are forwarded to the LD through the SDN in the form of packets, according to the Packet Data Convergence Protocol (PDCP). Alternatively, in the downlink channel, VLC SRS are transmitted from the RRLHC and RRLHs to be retrieved by the UE. The UE is equipped to measure the RSS of the VLC signals which are transmitted to the LD using either the IoRL RAN or WLAN link. The LD is a VNF within the IHIPG constructed of three tables, configured within a MySQL database, in which all location parameters are stored and retrieved. The first LD table (LD1) stores relevant mmWave and VLC location data of all currently connected UE devices retrieved by the RRLHCs. A single entry includes a unique UE ID, the RRLHC ID involved, the estimated mmWave and VLC parameters for all N RRLH sensors, denoted by S^i for $i = (1, \cdots, N)$ as well as a timestamp of when the measurements were taken. An example of the table structure is given in Table 2.2 and the parameter details are elaborated in Zhang *et al.* [212]. The use of TOA results is used to describe the relation between antenna coordinates and simplify the table entry as TDOA alone would require specifying the difference between which two antennas.

Table 2.2 - LD1: Measured location parameters

UE ID	**RRLHC ID**	**mmWave TOA**			**VLC RSS**			**Measurement**
		S^1	$\cdots$	S^N	S^1	$\cdots$	S^N	**Timestamp**
1	1		$\cdots$			$\cdots$		DD/MM/YYYY/hh:mm:ss:..

The second LD Table (LD2) contains the prior known mmWave receiver (Rx_{mm}) and VLC LED , Tx_{vlc} coordinates for each RRLH ($RRLH^i = [Rx^i_{mm}, Tx^i_{vlc}]$) where $i = (1, \cdots, N)$. MmWave Receiver and VLC LED cartesian coordinates are denoted as $Rx^i_{mm} = \left[x^i_{mm}, y^i_{mm}, z^i_{mm}\right]^T$ and $Tx^i_{vlc} = \left[x^i_{vlc}, y^i_{vlc}, z^i_{vlc}\right]$ respectively. The table contains the unique UE ID, the RRLHC ID, connected RRLH ID's and respective mmWave antenna and VLC LED coordinates. This table must be configured upon installation of the system. Table 2.3 illustrates the structure of IoRL LD2, the parameter details are elaborated in Zhang *et al.* [212].

Table 2.3 – LD2: mmWave Antenna and VLC source coordinates

UE ID	**RRLHC ID**	$\boldsymbol{RRLH^i}$						⋯	$\boldsymbol{RRLH^i}$					
		mmWave Tx			VLC LED			⋯	mmWave Tx			VLC LED		
		x^1_{mm}	y^1_{mm}	z^1_{mm}	x^1_{vlc}	y^1_{vlc}	z^1_{vlc}		x^N_{mm}	y^N_{mm}	z^N_{mm}	x^N_{vlc}	y^N_{vlc}	z^N_{vlc}
1	1													

The third LD table (LD3) stores the estimated locations of the user determined by the IoRL system. An entry consists of the UE ID, the global 3D coordinates of the UE and a timestamp of the estimate. The structure is illustrated in Table 2.4.

Table 2.4 - LD3: UE location estimates

UE ID	**UE coordinates**			**Estimate Timestamp**
	x^0	y^0	z^0	
1				DD/MM/YYYY/hh:mm:ss:..

The LS is a VNF within the IHIPG responsible for calculating the UE position estimates. This is carried out by acquiring the measurement values from LD1 and the respective antenna coordinates from LD3, performing the required TDOA estimation and RSS processes before carrying out data fusion. The position estimate result is then returned to the LD and stored in LD3. At this point, a LSC can request the relative location data and use it accordingly. An overview of the connections between the IoRL IPS components is illustrated in Figure 2.8.

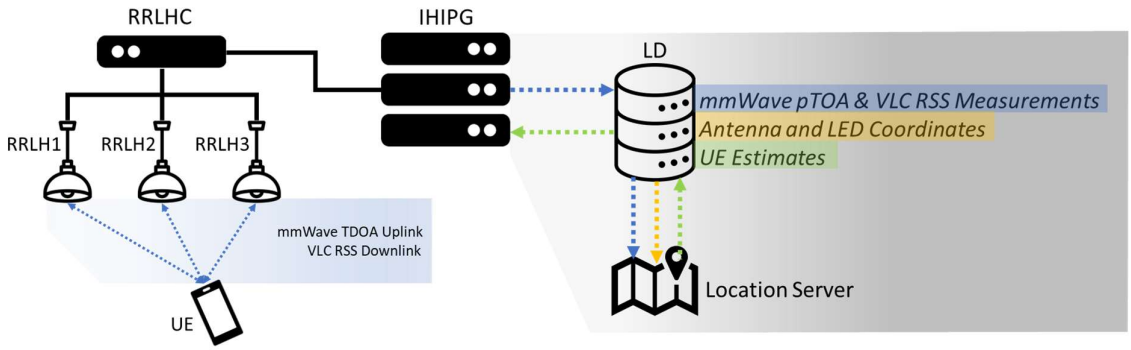

Figure 2.8 - IoRL IPS architecture, direction of arrows between components indicates the transfer of data (no arrow indicates bi-directional communication)

Remark 2 - The IoRL IPS configuration presented is developed for IoRL demonstration purposes and for handover between RRLHCs, implementation of floor plans or more complicated processes, would require further development of the processes and LD tables.

2.3.3.3.2 IoRL IPS Communication Protocol

This section builds upon the relationships and processes discussed in the previous section but introduces greater detail into the transmission of data, which is important with regards to both frequency, synchronisation, and latency. Continuous estimation of VLC RSS and mmWave TOA parameters is carried out between the UE and RRLHC. Only once an LBS request's location data are the relevant estimations transferred to the UE.

2.3.3.3.2.1 Millimetre Wave TOA Acquisition

Again, highlighting the research nature of the IoRL project, decisions are made due to time, cost and feasibility limitations. Additionally, with various partners collaboration between research institutes and industry, not all details are fully disclosed due to Intellection Property Rights concerns of industry.

While the IoRL system intends to perform TDOA location estimation processes, the proposed system directly synchronises the RRLHC with the UE to obtain TOA measurements. Once synchronisation is attained the UE is provided with UE assistance data, describing the base sequences, their group, sequence number, cyclic shift, frequency hopping scheme, etc. This prompts the UE to transmit a sequence of Sounding Reference Signals (SRSs) in the uplink channel. The number of SRSs transmitted is related to the number of RRLHs associated to the currently connected RRLHC. For a RRLHC connected to N RRLHs, the SRSs are contained within the last symbols of the first N sub-frames of the IoRL transmission frame as shown in Figure 2.9 [212] for four connected RRLHs. Each sub-frame pertains to a specific TOA measurement by a single RRLH.

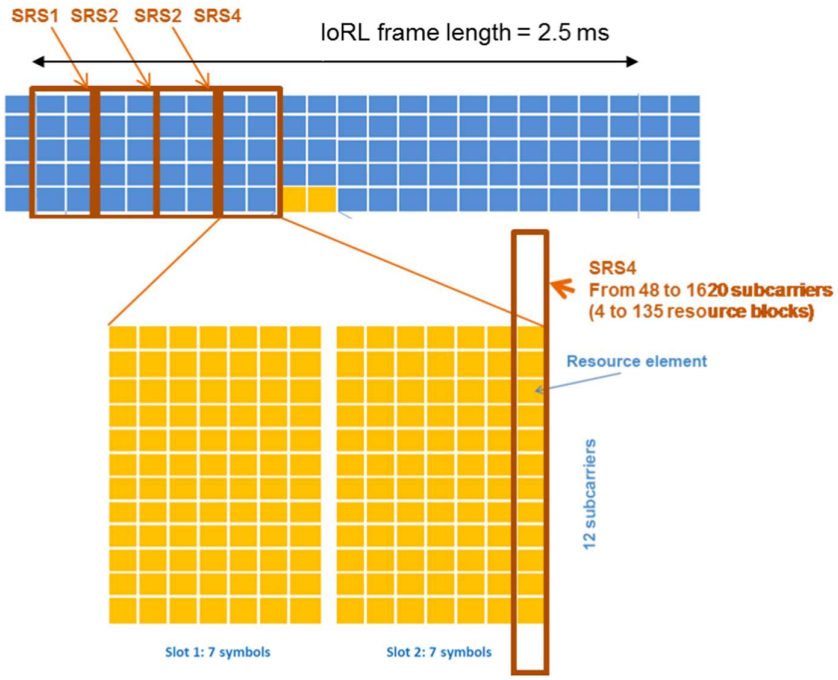

Figure 2.9 - mmWave SRS within the IoRL Transmission Frame

For a system bandwidth of 100MHz each SRS will fill 4 resource blocks, corresponding to 48 subcarriers. The maximum quantity of resource blocks to be occupied is 135, which is equivalent to 1620 subcarriers. The proposed system suggests that each SRS signal within the sequence is retrieved by a single RRLH. This is accomplished by sequentially activating only a single RRLH while the SRS is transmitting. This enforces the need for high synchronisation of the SRS and RRLH, and for a common understanding of the transmitted signal. The TOA is extracted by each RRLH during this round robin activation process, and while doing so the UE and RRLHC clocks are tightly synchronised. This ensures coherent reference time for TDOA computation, according to TOAs measured with respect to partial SRSs. The presented sequential approach reduces the number of parallel channels required between the RRLHC and RRLHs. This decreases the overall system complexity and cost of potential high frequency switches. These results are directly transmitted to the LD for storage in LD1 via the SDN.

2.3.3.3.2.2 Visible Light Communication RSS Acquisition

The VLC RSS measurement acquisition is similar to the mmWave TOA process but carried out in the downlink channel. In this instance the UE prompts the RRLHC to transfer a series of reference signals. As illustrated in Figure 2.10 [212], the relevant reference information is transmitted in the last OFDM symbol of the first N sub-frames of the 5G transport block. Transmitting a single OFDM to only

one of N RRLH VLC LEDS. The reference data only occupies a single subcarrier frequency to transmit the reference coordinates of the respective LED. The sequence and transmission frame are known by the UE prior to transmission to enable the UE to extract the correct information.

While the use of OFDM could be used to distinguish the RRLH identities by frequency, due to IoRL system limitations established by its research nature, the position data is again transmitted in a sequential manner. For N RRLHs connected to the RRLHC, the LED data is transmitted in the last symbol of the last slot in the first N subframes. Where the data in the $i'th$ subframe pertains to the $i'th$ RRLH for $i = (1, \cdots, N)$. The IoRL project intends to use VLC LEDS with 10 MHz bandwidth and SCS of 60 kHz, therefore, a single RSS measurement can be obtained every 1 ms according to the slot durations. Once received, the RSS measurements are transmitted to the LD from the UE.

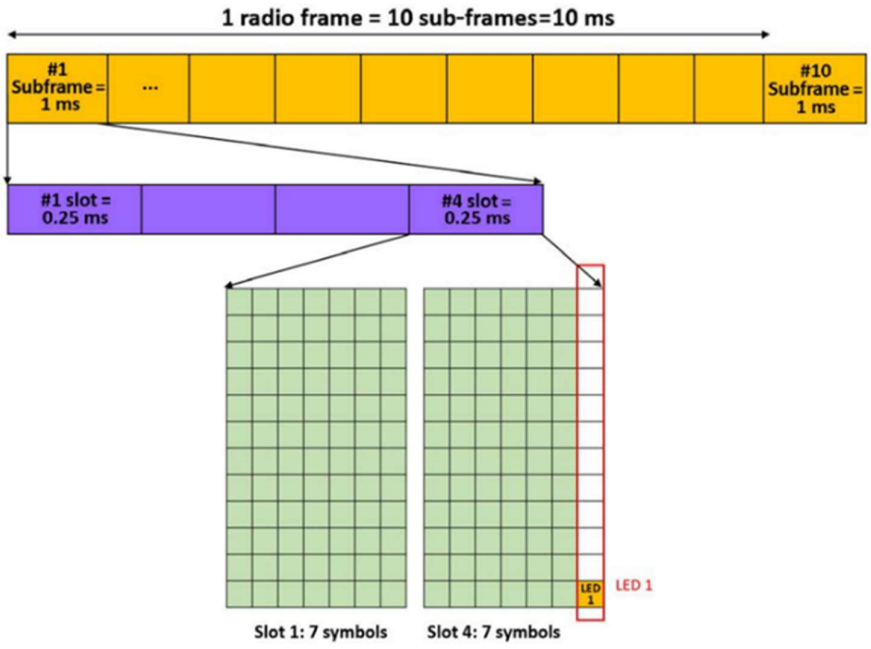

Figure 2.10 - 5G transport block and VLC transmission frames

Location data stored in LD1, and antenna coordinates from LD3 are continuously polled from the LD and processed within the LS. The LS initially uses the RSS and TOA measurements to provide respective position estimates. These estimates are then combined using sensor fusion to establish an optimal output. These results are transmitted back to the LD where the LSC can access the latest relevant location estimates to perform the relevant functions. The process of position estimation and sensor fusion is explored throughout this thesis. Figure 2.11 [212] illustrates the IoRL IPP.

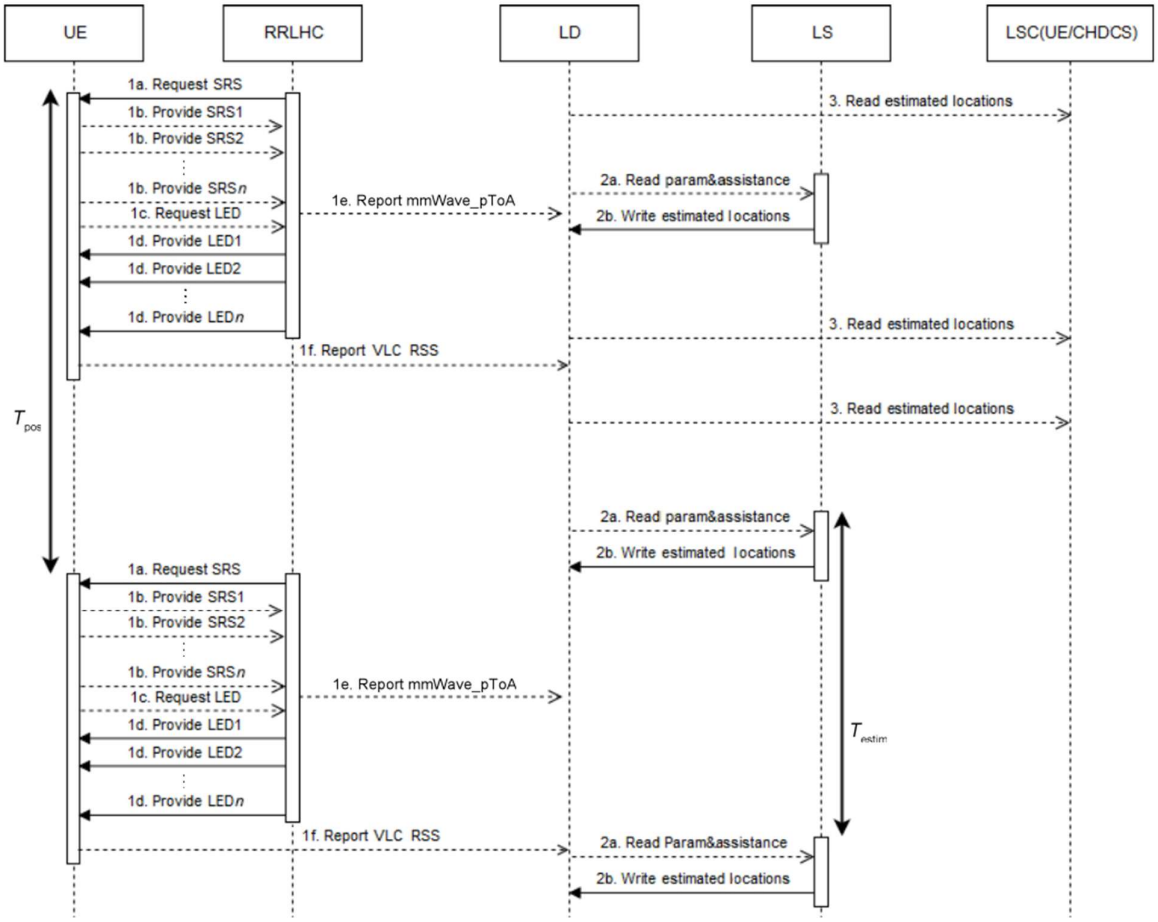

Figure 2.11 - Transmission of data throughout the IoRL IPP

The presented IoRL transmission frame in Figure 2.9 is not a 5G New Radio (NR) compatible frame structure. Through personal correspondence between the author of this thesis and the project partners, the 'IoRL frame structure' presented in Zhang *et al.* [212] is an assumption of the IoRL 5G NR frame structure, prior to standardisation. However, the same mmWave sequencing protocol can easily be translated to the 5G NR frame structure and made equivalent to the VLC positioning sequence where individual TOA measurements are then obtained once every millisecond in the last symbol of the first N subframes. In this regard, the 5G NR frame structure is considered and the mmWave TOA and VLC RSS measurements are obtained synchronously.

The sequential measurement acquisition employed in both the mmWave, and VLC channels separates the individual measurements by one millisecond and presents asynchronous measurement sampling within the IoRL project. The effects of this measurement sequencing is considered in later chapters.

2.3.4 IoRL 5G Localisation Research and Methods

The IoRL system intends to exploit both mmWave and VLC technology to achieve indoor localisation with accuracies below 10 cm. This section introduces and surveys existing localisation obtained through these technologies, to be applied in later chapters of this thesis when developing and testing the IoRL indoor positioning performance.

2.3.4.1 MmWave

2.3.4.1.1 Background to mmWave

Existing communication networks typically utilise frequencies below 2.5 GHz within the Ultra High Frequency (UHF) band of the EM spectrum. This is succeeded by the Super High Frequency band (SHF) band between 3 GHz – 30 GHZ, and the Extremely High Frequency (EHF) band ranging from 30–300 GHz. Wavelengths which are within the EHF range span from 10 mm to 1 mm at 3 GHz and 300 GHz respectively, and as such are referred to as the mmWave region [195]. Owing to the vast amount of available spectrum within the mmWave band, it is forecast as a key candidate technology to alleviate the congestion of existing communications within 5G wireless networks. Most of mmWave frequency bands that FCC deregulates for 5G communication systems such as 37-38.6 GHz, 38.6-40 or 64-71 GHz have an absolute bandwidth covering a couple of gigahertz. [209]. In recent years, the combination of research in the field of mmWave and the advances in the design of RF circuits capable of operating at these frequencies, have proven MMW to be commercially viable and a feasible communication technology. MMW signals can provide multi-gigabit communication services, such as device-to-device communication, high-definition television (HDTV), and ultra-high-definition video (UHDV).

2.3.4.1.1.1 Attenuation Characteristics

Due to the short wavelengths of mmWaves, these signals are commonly characterised by their high attenuation where, according to the Friis equation, the path loss can easily exhibit 30 to 40 dB more attenuation over typical link distances [95]. These high attenuation characteristics make mmWaves inherently an LOS based technology. Additionally, due to resonant frequencies with water and oxygen, further attenuation is noted across specific frequencies (e.g. 60GHz) within the EHF band. Signals can be attenuated by 10-15 dB/km which makes specific frequencies unsuitable for long distance communication (> 2 km). [213]. Conversely, however, reports referred to in Al-Samman *et al.* [195] lead the authors of the study to declare that the path loss effects of atmospheric absorption can be considered to be negligible for mmWave in cell sizes under 200m, especially at given frequencies of 6.5GHz, 10.5 GHz, 19 GHz, 15 GHz, 28 GHz, and 38 GHz. The additional attenuation due to molecular absorption of certain mmWave frequencies in the context of positioning is considered within the study

carried out by Prasad *et al.* [70]. However, as is commonly considered for indoor and short range applications, these effects are not as important [53]. While potentially limiting for large scale outdoor communications, for indoor scenarios or small cell environments the consideration of atmospheric absorption is unnecessary.

2.3.4.1.2 Millimetre Waves for Indoor Localisation

2.3.4.1.2.1 Multipath Components:

Following the overview covered throughout Section 2.1.2.1, multipath interference in indoor scenarios can lead to misrepresentation of transmitted signal characteristics and, therefore, alter the measured TOA, TDOA, RSS, or AOA of a signal to be used within a positioning algorithm. Low power multipath components present less interference to the received LOS signal than higher power ones, where the attenuation of a multipath component is a result of potential energy lost through both reflections and the additional propagation distances, which present further free space path loss.

In this respect, the multipath components in Extremely High Frequency (EHF) signals are minimised due to the higher free space attenuation characteristics, which greatly reduce the intensity of multipath signals propagated over extended distances. Therefore, a multipath component is rarely discernible from noise after more than two reflections [95]. Additionally, shorter wavelengths are prone to scattering as opposed to reflecting, however, Olivier *et al.* [95] argues that reflections within the mmWave band do not produce a significant amount of scattering, instead they adhere to Snell's law. Regardless, the harsh result of reflections on multipath components further reduces the magnitude of multipath components such that the line-of- sight (LOS) component is dominant even in the presence of scatterers [95]. This makes it easier to identify and eliminate NLOS interference [20].

These multipath features of mmWaves present a promising approach to indoor localisation, where multipath interference from nearby walls and obstacles is a significant challenge.

Whereas, conventionally, multipath mitigation techniques have been pursued in order to best identify the LOS parameters, the unique disparity between LOS and multipath components in such a system has spawned interest in exploiting multipath components for greater insight into environmental parameters and mapping [20]. Under the high attenuation characteristic of reflections, as shown in Lemic *et al.* [53], the authors of Lemic *et al.* [53] constructively apply one or two first-order reflections, leading to an improved localisation performance. Conversely, a study considered in Olivier *et al.* [95] finds second-order reflections to improve availability of the positioning estimates at the cost of reduced accuracy.

Studies in the field of mmWaves generally take into consideration only the desired LOS path and first-order reflections [20]. [214] considers not only the order of reflections but limits the applied

multipath model to one LOS path and the nearest NLOS path, which is the component expected to have the most impact on the LOS signal. Alternatively, for simplicity Gertzell *et al.* [215] considers a pure LOS path, free of all reflections.

Notably, where NLOS paths are considered, the additional propagation distance of a multipath component, referred to as the path separation from the LOS path, is explored in several studies for ranges between 0.4 m – 3 m [216] and 0 ns -2 ns [214][217] (equating to 0 m - 0.6 m using the propagation speed of light). These studies indicate that greater reflection distances reduce the positioning error, therefore, positioning within the centre of an environment, further away from reflective surfaces such as walls should result in improved localisation performance.

2.3.4.1.2.2 Literature on Localisation Methods using mmWave

Due to the properties of mmWaves and their strong involvement in 5G networks, there has already been a vast amount of interest in the application of mmWaves for localisation. Critically, the use of RSS within mmWave localisation solutions is limited by the strong attenuation characteristics of such high frequency signals [68] [53]. Despite this, Mtrack [218], a passive 60 GHz solution is developed using RSS and signal phase methods to obtain impressive 90th percentile errors of 12 mm for pen tracking. However, the authors of the study acknowledge the sensitivity to hand placement, propagation distance and background noise which limit the scale of the system.

While wavelengths in the order of millimetres have been shown to hinder the effective range of such systems, they conveniently allow for much smaller antenna dimensions which can be useful for both integration within portable devices as well as for forming antenna arrays. The use of high gain horn antennas and antenna arrays permit narrow and directional beams to compensate for the higher path loss [195]. With the interest in antenna arrays for massive MIMO, spatial multiplexing and beamforming, AOA solutions present an exciting opportunity for mmWaves. Regardless, the IoRL project does not consider arrays of antennas and, therefore, AOA techniques are not applicable.

Time-based solutions such as TOA and TDOA, however, benefit greatly from the large available bandwidth and reduced multipath effects which allow for higher resolution timing and easier distinction of the LOS path. This is highlighted in Kanhere & Rappaport [73] where the raw resolution, or smallest divisible difference in distance that can be measured, is defined as the propagating distance of EM radiation between consecutive sampling instants. The raw resolution (r_{res}) is calculated using [73]:

$$r_{res} = \frac{c}{BW}. \tag{2.73}$$

Here c is the speed of light $(3 * 10^8)$ and BW is the bandwidth of the signal in Hertz. Therefore, utilising the 2.16 GHz of 60 GHz channel bandwidth defined in IEEE 802.11ad the raw resolution achievable is approximately 15 cm.

While the IoRL system intended to employ TDOA over TOA to avoid the requirement for synchronisation between the user terminal and RAN, the accuracy of TOA solutions are closely related to TDOA as the greatest source of error in both is the estimation of the time delay in the received signal [70].

Zeb *et al.* [24] uses a timing advance mechanism for TOA detection with 500 MHz bandwidths and beamforming to compare performance of TOA ranging to UWB signals. This highlighting improved millimetre-level accuracy and, worst case, timing errors of a few nanoseconds even in NLOS conditions. Wang *et al.* [214] employs a hybrid AOA and TOA solution to achieve millimetre-level accuracies, resorting to bandwidths of 1 - 2 GHz. Experimental testing of 60 GHz indoor positioning using 1 GHz bandwidth and Two Way Ranging (TWR) [64] achieves sub - 0.05 m accuracies while sub - 0.1 m accuracies are achieved for TDOA systems [219] [220] using 3 GHz bandwidths.

Promising high range and positioning accuracies, in some cases, to the order of millimetres [217][221][72] [24] is achieved in various studies, where each consider the application of UWB signals, fusion techniques with AOA, or beamforming with antenna arrays to improve SNR, and obtain impressive results.

While these results described above are impressive, the IoRL system, as specified in Section 2.3.3, uses 100 MHz of bandwidth at 40 GHz with a single horn antenna for signal transmission. With both a reduced bandwidth and no means to perform AOA, the IoRL system can expect to achieve much lower estimation accuracies. Due to the popularity of UWB availability in mmWave systems, existing literature pertaining to a system configuration of single antenna sensors using mmWave frequencies at 100 MHz bandwidth for TDOA position estimation is scarce.

While the study incorporates antenna arrays and AOA [215] does distinguish the TDOA performance for a range of bandwidths. It is stated that TDOA measurements alone are inadequate in order to bring the position accuracy under 10 cm for a bandwidth of less than 100 MHz, whereas increases in bandwidth beyond 100 MHz indicate impressive centimetre level positioning results. The simulation results further indicate no effect to the TDOA measurements under variable numbers of array antennas and, therefore, the accuracy of TDOA positioning for mmWaves at 100 MHz bandwidth is shown to be approximately 8 – 10 cm.

2.3.4.1.3 MmWave Section Summary

The use of mmWaves for localisation has incredible potential for high precision accuracy, due to larger available bandwidths, highly directional beams, and antenna arrays. While there is growing interest in the field, there is an evident need for a clear and structured survey of recent mmWave localisation methods. Naturally TOA and TDOA methods are strongly reliant on accurate recognition of the signal delay. This is greatly dependant on the multipath interference, delay detection method and resolution of the system. MmWave frequencies present a promising solution for delay detection due to the reduction of multipath components aided by high attenuation factors and further increased by beamforming techniques. The resolution of the system is also highly dependent upon the bandwidth of the system, with frequency bands and standards providing an available bandwidth of 2 GHz; it may soon be possible to observe millimetre level tracking in practical experiments. Notably, the IoRL project stands as a proof of concept, where, if required, additional antenna systems and larger bandwidths could be explored. This fact, as well as the matter that the IoRL demonstrator does not yet have the capabilities to perform TDOA mmWave measurements, is why this thesis considers a range of time delay accuracies for the IoRL system in later chapters.

2.3.4.2 Visible Light Communications

Visible Light Communications (VLC) is an emerging technology in which visible light emitted from conventional LEDs can be modulated to transmit data. Unlike existing wireless positioning technologies for indoor environments, Visible Light Communications (VLC) offer vast amounts of license-free bandwidth, which can be used to achieve high positioning accuracy. Due to its highly Line-of-Sight (LOS) based nature and lack of Radio Frequency (RF) interference, VLC also lends itself to increased security suited to e.g., medical applications. Notably, the minimal adaptation required for existing lighting infrastructure in optimal LOS coverage locations and the use of standard, low-cost, and energy-efficient LEDs makes VLC a viable solution for widespread implementation and coverage. Research into the use of VLC for indoor positioning has seen significant improvements in location performance, with accuracies in the low-centimetre region [37], [199], [222]–[225].

2.3.4.2.1 Visible Light Positioning

Localisation through the means of Visible light technology is referred to as Visible Light Positioning (VLP). Two methods exist for receiving VLC signals, either a Photodiode (PD) or an image sensor, which is essentially an array of PDs. Referring back to the traditional positioning techniques discussed in Section 2.1.3, VLP has been explored within proximity [226], fingerprinting [227] [228], triangulation [37][225] [55][229], and image-based [230][231] solutions.

In keeping with the focus of this thesis, the IoRL project employs RSSI measurements which are received using a PD. Therefore, imaged based solutions are not applicable and not considered further. Additionally, proximity-based solutions may be applied but the accuracy is too generalised to be applied for high level accuracy applications. Both fingerprinting and triangulation, specifically lateration, are potential techniques for use within the IoRL 5G project demonstrator. The multilateration approach has been selected throughout this thesis due to the tedious nature of the necessary calibration phase of the fingerprinting approach, which, when considering the number of demonstrators sites, the IoRL 5G project intended to present at, was a considerable factor. The reader is referred to Zhuang *et al.*, Luo *et al.*, Chunyue Wang *et al.* [63][75][232] and the references therein for a more comprehensive overview of VLP systems.

2.3.4.2.1.1 Channel Model

In visible light positioning systems, signals are transmitted from LED lights to the receiver through a free-space channel. The LED source is often considered as a Lambertian emitter [39] where the signal is broadcasts according to Lambert's emission law, i.*e., the radiant intensity or luminous intensity, observed from an ideal diffusely reflecting surface or ideal diffuse radiator, is directly proportional to the cosine of the angle between the direction of the incident light and the surface normal* [33], [40]. The power received at the PD (P_R) is related to the power transmitted from the VLC source (P_T) and the channel $\big(H(0)\big)$ [199]:

$$P_R = H(0) * P_T. \tag{2.74}$$

Since the channel involves both the LED and the receiver, the LOS channel is described as follows [63]:

$$H(0) = \frac{(m+1)A_r \cos^m(\psi) \cos^{\mathrm{M}}(\theta)\, T(\theta) g(\theta)}{2\pi d^2}. \tag{2.75}$$

In which A_r is the effective area of the PD, ψ and θ represent the LOS paths' angle of irradiance and incidence, respectively, d is the Euclidian distance between the source and PD, and $T(\theta)$ and $g(\theta)$ are, respectively, the optical filter gain and optical concentrator gain at the receiver. m and M represent the order of Lambertian Emission and incidence respectively, as given by [63]:

$$m = -\frac{\ln(2)}{\ln\big(\cos\big(\psi_{1/2}\big)\big)}, \tag{2.76}$$

$$M = -\frac{\ln(2)}{\ln\left(\cos\left(\theta_{1/2}\right)\right)}. \tag{2.77}$$

Here, $\psi_{1/2}$ is the semi-angle at half power of the VLC source and $\theta_{1/2}$ is the semi-angle at half power of the PD. If no lens is used at the receiver, then $T(\theta) = 1$ and $g(\theta) = 1$. These relationships are illustrated in Figure 2.12 where $\hat{h}$ describes the vertical height between the PD and source.

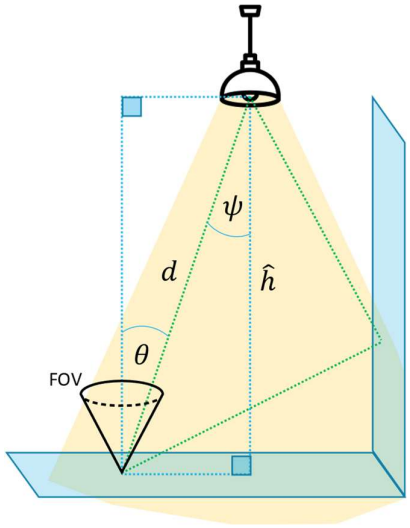

Figure 2.12 - 2D VLC trilateration localisation

A_r is considered a trade-off between bandwidth and sensitivity since an increase in A_r results in a PD able to receive more light, therefore, increasing sensitivity. However, the greater the photosensitive area, the greater the capacitance, which reduces bandwidth [63]. The influence of various PD dimensions on the estimation of the Euclidian distance are explored in Keskin *et al.* [233]. Across most literature, $M = 1$ on the assumption that the semi-angle at half power of the receiver, $\theta_{1/2} = 60°$. The semi-angle at half power of the source, m, is commonly extracted from the sources' datasheet or otherwise empirically calibrated for. Studies in Lin *et al.* [222], Alam *et al.* [223], and Li *et al.* [160] experimentally model the VLC source patterns to accurately calibrate channel parameters according to the Lambertian model and deem it a good fit. As m is decreased, the transmitters directivity is increased at the expense of the transmitter's concentration area. The effects of the semi-angle at half power of the transmitters are considered for positioning systems in [234] where distinct lighting systems are employed. The study suggests that larger values in a LOS case improve signal coverage across the room and, therefore, improve accuracy. Where multipaths are considered, the higher m values incur greater reflections which accumulate at higher transmission angles.

2.3.4.2.1.2 Multiplexing

Primarily due to the impracticality of light transmitting from a device a user may be using, VLC systems are only considered in the downlink channel. Therefore, the TOA, TDOA, RSS and AOA can only be calculated at the UE side, since two-way ranging methods are not possible to realise in this case. For these systems to function the UE device must receive assistance data in the transmission to be able to determine the correct parameters. AOA requires source ID, coordinate information, RSS methods additionally need the transmitted power whereas time-based methods require knowledge of the transmission time and transmission block structure. Common solutions to prevent signals interfering with one another is the use of TDM or FDM, where the total bandwidth is divided into different time slots or frequency bands. The IoRL project, like many VLC solutions, employs OFDM [222] where signals are orthogonally spaced in the frequency domain to overcome Inter Carrier Interference due to severe channel conditions as a result of Doppler such as narrowband interference and intersymbol interference (ISI) as a result of multipath frequency selective fading. Due to the dual-purpose nature of VLC for illumination and communication, systems must be configured avoid flickering and a reduction of brightness.

2.3.4.2.1.3 Types of Noise

Two types of noises are often associated with PD currents; the shot noise, which is the fluctuation in electric current due to incident optical power from all light sources in the environment and thermal noise, which describes fluctuations in current due to temperature changes in the receiver's circuitry. The total noise variance σ_{noise}^2, in the electric current domain is given by [235]:

$$\sigma_{noise}^2 = \sigma_{shot}^2 + \sigma_{therm}^2 \quad . \tag{2.78}$$

Ambient light from either artificial sources or the sun can directly affect the shot noise producing a larger background current [236]. However, due to multiplexing methods, experimental conditions under ambient lighting have also resulted in no visible difference in performance [160].

2.3.4.2.1.4 Multipath

VLC systems are often considerably more resilient to multipath components when considered against conventional RF systems. For RSS solutions, where the range is estimated by the LOS path loss, additional reflected paths introduce added power and lead to a divergence from the given LOS path loss model. Therefore, considering unwanted multipath components affects the range estimation and, consequently, the position error. Fortunately, compared to the LOS path, multipaths have reduced

power, both due to the poor reflectivity of a reflecting surface and due to the free space attenuation factor, therefore, the more reflections and the longer the path, the lower the received multipath signal power.

Under the assumption that attenuation from multipath components are high enough, the effects are negated, and only the LOS path is considered [222]. The error without considering multipath is only affected by receiver noise (σ_{noise}^2) and free space attenuation, therefore, the further from the lights, the worse the SNR and, subsequently, the worse the range estimate is [237]. In Almadani *et al.* [98] the authors of the study note that use of the three strongest signals are shown to reduce impacts of multipath and improve accuracy as presented in Gu *et al.* [235]. However, studies in Kwonhyung Lee *et al.* [238] and Shi *et al.* [239] indicate that VLP results are differently affected by reflective materials across the VLC spectrum. The greatest effects from multipath components are seen near reflective surfaces [235] [234] such as near walls and corners. Closer to the centre of the room, the multipath signals attenuate and reduce in intensity [160]. This is experimentally validated by Almadani *et al.* [38], where positioning errors due to reflections are noted to increase to a minimum of 56% and a maximum of 133%. Filters and increasing the transmission power have been analysed to reduce the effects of interference within VLP systems [234] [239], which is effective until the multipath and LOS components stabilise.

2.3.4.2.1.5 Field of View (FOV)

A receiver will only retrieve signals within its Field of View (FOV), as indicated by a cone in Figure 2.12 with an angle related to the normal of the PD and denoted by (θ_{FOV}). Incoming signals with incidence angles greater than the FOV angle ($\theta > \theta_{FOV}$) are not received at the PD. To ensure signal reception, especially in larger environments, the PD FOV should be large enough to always be in LOS of a VLC source. In cases where multiple sources should be retrieved simultaneously, such as for fingerprinting or triangulation, the source separation distances and FOV should be carefully considered. Simply tilting [63] or raising a PD too high [37] [17][234] can increase noise, due to higher incident and radiant angles, or prevent the reception of LOS signals altogether. Additionally a trade-off must be considered between capturing more useful signals and potentially receiving more undesired signals from other sources, multipath components, or ambient light which can lead to poorer positioning performance [239] [234]. As described above, due to the limited LOS, receiver FOV, source separation distances and the transmitters emission pattern, maintaining LOS signal reception is not trivial.

2.3.4.2.2 VLC RSS Trilateration

Since the incidence and radiance angles affect the RSS in the VLP trilateration method, a 3D configuration such as that illustrated in Figure 2.12, is often simplified to a 2D solution where the target is considered to move along a surface parallel to the floor. This is applicable for scenarios considering autonomous ground vehicles (AGVs) and robots in a smart home [240].

2.3.4.2.2.1 Existing 2D VLC Trilateration RSS Literature

Experimental VLP systems are shown to attain mean positioning errors of 1.68 cm, 18 cm, 3.9 cm and 30 cm from Lin *et al.* [222], Shi *et al.* [199], Alam *et al.* [223], and Li *et al.* [160], respectively. Overall centimetre level performance obtained across a wide variety of lighting arrangements and coverage areas highlights the impressive nature of VLP systems. Authors of Li *et al.* [160] experimentally evaluate a 2D VLP system through integration of PD based trilateration and IMU sensors within a mobile phone. The orientation of sensors help to determine any potential tilt in the device and transform it back to the assumed horizontal attitude. Experimental results achieve median error of 30 cm for all environments, with 90^{th} percentile errors of 45 cm, 70 cm and 80 cm in the conference room, cubicle, and corridor environments in which the experiments were conducted. The authors of the study attribute the variation in errors to the arrangements of LEDs and number of reflective objects. This highlights a need to evenly deploy LEDs for optimal coverage. Where mentioned in the relevant literature, the common practice when considering OFDM modulation is to retrieve the RSS measurements from the subcarriers with the highest received signal intensity [199] [222]**.** Mapped position estimation results, as presented in Shi *et al.* [199]**,** clearly illustrate a prominent skew attributed to the reflections from walls, as central results perform much better. The use of multiple receivers to address the effects of shadowing from dynamic environments were considered by Lin *et al.* [222] while Se Hoon Yang *et al.* [241] implements multiple PD receivers for a single transmitter on a rotating platform to overcome inter symbol interference.

2.3.4.2.2.2 Existing 3D VLC Trilateration RSS Literature

VLP solutions for 3D position estimation are non-trivial due to the number of unknown parameters including the received power and either the targets height or incidence and radiance angles. An adaptive parameter particle swarm optimisation (AP-PSO) algorithm is proposed and applied by Xu *et al.* [242] to estimate 3D coordinates under an assumed gaussian LOS and NLOS model. Alternative approaches in Plets *et al.* [17] and Almadani *et al.* [38] consider iterative trilateration methods for discrete increments in the third dimension (height). This iterative approach is affected by the resolution of the height intervals used. While results obtained for both the PSO and iterative

approaches maintain centimetre-level accuracies, the solutions are computationally inefficient and are shown to take 11.3 ms [242] and 17 ms [17], respectively. Furthermore, previously presented studies have simplified the solutions by considering the PD to be parallel to the ceiling where the LEDs are mounted. For real world use cases, this assumption is a key limitation. Building on their previous work in Almadani *et al.* [38], the authors of the study consider the same iterative height 2D trilateration. However, they include the consideration of the receivers tilt [98]. The obtained results highlight that the greater the tilt of the receiver and level of induced multipath components, the greater the positioning errors. Conversely Kim *et al.* [243], proposes a gradient search method to determine the position that corresponds to the minimal cost function value. Experimental results using four LEDs provides an average 3D positioning error of 7.95 cm with 70 % of points under 5.5 cm. The tilt is shown to have an almost negligible effect on the position estimation with a standard deviation of 5.2 cm. Alternatively, researchers have mitigated the unknown parameters by considering estimation of the receiver angles through use of additional sensors. implementing additional sensors such as Inertial Measurement Units (IMU) [225] to determine the receivers orientation. This approach relies on static sequential measurements and the user performing controlled re-orientations. The study fails to describe the effects of orientation magnitude on the resulting position error performance.

2.3.4.2.3 Practical Effects of LED Shape and Emission Patterns

The effects of LED structures on illumination and communication for VLC have been studied and compared in both Jenilla & Jeyachitra [244] and Nguyen *et al.* [245]. However, very little research has been conducted considering source LED characteristics effects on VLP performance. Considered VLP works discussed so far have all relied on the channel model (2.75) in some form or another to describe the RSS at specific coordinates. The applied channel model conventionally assumes the radiation patterns of the VLC source to be Lambertian with a fixed order of Lambertian value, m. The order of Lambertian emission describes the directivity of the source and is inversely related to the semi-angle at half power, $\psi_{1/2}$ of the source. m can be considered to describe the rate of decay in intensity and, therefore, is critical in correctly describing the intensity of the source at various angles or distances.

The semi-angle at half power of a VLC source is commonly detailed by the manufacturer and can be applied directly to determine m. However, various studies have identified variability within the Lambertian values in practical scenarios.

The study set out in Alam *et al.* [223], presents two calibration processes to determine the optimal values of the channel model that best represent the practical environment. This involves an offline process of collecting RSS measurements at known coordinates. The authors of the study

substitute and rearrange the channel model equations given in (2.74) and (2.75) to give (2.79) and (2.80) [223].

$$P_R = \frac{(m+1)A_r\hat{h}^{m+1}P_T}{2\pi d^{m+3}}\ , \tag{2.79}$$

and

$$d = \sqrt[m+3]{\left(\frac{\tilde{G}(m+1)\hat{h}^{(m)}}{P_R}\right)}. \tag{2.80}$$

In which the gain term $\tilde{G} = \frac{A_r\hat{h}P_T}{2\pi}$ and $\hat{h}$ is the known height difference between the PD and source resolved through trigonometric relationships pertaining to the angle of incidence and radiance. This is elaborated on further in the following chapter.

The first calibration process is two parameter calibration where the variables $\tilde{G}$ and m are calculated to be the values that attain the least range error across all points as given by [223]:

$$\left(\hat{\tilde{G}}, \hat{m}\right) = \arg\min_{\tilde{G},m} \sum\left(\hat{d} - d\right)^2. \tag{2.81}$$

Here $\hat{d}$ is the Euclidian distance estimate calculated using the allocated $\tilde{G}$ and $\hat{m}$ variables as part of (2.80), and d is the known true Euclidian distance. The second proposed process is a single parameter calibration, where a reference RSS measurement (P_R^{REF}) is taken, preferably directly under the luminaire for simplicity in calculating d_{REF}. Dividing (2.79) by its reference point counterpart, one eliminates the gain and height terms to obtain [223]:

$$P_R = P_R^{REF}\left(\frac{d_{REF}}{d}\right)^{m+3}. \tag{2.82}$$

Estimates for m can be acquired solving (2.82) for all calibration measurements. The optimal m is obtained by [223]:

$$\hat{m} = \arg\min_{m} \sum\left(P_R - \hat{P}_R\right)^2. \tag{2.83}$$

Where P_R is the measured RSS and $\hat{P}_R$ describes the RSS estimate obtained by (2.84) and the given value of m. Resultantly distance estimates can be calculated by re-arranging (2.82) for d. Both calibration processes are conducted for each individual sources, each one belonging to one of two types of lights.

From the Lambertian calibration study conducted in Alam *et al.* [223], the calibration process using as little as 12 measurements per light achieves high positioning accuracy which is comparable to large database fingerprinting methods with 187 measurements overall.

Notably the work highlights irregularity in emission characteristics, not only between different models of light sources but, more significantly, variability was observed among the same types of lights. This is attributed to asymmetric light distribution, which means the attenuation is found to be inconsistent as the source is turned around about its vertical axis. Furthermore, the same set of lights are calibrated twice in two experiments and are found to have varied values of m which is credited to small changes in the environment. This trend regarding the variation in power among similar lights is also noted in Li *et al.* [160], where the authors of the study experimentally validate the Lambertian model by plotting the measured signal strength across a range of distances between the receiver and transmitter. The experiments concluded a good model fit but described a variation in power across all lights. Again, similar findings are discussed in Almdani *et al.* [38] where LEDs' true transmitted power is shown to vary by 20% from their advertised values. Applying this understanding, Almadani *et al.* [38] and Shi *et al.* [199] experimentally obtain reference powers for individual lighting systems using reference points directly under the sources.

Alam *et al.* [223] also identifies three distinct regions of the Lambertian attenuation model: the plateau directly under the source, the middle descent, and a tail at the end. The calibration is said to model the channel effectively if these three regions are captured by enough offline measurements. Following on from this study, Du *et al.* [240] suggests only two reference positions are required, as long as the span of the reference measurements represents the location coverage or range of SNR. For each light two reference RSS measurements are obtained and used in a process similar to that described by the single parameter calibration of Alam *et al.* [223].

While calibrating for practical VLC source Lambertian characteristics is shown to be effective, some literature suggests the Lambertian property may not always be expressed in practical systems. Kim *et al.* [246] stipulates that VLC sources are usually developed as LEDs fitted with a lens, where the source's radiation pattern is affected by the lens' shape, the lens' internal refractive index and the arrangement of potential multiple LEDs inside. The lens, therefore, may alter the assumed Lambertian properties of the system. Because of this, a generalised channel model is proposed by Kim *et al.* [246], and summarised neatly in Zhuang *et al.* [63] as.

$$P_R = \left(\frac{P_T}{d^2}\right) C_{opt} G_r(\psi) G_i(\theta). \tag{2.85}$$

Here C_{opt} is the is the optical power constant related to the radiation intensity of the transmitter, the concentrator gain, the optical filter gain, the physical area of the detector under normal radiation and incident angles. $G_r(\theta)$ and $G_i(\psi)$ are the normalised radiation and incidence gains of the transmitter and receiver with respect to θ and ψ. Due to empirical testing of the emission patterns, the authors of the study propose an exponential model as opposed to the Lambertian model where the angular gain components are given as [246]:

$$G_r(\psi) = \exp\left(-\frac{(\psi)^{S_r}}{k_r}\right), \tag{2.86}$$

and

$$G_i(\theta) = \exp\left(-\frac{(\theta)^{S_i}}{k_i}\right). \tag{2.87}$$

In which S_r and S_i are slope constants according to $G_r(\psi)$ and $G_i(\theta)$ respectively. k_r and k_i are related to the semi-angle at half power of both the transmitter $\theta_{1/2}$ and receiver $\psi_{1/2}$ by [246]:

$$k_r = \left(\theta_{1/2}\right)^{S_r}/\ln(1/2), \tag{2.88}$$

and

$$k_i = \left(\theta_{1/2}\right)^{S_i}/\ln(1/2). \tag{2.89}$$

The positioning study which uses the exponential model in Kim *et al.* [246] goes on to achieve average positioning errors of 2.4 cm over 18 points within the area of a 60 cm equilateral triangular prism. In Se Hoon Yang *et al.* [241], the exponential model is applied again to model the optical channel. During this study, a single transmitter is used for a positioning system that utilises multiple receivers on a rotating platform. Results using the exponential model achieved average distance errors of 0.65 cm with a maximum error of only 1.5 cm. More recent works [38], in which the Lambertian model is applied, have attributed various positioning errors towards the possibility that the transmitters radiation pattern is not 'perfectly Lambertian'.

Wu *et al.* [247] highlights the effect of the transmitting LED lens structure on resultant emission pattern and exploits this to design a lens structure to linearise the horizontal intensity. In doing so the distribution is easier to model and improves the positioning accuracy by 44 % to an average of 4 cm, when compared to LED transmission with no lens.

2.3.4.2.4 Summary of VLC Localisation

VLC is a promising technology owing to its vast number of benefits in energy efficiency, cost and illumination properties. VLP is growing in interest due to the accessibility of the technology and the

high positioning performance that can be obtained. However, due to the Lambertian channel model with multiple unknown variables, VLP is commonly limited to 2D solutions, as is explored in this thesis. Techniques for 3D positioning in 3D space require more complex processes and often entail additional sensors. Nevertheless, most literature, whether describing 2D or 3D solutions relies on the Lambertian model assumption. While Lambertian parameters can be obtained from the source manufacturers datasheets, a few sources emphasize the need to calibrate the model parameters to specific light sources and identify the effects of individual lighting features, such as lens structure, on the positioning performance. In contrast to Lambertian models, exponential models have also been presented, however these follow a very similar trend to the Lambertian model.

In a unique sense, VLC technology offers a cheap and minimally invasive solution enabling existing light sources to achieve 5G transmission and high-performance localisation. However, lighting system options are diverse, such that if VLC is to be widely deployed, a plethora of different VLC compatible lighting configurations and structures are likely to emerge. Solutions are required to ensure that a VLC system, used within various, old and new, existing lighting structures which may not have Lambertian properties, should maintain the ability to perform high end localisation. In this regard this thesis considers the effects of VLP from sources with non-Lambertian properties.

2.4 Thesis Focus

From observing various existing technologies, processes, and technologies it is evident that the Indoor Positioning Systems' application, and its subsequent requirements, dictate the suitability of a positioning system. In which suitability refers to the compromise between high accuracy and reliability, and the complexity, latency, energy efficiency and costs that come with it. These latter parameters are correlated to the computational runtime of a solution as considered throughout this thesis.

Data fusion through various Kalman Filtering processes provides numerous benefits to increase a systems reliability and reduce noise. However, the response of these techniques is highly dependent on the noise parameters, that are applied as weightings, between predictions and measurements. Moreover, where non-linear measurements or processes are concerned the EKF and UKF techniques present significantly higher computational demand.

The above understanding is then applied to the development and evaluation of the IoRL IPS, which incorporates both mmWave and VLC technology in a hybrid manner. These emerging LOS technologies have great potential for high positioning accuracy over short propagation distances. Owing to the ubiquitous deployment of existing lighting systems, VLC solutions present a cheap and simple solution for widespread 5G connectivity and energy efficient high positioning accuracy. The

literature pertaining to these solutions however is primarily concerned with Lambertian channel models, which due to different lens structures may not always be maintained. This restricts the lens structures which can be used or if they are used produces poor positioning performance if Lambertian conditions are not met.

Owing to the structure of the IoRL architecture, the IoRL IPS exhibits asynchronous sampling, indicating the need to apply localisation methods for asynchronous sampling of non-linear measurements. However, while computational efficiency is mentioned in various literature sources regarding these solutions, additional processes are required which add further computations to the system and yet the computational costs of these additions are not evaluated.

Moreover, the degree to which a system may be asynchronous is variable, therefore the necessity of these more complex solutions, to improve accuracy or reliability, within given scenarios is unclear. While the compromise between accuracy and latency related costs is a subjective matter regarding the IPS application, these factors should be evaluated to assess the extent of the benefit to cost trade-off.

2.4.1 Thesis Outline

The structure of this thesis is outlined below.

Chapter 3 presents an evaluation of VLC RSS data obtained from the IoRL IPS. Initial findings highlight poor performance, due to applying Lambertian models to non-Lambertian sources. This is resolved through the development of a more appropriate novel calibration procedure to achieve high accuracy centimetre level positioning, accommodating the non-Lambertian light sources.

This proposed new technique is then evaluated in chapter 4 using the IoRL IPS. Where through data fusion with mmWaves, the system is shown to achieve performance that exceeds the 5G criteria and IoRL case requirements. Evaluation of the IoRL IPS highlights the asynchronous sampling, which is previously assumed negligible, and the potential need for asynchronous sampling localisation techniques.

Chapter 5 provides a more comprehensive evaluation of the asynchronous sampling effects on various existing positioning techniques, regarding variable sensor measurement noises, latencies, and trajectories.

Building on the analysis provided in chapter 5, chapter 6 shows that the asynchronous sampling solutions significantly increase computational demand. Through application of more efficient methods, a novel asynchronous sampling localisation technique for non-linear measurements is proposed and tested, to achieve superior performance and significant energy reductions over 50%.

3 Compensating for Lens Distortion in Visible Light Positioning

3.1 Introduction

This chapter focusses on visible light positioning and the compensation required for potential lens distortion found in typical home lighting. Visible Light Communications (VLC), as detailed in the literature review, have emission patterns which are generally assumed to follow a Lambertian distribution. It is widely understood that the lens structure of the emission can affect the light distribution although there is very little research on Visible Light Positioning (VLP), for lights with non-Lambertian characteristics. VLP experiments using trilateration methods tend to be conducted in laboratory settings, using standard commercial light sources which either exhibit or are assumed to exhibit conventional Lambertian emission patterns. However, it is necessary to consider VLP across diverse settings and circumstances including non-Lambertian sources in non-ideal systems. Experimental research models of VLC source patterns from Lin *et al.* [222], Alam *et al.* [223], and Li *et al.* [160] accurately calibrate channel parameters following a Lambertian distribution. In Alam *et al.* [223], the experiments emphasise the difference in source parameters coming from identical light sources. Interestingly, due to the refractive index of LED lenses, an exponential model has been proposed in Kim *et al.* [246] and applied in Se Hoon Yang *et al.* [241] which suits the emission pattern of LED lenses better than the Lambertian model.

3.1.1 Aims

This chapter aims to describe and evaluate the performance of the Internet of Radio Light (IoRL) VLP system through practical experimentation including analysing the behaviour of the system by applying conventional approaches as well as comparing these to calibration procedures sourced from the literature.

3.1.2 Contributions

The contributions in this chapter include the experimental validation of the negative effects that the lens structure can have on VLP performance and the proposal of a novel corrective VLP process which resolves the effects of lens deformation produced by Total Internal Reflection (TIR) lenses with a frosted central coating or other lens types producing a halo ring effect. These will be presented in three sections. Firstly, the data and analysis of the IoRL 5G 2D VLP measurement campaign taken in a home environment resulting in an average Positioning Error (PE) of less than 5 cm. Secondly the non-Lambertian emission pattern and Halo ring lighting effect identified as a result of the commercial

lenses used in this campaign. Lastly the proposal of a calibration method to accommodate for the Halo ring lens distortions observed in VLP.

3.1.3 Summary

Firstly, the Internet of Radio Light (IoRL) measurement campaign and the VLC specific results obtained, secondly the analysis of the positioning performance under existing channel models using the experimental data and thirdly the development of the proposed corrective algorithm for VLP within the IoRL Indoor Positioning System (IPS) will be presented.

3.2 The IoRL Measurement Campaign

The IoRL Measurement Campaign was part of the IoRL Horizon 2020 project and is detailed in Ali *et al.* [248]. To identify components of practical significance, the experimental methodology and main hardware required to obtain the VLC RSS measurement datasets are summarised in this chapter.

3.2.1 Objectives of the Study

The IoRL measurement campaign aimed to undertake various signal quality measurements and demonstrate the functionality of the system in the various scenarios that the IoRL project was set to exhibit in [206]–[209]. The Covid 19 pandemic and government-imposed travel restrictions limited the construction of the model to a single scenario which was the home environment. The system was also restricted to downlink only, which meant that the Time of Arrival/Time Distance of Arrival (TOA/TDOA) testing could not be performed. The tests which could be conducted were the downlink VLC transmission of HD video content, the Error Vector Magnitude on both VLC and mmWave downlink channels, to identify channel quality, and Visible Light RSS testing, which is the focus of this chapter.

3.2.2 The Overall Setup – Connections, Environment

The IoRL measurement campaign was carried out at the Building Research Establishment (BRE) in the UK, using a furnished open plan sitting room designed for a home environment. The Experimental setup matched one of the environments required in the IoRL project. The hardware was fixed to a 0.4m wide square cross-section aluminium extrusion frame measuring $(2.5 * 2.5 * 2)$, $(Length * Width * Height)$/m. A centimetre grid was placed horizontally on a flat surface 0.7 m from the floor. Measurements were taken in the centre of the grid. There were four VLC transmitters $(N = 4)$ placed over the grid. The Cartesian coordinates $x^i, y^i, z^i/$ m were respectively $(-.29, -0.26, 1.424), (-0.285, 0.275, 1.524), (0.235, 0.275, 1.524)$ and $(0.24, -0.28, 1.424)$, where z^i describes the height from the surface of the grid. Figure 3.1 shows the live setup and the position

of the VLC lights and the position of the raised grid. The VLC link used Orthogonal Frequency Division Multiplexing (OFDM) a carrier frequency of 15MHz, 10MHz Bandwidth and 30kHz subcarrier spacing. The IoRL project was originally planned to be compliant to Third Generation Partnership Project (3GPP) release 15 (LTE) standard. Hermitian symmetry was imposed on the OFDM subcarriers, and a DC bias added to the bipolar OFDM time-domain signal to ensure the signal is always positive, and thus compliant with the requirements for OFDM symbol transmission in a VLC medium.

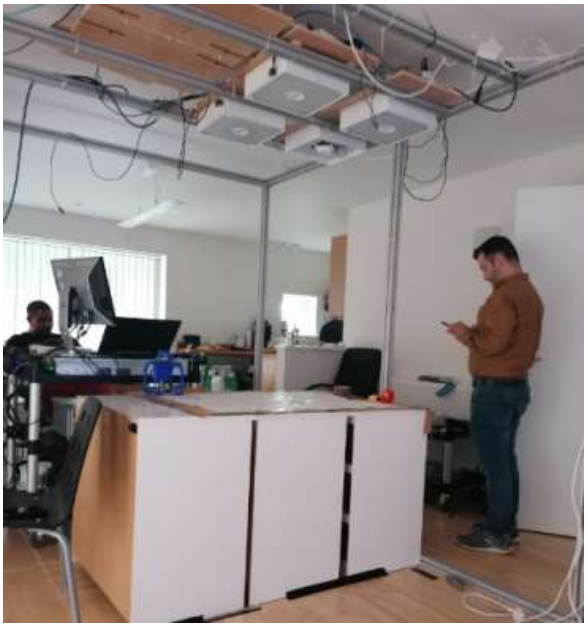

Figure 3.1 - IoRL demonstrator within the Home Scenario of the BRE smart-home demonstration site

3.2.3 Critical Hardware Components and Design Factors

3.2.3.1 Gimbal and Challenges with Original Lens

A large glass convex lens was used to focus the VLC signal onto the receiver Photo Diode (PD). The focal point of the lens required the lens to have a separation distance of 1.5 cm from the PD. The extended focal length of the receiver prevented any VLC signal reaching the PD surface, if the angle of incidence became greater than half a degree[4]. This meant that the receiver module needed to be orientated to point directly at the source of transmission, and that each source had to be tested individually. To reach stable measurements the receiver required re-orientating to face each transmitter without interfering with the position of the PD. To achieve this, a custom made gimbal shown in Figure 3.2, was designed and custom made by the author of this thesis, to house the receiver module.

[4] Alternative smaller and wide-angle lenses were tested but drastically reduced reception of the VLC signal.

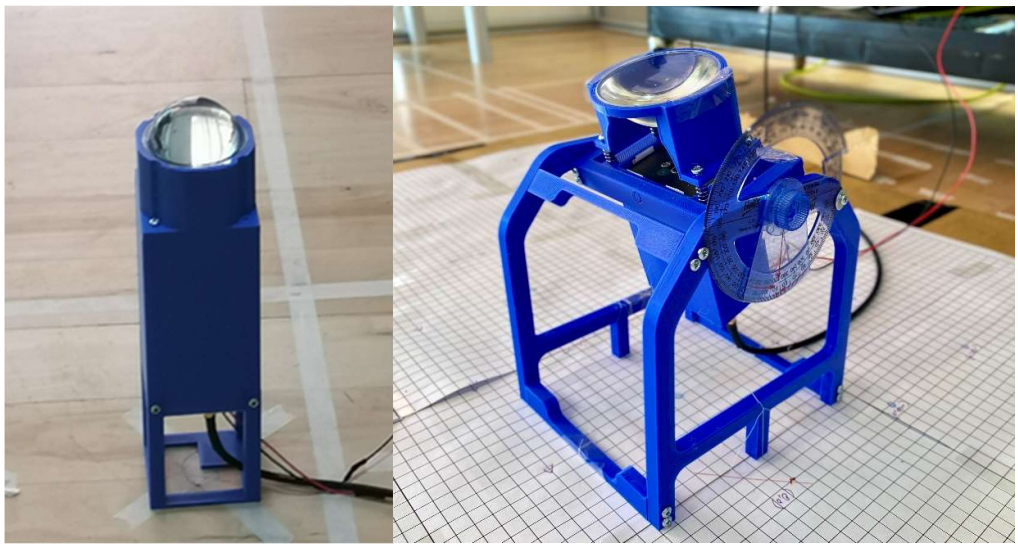

Figure 3.2 – (Left) Upright IoRL VLC receiver casing. (Right) IoRL Receiver Gimbal mounted with VLC receiver and convex lens

The gimbal eliminated the issue of the angle of incidence which is often a variable difficult to obtain in practice. Additionally, the height of the gimbal ($\hat{h}_{PD} = 15.5$ cm) must be accounted for in the following solutions.

3.2.3.2 Remote Radio Light Head (RRLH) Designs

Specific environments typically use different lighting designs. The IoRL project carefully considered both the design aspects of the light source as well as style. The Home scenario uses a standard ceiling light design and pendant rose concept that can be applicable to both strip lights and single pendant lights. Underground tunnels typically consider 'warm' coloured tube lighting systems using IP65 ratings for dust and water control. This impacts the potential for positioning given the large source size, non-translucent casings, and general complexity of the system. An additional attachment was therefore designed for underground tunnel strip lights. The museum scenario-imposed spotlights for directing user attention and minimising the light affecting the artefacts. Original concepts envisaged existing lighting systems being retrofitted with IoRL technology, however, due to the given form factors and requirements of the project regarding antenna positions, cooling, accessibility and manufacturing concerns, original light housings were later manufactured.

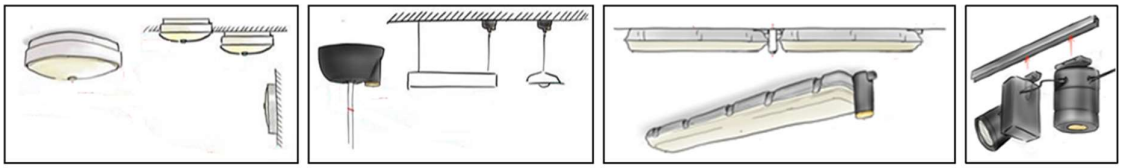

Figure 3.3 - IoRL project RRLH concept designs for different scenarios. (left to right) Ceiling light concept, pendant light, strip light attachment, spotlight

For the actual IoRL measurement campaign, the resulting RRLH was selected to be the ceiling light within the home scenario.

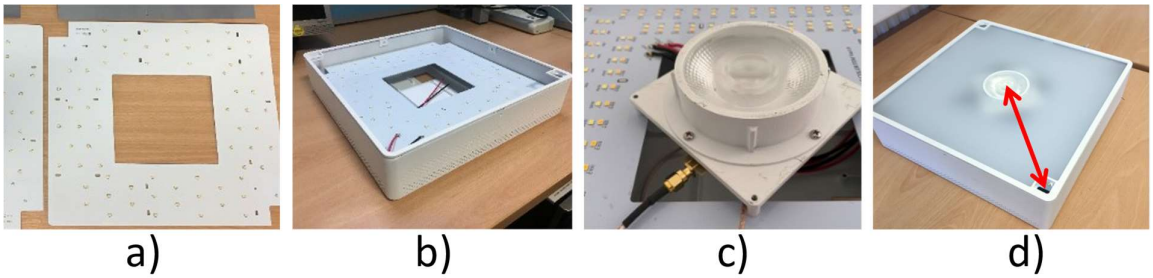

Figure 3.4 - Ceiling Light RRLH design: a) Illumination LED board, b) RRLH casing, c) central VLC COB and d) Illumination diffuser panel and millimetre wave patch antenna corner mounts

Figure 3.4 displays a RRLH ceiling light used in the IoRL Measurement Campaign and various components that contribute towards analysis within this thesis. Figure 3.4a depicts the LED board used for general illumination which is mounted in the RRLH as shown in Figure 3.4b. Due to high capacitance, necessary diffusion, and overall large coverage area, this was not suitable for VLC communication and pinpoint localisation. Throughout the RSSI measurement collection, these illumination LEDs were not powered. Figure 3.4c shows the COB light source and lens which are mounted in the centre of the RRLH. Notably there is a handmade PCB used as an adapter for the coaxial cable input. This may contribute towards disparity in performance among the sources. Lastly, Figure 3.4d illustrates the diffuser panel which does not cover the central VLC source. The mmWave patch antennas are designed to be fitted in the corner holes of the design. The red line in Figure 3.4d indicates the Euclidian distance between the centre of the VLC source and the centre of the mounting for the mmWave patch antennas. This distance is equivalent to 14.71 cm, and is used in later modelling of the system.

3.2.3.2.1 Lens Design

The design of the lighting source includes a circular Chip on Board (COB) and a 70 mm diameter Total Internal Reflection (TIR) lens [249], as shown in Figure 3.5. To reduce the overall form factor an internal Fresnel lens is included in the optics, which evenly spreads near incident light rays as shown in Figure 3.5a. A centralised area of frosted glass, as shown in Figure 3.5d, diffuses the light emitted through the Fresnel lens impacting the light intensity at low radiation angles. There is also a reflector surface around the COB source, which captures wider rays of light, directing these in a collimated and controlled manner according to the principles of TIR resulting in a narrower and more direct e mission pattern.

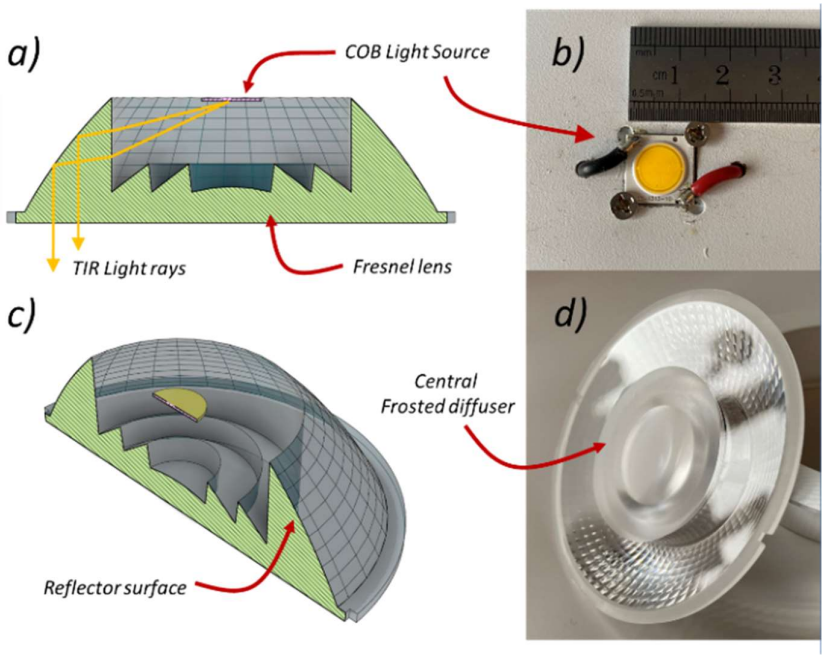

Figure 3.5- TIR lens and COB source. a) Cross-section view; b) COB VLC source; c) Angled cross-section view; d) Flat face of the lens with central frosted diffuser.

The datasheet of the combined light source and lens provides the Luminous Intensity Graph (LIG) given in Figure 3.6for two orientations of the light. The two orientations give different semi-angle half-powers of 22.5° and 21.9° which are averaged to 22.2°

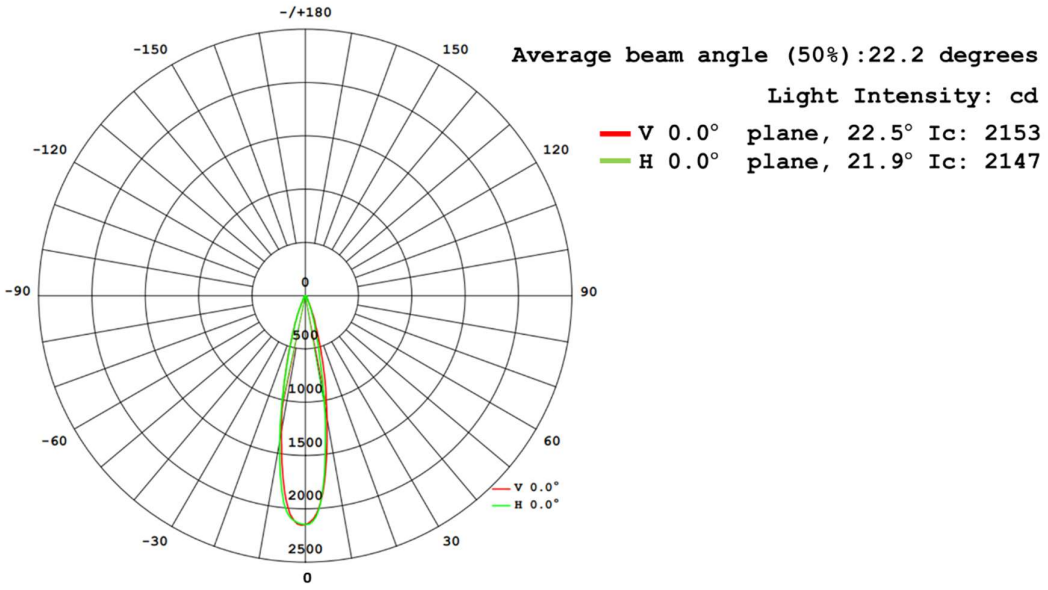

Figure 3.6 - Luminous Intensity Graph (LIG) obtained from Datasheet of TIR lens

3.2.4 Methodology

It should be specified that throughout this study the IoRL project utilises Received Signal Strength Indicator (RSSI) measurements, with arbitrary values, as opposed to Received Signal Strength (RSS) measurements which are the true measure of power.

The centre points of each transmitter's VLC source are mapped using a plumb line, directly downward onto the 2D grid. Each point representing each light's origin. Each marked origin point forms the initial reference RSSI measurement point directly below each light source. RSSI measurements are stored using a custom Python code, at the User Equipment (UE) which is connected to the VLC Rx. The receiver is then positioned across both the x and y-axis at 10 cm intervals, totalling 64 potential positions. A single VLC transmitter is activated at each position, to continually transmit data. At each position the receiver gimbal is orientated visually using both mounted protractors to ensure that the VLC signal is in contact with the PD. The signal is allowed to stabilise, leaving all equipment stationary, before a series of continuous RSSI measurements are taken. Leaving the gimbal in position, the first VLC source is disconnected whilst the next is activated. The receiver gimbal is then re-orientated, and the process repeated until all four lights have given a clear RSS measurement. A collection of (x, y) coordinate specific RSSI data files $\left(DF_{x,y}^{i}\right)$ are thereby obtained for each VLC source $(i = 1,2,3,4)$. At the origin point of each source separate RSSI reference data file (RDF_i) are additionally recorded. Table 3.1 illustrates a sample of a single $DF_{x,y}^{i}$, where each $DF_{x,y}^{i}$ contains 40 measured timepoints. At each time point (t), the RSSI of all 191 Subcarriers (Sub) is given. For clarity,

the notation $t_{i,1-40}^{x,y}$ is used to represent each of the 40 individual measurement timepoints relative to the position coordinates and $i'th$ VLC source.

3.2.4.1 Data Acquired – Type, Number of Datapoints, Subcarrier Frequencies

Table 3.1 - Example of a single DF of recorded RSSI measurements for the global coordinates x, y

$\boldsymbol{DataFile - DF_{x,y}^{i}}$			
	$\boldsymbol{Sub}$		
Timestamp	**1**	⋯	**191**
$\boldsymbol{t_{i,1}^{x,y}}$	RSSI $(t_{i,1}^{x,y}, Sub = 1)$	⋯	RSSI $(t_{i,1}^{x,y}, Sub = 191)$
⋮	⋮	⋯	⋮
$\boldsymbol{t_{i,40}^{x,y}}$	RSSI $(t_{i,40}^{x,y}, Sub = 1)$	⋯	RSSI $(t_{i,40}^{x,y}, Sub = 191)$

Table 3.2 - Summary of measurement campaign parameters

Parameter		**Value**
Effective Area of PD $(\boldsymbol{A_r})/\mathbf{m^2}$		$7.07e^{-4}$
PD height $(\boldsymbol{h_{PD}})/\mathbf{m}$		0.155
Grid Height from floor $(\boldsymbol{\hat{h}_g})/\mathbf{m}$		0.7
VLC Source $\boldsymbol{\psi_{1/2}^{i}}$ /°		22.2
VLC source coordinates $\boldsymbol{S^i = (x, y, z)/m}$	S^1	$(-0.29, -0.26, 2.124)$
	S^2	$(-0.285, 0.275, 2.134)$
	S^3	$(0.235, 0.275, 2.124)$
	S^4	$(0.24, -0.28, 2.124)$
Vertical difference between PD and Lights $(\boldsymbol{\hat{h}_i})/\mathbf{m}$	$\hat{h}_1$ & $\hat{h}_2$	1.2690
	$\hat{h}_3$ & $\hat{h}_4$	1.2790
Grid x-axis $/\mathbf{m}$		$[-0.3: 0.1: 0.4]$
Grid y-axis $/\mathbf{m}$		$[-0.4: 0.1: 0.3]$
Positioning area $(\boldsymbol{Length * Width})/\mathbf{m}$		$0.8 * 0.8$
Number of coordinates measured $(\boldsymbol{N_i})$	1	64
	2	43
	3	63
	4	59

A mapped illustration of the layout and setup used to conduct the VLP experiments, at the BRE facility, is provided in Appendix A of this thesis.

Remark 3 - During the measurement campaign data files were not collected at every point for all lights due to poor signal reception effecting the systems ability to retrieve a signal from specific VLC sources at certain coordinates. This is due to the variable transmission power and coverage between sources.

3.3 Adapted VLC Processing Method

Conventional VLC positioning algorithms make the assumption that the light source follows a Lambertian radiation pattern. Lambert's cosine law states that a light source's intensity is proportional to the cosine of the angle between the path of radiation and the normal. Considering only the Line of Sight (LOS) path and using this cosine law, the RSSI and Euclidian distance (d^i) between the PD and the $i'th$ transmitter can be described by the VLC channel model [199]:

$$P_{R_i} = H(0) * P_{T_i}. \tag{3.1}$$

Where P_{R_i} and P_{T_i} represent the RSSI and Transmitted Power respectively and $H_i(0)$ represents the VLC LOS channel gain between the $i'th$ source and the receiver, given as [199]:

$$H_i(0) = \frac{(m_i + 1)A_r \cos^{m_i}(\psi_i) \cos(\theta_i)}{2\pi(d^i)^2}. \tag{3.2}$$

Where A_r is the previously known effective area of the PD, ψ_i and θ_i denote the angle of emission and incidence respectively and m_i is the order of Lambertian emission given by [199]:

$$m_i = -\frac{\ln(2)}{\ln\left(\cos\left(\psi_{1/2}^i\right)\right)}. \tag{3.3}$$

Where $\psi_{1/2}^i$ is the semi-angle at half power of the source. The relationship between ψ_i and θ_i and the normal of the $i'th$ transmitter and receiver PD are depicted in Figure 3.7. Exploiting the trigonometric relationships between the right-angled triangles of Figure 3.7 one can obtain the following expressions:

$$\cos(\theta_i) = \cos(\psi_i) = \frac{\hat{h}_i}{d^i}, \tag{3.4}$$

$$\therefore \cos^{m_i}(\psi_i) = \left(\frac{\hat{h}_i}{d^i}\right)^{m_i} = \frac{\hat{h}_i^{m_i}}{(d^i)^{m_i}}. \tag{3.5}$$

Substituting (3.4) and (3.5) into (3.2) and then (3.2) into (3.1) and re-arranging for d^i produces the well-established VLP range equation (3.6) [98].

$$d^i = \sqrt[m_i+3]{\left(\frac{(m_i + 1)A_r \hat{h}_i^{(m_i+1)}}{2\pi}\right)\frac{P_{T_i}}{P_{R_i}}}. \tag{3.6}$$

(3.6) eliminates the need for known emission and incidence angles but introduces a known vertical height assumption.

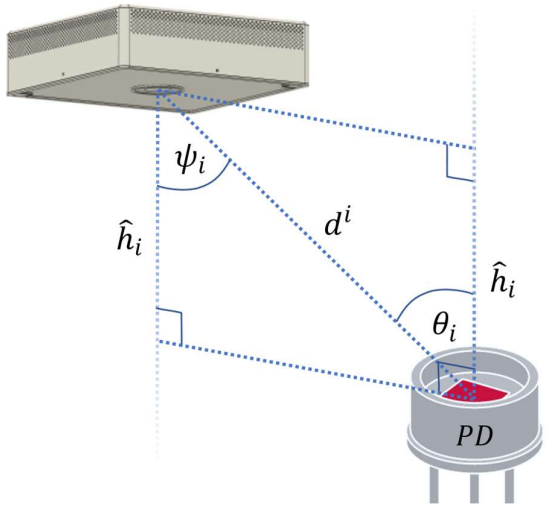

Figure 3.7 - Geometric relationship between $i'th$ transmitter and receiver PD

In practice however, the gimbal used during the experiments effects the calculations described in Section 2.3.4.2.1.1. These must be modified to compensate for an angle of incidence consistently equivalent to zero $(\theta = 0)$. Subsequently, the relationship in (3.4) becomes $\cos(\theta) = 1$ and the following derivation of d^i carried out using (3.1) - (3.6) gives [199]:

$$d^i = \left|S^i - S^0\right| = \sqrt[m_i+2]{\left(\frac{(m_i+1)A_r\hat{h}_i^{(m_i)}}{2\pi}\right)\frac{P_{T_i}}{P_{R_i}}} \tag{3.7}$$

3.3.1.1.1 Multilateration Position Estimation

Given the known vertical height difference $\hat{h}_i$ and the estimated Euclidian distance $\hat{d}^i$ between the lens and the receiver, calculated from (3.6), the Pythagoras theorem can be applied to determine the horizontal distance component r_i (3.8). Reducing the overall problem to a 2D multilateration solution [199]:

$$r_i = \sqrt{(\hat{d}^i)^2 - \hat{h}_i^2}. \tag{3.8}$$

In which,

$$r_i = \sqrt{(x^0 - x^i)^2 + (y^0 - y^i)^2}. \tag{3.9}$$

From (3.9), squaring both sides, expanding and re-arrangement leads to:

$$((x^0)^2 + (y^0)^2) - 2x^i x^0 - 2y^i y^0 = r_i^2 \ - (x^i)^2 - (y^i)^2 \tag{3.10}$$

Repeating (3.6) - (3.10) for each transmitter provides an overdetermined set of equations expressed in matrix form [199]:

$$G\hat{\vartheta} = \hat{b}. \tag{3.11}$$

Where,

$$G = \begin{bmatrix} -2x^1 & -2y^1 & 1 \\ \vdots & \vdots & \vdots \\ -2x^4 & -2y^4 & 1 \end{bmatrix}, \hat{\vartheta} = \begin{bmatrix} x^0 \\ y^0 \\ (x^0)^2 + (y^0)^2 \end{bmatrix}, \quad \hat{b} = \begin{bmatrix} r_1^2 & -(x^1)^2 & -(y^1)^2 \\ \vdots & \vdots & \vdots \\ r_4^2 & -(x^4)^2 & -(y^4)^2 \end{bmatrix}. \tag{3.12}$$

The 2D coordinates of the PD ($S^0 = [x^0, y^0]^T$) can be solved for using the LSS to determine $\hat{\vartheta}$. The LSS solution is given by [98][199]:

$$\hat{\vartheta} = (G^T G)^{-1} G^T \hat{b}. \tag{3.13}$$

3.3.2 Calibration Process using Lambertian Model and Source Data

The performance of any VLP system depends mainly on the $\psi_{1/2}$ of the VLC source as this strongly influences the relationship between the RSSI and estimated Euclidian distance. This finding is both evident within and in the literature [223].

Typically, a $\psi_{1/2}$ value can be retrieved from the datasheet of a light source as described in Section 3.2.3.2.1. In practice however identical lights may exhibit varied performance. This has been shown by calibrating for the $\psi_{1/2}$ in Alam *et al.* [223]. Therefore the $\psi_{1/2}^i$ value needs to be determined empirically for each light i. While some existing literature suggests using the highest power subcarriers (sub) [199], [222], the measurement campaign retrieved RSSI data for all 191 subcarriers therefore a brief evaluation of subcarrier options is given.

This section introduces the calibration phase conducted to determine the optimal calibration parameters for each source denoted by $CP^i = [\ \psi_{1/2}^i\ ,\ sub^i\ ]$. The data files for all points, excluding the reference data files, are halved, resulting in both calibration datafiles $CDF_{x,y}^i$ and measurement datafiles $MDF_{x,y}^i$ each containing 20 sets (rows) of measurements. This is illustrated in Figure 3.8.

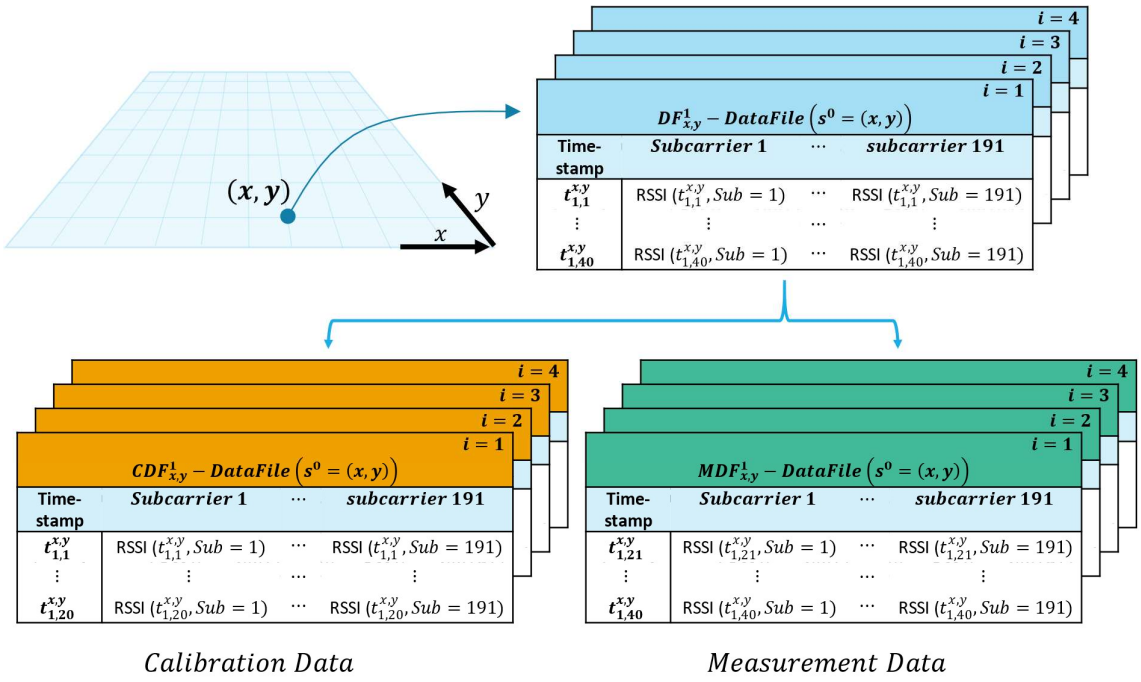

Figure 3.8 - Division of measurement campaign datafiles for calibration and measurement phases

The calibration method described below is effectively equivalent to the two-stage process proposed by Alam *et al*. [223] but where the gain term is known such that only the optimal order of Lambertian must be resolved through comparison of modelled vs known distances. In addition, the optimal subcarrier is also evaluated. The explanation considers the process to determine CP^i using an absolute search approach to assess all possible suitable combinations of subcarriers (sub^i) and $\psi^i_{1/2}$ values. Where $\psi^i_{1/2} = [5: 0.2: 60]$ is given in degrees and $sub^i = [1,192]$ refers to the column in Table 3.1.

3.3.2.1 Determine P_{T_i}

The power of the VLC signal transmitted from the $i'th$ transmitter is determined using the reference datafile $\left(RDF^i\right)$ collected directly below the $i'th$ transmitter. At this location ψ_i and θ_i are zero such that (3.2) simplifies to (3.14):

$$H_i(0) = \frac{(m_i + 1)A_r}{2\pi(d^i)^2}. \tag{3.14}$$

where m_i is calculated using (3.3) and the allotted $\psi^i_{1/2}$ value. At the reference point d^i is known and equivalent to $\hat{h}_i$. One can apply the channel gain of (3.2) to (3.1), where the RSSI is the relative power received at the reference point, $(P^{REF}_{R_i})$ and is taken to be the average RSSI of RDF^i using the assigned sub^i column data. Finally rearranging for P_{T_i} concludes this process.

3.3.2.2 Determining the Optimal Parameter Values

The optimal CP^i are the set of values that reduce the average range error. To determine this, range estimation is performed for all measured coordinates using the acquired value of P_{T_i} from 3.3.2.1 and . The RSSI value employed at each position is acquired from the respective $CDF_{x,y}^i$ where the allocated sub^i column data is used for the calibration phase $CDF_{x,y}^i(:, sub^i)$. For each coordinate the range error of the $i'th$ VLC source ($\varepsilon_{x,y}^{R,i}$) is given by the absolute difference in distance between the estimated range ($\hat{d}_{x,y}^i$) and the true range ($d_{x,y}^i$):

$$\varepsilon_{x,y}^{R,i} = \left\| \hat{d}_{x,y}^i - d_{x,y}^i \right\|. \tag{3.15}$$

The absolute error for all measured coordinates are averaged as in (3.16) to determine the $\psi_{1/2}^i$ and sub^i pair that provide the minimum average range error $\left(\varepsilon_{\psi_{1/2}^i, Su\ ^i}^{R,i} \right)$:

$$\varepsilon_{\psi_{1/2}^i, Sub^i}^{R,i} = \frac{\left(\sum_{j=1}^{N_i} \varepsilon_{x,y}^{R,i} \right)}{N_i}. \tag{3.16}$$

This process is summarised in Algorithm 1 and is repeated for each light.

Algorithm 1: Calibration: Absolute Search for Optimal $\boldsymbol{CP^i}$ Values[5]

1: For: $\psi_{1/2}^{i} = (5 : 0.2 : 60)$

2: For: $sub^{i} = (1 : 191)$

Determine $\boldsymbol{P_{T_i}}$

3: Calculate m_i using $\psi_{1/2}^{i}$ in (3.3)

4: Determine $P_{R_i}^{REF}$ from RDF^{i} using the averaged sub^{i} column data

5: Calculate P_{T_i} from (3.14) and (3.1)

Determine Average Error

6: For: Each (x^0, y^0) in the set of N_i retrieved measurements

7: Obtain the coordinate specific RSSI ($P_{R_i}^{x,y}$) by averaging $CDF_{x,y}^{i}(:, sub^{i})$.

8: By setting $P_{R_i}^{x,y} \rightarrow P_{R_i}$ use to estimate the distance $\hat{d}_{x,y}^{i}$

9: Determine range error $\varepsilon_{x,y}^{R,i}$ from (3.15)

10: End

11: Average all coordinate range errors (3.16)

12: End

13: End

14: Ascertain the CP^{i} that produces the lowest Average error

3.3.2.3 Position Estimation

With a determined set of optimal parameters $CP = [CP^1; CP^2; CP^3; CP^4]$, position estimation is carried out using the multilateration process described in Section 3.3.1.1.1 where the P_{R_i} in is evaluated in two ways:

- ***Averaged RSSI:*** *The RSSI applied is simply the average of the respective* $MDF_{x,y}^{\mathrm{i}}$.
- ***Individual RSSI:*** *Individual RSSI measurements from the* sub_i *column of each respective* $MDF_{x,y}^{\mathrm{i}}$ *are used. Due to the non-synchronous acquisition of the measurements during the measurement campaign, the combination of individual RSSI measurements within the multilateration process is arbitrary. Therefore, individual RSSI measurements from each VLC source are evaluated with every combination of individual RSSI from the other respective measurement sets.*

[5] Ranges of values are represented in the following manner: (initial value : incremental value : end value) and may, in some cases, be assigned equivalent to a variable. Where an incremental value is not given, the increments are defaulted to integers of one. When used as part of a '*For'* loop each value in the given range is applied individually as part of a single loop.

$$P_{R_i}^{x,y}\begin{cases} mean\left(MDF_{x,y}^{\mathrm{i}}(:,sub^i)\right), Averaged \\ MDF_{x,y}^{\mathrm{i}}(1{:}20,sub^i), Individual \end{cases}. \quad (3.17)$$

The PE is given by the Euclidian distance between the estimated position ($\hat{S}^0$) and the true position (S^0):

$$\varepsilon^{PE} = \left|\hat{S}^0 \; - \; S^0\right|. \quad (3.18)$$

The position estimation process is summarised in Algorithm 2 .

Algorithm 2: VLC Multilateration Position Estimation[6]

Initalise CP

1: *For* $i = (1{:}4)$

  Determine $\boldsymbol{P_{T_i}}$

2: Calculate m_i using $\psi_{1/2}^i$ in (3.3)

3: Determine $P_{R_i}^{REF}$ from RDF^i using the average sub^i column data $\left(RDF^i(:,sub^i)\right)$

4: Calculate P_{T_i} from (3.14) and (3.1)

5: *End*

Position Estimate Error (Averaged)

6: *For*: Each (x^0, y^0) in the set of N_i retrieved measurements

7: *For*: $i = (1{:}4)$

8: Attain $P_{R_i}^{x,y}$ from (3.17) by taking the mean of $MDF_{x,y}^i(:,sub^i)$:

9: Use to estimate the distance $\hat{d}_{x,y}^i$

10: *End*

11: Use (3.8)-(3.13) to estimate the targets position coordinates $S^0 = [x^0, y^0]$

12: Determine the PE Error(ε^{PE}) using (3.18)

13: *End*

Position Estimate Error (Individual)

14: *For*: Each (x^0, y^0) in the set of retrieved measurements

15: *For* $P_{R_1} = MDF_{x,y}^1((1{:}20), sub^1)$:

16: *For* $P_{R_2} = MDF_{x,y}^2((1{:}20), sub^2)$:

17: *For* $P_{R_3} = MDF_{x,y}^3((1{:}20), sub^3)$:

18: *For* $P_{R_4} = MDF_{x,y}^4((1{:}20), sub^4)$:

[6] Ranges of values are represented in the following manner: (initial value : incremental value : end value) and may, in some cases, be assigned equivalent to a variable. Where an incremental value is not given, the increments are defaulted to integers of one. When used as part of a '*For'* loop each value in the given range is applied individually as part of a single loop. Where only the ':' is present describes the use of all available values. When used as part of a table/matrix e.g ($RDF^i(:,sub^i)$) this refers to all the column data of the $sub^{i'}th$ column in theRDF^i table.

19: Use to estimate the distances $\hat{d}^1_{x,y}$, $\hat{d}^2_{x,y}$, $\hat{d}^3_{x,y}$ and $\hat{d}^4_{x,y}$

20: Use (3.8)-(3.13) to estimate the position coordinates x^0 and y^0

21: *End*

22: *End*

23: *End*

24: *End*

25: Average the estimated position coordinates

26: Determine the PE Error using (3.18)

27: *End*

Remark 4 - As stated in Remark 3, datasets are inconsistent; therefore, not all coordinates may obtain a range estimate from all four sources, in which case trilateration is performed. No estimate is given where less than three range estimates are provided.

3.4 Initial Results & Discussion

For comparison the following analysis of the calibrated results is compared against applying the $\psi_{1/2}$ of 22.2° taken from the manufacturers datasheet, to all VLC Sources. This value is provided in the datasheet extract given in Figure 3.6, hereafter referred to as the *Control*.

3.4.1 Calibration of CP^i

The optimal CP^i values obtained from Algorithm 1 are presented in Table 3.3. Figure 3.9 illustrates the output of Algorithm 1, where the response is much more sensitive to changes in $\psi_{1/2}$ values, where a clear optimal value can be observed. Alternatively, the selection of subcarriers appears to have a much less drastic effect on the average range error performance. The standard deviation of average range errors for all subcarrier options at the optimal $\psi^i_{1/2}$ value is 1.1 mm, 2 mm, 0.8 mm, and 4.1 mm for Lights 1, 2, 3 and 4, respectively.

Table 3.3 - Optimal CP^i

VLC Source 1		VLC Source 2		VLC Source 3		VLC Source 4	
$\boldsymbol{\psi^1_{1/2}}/°$	sub^1	$\psi^2_{1/2}/°$	sub^2	$\psi^3_{1/2}/°$	sub^3	$\psi^4_{1/2}/°$	sub^4
25.6	142	24.4	165	24	110	25.8	87
Control values							
22.2	135	22.2	100	22.2	53	22.2	61

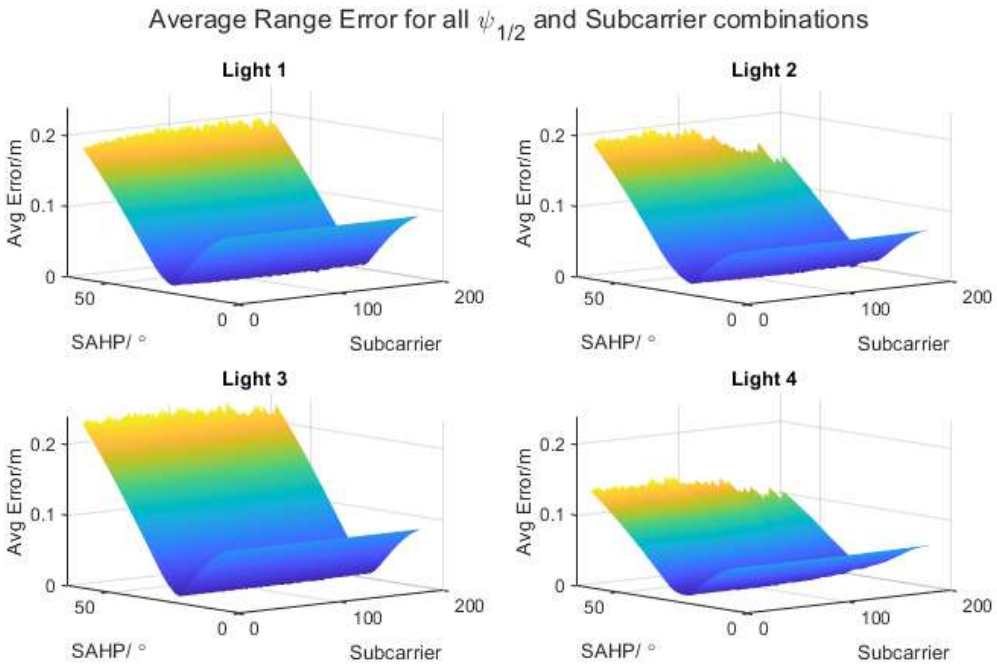

Figure 3.9 - Average range errors across all measured points for all subcarrier and $\psi_{1/2}$.

3.4.2 Range Errors

To evaluate how individual lights compared to one another, a comparison of the individual range errors is given in Table 3.4. The mean values given are reflective of all the coordinates measured during the measurement campaign for each light. From Table 3.4 it is evident that not all lights performed equally. Light 1 and 3 obtain the lowest mean error and standard deviation across all points, followed by Light 4 and Light 2. This pattern correlates with the coverage measured during the measurement campaign in Ali *et al.* [248]. The calibration process has proven to reduce the mean range errors for lights 1, 2, 3 and 4 by 60%, 4%, 22% and 13% respectively.

Table 3.4 - Range Error results for Individual lights

VLC Source 1		VLC Source 2		VLC Source 3		VLC Source 4	
Mean /cm	Std. /cm	Mean /cm	Std. /cm	Mean /cm	Std. /cm	Mean /cm	Std. /cm
Control Results							
2.37	1.75	1.34	1.63	**1.27**	1.25	1.44	1.67
Calibrated Results							
0.99	1.35	1.33	1.82	1.03	1.36	1.28	1.77

3.4.3 Identifying Practical Irregularities in the Lambertian Model

Taking a closer look at the spread of range errors for individual lights, Figure 3.10 presents the non-absolute range errors for all lights across all measured points.

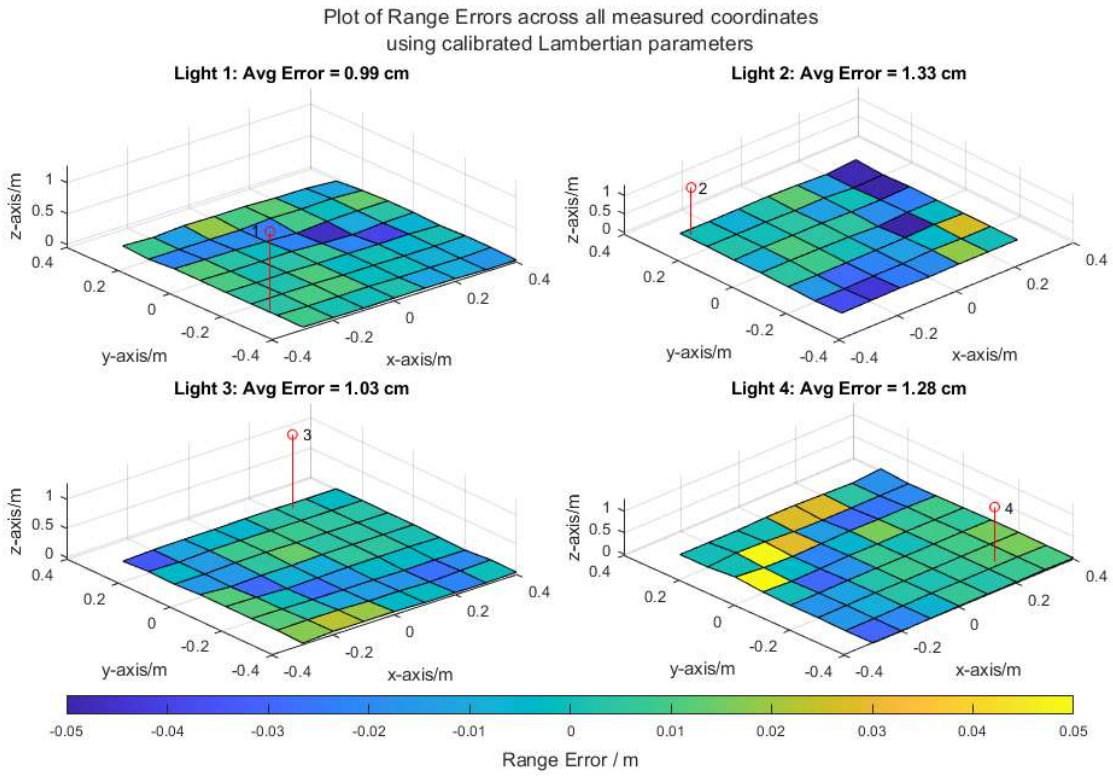

Figure 3.10 - Individual light ranging errors across all points

Noticeably, each light exhibits a common circular region in which the range errors are negative. A negative range error from the non-absolute adaptation of (14) indicates the estimated distance is less than the actual distance. Given the negative correlation between P_{R_i} and $\hat{d}^i$ in , a reduced distance indicates an increased RSSI. This region shows an irregularity in the Lambertian relationship between P_{R_i} and $\hat{d}^i$ given by .

Figure 3.11 depicts the differences between the actual RSSI measurements ($MDF^i_{x,y}$) at given distances and the expected RSSI due to the modelled Lambertian fit using the optimal CP^i values. From Figure 3.11, the area at which the RSSI are higher than the expected RSSI is more evident and can be seen to occur at roughly the same region of Euclidian distances for each light. However, the magnitude of the effect varies among the individual lights, explaining the disparity in Range error percentage improvements. Given that this uniform circular region is consistent throughout all lights and at seemingly constant radii, it is reasonable to conclude that the area exists due to the construct of the RRLH lens. The lens distorts the light, focusing it in a non-Lambertian manner causing a region

of higher-than-expected light intensity and higher RSSI measurements. Observing the Lens characteristics, presented in Section 3.2.3.2.1, the cause of this non-Lambertian emission pattern is likely to be both the central diffuser, which reduces the intensity of incident light rays, and the lens reflector that refocuses light directly downward as opposed to outward as Lambert's cosine function suggests. The region of lens distortion, or higher RSSI, is hereafter referred to as the 'Halo Region' (HR). This draws further attention to the need for calibrating when performing VLP processes as not all light emission patterns are Lambertian. The HR can be seen to cause errors in two significant ways. Firstly, the Lambertian assumption is inappropriate for this distribution and will consistently misrepresent the distance to the RSSI relationship. Secondly, during the calibration phase, as described in Section 3.3.2, the optimal CP^i values will resort to the best fit that reduces the overall error. This not only leads to a poor fit for the ranges within the HR but also for those outside it, as the Lambertian model is forced to accommodate all values.

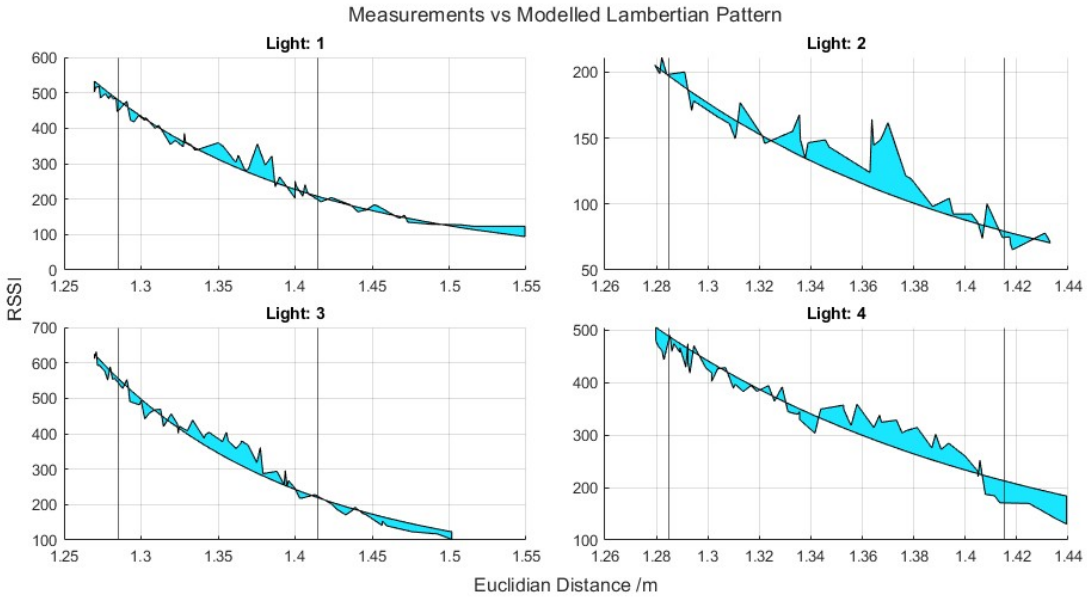

Figure 3.11 - Measured RSSI against distance compared against the fitted Lambertian model. Coloured regions indicate the disparity between the model and measurements. Black lines indicate exaggerated assumptions of the HR considered later.

3.5 Proposed Halo-Lens Compensation Method

To reduce the effects of the HR, the model based on the Lambertian assumption should be corrected to reflect the genuine relationship between RSSI and distance. The following section describes the calibration procedure to mitigate the errors caused by a Lens-Halo. More simply termed the Halo Lens Compensation (HLC) method.

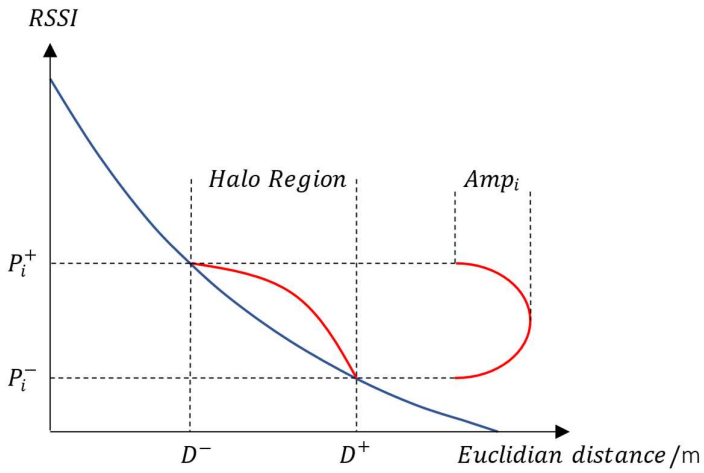

Figure 3.12 - A general overview of the proposed solution where a peak is included across the RSSI range that relates to the HR to compensate for the higher RSSI values.

3.5.1 Overview of the Proposed Halo-Lens Compensation Solution

The proposed halo lens compensation method fits an ideal Lambertian distribution across all points outside the HR before applying a piecewise skewed peak across the HR, with a calibrated amplitude and skew to match the actual distribution. Figure 3.12 illustrates the solution concept to adjust the higher RSSI values within the HR using a fitted peak.

The HR is defined by the minimum and maximum Euclidian distances at which it occurs, represented by D^- and D^+ respectively. P_i^+ and P_i^- denote the VLC source specific region limits of RSSI values that correlate to D^- and D^+ respectively. One can summarise $P_i^r = [P_i^+, P_i^-]$ and $D^r = [D^-, D^+]$:

$$\hat{f}(\phi_i) = \frac{Amp_i}{\xi_i} tan^{-1}\left(\frac{\xi_i * sin(\phi_i)}{1 - \xi_i * cos(\phi_i)}\right). \tag{3.19}$$

The peak to be applied is generated using (3.19) where Amp_i is a calibrated scaling factor relating to the amplitude of the peak and ξ_i denotes the Skew factor as illustrated in Figure 3.13.

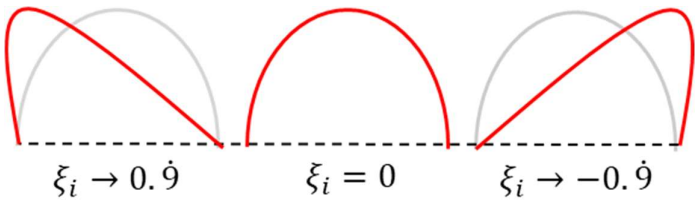

Figure 3.13 - Effects of the Skew Factor (ξ_i) on the skew of the peak.

The RSSI values are mapped to (3.19) using (3.20).

$$\phi_i = \left(\frac{\pi}{P_i^+ - P_i^-}\right) P_{R_i} - P_i^-. \tag{3.20}$$

Finally, the solution is given in (3.21), using a piecewise function to isolate the peak and range according to P^+ and P^-:

$$\hat{d}^i = \begin{cases} \sqrt[m_i+2]{\left(\frac{(m_i+1)A_r\hat{h}_i^{(m_i)}}{2\pi}\right)\frac{P_{T_i}}{P_{R_i}}} & , P^+ \leq P_{R_i} \leq P^- \\ \sqrt[m_i+2]{\left(\frac{(m_i+1)A_r\hat{h}_i^{(m_i)}}{2\pi}\right)\frac{P_{T_i}}{P_{R_i}}} + \hat{f}(\phi), & P^- \leq P_{R_i} \leq P^+ \end{cases}. \tag{3.21}$$

3.5.2 Estimating the Halo Region

The HR can be assumed to be the Euclidian distances at which the RSSI values increase beyond the Lambertian model as a result of lens distortion. This region is not well defined by the available data and varies slightly among the four light sources. The differences are potentially caused by subcarrier frequencies, environmental factors, or practical dissimilarities such as the simplistic COB source mounting method seen in Figure 3.5d. It is of note that under a few given data points, the region is considered subjective, and a quantitative measure for calculating the HR cannot be provided.

The proposed approach to estimate the HR builds on the notion that by ignoring the values within the HR, the Lambertian model can correctly fit all the other data points that are accurately modelled by the Lambertian distribution. Once compared against all measurements, this highlights the HR where measurements are most distorted and no longer adhere to the ideal Lambertian fit.

For this analysis, using Figure 3.11, the author of this thesis applies the assumed initial exaggerated estimates of $\widehat{D}_{init}^r = [\,1.285, 1.415]$ as indicated by black lines in Figure 3.11. These values are selected to capture both ends of the distribution while allowing enough leniency for the HR to potentially widen. The proposed solution applied to estimate the HR is summarised in Algorithm 3.

Algorithm 3: Halo Region Estimation

1. **Fit**: Determine original CP using Algorithm 1 and the given calibration data
2. **Plot**: Plot the Lambertian model of CP values against calibration data *(similar to* Figure 3.11*)*
3. **Assume:** Make an initial assumption of HR bounds (D^r_{init}). *(HR approximated by the distances at which the RSSI are regularly more significant than the expected Lambertian RSSI)*
4. **Buffer region:** Exaggerate the assumed HR bounds to increase the assumed region $\widehat{D}^r_{init}$. *(Making a note to leave measurements outside the exaggerated region. Especially at the higher distances, as this is where the Lambertian fit is most sensitive*).
5. **Re-fit:** Repeat Algorithm 1 to obtain Updated CP (UCP) values but ignore all measurements within the exaggerated HR.
6. **Re-Plot**: Repeat 2. - Plotting the new Lambertian model against the data highlights the region in which the Lambertian model and more accurate bounds of the HR can be identified.
7. **Inspect**: Visually estimate the common HR bounds $D^-$and D^+ among all lights
8. **Power range**: Using the determined D^r values, attain the corresponding P^r_i for each light.

Remark 5 - It is of note that varying amounts of calibration data were evaluated, and while ambiguities were expected, the HR was evident for all.

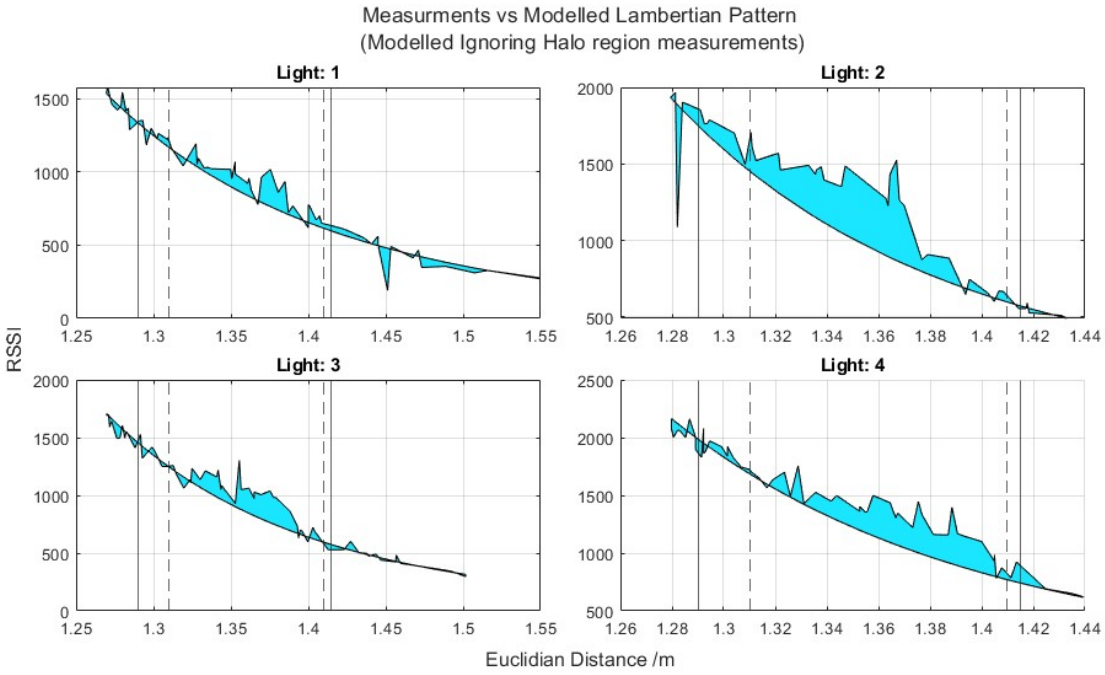

Figure 3.14 - Optimal Lambertian fit which ignores the measurements within the exaggerated HR. Dashed and solid lines represent D^r and $\widehat{D}^r_{init}$ respectively.

Figure 3.14 presents the results of step 6 of Algorithm 3,the Re-Fit, where the UCP^i data generated is used to plot the Lambertian relationship against the subcarrier specific measurements. The HR is

amplified when considered against the similar plots in Figure 3.11 but is now clearer to identify. From Figure 3.14, the final estimate of $D^r = [1.305, 1.412]$ can be obtained and are presented as dashed vertical lines. Finally, D^r can be applied to obtain the corresponding P_i^r of the HR for the respective UCP^i values.

3.5.3 Optimal Amplitude and Skew

The CP^i values retrieved from step 6 of Algorithm 3 are subsequently used to determine the optimal Amp_i and ξ_i values through the absolute search process given in Algorithm 4.

Algorithm 4: Calibration: absolute search optimal UCP^i search[7]

INPUT: P_i^r, $\psi_{1/2}^i$ *and* sub^i, for all lights and D^r

OUTPUT: Amp_i, ξ_i for all lights

Determine $\boldsymbol{P_{T_i}}$

1) Calculate m_i using $\psi_{1/2}^i$ in (2)
2) Determine $P_{R_i}^{REF}$ from (12) & (13) using sub^i
3) Calculate P_{T_i} from (11) and (3)
4) *For*: $Amp_i = (0: 0.01: 0.4)$
5) | *For*: $\xi_i = (-0.99: 0.001: 0.99)$
| | ***Determine Average Error***
6) | | *For*: Each (x^0, y^0) in the set of retrieved measurements
7) | | | Attain $P_{R_i}^{x,y}$ from the sub^i column of $MDF_{x,y}^i$
8) | | | Use (3.21) to estimate the distance $\hat{d}_{x,y}^i$
9) | | | Determine range error $\varepsilon_{x,y}^{R,i}$ from (3.15)
10) | | *End*
11) | | Average all errors with (3.16)
12) | *End*
13) *End*
14) Ascertain the UCP^i that produces the lowest Average error

[7] Ranges of values are represented in the following manner: (initial value : incremental value : end value) and may, in some cases, be assigned equivalent to a variable. Where an incremental value is not given, the increments are defaulted to integers of one. When used as part of a '*For'* loop, each value in the given range is applied individually within a single loop.

This concludes the necessary steps required to estimate the Updated Calibrated Parameters $(UCP^i) = \left[\psi_{1/2}^i, sub^i, P_i^r, Amp_i, \xi_i\right]^T$ for the HLC method. Step 5 of Algorithm 3 obtains the $\psi_{1/2}^i$ and sub^i values given in the first and second rows of Table 3.5. The range of power values P_i^r are determined from step 8 of Algorithm 3 and are given in rows four and five of Table 3.5.The Amp_i and ξ_i results obtained from Algorithm 4 finalise the collection of necessary UCP^i values and can be found in rows six and seven of Table 3.5.

Table 3.5 - Updated Calibration Parameters ($\boldsymbol{UCP}$)

Row		**VLC Source 1**	**VLC Source 2**	**VLC Source 3**	**VLC Source 4**
1	$\boldsymbol{\psi_{1/2}^i}$	25.6	21	23.4	22.6
2	$\boldsymbol{sub^i}$	64	12	31	3
3	$\boldsymbol{P_i^-}$	1206.82	1522.44	1295.33	1757.33
4	$\boldsymbol{P_i^+}$	607.58	587.40	585.50	757.70
5	$\boldsymbol{Amp_i}$	0.0236	0.0304	0.0300	0.0300
6	$\boldsymbol{\xi_i}$	0.3831	-0.9204	0.0149	0.3831

The proposed HLC solution has both an offline calibration phase to determine the necessary source specific parameters UCP^i and online estimation phase for range estimation. The generalised online estimation phase of the HLC solution for a system of N VLC sources is summarised in Algorithm 5 In which the $i'th$ VLC source, denoted by S^i, is described by its three-dimensional Cartesian coordinates as $S^i = \left[x^i, y^i, z^i\right]^T$. Where $i = 0$ denotes the target UE location in Cartesian coordinates given by $S^0 = [x^0, y^0, z^0]^T$. The estimated coordinates are given by $\hat{S}^0 = [\hat{x}^0, \hat{y}^0, \hat{z}^0]^T$ where z^0 is assumed to be known and therefore equivalent to $\hat{z}^0$. During the $k'th$ sampling period a set of N individual RSSI measurements P_{R_i}, each pertaining to the respective $i'th$ source, are obtained. The source specific calibration parameters, Sensor coordinates and RSSI measurements are grouped as $UCP = \left[UCP^i, \cdots, UCP^N\right]$, $S = [S^1, \cdots, S^N]$ and $\bar{P}_R = \left[P_{R_1}, \cdots, P_{R_N}\right]^T$ respectively.

Algorithm 5: VLC RSSI state estimation using the HLC method[8]

INPUT: $\bar{P}_R, S, UCP, z^0$

OUTPUT: $\hat{S}^0$

Range Estimation

1: *For* $i = (1:N)$

2: | *If* $P_i^- \leq P_{R_i} \leq P_i^+$

3: | | Calculate Euclidian distance $\hat{d}^i$ using UCP^i parameters in (3.21) for $P_i^- \leq P_{R_i} \leq P_i^+$

4: | *Else*

5: | | Calculate Euclidian distance $\hat{d}^i$ using UCP^i parameters in (3.21) for $P_i^+ \leq P_{R_i} \leq P_i^-$

6: | *End*

7: | Using the height difference $\hat{h}_i$, calculate the horizontal range component r_i using (3.8)

8: *End*

Multilateration Position Estimation

9: Collate the set of 2D range measurements $r = [r_i, \cdots, r_N]^T$

10: Using S and r, execute 2D LSS multilateration (3.13) with the matrices given in (3.12)

11: Extract the $\hat{x}^0$ and $\hat{y}^0$ components from the LSS result to form the position estimate $\hat{S}^0 = [\hat{x}^0, \hat{y}^0, \hat{z}^0]^T$

3.6 Halo-Lens Compensation Results & Discussion

Applying the UCP^i values from Table 3.5, range estimation and multilateration can be performed by simply replacing with (3.21). Figure 3.15 illustrates the proposed modified Lambertian relationship compared to the measured calibration data. For reference, the original Lambertian model is also compared to the measured calibration data. Notably, the arch in the proposed fit accommodates the HR better than the original fit. Comparing Table 3.3 and Table 3.5 reveals that $\psi_{1/2}^i$ values decrease, as expected from ignoring measurements in the HR. The subcarrier values generally tend to decrease too. This may be due to the higher powers of the lower subcarrier frequencies, which are more affected by the physical environment. Thus, creating more significant variability in measurements which applies better to a narrower beam angle indicated by the higher order of Lambertian fit. This can be observed in Figure 3.15, where the proposed model fit appears to deviate more from the measurements. This is simply due to the lower variation in power between higher subcarrier frequencies.

[8] Ranges of values are represented in the following manner: (initial value : incremental value : end value) and may, in some cases, be assigned equivalent to a variable. Where an incremental value is not given, the increments are defaulted to integers of one. When used as part of a '*For'* loop, each value in the given range is applied individually within a single loop.

3.6.1 Range Estimation Error

Range estimation is carried out for each light using the $MDF_{x,y}^{i}$ and the average for all coordinates is given in Table 3.6 and compared to the previous Lambertian model results, provided in Table 3.4. Overall, the proposed solution leads to a consistent reduction in error across all lights with mean range errors of 5.9 mm, 6 mm, 6.9 mm and 5.4 mm. Thus producing average percentage reductions of 40.2 %, 54.5 %, 33.1 % and 57.9 % for lights 1, 2, 3 and 4 respectively, when compared to the previously calibrated results. Due to these reductions, light 1 is no longer the highest performing light system. Notably, in Figure 3.16, the HR effect is significantly reduced, and errors become more uniform across all points. The choice of subcarrier options appears to have a more significant effect on the results. As the standard deviation of average range errors for all subcarrier options, at the optimal $\psi_{1/2}^{i}$ value, is 2 mm, 4.4 mm, 2.6 mm and 4.9 mm for lights 1, 2, 3 and 4 respectively. While this is an increase from those reported in Section 3.4.1, the effects of subcarrier option appear minimal.

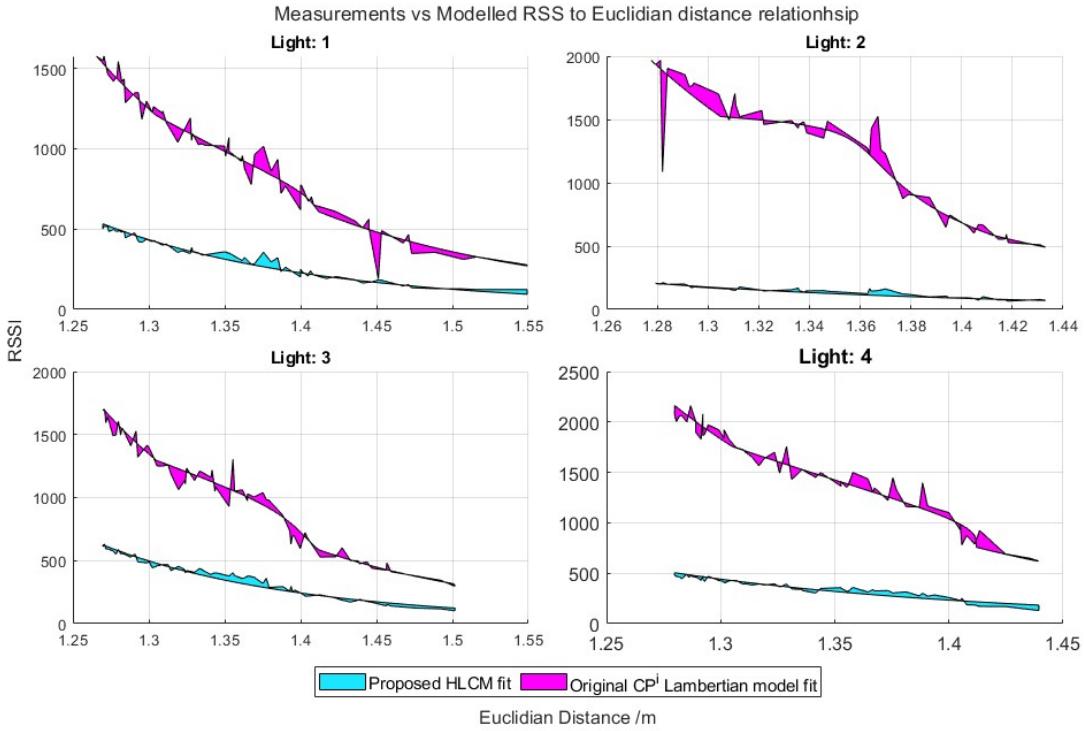

Figure 3.15 - Original CP^{i} Lambertian relationship fit vs proposed (HLC) model fit

Table 3.6 – Individual Light Range Error Results

VLC source 1		VLC source 2		VLC source 3		VLC source 4	
Mean /cm	Std. /cm	Mean /cm	Std. /cm	Mean /cm	Std. /cm	Mean /cm	Std. /cm
Lambertian Model - using CP^i							
0.99	1.35	1.33	1.82	1.03	1.36	1.28	1.77
Proposed Model – HLC							
0.59	0.84	0.60	0.81	0.69	0.77	**0.54**	0.73
Percentage Decrease in Range Error (%)							
40.15	38.19	54.51	55.61	33.10	43.22	**57.95**	58.77

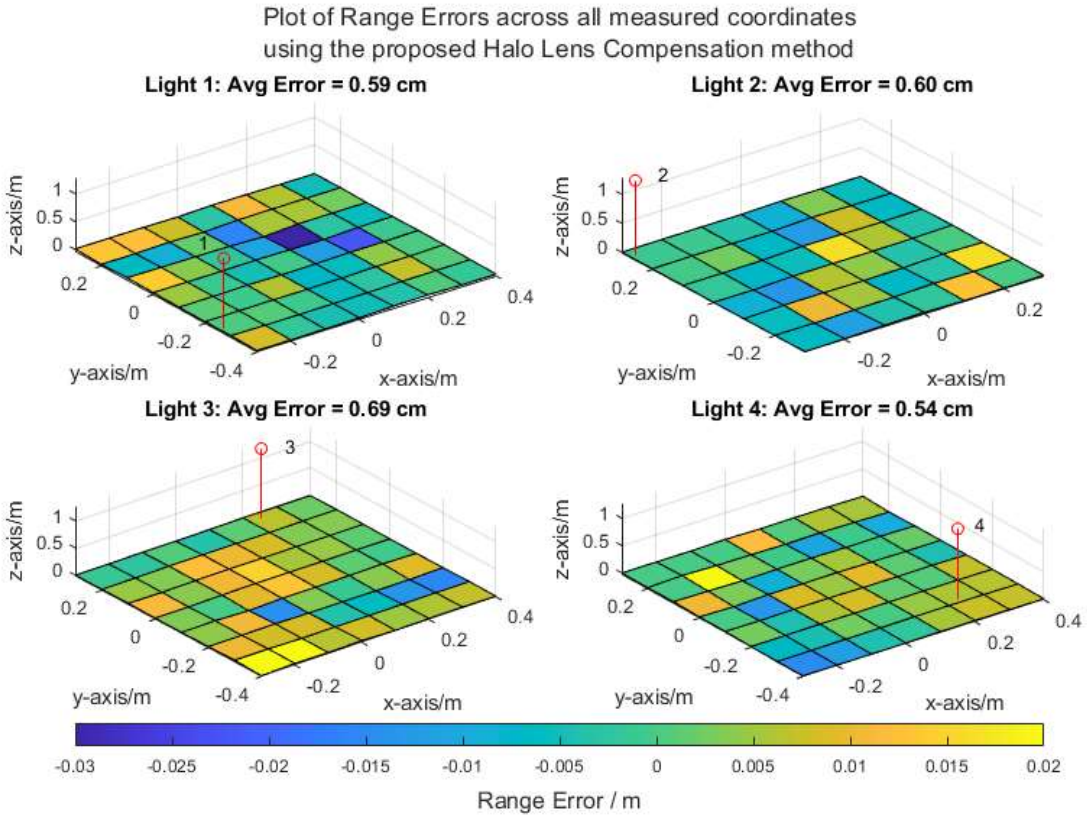

Figure 3.16 - Range errors for individual lights using the proposed Halo Lens Compensation (HLC) method. VLC Light sources are indicated by red vertical lines. Colour bar scale given in centimetres.

3.6.2 Position Estimation Error

The comparative positioning error results in Table 3.7 indicate substantial improvements in PE from applying the Proposed Halo lens model. Compared with the previously calibrated Lambertian model, average errors for averaged and individually used measurement sets achieve a near 50% and 40%

reduction in error. Individual measurement sets naturally show a higher error due to the higher noise expected in individual results; however, average results are still less than 4 cm. These results are a vast improvement on the direct application of Datasheet values reaching mean error improvements of near 60% and 40% for averaged and individual datasets respectively. Figure 3.17 illustrates the comparison of position estimates from both Lambertian and the proposed HLC method.

Table 3.7 – Multilateration PE Results

Averaged Measurements				**Individual Measurements**			
Mean /cm	Min /cm	Max /cm	Std. /cm	Mean /cm	Min /cm	Max /cm	Std. /cm
Lambertian Model – using Datasheet $\psi_{1/2}$ *(Control)*							
7.37	1.10	14.13	3.24	7.37	1.67	12.77	3.15
Lambertian Model – using CP^i							
6.10	0.59	25.77	4.05	7.55	1.10	29.12	5.27
Proposed Model – HLC							
3.06	0.30	8.34	1.78	4.64	0.64	17.79	3.52
HLC vs *Control* - Percentage Decrease in Range Error (%)							
58.53	72.32	40.95	44.95	37.02	61.74	-39.30	-11.77
HLC vs CP^i - Percentage Decrease in Range Error (%)							
49.88	48.73	67.63	55.99	38.51	41.92	38.91	33.23

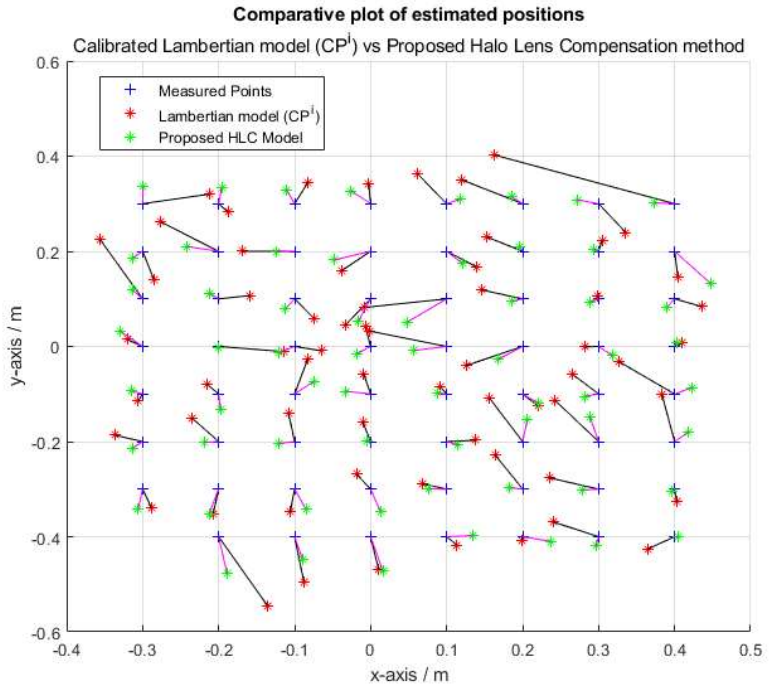

Figure 3.17 - Plot of the 63 measured coordinates and position estimates for both Lambertian and proposed solutions

3.7 Chapter Conclusions

VLC solutions are a immensely viable and exciting potential solution for 5G networks owing to their minimal required adaptations to existing infrastructure as well as illumination, energy and cost benefits. To encourage widespread deployment, VLC sources should be expected in all manner of existing lighting systems and as such the necessary measures need to be taken to ensure that despite the lens or source structure, the potential for highly accurate localisation performance is not hindered.

This study has highlighted the importance of source characteristics, primarily lens form factors, on VLP performance. This emphasises that while Lambertian models may serve well for simulations, it is crucial to calibrate experimental VLP systems accordingly. The proposed HLC solution is shown, using real-world data, to significantly improve the position estimation performance. Further developments should consider the effects of varied quantities of datasets both with regards to the number of measured positions and quantity of RSSI measurements acquired at each point as this may impact the resolution of the calibration and subsequently the effectiveness of the HLC method.

While performance of the IoRL IPS system is shown to be impressive with centimetre level accuracies one must acknowledge the ideal LOS case in which this data is acquired using a gimbal to eliminate the angle of incidence. The following chapter considers applying this solution to what is known of the IoRL Indoor Positioning System (IPS) to appropriately evaluate the expected IoRL IPS performance.

4 Evaluation of the Internet of Radio Light Indoor Positioning Service

4.1 Introduction

Building on the work covered in chapter 3, where Visible Light Communications (VLC), within the Internet of Radio Light (IoRL) project was studied for non-Lambertian VLC emitters, this chapter considers the implementation of the proposed Halo-Lens Compensation (HLC) within the IoRL projects' Indoor Positioning Service (IPS). In this model tracking is achieved through fusion of mmWave and VLC data from a dynamic target.

As promising technologies alone, the combined application of millimetre waves (mmWaves) and VLC for modern networks is recently explored for high speed and secure LOS communications [250]–[253]. However, regarding their combined use within localisation systems, the available research focuses on the application of VLC localisation methods to facilitate mmWave communications [254] [255] or handover protocols [256]. Nor *et al.* [254] propose the use of VLC RSSI localisation to reduce the complexity of exhaustive mmWave beamforming training processes and Hsu *et al.* [255] successfully evaluate this concept practically. Alternatively, Sheikholeslami *et al.* [256] apply VLC localisation to improve communication handover.

Here the author, of this thesis, recognises that to the best of their knowledge, the only research evaluating the hybrid fusion of mmWave and VLC localisation schemes comes from the IoRL project, published by the author of this thesis [257]. This previous work describes an oversimplified study of the potential of the IoRL positioning system and focusses on Virtual Reality (VR) applications. This chapter presents a novel analysis of a hybrid mmWave and VLC localisation scheme applying real world data obtained through the IoRL measurement campaign.

4.1.1 Aims

The aims of this study are to better understand the potential of the IoRL IPS system, to evaluate its suitability for location-based applications presented by both the 3GPP and the IoRL project consortium, and to identify the key challenges for localisation to be evaluated in later chapters.

4.1.2 Contributions

This chapter presents a more complete evaluation of the novel VLC and mmWave hybrid fusion of the IoRL project IPS which includes the proposed novel HLC algorithm for dynamic target tracking.

4.1.3 Summary

The chapter first reviews existing work, written by the author of this thesis, on this subject to highlight the various simplifications made. Following this, an outline of the IoRL IPS is provided to detail the considered implementation for the IoRL demonstration case. Considerations and modelling of parameters are then presented and various tests conducted. These parameters all culminate in a final simulation study.

4.2 Previous IoRL IPS Studies

Within previous work, the author of this thesis proposed the concept of the IoRL architecture for use within Virtual Reality (VR) tracking [258]. The concept provided a means for virtual reality users on different platforms (mobile, PC or Standalone) to benefit from a 5G localisation scheme in which cables, tracking boundaries or limitations of the users' freedom would be evaded. However, for such a system to exist, the tracking performance would have to meet or to exceed the requirements of existing VR tracking technologies. As presented in Section 2.1.4.2.2.1 the accuracies and latencies of such systems are within the order of millimetres and milliseconds respectively. Such high specifications are not only required to provide the user with a more immersive experience but must be enforced to ensure that the user does not suffer simulation sickness. Simulation sickness is akin to motion sickness brought on by a perceivable misalignment between the users' actions and the respective change in media to reflect the users' actions. This is attributed to poor accuracy and perceivable latencies between the target's motion and the respective media shown, described as the Motion to Photon Latency (MTPL). While tolerances to simulation sickness are subjective, the general understanding is that a system's accuracy and latency must be within millimetres and milliseconds.

To evaluate the feasibility of the IoRL project to reach such performance standards, previous work [257] focused on establishing a model a model of the IoRL IPS. The study specifically looked at the system latency and accuracy expected of the IoRL IPS through simplistic modelling of the millimetre wave, VLC and Location Server (LS) components. The results highlighted the unfeasibility of a system meeting such tracking requirements for VR applications.

This original study considers the IoRL tracking environment in which only a single user is connected and requires localisation data. As such, a rudimentary LS is established in which only data pertaining to a single user are retrieved from the Location database. Under this single target assumption, the measurements are directly applied to the update stage of a Linear Kalman filter. This structure ignores the potential for any other target data within the Location database. Using this configuration, latency tests are conducted and used to assess the overall MTPL and update frequency.

Nevertheless, these latency components are reflective of an oversimplified LS process and carry an optimistic view of the actual performance.

Additionally, the measurement noise values applied to model both the mmWave and VLC measurements are related loosely to existing literature. VLC noise was applied as AWGN, using the distribution attained from an experiment conducted by IoRL project partners [199]. However, this experiment considered a 2D scenario and therefore lacked details about the third axis (z). The noise in height measurements were taken to be an average of the noise in x and y. This is not suitable as VLC 2D trilateration is not directly applicable to 3D space, where computing the height requires more complex solutions that may affect not only z but also x and y error distributions. The mmWave measurements were extracted from the 'optimistic' region of existing literature [68] in which the bandwidths of the systems considered far exceeded those to be implemented within the IoRL system.

Moreover, the target trajectories assessed within this original study are observations of a single user and therefore, one cannot ignore the subjective nature due to the bias of age, gender, ability of the participant and the tracking assessment.

To build on this previous work and better evaluate the IoRL performance, a secondary study is considered within this thesis. In which the previously oversimplified approaches are re-considered to better replicate the response of the IoRL system.

At the time of writing this thesis, a fully realised IoRL IPS is not available, therefore simulating the response is still necessary. The approach taken within this chapter is to utilise the Halo-Lens Compensation method and IoRL Measurement campaign results to better model real-world performance. As these VLC data reflect the measurement campaign conditions (RRLH positions, tracking distances, 2D implementation), the simulation within this chapter replicates the same setting and conditions. With a lack of mmWave TDOA data, this technology is evaluated for various degrees of noise within the time delay measurements, where errors within time-delay are related to the bandwidth of the system.

The overall approach conducted throughout this chapter is like the methodology of the original study. The latency components are evaluated and later applied to the model where data fusion is carried out to locate a moving target. However, the Location Database is reconstructed to better characterize the experimental parameters needed and the LS is designed to better reflect the performance of a system capable of assisting multiple users. This avoids the latency bias that occurs from ignoring the matter completely. Furthermore, as opposed to the non-repeatable and subjective VR trace used in the previous study, the trajectory is kept here in a repeatable and consistent circular pattern.

In this respect the following chapter evaluates the proposed IoRL IPS with regards to both accuracy and latency. It can be seen from previous discussions that the latency not only indicates the rate of estimations and delay but also conveys the complexity and energy consumption of an IPS. This in turn relates to the maintenance costs and processing demand placed on the IoRL architecture.

4.3 Implementation of the IoRL IPS

The author, of this thesis, acknowledges that as a research venture, the IoRL project demonstration is not yet finalised at the time of writing. To evaluate the IoRL system performance without a fully realised system entails modelling the features not yet available, namely the mmWave Uplink transmission which permits the ability to perform uplink TDOA measurements. Constructing a more realistic model can however be achieved by evaluating the system performance of the features that are practically available.

This section considers the design and implementation of the IoRL IPS providing context to the processes described later and verifying the system latency. The VLC location results are also briefly evaluated.

In this implementation of the IoRL IPS, the system is limited to that of the IoRL demonstration use case to be established in a Home, in keeping with the IoRL Measurement Campaign setup. This allows the obtained VLC data to be appropriately applied.

In this manner, this chapter can be considered a study into what the response of the IoRL IPS could have been during the measurement campaign, if the mmWave uplink and LS were operational. This scenario consists of four RRLHs connected to a singular RRLHC with the intent to track a single UE device. In a similar but more comprehensive approach, to that of previous work, the following describes the IoRL IPS features, latency, and measurement evaluations, and finally the results of the model.

As discussed in the literature review, the key performance metrics considered throughout this thesis are accuracy, reliability, and latency. The latency is not only a descriptor of the response time and estimation frequency but it also directly correlates with the system's complexity, cost and energy efficiency.

4.3.1 IoRL IPS Communications

The design of the IoRL IPS follows the description given within Section 2.3.3.3. For more intuitive reading, the Location Database Tables (LD1, LD2 & LD3), given by Table 2.2-Table 2.4, are further referred to as:

- LD1 – Measurement Table
- LD2 – Anchor Table
- LD3 – Estimates Table

The LS is tasked with processing the raw mmWave TDOA and VLC RSSI data stored within The Measurement Table of the IoRL LD, using sensor position data stored in the Anchor Table of the IoRL LD. These estimates are returned to the LD and stored in the Estimates Table, to be accessed by Location Based Services. In a general sense the LS performs state estimation on both measurement datasets and then data fusion, using a Kalman Filter (KF) for tracking.

Within the LS, the data fusion utilises a Linear Kalman Filter (LKF) since the location estimates provided through the TDOA and VLC processes are linear with regards to the state of the target being tracked.

The KF process follows two stages, Prediction and Update, the recursive nature of the KF is beneficial in this application since minimal prior data is required. The KF can be run recursively within the LS as more observations are given for a singular UE device. This approach however, applies to a system considering only a singular UE device. To facilitate multiple UE devices, the implementation of multitarget tracking filters such as Probability Hypothesis Density (PHD) filters [115], [116] may be appropriately considered. Nevertheless, due to the consideration of a singular UE device within the IoRL demonstration a singular KF is more simply employed. This approach, however, can be expanded for multiple UE devices in which multiple singular Prediction and Update stages can be executed for each device in a round robin arrangement. An increasing number of devices will drastically affect the performance of such an architecture.

Previous implementation of the LS [257] considered an IoRL demonstration use case in which only a singular UE was to be tracked. While this is no exception within this thesis, the LS latency components presented in Meunier *et al.* [257] represent a system in which the state and state covariance matrices are stored directly within the LS, for repeated use within the KFs recursive stages. Within this study, the LS is designed to be capable of performing location estimation for multiple devices in the round robin format. This is done to appropriately reflect the fact that both a PHD filter

and a KF, carrying out this round robin pattern, would not be able to store all the previous data within the LS.

These processes both require an initial state estimate and the corresponding probability density, given as the initial state estimate covariance matrix. Because of this requirement the LD must be adapted to appropriately store both the target state and its covariance matrix. The LS is then capable of extracting both the measurement data for the target and the corresponding previous state information from the Estimates Table in the LD. This additional dataset and process, required to obtain the previous data, can be expected to invoke additional latency within the system. For the reasons discussed above, the implementation of the LS and LD are described and the resulting latencies are evaluated.

4.3.1.1 The Location Server

The implementation of the LS realised in this thesis is constructed in MATLAB R2021a which uses an Open Database Connectivity (ODBC) driver to link with the MySQL Location Database. The process of the LS is considered in Section 2.3.3.3 but elaborated further within this section. This section describes the position estimation stages using data fusion of initial state estimates. The following explanation considers a general system of N Remote Radio Light Head (RRLH) transceivers monitoring a single UE device. It is assumed that all N RRLHs obtain both mmWave TDOA and VLC RSSI LOS measurements throughout the tracking period. The $i'th$ Remote Radio Light Head (RRLH) is described by the position of the mmWave receiver antenna $Rx_{mm}^{i} = \left[x_{mm}^{i}, y_{mm}^{i}, z_{mm}^{i}\right]^{T}$ and VLC source $Tx_{vlc}^{i} = \left[x_{vlc}^{i}, y_{vlc}^{i}, z_{vlc}^{i}\right]^{T}$ given by $RRLH^{i} = \left[Rx_{mm}^{i}, Tx_{vlc}^{i}\right]$ in which x, y and z describe the coordinates of the VLC source and mmWave receiver in world space, as denoted by the subscripts vlc and mm respectively. The set of N RRLH parameters are collected as $RRLHs = [RRLH^{1}, \cdots, RRLH^{N}]$. The singular UE target position is described by its Cartesian coordinates in world space given by $S^{0} = [x^{0}, y^{0}, z^{0}]^{T}$. During the $k'th$ sampling instant, given by $(t_k, t_{k-1}]$, a set of VLC RSSI ($\bar{P}_{R,t_k}$) and mmWave TDOA ($\bar{\tau}_{t_k}$) measurements are obtained. In which $\bar{P}_{R,t_k}$ is a set of N individual P_{R_i,t_k} measurements relating to each RRLH and $\bar{\tau}_{t_k}$ describes a set of $N-1$ measurements in which $RRLH^{1}$ has been arbitrarily selected as the reference node. Therefore $\hat{\tau}_{t_k}^{i,1}$ denotes the TOA difference obtained between the $RRLH^{i}$ and $RRLH^{1}$ at the $k'th$ sampling instant (t_k):

$$\bar{P}_{R,t_k} = \left[P_{R_1,t_k}, \cdots, P_{R_N,t_k}\right], \tag{4.1}$$

$$\bar{\tau}_{t_k} = \left[\hat{\tau}_{t_k}^{2,1}, \cdots, \hat{\tau}_{t_k}^{N,1}\right]. \quad (4.2)$$

4.3.1.1.1 State Estimation

Once measurement data has been acquired, the initial stage requires processing of the raw VLC RSSI and TDOA mmWave measurements to produce initial estimates of the UE position $\hat{S}_{vlc}^{0}$ and $\hat{S}_{mm}^{0}$ for VLC and mmWave datasets respectively. The following section describes the individual state estimation processes adopted within the LS of the IoRL IPS.

4.3.1.1.1.1 VLC RSSI State Estimation

State estimation using the VLC RSSI measurement dataset employs the Halo Lens Compensation (HLC) method, proposed in the previous chapter of this thesis, designed for use within the IoRL system to mitigate the effects of the non-Lambertian emitters. In this respect the solution is limited to target tracking within a 2D plane where the height or z^0 coordinate of the receiver is fixed and known. The proposed HLC solution entails an offline calibration phase to obtain the light specific HCL Updated Calibration Parameters $\left(UCP^i\right) = \left[\psi_{1/2}^i, sub^i, P_i^r, Amp_i, \xi_i\right]^T$ for $i = (1, \cdots, N)$ in which the Halo Region (HR) power range is given by $P_i^r = [P_i^+, P_i^-]$. $\psi_{1/2}^i, sub^i, Amp_i, \xi_i$ denotes the optimal Semi-angle at half power, Subcarrier column, Halo Lens Compensation Amplitude and Skew respectively. These parameters are grouped as $UCP = [UCP^1, \cdots, UCP^N]$.

During an offline phase a training dataset, of 20 RSSI measurements at every 10 cm^2 position, must be obtained for each light. As discussed in the conclusion of the previous chapter, this quantity and spatial resolution may further affect the performance. However, for consistency, the same parameters applied in Chapter 3 are considered. Using the obtained RSSI training data set, the Halo region is estimated using Algorithm 3 and the calibration is completed using Algorithm 4.

The complete details of the HLC process are defined in the previous chapter where Algorithm 5 summarises the online estimation process for the $k'th$ estimation instant in which $\bar{P}_{R,t_k} \rightarrow \bar{P}_R$ and $Tx_{vlc}^i \rightarrow S^i$.

4.3.1.1.1.2 MmWave TDOA State Estimation

As discussed within the literature review (Section 0) the applied TDOA estimation process within this thesis is the Taylor Series (TS) solution. This solution relies on an initial estimate in which iterative calculations converge on a local estimate, however a single iteration is sufficient and considered within this thesis. Due to the requirement of an initial estimate, the VLC estimate is directly applied. Though this means the errors of both estimates are correlated, for simplicity they are assumed independent

to satisfy the LKF process. As discussed in the following Data fusion section there is only a single instance where the VLC and mmWave noises are evaluated together, hence this assumption is considered valid.

The TS solution is presented in the literature review and is summarised for a homogenous set of sensors, thereby applying the LSS and not WLS, below in Algorithm 6.

Algorithm 6: Taylor Series TDOA solution[9]

INPUT: $\bar{\tau}_{t_k}$, ***RRLH***, $\widehat{\boldsymbol{S}}^{\boldsymbol{0}}_{\boldsymbol{vlc}}$

OUTPUT: $\widehat{\boldsymbol{S}}^{\boldsymbol{0}}_{\boldsymbol{mm}}$

1: Using the initial estimate $\hat{S}^0_{vlc}$ and Rx^1_{mm} estimate the Euclidian distance $\hat{d}^1$ from (2.11)

2: *For* $i = (2:N)$

3: Using the initial estimate $\hat{S}^0_{vlc}$ and Rx^i_{mm} estimate the Euclidian distance $\hat{d}^i$ from (2.11)

4: Calculate the Jacobians $a_{i,1}, a_{i,2}$ and $a_{i,3}$ from (2.21)

5: *End*

6: Populate *G* and *D* matrices according to (2.23)

7: Carry out LSS using (2.24) to determine the coordinate errors $\delta\hat{S}^0$ in the initial estimate

8: Update the initial estimate to determine the mmWave TDOA solution. $\hat{S}^0_{mm} = \hat{S}^0_{vlc} + \delta\hat{S}^0$

Remark 6 – Both the Chan and TS solutions were applied during initial testing however findings resulted in much greater ambiguities for the Chan solution under vastly lower noise parameters. For this reason, the TS solution is taken forward.

4.3.1.1.2 Data Fusion

Data fusion, as shown in the literature review, provides an efficient means to improve the response of a system through the combination of individual datasets. Within the IoRL IPS, the state estimates $\hat{S}^0_{vlc}$ and $\hat{S}^0_{mm}$ derived in the above section, along with their respective covariances, are subsequently fused together using a LKF to form an optimal output. The state of the filter is given by $X = [x^0, y^0, v^x, v^y]^T$where x^0 and y^0 denote the Cartesian coordinates of the target in reference to the RRLHs and v^x and v^y represent the targets velocity components in each respective axis. The state estimates $\hat{S}^0_{vlc}$ and $\hat{S}^0_{mm}$ obtained from the mmWave and VLC datasets, during the $k'th$ sampling period, are submitted to the LKF as $z^{vlc}_{t_k}$ and $z^{mmw}_{t_k}$ respectively:

[9] Ranges of values are represented in the following manner: (initial value : incremental value : end value) and may, in some cases, be assigned equivalent to a variable. Where an incremental value is not given, the increments are defaulted to integers of one. When used as part of a '*For'* loop, each value in the given range is applied individually within a single loop.

$$\hat{S}_{mm}^{0} \rightarrow z_{t_k}^{mmw}, \quad \hat{S}_{vlc}^{0} \rightarrow z_{t_k}^{vlc}. \tag{4.3}$$

The LKF equations from Section 2.1.3.2.1.1 are repeated here for readability.

Prediction stage		**Update stage**	
$\hat{X}_{t_k}^{-} = A\hat{X}_{t_{k-1}} + Bu_{t_k}$ $P_{t_k}^{-} = AP_{t_{k-1}}A^T + Q$	(2.38) (2.39)	$K_{t_k} = P_{t_k}^{-}H^T\left(HP_{t_k}^{-}H^T + R\right)^{-1}$ $\hat{X}_{t_k} = \hat{X}_{t_k}^{-} + K_{t_k}(z_{t_k} - H\hat{X}_{t_k}^{-})$ $P_{t_k} = \left(I - K_{t_k}H\right)P_{t_k}^{-}$	(2.40) (2.41) (2.42)

There are no control inputs, therefore B and u_{t_k} are ignored. The applied process model is given as a Constant Velocity (CV) model with the following state transition matrix [133]:

$$A = \begin{bmatrix} 1 & 0 & \Delta T & 0 \\ 0 & 1 & 0 & \Delta T \\ 0 & 0 & 1 & 0 \\ 0 & 0 & 0 & 1 \end{bmatrix} \tag{4.4}$$

As stated above, the LS requires prior data to form a prediction of the target's state using the state transition matrix. The obtained state estimates are then fused together with the predicted state to obtain an optimal output. The prior state information of a UE ($\hat{X}_{t_{k-1}}$ and $P_{t_{k-1}}$) is acquired by scanning the Estimates Table to find previously generated position estimates. Due to potential fluctuations in computational time and consideration for potential multiple targets, the time between consecutive estimations, given by ΔT, may not be consistent. Therefore ΔT is calculated dynamically by comparing the timestamp of the current measurement dataset, denoted as t_k and the timestamp of the previously generated estimate given by t_{k-1}:

$$\Delta T = t_k - t_{k-1}. \tag{4.5}$$

For instances where there is no available prior state information ($\hat{X}_{t_{k-1}}$ or $P_{t_{k-1}}$) such as when a new device is connected or on the initial iteration of the LS, the prediction stage is ignored, and state estimates are directly fused together. An initial estimate is instead produced using the Update stage

alone. In this case the TDOA state estimate and covariance are applied as $\hat{X}_{t_k}^{-}$ and $P_{t_k}^{-}$ respectively. The VLC state estimate and its covariance matrix are given as z_{t_k} and R respectively.

To simplify the further processes throughout this chapter, the Anchor Table is only queried on initialisation as the evaluated scenario assumes a single RRLHC system limited to a set of four receivers required for localisation. In this case the Anchor data is not expected to change. The summary of the LS Algorithm applied within this thesis is given below in Algorithm **7**.

Algorithm 7: IoRL Location Server Algorithm[10]

Initialisation

Establish connection with LD

Query 1: SQL READ LD Table 2 - Retrieve RRLH coordinates and VLC parameters

Initialise fixed parameter values

Estimation Loop

While (Devices connected)

    Query 2: SQL READ LD Table 1 - Obtain measurement data and number of currently connected UE devices (N_{UE})

    For $i = (1{:}\, N_{UE})$

        Extract measurement data $\left(\bar{\tau}_{t_k}, \bar{P}_{R,t_k}\right)$ for the $j'th$ UE from Query 2 data

        Query 3: SQL SELECT LD Table 3 for prior estimation of the $j'th$ UE $\left(\hat{X}^{j}_{t_{k-1}}, P^{j}_{t_{k-1}}\right)$

        If Query 3 returns prior data

            Compute ΔT from timestamps of measurement and priory estimation data

            If $\Delta T \neq 0$

                Establish matrices A & Q within the Kalman filter with ΔT

                Determine initial state estimate and covariance matrix (2.38) & (2.39)

                Compute VLC position estimate $\hat{S}^{0}_{vlc}$ through Algorithm 5

                Fuse VLC estimate ($\hat{S}^{0}_{vlc} \rightarrow z^{vlc}_{t_k}$) with update step equations (2.40) - (2.42)

                Compute TDOA state estimate $\hat{S}^{0}_{mm}$ with Algorithm 6 and initial estimate $\hat{S}^{0}_{vlc}$

                Fuse TDOA estimate ($\hat{S}^{0}_{mm} \rightarrow z^{mmw}_{t_k}$) with Update step equations (2.40) - (2.42)

                Query 4: SQL UPDATE LD Table 3 with state estimate and covariance matrix

            End

        Else

            Compute VLC state estimate $\hat{S}^{0}_{vlc}$ through Algorithm 5

            Compute TDOA state estimate $\hat{S}^{0}_{mm}$ with Algorithm 6 and initial estimate $\hat{S}^{0}_{vlc}$

            Fuse TDOA and VLC estimate with Update step equations (2.40) - (2.42)

            Output state estimate and covariance matrix to LD3

        End

    End

End

[10] Ranges of values are represented in the following manner: (initial value : incremental value : end value) and may, in some cases, be assigned equivalent to a variable. Where an incremental value is not given, the increments are defaulted to integers of one. When used as part of a '*For'* loop, each value in the given range is applied individually within a single loop.

4.3.1.2 Design of Implemented Location Database

The Location Database is established as a MySQL database within the IHIPG containing the three tables described in Section 2.3.3.3. However due to the VLC process and proposed VLC Lens computation, VLC light specific parameters ($\psi_{1/2}^{i}$, P_{T_i}, P_i^-, P_i^+, Amp_i, ξ_i) for $i = (1, \dots, N)$ are calibrated as described in Algorithm 3 and Algorithm 4 to be stored within the LD. This requires modifications to the table to store the additional RRLH specific parameters as shown in Table 4.1.

Table 4.1 - LD2: Antenna and LED coordinates

RRLHC ID	**RRLH ID**	**mmWave Tx**			**VLC LED**			**VLC Estimation Parameters**					
		x_{mm}^{i}	y_{mm}^{i}	z_{mm}^{i}	x_{vlc}^{i}	y_{vlc}^{i}	z_{vlc}^{i}	$\psi_{1/2}^{i}$	P_{T_i}	P_i^-	P_i^+	Amp_i	ξ_i
1	1												

The implemented LS considers a single propagation approach in which prior data is retrieved, processed, fused with the generated state estimates, and then transmitted directly back to the LD before searching for new measurement data. Therefore, the estimated target states are to be stored in the LD Estimates Table with their respective covariance matrices. To accommodate the size of the covariance matrix, the values are stored within a single database column as a String array. Additionally, due to the state matrix of the applied KF, the estimated target velocity components are stored to be applied as priory data within the KF process. The addition of this necessary data requires the Estimates Table to be updated, as presented in Table 4.2.

Table 4.2 - LD3: UE location estimates

UE ID	**UE coordinates**			**UE Velocity**			**Covariance matrix**	**Estimate Timestamp**
	x^0	y^0	z^0	v^x	v^y	v^z	P	
1								DD/MM/YYYY hh:mm:ss:..

As identified within the literature review (Section 2.3.3.3), the IoRL project's Indoor Positioning Protocol (IPP) applies the 5G New Radio frame structure to both the mmWave and VLC channels. With regards to the transmission of location data, the sequencing is always within the last symbol of the last slot of the first N sub-frames. In this sense the VLC and mmWave measurements are acquired

synchronously. Therefore, it should be noted that the timestamp given to measurement datasets, stored within the Measurement Table, refers to the timepoint the measurements, which are assumed to be synchronous, are acquired. This same timestamp is maintained throughout the state estimation process and is applied to the uploaded target state within the Estimates Table. In this way the timestamp of the estimate correlates to the point in time at which the respective measurements were acquired. This is achieved using a common clock within the IoRL IHIPG where both the LS and LD are situated.

4.4 Obtaining Simulation Parameters from Available Datasets

4.4.1 Determining System Latencies

The aim here is to acquire the latency components of the IoRL IPS to better understand the system and subsequently to identify the effects that these have on performance. These latencies can then be applied to the overall system model to improve the consistency between simulated and expected performance.

Observing the IoRL IPP discussed within the literature review, the measurements between the VLC and mmWave are shown to be synchronous to one another according to the same transmission sequence. However, each technology is asynchronous due to the sequential sampling structure of each technology's respective measurements. This is caused by the transmission of individual location reference signals within separate sub-frames of the 5G transmission block. This results in millisecond delays between consecutive measurements for both the mmWave and VLC technologies. Within this chapter the sequential sampling is assumed to have a negligible effect and therefore the measurements are assumed to be sampled synchronously. The effects of these asynchronous assumptions are evaluated further in later chapters.

Additionally, within this study, to avoid the latency assumption made in Meunier *et al.* [257] regarding the transmission period between the Radio Access Network (RAN) and the UE, and the subsequent rendering time on the UE side, the considerations of latency are limited to those within the RAN.

Following the protocol of the IoRL IPS described in Section 2.3.3.3.2, both the Estimation Period Latency Component (EPLC) and the Round-Trip Time (RTT) are evaluated within this study:

1) The EPLC describes the time taken for the LS to retrieve new data, generate an estimate and return it to the LD. The frequency at which new data can be resolved can be used to model the period of estimation within the KF ΔT. Given that the LS is only capable of processing a

single dataset at any given time, the EPLC dictates the number of acquired measurements that may be ignored during the estimation period.

2) The RTT is the duration of time it takes for a single dataset to be acquired, processed and the resulting position estimate to be received. To avoid the assumptions made within previous work regarding transmission and rendering times at the UE, the RTT is considered from RRLHC transmission to RRLHC reception.

The latency components described above and the considered system for the following study is illustrated below:

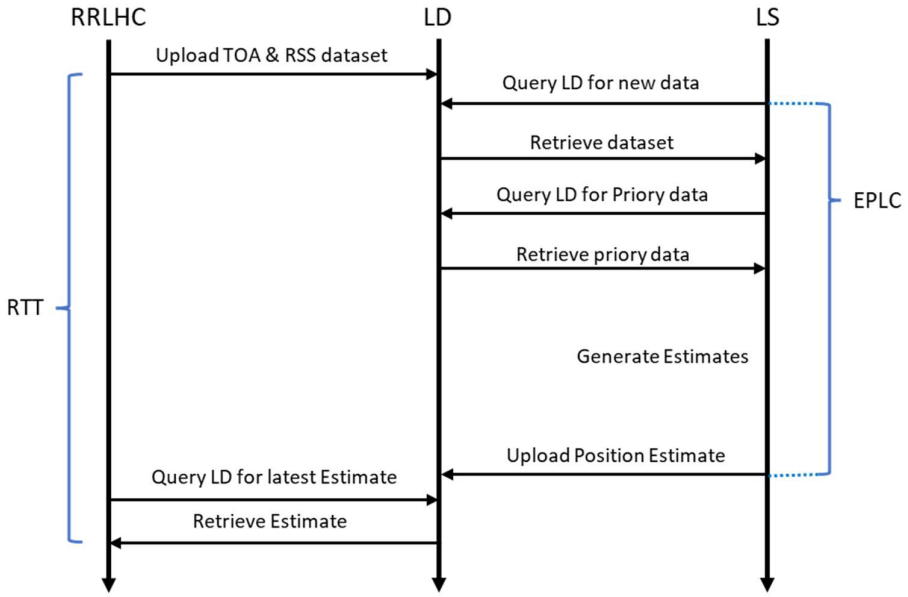

Figure 4.1 - Evaluated processes, data transmissions and latencies within the simulated model for a single estimation

4.4.1.1 Methodology

All tests are conducted on a DELL Intel(R) Core(TM) i7-10700 CPU @ 2.90GHz using MATLAB R2021a. The inbuilt tic/toc stopwatch function within MATLAB is utilised for measuring the duration of the respective processes. As advised within the MATLAB documentation [259] the tic/toc function is not recommended for durations less than 0.1s. For this reason, the programmes are looped N_L times, allowing for the average execution time of a single loop $\widehat{\Delta T_L}$ to be calculated:

$$\widehat{\Delta T_L} = \Delta T_{N_L} / N_L. \tag{4.6}$$

Where ΔT_{N_L} is the recorded runtime over N_L iterations. To assess the various computation times, namely the RTT, without interrupting the LS, a RRLHC is modelled on an additional instance of MATLAB. The RRLHC is tasked with uploading mock datasets to, and retrieving relevant estimates from

the LD. It should be noted that the measurement datasets applied are not considered important in this specific study and are exactly the same for each upload, except for the timestamp. The timestamps are simplified to an integer count starting from 1 due to the lack of sub-second time data available and its irrelevance in this study to have correct timestamp data. Prior to testing, the Anchor Table is pre-configured with calibration data from Table 3.3.

4.4.1.2 EPLC Testing

The '*While (Devices Connected)* 'statement within Algorithm **7** imposes a loop where, if $N_{UE} > 0$, there is considered to be device data within the Location Database. For latency testing this While loop is reconfigured to count N_L completed estimations using a simple counter variable, which is incremented by one after each uploaded estimate. The RRLHC is initially run on a separate instance of MATLAB and continually uploads measurement datasets with increasing timestamps. The LS is then executed to perform $N_L = 500$ estimations. To specifically measure the runtime of the LS processing the stopwatch *'tic'* is triggered just prior to the main loop *(line 4 of* Algorithm **7***).* The stopwatch *'toc'* is triggered again once all 500 estimations are carried out and the average runtime is calculated. This process is repeated 50 times .

Additionally, to gain further insight into the key contributors of latency within the IoRL IPS, several further tests are conducted. These tests consider the computational impact of three Queries (2, 3 and 4) carried out within each LS estimation period. While these queries are necessary to retrieve new data at each loop, the LS is set to repeatedly process the same data by manually setting ΔT equal to 1, in line 10 of Algorithm **7**. The latencies reported for each scenario are given in Table 4.3.

Table 4.3 - IoRL latency test results

Evaluated system	EPLC with RRLHC /ms	Removed Query Contribution /ms	EPLC without RRLHC /ms	Removed Query Contribution /ms
LS as presented in **Algorithm 7**	14.98	n/a	8.74	n/a
LS without Query 2	6.25	8.73	5.80	2.94
LS without Query 2 & 3	4.34	1.91	3.98	1.82
LS without Query 2, 3 & 4	1.43	2.91	1.33	2.65

4.4.1.3 PELC Analysis

From Table 4.3 it is evident that the LD queries clearly have a pronounced effect on the computation time of the LS, where the actual estimation process, without any LD Queries, takes as little as 1.43ms

to compute. The latency contribution of each removed Query is also extracted to highlight the disparity between Query 2, 3 and 4. Query 2, entails requesting all the available LD data and therefore presents a significantly higher latency increase. In addition to reducing the numbers of queries, the effects of the RRLHC updates are also considered for each system. The RRLHC is either enabled, or not, to upload measurements to the LD in parallel to the LS while trying to retrieve or upload data. Evidently where the RRLHC is not enabled there is a prominent reduction in EPLC values. Where no Queries are performed, the slight disparity between the computation times can reasonably be attributed to the host computer running parallel instances of MATLAB. The RRLHC effects are generally moderate for Queries 3 and 4 however the RRLHC presents a drastically greater amount of latency, when running simultaneously while Query 2 is performed. Query 2 involves attempting to obtain Measurement Table data while the RRLHC is continually providing parallel updates to the same Measurement Table. Whereas Queries 3 and 4 relate to the LD Estimates Table which is not simultaneously updated by the RRLHC.

4.4.1.4 RTT Testing

To evaluate the RTT, the RRLHC is reconfigured to upload a measurement dataset before continually querying the LD for the respective estimation. The RRLHC achieves this by comparing the timestamps of the uploaded data with timestamps from the relative UE in the Estimates Table. Once the result with a matching timestamp is obtained the next measurement is transmitted. In this manner the process illustrated in Figure 4.1 is looped $N_L = 500$ times. The average RTT over 50 tests is given as 24.01 ms. While the RTT involves more LD queries, the substantial increase in computation time can be related to the parallel table access finding from the EPLC results. Due to the RRLHC now continually querying the LD Estimates table during the LS process, Queries 3 and 4 can be expected to suffer greater latencies.

These results indicate potential optimisation of the LS, LD and RRLHC structure to reduce increased computation times from increased queries. This may be even more pronounced for networks considering multiple UE devices continually requesting data from the LD. Regardless, this is beyond the scope of this this study which concentrates on a single UE demonstration case.

The obtained EPLC and RTT can be applied to the simulated model, where measurement sets are processed every 14.98 ms and estimates are compared to the state of the target 24.01 ms from when they were obtained.

Due to the structure of the location data transmission sequence, new datasets are acquired at the end of the $N'th$ sub-frame and updated every 10 ms according to the duration of the 5G New Radio

(NR) frame. As discussed previously, the individual measurements are assumed to be sampled synchronously. The duration of the EPLC is greater than the 10 ms update frequency, therefore to avoid complicated synchronisation measures, every other measurement is ignored. This invokes a slight delay of approximately 5 ms before the next dataset is acquired at the database. In practice this additional buffer period allows for the likely delay in VLC RSS measurements that must be transmitted from the UE side to the LD. Therefore, due to the EPLC being greater than the NR frame, the delay buffer is included and a new dataset is processed every to 20 ms, or two NR frames. The sequence of location data processing, equivalent for both the VLC and mmWave channels, is illustrated in Figure 4.2. Each 10ms NR frame contains 10 subframes of 1ms duration. The location data for both mmWave and VLC signals are transmitted in the last symbol of the last slot in the first N subframes of each NR frame. The transmission of this data is indicated by black arrows. During this chapter the sampling is considered synchronous therefore location data is transmitted and received at the $N'th$ subframe as indicated by the green arrow. The duration of the LS process, given by the EPLC, is shown with a blue arrow and the ignored dataset is in red.

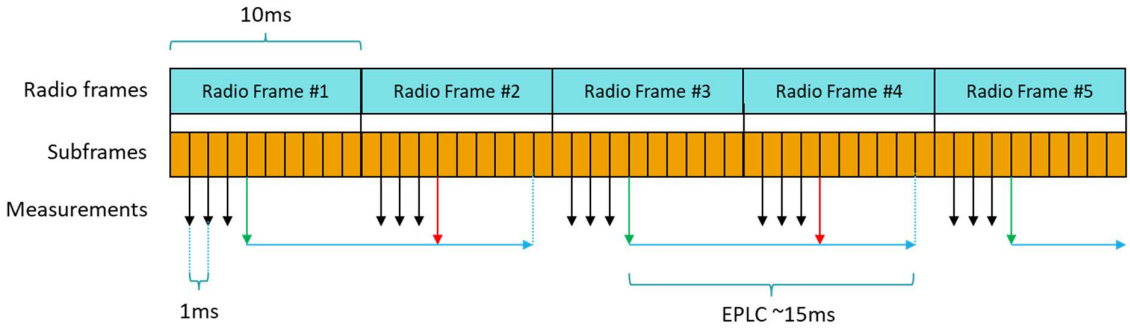

Figure 4.2 – Sampling and processing sequence of the IoRL IPS for four RRLHs.

4.4.2 Determining System Accuracies

4.4.2.1 VLC Modelling

To model the performance of the IoRL system, the VLC RSSI data obtained from the measurement campaign and corrected in chapter 3 is analysed. These measurements are reflective of discrete points within a 2D plane at a fixed distance from the RRLHs, therefore to model the IoRL VLC RSSI response for all points within the 2D plane, the error distribution is evaluated and applied within the model as AWGN with covariance matrix R^{vlc} given by:

$$R^{vlc} = \begin{bmatrix} \sigma^2_{x,vlc} & 0 \\ 0 & \sigma^2_{y,vlc} \end{bmatrix}. \tag{4.7}$$

To attain the proper distribution the measurement Dataset described in Section 3.2.4.1 is used. The 'averaged' datasets described provide the response obtained by averaging over all 20 measurements and the individual datasets consider all possible combinations of measurements which are cross correlated. For this distribution the RSSI measurements are processed according to the HLC method, presented in Chapter 3, and applied within the multilateration scheme in a consecutive format, such that the first measurement for each RRLH is compared to the first measurement of the others and so on. In this respect, 20 Position estimates are computed for all evaluated points. The errors in both x and y axes are recorded for all estimations to obtain the means and standard deviations for both the x and y axes. The error distribution given in Figure 4.3a follows a normal distribution very closely, where the calculated means of the errors for x and y axes are -5.4 mm and -8.6 mm respectively. The standard deviations of this distribution are, $\sigma_{x,vlc} = 11.06$ cm and $\sigma_{y,vlc} = 12.12$ cm. The applied distributions are shown in Figure 4.3a with red and yellow for the x and y axes respectively. These distributions visibly indicate a poor fit due to outlying datapoints. To remove the outlying data from the normal distributions, the Grubbs' test [260] was applied using the inbuilt MATLAB function. This proceeded to remove 59 outliers within the dataset which equates to 4.91 % of the overall sample. Post Grub fit distributions, as shown in Figure 4.3b, are visibly more appropriate with mean errors in the x and y axis of -7.2 mm and -3.2 mm respectively and standard deviations of $\sigma_{x,vlc} = 4.77$ cm and $\sigma_{y,vlc} = 4.5$ cm.

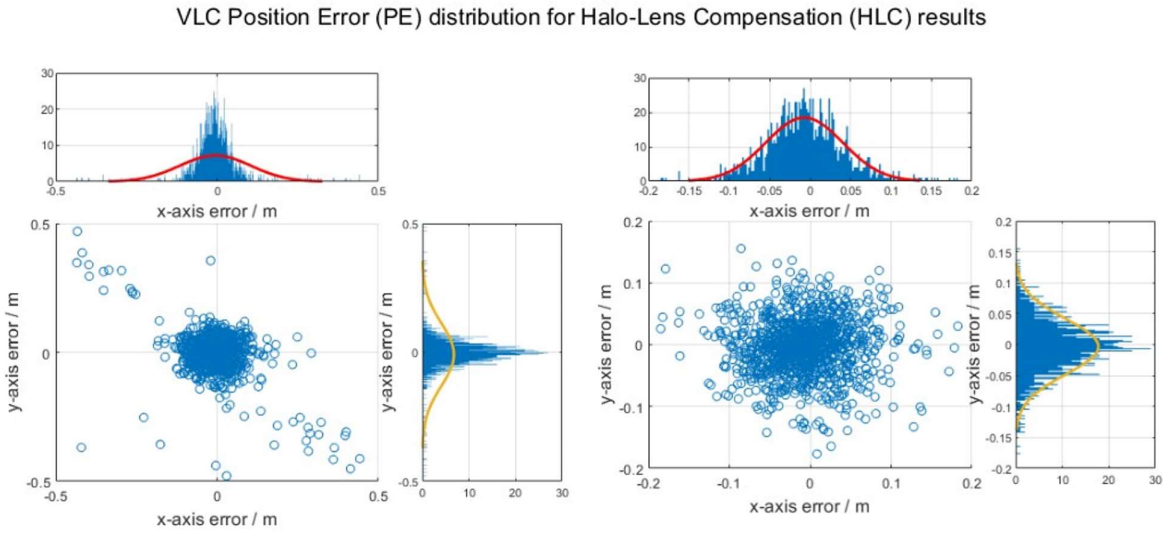

a) Original VLC Error distribution

b) VLC Error distribution (outliers removed)

Figure 4.3 - VLC HLC position estimate error distribution a) prior to outlier removal b) post outlier removal

4.4.2.2 MmWave Modelling

Given the IoRL system's research status, mmWave results are unavailable at the time of writing this thesis. Therefore, the need to completely simulate the response from the mmWave solution is necessary. From the literature discussed in Section 2.3.4.1.2 there are two main methods for modelling TDOA or TOA signal propagation: Raytracing or applying a Gaussian distribution to the true range or position of the target.

Raytracing methods provide a means to suitably model the received signal parameters according to the geometry of the environment. This enables a more realistic signal characteristic in accordance with shadowing, reflections, scattering, attenuations, and multipath components. Despite these qualities, raytracing is computationally extremely demanding and various studies in the existing literature have adopted less complicated means of AWGN modelling for LOS channels. Moreover, the simulation study considered within this thesis is reflective of the IoRL measurement campaign setup, effectively imitating a real time solution with both mmWave and VLC measurements working simultaneously. Under this consideration, the simulated environment is centred within a large living room environment where the nearest wall is more than 2 m from the tracked area. Using what is known of multipath attenuation from mmWave technology, the path separation from reflecting surfaces and assuming LOS transmission, the tracking area can be expected to experience very few effects from multipath components [216] [214][217].

In this respect, AWGN modelling is a reasonable and less complex approach for the given LOS scenario and has been implemented within this study to model the mmWave TOA signal transmission. Furthermore, the AWGN component is applied to the individual time delays measured at each sensor $\tau_{t_k}^i \; for \; i = (1, \cdots, N)$:

$$\hat{\tau}_{t_k}^i = \tau_{t_k}^i + v_{t_k}^i. \tag{4.8}$$

Where $v_{t_k}^i$ is the zero mean AWGN component given by,

$$v_{t_k}^i \sim N(0, \sigma_\tau). \tag{4.9}$$

Drawing on existing literature, zero mean Gaussian distributions have been applied for mmWave TOA, for both optimistic and pessimistic ranges between 0.3 ns – 1 ns [68] and 1 ns – 2 ns [53] respectively. Furthermore, various promising millimetre level results have been demonstrated for TOA based mmWave solutions [24], [72], [214], [217]. To encapsulate this range of values this thesis considers a range of TOA noise standard deviations σ_τ from 10 ns to 0.0001 ns (1 ps). For Electro-Magnetic (EM) wave propagation at the speed of light ($3 * 10^8$) this translates to a resolution of 3 m - 0.0003 m (0.3 mm).

4.5 Simulation Setup

4.5.1 Model Layout

The following scenario is established to reflect the parameters of the IoRL measurement campaign to make suitable use of the VLC datasets. In this regard the relative distances between RRLHs and the tracking region are maintained. The mmWave antennas' positions are given by the respective distances between the VLC transmitters and the mmWave antennas, as designed and presented in Figure 3.4d. This configuration of mmWave antennas has been selected to alleviate the issues that arise from square configurations for 3D tracking. A summary of the model parameters is given in Table 4.4 and the model layout is illustrated in Figure 4.4.

Table 4.4 - Summary of simulated model parameters

Parameter	**Value**	
Sensor Locations (x^i, y^i, z^i)/m	***VLC Tx***	***Active mmWave Rx***
$\boldsymbol{RRLH^1}$	(0.1471,0.1671,1.2690)	(0.0000,0.0200,1.2690)
$\boldsymbol{RRLH^2}$	(0.1521,0.7021,1.2790)	(0.2992,0.8492,1.2790)
$\boldsymbol{RRLH^3}$	(0.6721,0.7021,1.2690)	(0.8192,0.8492,1.2690)
$\boldsymbol{RRLH^4}$	(0.6771,0.1471,1.2790)	(0.8242,0.0000,1.2790)
	Target Tracking Area	
$\boldsymbol{x-axis}$ $(\boldsymbol{min}, \boldsymbol{max})$/m	$\boldsymbol{y-axis}(\boldsymbol{min}, \boldsymbol{max})$/m	**Origin** $(\boldsymbol{x}, \boldsymbol{y})$/m
$(\mathbf{0.1371}, \mathbf{0.8371})$	(0.0271,0.7271)	(0.4871,0.3771)

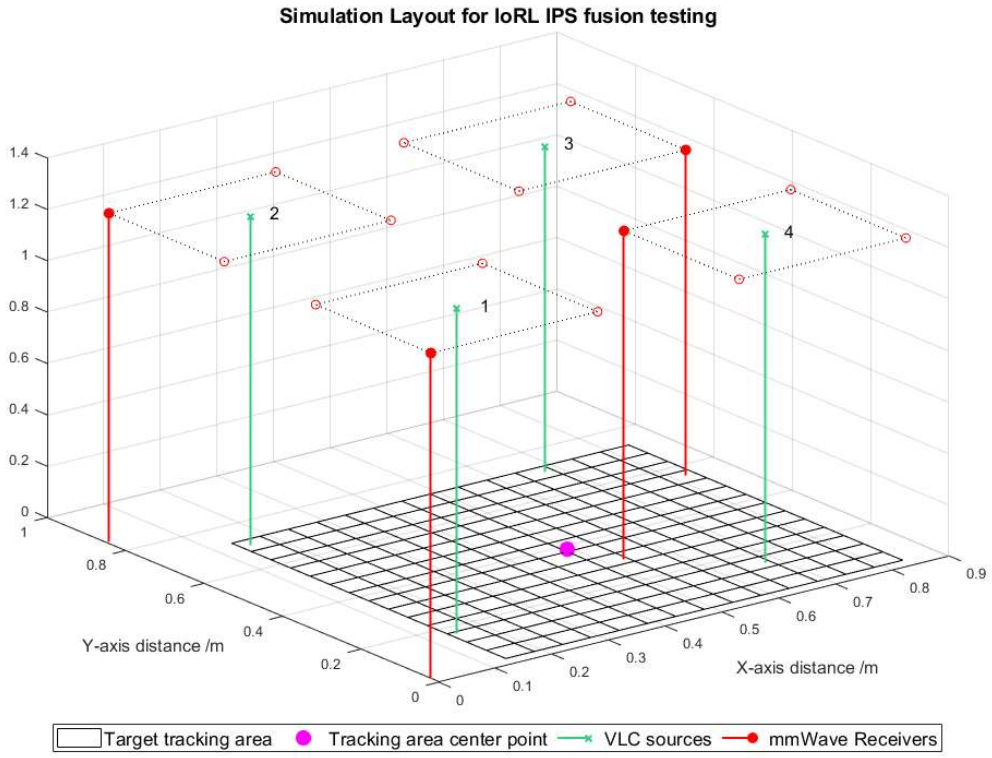

Figure 4.4 - Simulation layout considering active sensor positions and tracking plane

4.5.2 Target Trajectory

The target to be tracked is described by its Cartesian coordinates, at time t_k as $S_{t_k}^0 = \left[x_{t_k}^0, y_{t_k}^0\right]^T$. Throughout the simulation the target travels at a constant velocity of 0.2 m/s. If the trajectory is ideally described by the process model, the process noise of the KF will tend towards zero and measurements will be ignored. This case is neither practical nor realistic. Therefore, due to the predictive nature of the KF process, one must refrain from considering a pure Constant Velocity (CV) target trajectory due to potential overfitting of the process noise. Instead, the tracking performance of the used location estimation techniques is evaluated for a circular path. In this setting, the target maintains a constant angular velocity equivalent to a 0.2 m/s velocity along the circumference of the circular path. Variable nonlinearity is introduced by means of adjusting the angle θ_{path} of the path under a constant arc length of 1 m.

$$Arc\ Length\ (1\ \text{m}) = Radius(\text{m}) * \theta_{path}(\text{radians}). \tag{4.10}$$

An increase in θ_{path} decreases the path radius while increasing the angle of the target's path and hence the non-linearity of the Target trajectory. The centre point of the circle is given by the origin of

the tracking plane as shown in Figure 4.4. It is notable that the centre point of the tracking plane and the centre point of the RRLHs are not equivalent. The CenterPoint of the tracking plane has been selected to maximise the variable path trajectory.

Throughout the following simulations, the θ_{path} is considered at values of 3 rad, 5 rad and 5 rad with path radii of 33.3, 20 and 10 cm respectively. The target trajectories for various θ_{path} values are illustrated in Figure 4.5.

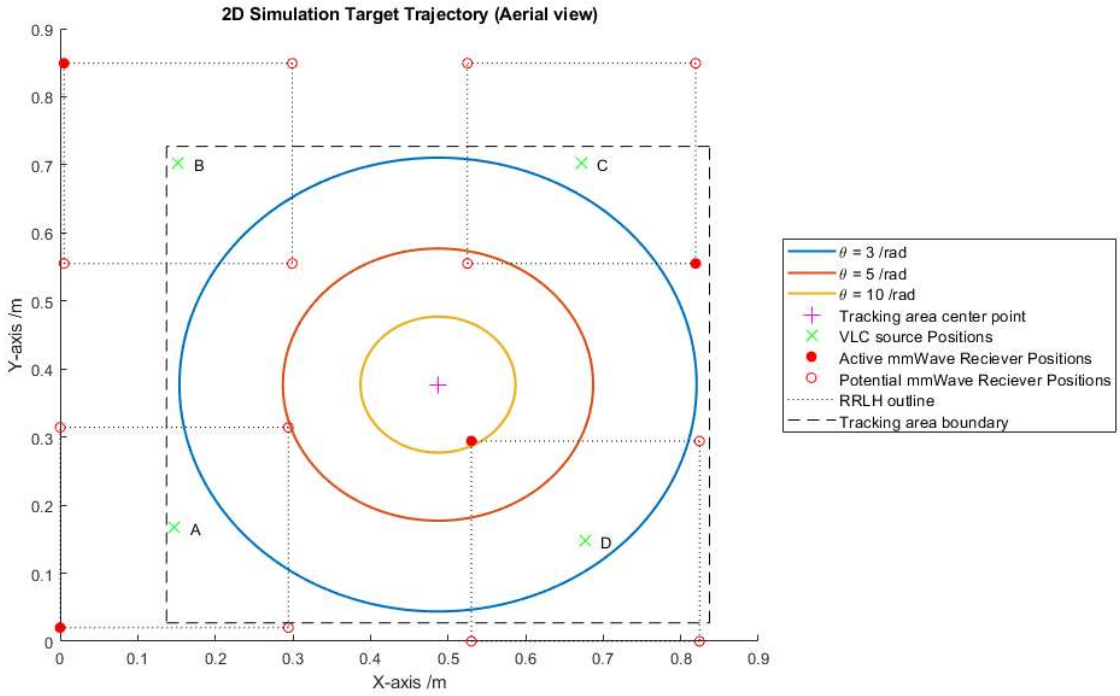

Figure 4.5 - Ariel View of simulation layout with target trajectory plots

Due to the differing lengths of path circumferences, the number of estimations carried out for a single circumference length are inconsistent. For a fair comparison, the number of estimations must be equivalent, therefore the target continues along the shorter circumference trajectories, until the number of computed position estimations is equal to the number of estimations obtained for a single length of the longest circumference path. Consequently, the number of position estimations evaluated for all paths is given by:

$$N_{PE} = \left(\frac{2\pi * Radius_{max}}{1m/s}\right) / T_{EPLC}. \tag{4.11}$$

Where $Radius_{max}$ is the maximum evaluated radius and T_{EPLC} is the EPLC measured in Section 4.4.1. As such, given a maximum radius of 33.33 m, and EPLC of 15 ms the target is evaluated at 7027 individual points around the given path.

4.5.3 Error Metrics

The following performance metrics are obtained throughout the simulation. The Position Error (PE) for each position estimate is given as the Euclidian distance between the estimated location ($\hat{S}_{t_k}^0 = \left[\hat{x}_{t_k}^0, \hat{y}_{t_k}^0\right]^T$) and the true targets position $\left(S_{t_k}^0\right)$ at t_k:

$$\varepsilon_{t_k}^{PE} = \left\| S_{t_k}^0 - \hat{S}_{t_k}^0 \right\|. \tag{4.12}$$

Once all 7027 estimations have been provided, this concludes a single simulation iteration denoted with subscript It. The simulation is repeated $N_{Iterations}$ times for each combination measurement noise and path angle. Once position errors have been obtained for all iterations ($\varepsilon_{t_k,It}^{PE}$) where $It = (1, \cdots, N_{Iterations})$, the average error for each estimation interval is calculated and described as the Mean Point Error (MPE):

$$\hat{\varepsilon}_{t_k}^{MPE} = \frac{1}{N_{Iterations}} \sum_{I=1}^{N_{Iterations}} \varepsilon_{t_k,It}^{PE}. \tag{4.13}$$

The Root Mean Square Error (RMSE) is then used to determine the overall error across all estimations and iterations:

$$RMSE = \sqrt{\frac{1}{7027} \sum_{k=1}^{k=7027} \hat{\varepsilon}_{t_k}^{MPE}}. \tag{4.14}$$

4.5.4 Kalman Filter Tuning

Certain variables and quantities must be established during the KF design for an optimal solution. As discussed in Section 2.1.3.2.1.1, the noise parameters of both the process and measurements are important to define the response to the scenario. This section presents the evaluations and prior studies that are carried out to tune the KF.

4.5.4.1 Measurement Noise Distribution

During the KF update stage of the $k'th$ estimation period, the VLC and mmWaves state estimates are inputted as measurements denoted by $z_{t_k}^{vlc}\ and\ z_{t_k}^{mmw}$ and computed through Algorithm 5 and Algorithm 6 respectively. These are related to the target state X_{t_k}, using the measurement translation matrix H:

$$z_{t_k}^{vlc} = H(X_{t_k}) + v_{t_k}^{vlc}$$
$$z_{t_k}^{mmw} = H(X_{t_k}) + v_{t_k}^{mmw} \tag{4.15}$$

In which

$$H = \begin{bmatrix} 1 & 0 & 0 & 0 \\ 0 & 1 & 0 & 0 \end{bmatrix} \tag{4.16}$$

Where $v_{t_k}^{vlc}$ and $v_{t_k}^{mmw}$ describe the normally distributed additive white Gaussian estimation noises, which are assumed independent from the KF process noise w_{t_k} and have respective covariance matrices R^{vlc} and R^{mmw}. Typically, these noise values can be obtained from empirical testing to determine the noise within the measurements as described by Welch & Bishop [120]. Using this approach, one can directly obtain the R^{vlc} values from the measurement data as explained in Section 2.1.3.2.1.1 and presented in (4.7). To obtain the mmWave measurement noise covariance matrix, a similar yet completely simulated approach is taken to generate the PE distribution from completely synthetic data. As this study considers the effects of variable TOA ranging errors σ_τ on the IoRL system performance, a new R^{mmw} matrix is required to be configured for each value of σ_τ applied.

To establish the measurement noise covariance matrix R^{mmw}, for the TDOA state estimation, a subtest is carried out within the virtual environment described in Section 4.5.1. for each level of applied noise. Position estimates, using Algorithm 6, are carried out across the target tracking area in increments of 5 cm. The TOA measurements are each corrupted by AWGN as described in (4.8). This process is repeated for each considered value of σ_τ. Each coordinate is evaluated 20 times as featured in the analysis of the VLC measurement campaign.

The computed standard deviations of the mmWave estimates, for both the x and y axis, are given below in Table 4.5 and applied to the system model as required.

Table 4.5 - mmWave position error distribution values for different time delay errors

σ_τ/s	1.00e-12	2.15e-12	4.64e-12	1.00e-11	2.15e-11	4.64e-11	1.00e-10
$\sigma_{x,mmw}$/m	2.79e-03	5.41e-03	1.13e-02	2.43e-02	5.25e-02	1.13e-01	2.44e-01
$\sigma_{y,mmw}$/m	2.75e-03	5.27e-03	1.10e-02	2.36e-02	5.09e-02	1.09e-01	2.36e-01
σ_τ/s	**2.15e-10**	**4.64e-10**	**1.00e-09**	**2.15e-09**	**4.64e-09**	**1.00e-08**	
$\sigma_{x,mmw}$/m	5.23e-01	1.12e+00	2.41e+00	5.20e+00	1.12e+01	2.41e+01	
$\sigma_{y,mmw}$/m	5.08e-01	1.09e+00	2.35e+00	5.04e+00	1.09e+01	2.33e+01	

4.5.4.2 System Identification for Process Noise

Unlike the measurement noise, the process noise w_{t_k}, with covariance matrix Q_{t_k}, is less trivial to determine. The process model applied (4.4) is a Constant Velocity (CV) model and therefore, as described in the literature review, commonly uses the Discrete-time Nearly Constant Velocity (DNCV) process noise covariance matrix structure given by Li & Jilkov [25] but for a two dimension system:

$$Q_{t_k} = \begin{bmatrix} \Delta T^4/4 & 0 & \Delta T^3/3 & 0 \\ 0 & \Delta T^4/4 & 0 & \Delta T^3/3 \\ \Delta T^3/3 & 0 & \Delta T^2 & 0 \\ 0 & \Delta T^3/3 & 0 & \Delta T^2 \end{bmatrix} * \sigma_a^2. \tag{4.17}$$

While the estimation period ΔT is shown to be given by the consecutive timestamps of the incoming data, as shown in (4.5), for simulation purposes, this value has been estimated to 20ms in the previous latency testing of Section 4.4.1. Therefore the Q matrix is a fixed value throughout and the estimation subscript 't_k' is omitted. The Acceleration noise magnitude σ_a is the tuning parameter to be determined through empirical testing. In this regard, the system is assumed to have known measurement noises, as given above, and a fixed estimation period (ΔT). Therefore, simulations are conducted to determine the optimal process noise through trial and error. Various values of σ_a are tried and tested through numerous iterations of Algorithm 8, the optimal value is the one that obtains the lowest overall RMSE.

This tuning process may be subject to overfitting, where the process noise is adjusted to handle a specific target trajectory. While this leads to optimal filter performance for the specified trajectory, for alternative target trajectories this process noise may be suboptimal and lead to degrading tracking performance.

To avert the issue of overfitting, the system is tuned for both the maximum and minimum path angles θ_{path} considered. The responses are averaged to provide the optimal σ_a value across all intermediate path angles, thereby reducing the effects of overfitting. This tuning process is carried out for all mmWave measurement noise values considered. In addition, the process is computed to obtain the optimal σ_a value for both estimates delayed by the RRLHC RTT and considering no computation delay denoted by $\hat{\sigma}_a$ and $\check{\sigma}_a$ respectively. The optimal $\hat{\sigma}_a$ and $\check{\sigma}_a$ values are given for each degree of measurement noise in Table 4.6.

Table 4.6 - Optimal acceleration noise components for the Location Server tracking filter at different levels of time delay noise

$\boldsymbol{\sigma_\tau}$/s	1.00e-12	2.15e-12	4.64e-12	1.00e-11	2.15e-11	4.64e-11	1.00e-10
$\boldsymbol{\hat{\sigma}_a}$/m	1.50e+00	1.50e+00	1.69e+00	1.69e+00	1.50e+00	1.50e+00	1.50e+00
$\boldsymbol{\check{\sigma}_a}$/m	1.06e+00	1.34e+00	1.34e+00	1.50e+00	1.34e+00	1.19e+00	1.34e+00
$\boldsymbol{\sigma_\tau}$/s	**2.15e-10**	**4.64e-10**	**1.00e-09**	**2.15e-09**	**4.64e-09**	**1.00e-08**	
$\boldsymbol{\hat{\sigma}_a}$/m	1.50e+00	1.34e+00	1.34e+00	1.50e+00	1.50e+00	1.50e+00	
$\boldsymbol{\check{\sigma}_a}$/m	1.19e+00	1.19e+00	1.19e+00	1.19e+00	1.19e+00	1.34e+00	

4.5.5 Simulation Algorithm

The simulation used to test the IoRL IPS is summarised as pseudocode in Algorithm 8.

Algorithm 8: IoRL IPS Test[11]

INPUT: mmWave Measurement noise values from Table 4.5 and respective optimal acceleration noise magnitudes from Table 4.6.

For σ_τ *= (1e-8, 1e-9, 1e-10, 1e-11, 1e-12)*
  For $\theta_{path} = (3, 5, 10)$
    For $It = (1{:}N_{Iterations})$
      Initialise KF
      Assign ΔT equivalent to the EPLC of 20 ms
      With $k = 1$, initialise $X_{t_1} = \left[x_{t_1}^0, y_{t_1}^0, v_{t_1}^x, v_{t_1}^y\right]^T$ and P_{t_1} as identity matrix I_{4*4}
      Configure A, Q *and* H from (4.4), (4.17) and (4.16) respectively
      Loop simulation
      For k = (1:7027)
        Move target along trajectory defined by θ_{path} by 0.2 m/s for 20 ms
        Generate VLC noisy estimate $z_{t_k}^{vlc}$ using targets true position and normally distributed noise with covariance matrix R^{vlc} given by (4.7) and standard deviations $\sigma_{x,vlc}$ *and* $\sigma_{y,vlc}$ acquired from HLC results.
        Generate noisy TOA $\hat{\tau}_{t_k}^i$ measurements from the true TOA $\tau_{t_k}^i$ (4.8) using (4.9)
        Establish TDOA measurements using sensor $i = 1$ as the reference
        Obtain mmWave estimate $z_{t_k}^{mmw}$ from Taylor Series (TS) solution Algorithm **6**
        Kalman filter fusion
        Obtain $\hat{X}_{t_k}^-$ and $P_{t_k}^-$ from prediction stage measurements using (2.38) & (2.39) and respective $\hat{\sigma}_a$ (or $\check{\sigma}_a$ if not testing delayed measurements)
        Fuse VLC estimate $z_{t_k}^{vlc}$ and covariance R^{vlc} using update equations, (2.40) - (2.42)
        Fuse mmWave estimate $z_{t_k}^{mmw}$ and covariance R^{mmw} using update equations, (2.40) - (2.42)
        Calculate respective PE using (4.12) (for delayed measurements PE is calculated with respect to the target's position at the targets future position 24.01 ms further along the trajectory)
      End
    End
    Calculate Mean point Error for $N_{Iterations}$ (5.23)
    Determine RMSE values for $N_{Iterations}$ (5.24)

[11] Ranges of values are represented in the following manner: (initial value : incremental value : end value) and may, in some cases, be assigned equivalent to a variable. Where an incremental value is not given, the increments are defaulted to integers of one. When used as part of a '*For'* loop, each value in the given range is applied individually within a single loop.

22: | *End*

23: *End*

4.6 Results

The following section presents the results obtained from Algorithm 8 for 500 iterations, using the EPLC, RTT and VLC measurement noise values. To assess the mmWave performance at various levels of noise the timing noise is varied from 0.001 ns – 10 ns. For each value of timing noise in the TOA measurements, the respective mmWave measurement noise covariance values are applied as given in Table 4.5 and optimal acceleration noise magnitudes are applied from Table 4.6. For comparison, errors are collected for results obtained with and without the RTT. The results obtained from the simulation are presented below in Table 4.7 and illustrated in Figure 4.6.

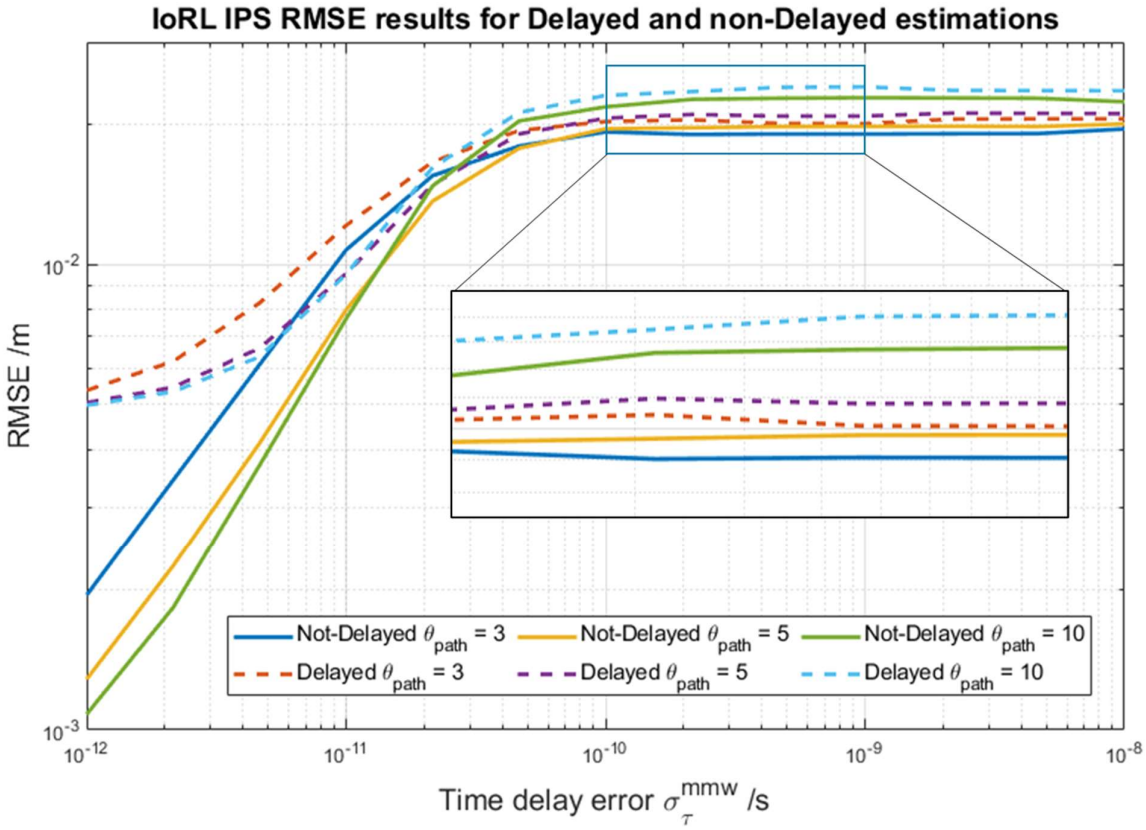

Figure 4.6 - IoRL IPS RMSE results for Delayed and non-Delayed estimations

Table 4.7 - IoRL IPS RMSE results for Delayed and non-Delayed estimates

	Not delayed RMSE/cm			Delayed Results RMSE /cm		
$\boldsymbol{\sigma_\tau}$/s	$\theta_{path} = 3\,rad$	$\theta_{path} = 5\,rad$	$\theta_{path} = 10\,rad$	$\theta_{path} = 3\,rad$	$\theta_{path} = 5\,rad$	$\theta_{path} = 10\,rad$
1.00E-12	0.19	0.13	0.11	0.54	0.51	0.50
2.15E-12	0.34	0.22	0.18	0.62	0.55	0.53
4.64E-12	0.61	0.41	0.37	0.83	0.66	0.63
1.00E-11	1.07	0.80	0.76	1.21	0.96	0.95
2.15E-11	1.55	1.37	1.47	1.66	1.48	1.61
4.64E-11	1.80	1.78	2.03	1.94	1.91	2.12
1.00E-10	1.93	1.96	2.18	2.03	2.06	2.31
2.15E-10	1.90	1.97	2.26	2.04	2.10	2.35
4.64E-10	1.91	1.98	2.27	2.01	2.08	2.40
1.00E-09	1.90	1.98	2.28	2.01	2.08	2.41
2.15E-09	1.91	1.98	2.28	2.05	2.11	2.36
4.64E-09	1.91	1.98	2.27	2.05	2.11	2.36
1.00E-08	1.95	2.00	2.23	2.05	2.11	2.36

4.7 Simulation Analysis

Performance across the range of results indicates promisingly low centimetre level accuracies with a maximum RMSE of 2.41 cm. Accuracies within the millimetre region are shown to be attainable for mmWave time delay noises of less than 0.01 ns.

The mmWave measurement noise is shown to have a prominent effect on the results for values below 0.1ns. The RMSE reaches a plateau as the mmWave noises surpass this region, at which point the errors within the mmWave covariance matrix are so great, that the mmWave estimates are effectively redundant, in comparison to the centimetre level accuracy of the VLC estimates. During this plateau region, the position estimates are purely dependant on the VLC state estimates and the process model.

It can also be seen that, during this transition from strongly mmWave weighted estimates to more reliance on the process model, the performance for different path angles is seen to invert. Higher reliance on the process model favours larger path angles, since the trajectory better reflects the CV model applied. Conversely, where slightly noisy measurements are favoured, the more linear trajectories show worse performance.

For a dynamic target, the displacement encountered during the processing time of the estimation leads to errors. While the target travels at only 0.2 m/s around the circumference of the

path and with a RTT of only 24 ms, the error attributed to the computational delay of the estimates is evident throughout all measurement ranges. Notably, this latency effect is more prominent at lower noise levels where the latency component is the main source of error. As estimates become less accurate, the effects of the estimation delay are less prominent.

4.8 Chapter Conclusions

This chapter presents an evaluation of the performance of the IoRL 5G IPS using the proposed HLC method and a combination of simulated and measured data. The proposed IoRL performance, even at the highest point of error achieves low centimetre level accuracies. While the mmWave error, within the IoRL system, is expected to be limited by available BW, the tracking solution relying on VLC estimates alone is shown to achieve reliable centimetre level positioning error. Where the mmWave errors are not substantially greater than those of the VLC solution, the use of data fusion exploits the benefit of both technologies, With regards to potential system improvements, the basic LD table requests, given by Query 2 and employed within the LS, are shown to increase the overall EPLC. More efficient mechanisms could present lower EPLC values. This may enable the efficient use of all available datasets and facilitate more frequent updates.

4.8.1 Suitability of the Evaluated System in Satisfying Application Requirements

The 5G standards, outlined by 3GPP in Release 16 [200] present various service levels where localisation requirements are set. The most stringent of which dictates horizontal and vertical accuracies under 20 cm with 99 % confidence and a latency of 1 second at a potential target velocity of 30Km/h. While the target velocity and confidence levels are not evaluated within this chapter, the performance of the modelled IoRL project appears promising in meeting these requirements in terms of accuracy and latency.

The IoRL project documented several use case applications [211] for different demonstration sites. The Home scenario suggests a Follow Me Service (FMS) in which room level positioning is required to identify the most suitable monitor to display a user's content. In this case the results obtained exceed the positioning performance required. However, the Train station scenario suggests applications for both locating maintenance workers and overlay of virtual models on Virtual Reality (VR) displays. locating workers to the degree of a few centimetres can be expected to satisfy application demands. However, VR systems require millimetric resolutions, which can be achieved only if the timing error of the mmWave solution is less than 0.001 ns.

While this study presents significant Improvements on the previous publication [257] presented by the author of this thesis, one must acknowledge the various assumptions made throughout this study.

First, typical positioning applications, like those presented in the 3GPP specifications and IoRL project, require 3D positioning in which additional processes for VLC triangulation are required and larger levels of noise can be expected for longer propagation distances due to RSSI attenuation.

Second, the tilt of the receiver affects the VLC RSS signal attenuation due to greater incident angles. While this is ignored in many VLP studies, the VLC results obtained during the IoRL measurement campaign and used within this study are reflecting ideal LOS conditions that cannot be expected to be met in practical settings. These measurements are obtained using a gimbal with a zero-degree angle of incidence such that optimal LOS is achieved. Results obtained without the use of the gimbal can be expected to suffer a much greater level of noise due to larger incidence angles.

Regardless, the study provides a basis on which evaluations and observations of the IoRL IPS can be made. One significant assumption made early in the chapter relates to the asynchronous sampling nature of both mmWave and VLC measurements. The IoRL IPS specifies millisecond latencies between consecutive measurements however these were assumed negligible during this initial study. The following chapter considers the asynchronous sampling of the IoRL project further.

5 An Evaluation of Asynchronous Sampling Effects on Wireless Localisation for Range Measurements

5.1 Introduction

So far, the body of work considered in chapters 3 and 4 has assumed that the IoRL Indoor Positioning system (IPS) measurement sampling, between the Remote Radio Light Heads (RRLHs) and User Equipment (UE) is achieved synchronously. However, this reviewing the communication protocol of the IoRL IPS from Section 2, the system is designed to sample individual millimetre wave (mmWave) Time of Arrival (TOA) and Visible Light Communication (VLC) Received Signal Strength Indicator (RSSI) measurements asynchronously, or more specifically in a sequential manner. The Internet of Radio Light (IoRL) Indoor Positioning Protocol (IPP), described in Section 2.3.3.3.2, defines that the individual Position Reference Signals (PRS) and LED signals are transmitted and received sequentially. This feature of asynchronous sequential sampling is evaluated throughout the remainder of this thesis and is illustrated by the individual Sounding Reference Signals (SRSs) and LED transmissions in Figure 5.1.

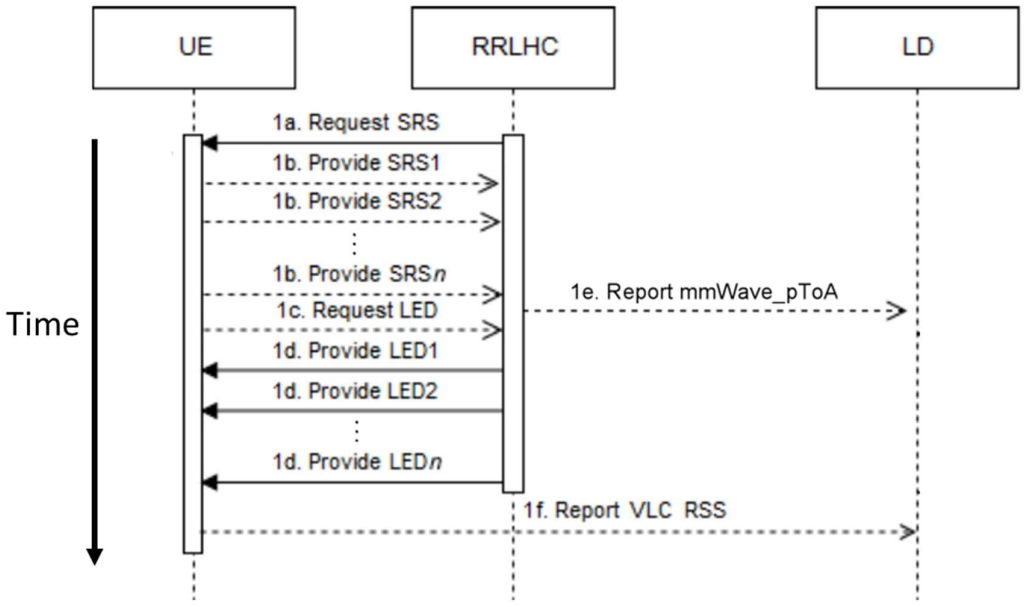

Figure 5.1 – The measurement sampling extract from the IoRL Indoor Position Protocol. Transmission of Sounding Reference Signals (SRSs) and LED position data between the User Equipment (UE) and the Remote Radio Light Head Controller (RRLHC) prior to dataset transmission to the Location Database (LD).

Within the IoRL IPP, both mmWave SRS and VLC LED ID data is transmitted within separate subframes of the 5G transport block and therefore individual TOA and RSSI measurements are obtained each millisecond. Additionally, changes to the IoRL project system and performance are to be expected, due to its research nature. The current system implemented for the 5G demonstrations is designed to obtain individual mmWave TOA measurements in the uplink channel every 10 ms at individual RRLHs. This process of sequential measurement acquisition is notably an order of magnitude slower and introduces increased potential for estimation error.

Given the asynchronous sampling of nonlinear range measurements, within the IoRL system, this chapter considers localisation estimation using nonlinear range measurements obtained from TOA and RSSI, under sequential sampling.

Within the context of asynchronous sampling of data for localisation applications, one can take the separation between consecutive measurements, referred to as the Inter Measurement Latency (IML), denoted by Δt_m, to be the measure of how asynchronous a system is. In this respect, the IoRL system exhibits a smaller (1 ms) and greater (10 ms) level of asynchronous sampling than the revised VLC and mmWave sampling protocols discussed.

It is commonly accepted that additional processes are generally required to compensate for measurements' temporal and spatial misalignments. The added complexity of such techniques requires more energy and consequently add cost to the overall system. Therefore, asynchronous sampling localisation techniques should not be used where the costings outweigh the potential accuracy improvements. The degree to which asynchronous sampling localisation techniques are suitable needs to be evaluated, where suitability refers to the subjective trade-off between computational efficiency vs accuracy.

To run a cost benefit analysis on the IoRL asynchronous 1 ms and 10 ms cases, one needs to quantify the effect of the asynchronous sampling on the performance of the system. Existing literature is quick to highlight the need for asynchronous localisation methods, citing that the misalignments of measurements are erroneous and therefore expected to be detrimental to accuracy. However, the extent of these implications is not evaluated. Within studies on the various techniques, comparisons are drawn between solutions under a single set of conditions, where the measurement noise, time between consecutive measurement samples, and target trajectory, are confined to fixed values.

Whilst the potential for errors within asynchronous systems is evident, the effects of sequentially asynchronous sampling on various localisation methods are not described within existing literature. The existing studies that are available, fail to clearly indicate the suitability of asynchronous solutions for variable degrees of IML. Moreover, the existing solutions may be applicable under set

conditions, but as part of a wider scope, should still present strong resilience to noise and suitability under variable trajectories.

5.1.1 Chapter Aims

This chapter evaluates the impact of asynchronous sampling on different existing localisation solutions, so that the performance of existing systems under variable measurement noise, IML and target trajectories can be assessed. In doing so, the suitability of asynchronous solutions can be determined, with regard to their position error, latency and performance with added noise. This work highlights the effective regions of existing asynchronous solutions and fundamental challenges for efficient asynchronous localisation techniques which is discussed in the following chapters.

5.1.2 Chapter Contributions

The primary contribution of this chapter is an in-depth analysis of the effects of asynchronous sampling on existing techniques, under a broader range of parameters than previously considered. This includes exploration of path nonlinearity, magnitude of sampling delay and variable noise. In addition to this, a modified location estimation solution for asynchronous sampling of range measurements is also presented.

5.1.3 Overview of Chapter

The first section of this chapter explores the effects of the latency component within sequential sampling on range estimation for a single sensor system. In subsequent sections, this concept is evaluated under multisensor systems and various position estimation methods, that both do, and do not, consider the asynchronous sampling element. Within these sections, a proposal and analysis of modified existing asynchronous solutions is put forward, and a comparison and discussion of existing location estimation techniques is carried out, which is concluded in the summary section.

5.2 Sequentially Asynchronous Localisation Problem Statement

To better understand the effects of asynchronous sampling on target localisation, this chapter first considers the effects on the range measurements used within the estimation processes. First the scenario is described and then analysis on the range estimates for single sensor systems is presented. To retain emphasis on the IoRL IPS, this chapter explores a centralised network in which N sensors are estimating the distance between themselves and a dynamic target. The Fusion Centre (FC) describes the component tasked with performing the location estimation process, which may be a single sensor

within the network at one point in time or an external device. We assume that: the clocks of the various sensors are also synchronised, the transmission delays are negligible, and no packets are delayed, missing or corrupted. The sensors are configured to obtain individual distance measurements $z^{i}_{t^{i}_{k}}$ for $i = (1, \cdots, N)$ in sequence, such that $t^{1}_{k} < t^{2}_{k} < \cdots t^{3}_{k} < \cdots t^{N}_{k}$ where t^{i}_{k} denotes the instant the $i'th$ sensor produces a measurement within the sampling period $[t_k, t_{k-1})$. Within the described network, the sensors are assumed to be homogenous such that they have the same Additive White Gaussian Noise (AWGN) measurement noise $v_{t_k} = N(0, \sigma_z)$ and the same constant sampling period (ΔT):

$$\Delta T = t^{i}_{k} - t^{i}_{k-1} \;\; i = (1, \dots, N). \tag{5.1}$$

The time between each consecutive sensors' sampling is assumed equivalent and is referred to as the Inter-Measurement Latency (IML) denoted using the term (Δt_m):

$$\Delta t_m \; = t^{i}_{k} - t^{i-1}_{k} \;\; i = (2, \dots, N). \tag{5.2}$$

All measurements are delivered to a Fusion Centre (FC) where periodic state estimation is carried out at the instant of the last measurement being received:

$$t_k = t^{N}_{k}. \tag{5.3}$$

From the relationships defined in (5.1), (5.2) and (5.3) the period of estimation or sampling period of the FC is simply the product of the number of sensors and the IML:

$$\Delta T = t_k - t_{k-1} = N * \Delta t_m. \tag{5.4}$$

An illustration of the scenario and relationships is presented below in Figure 5.2.

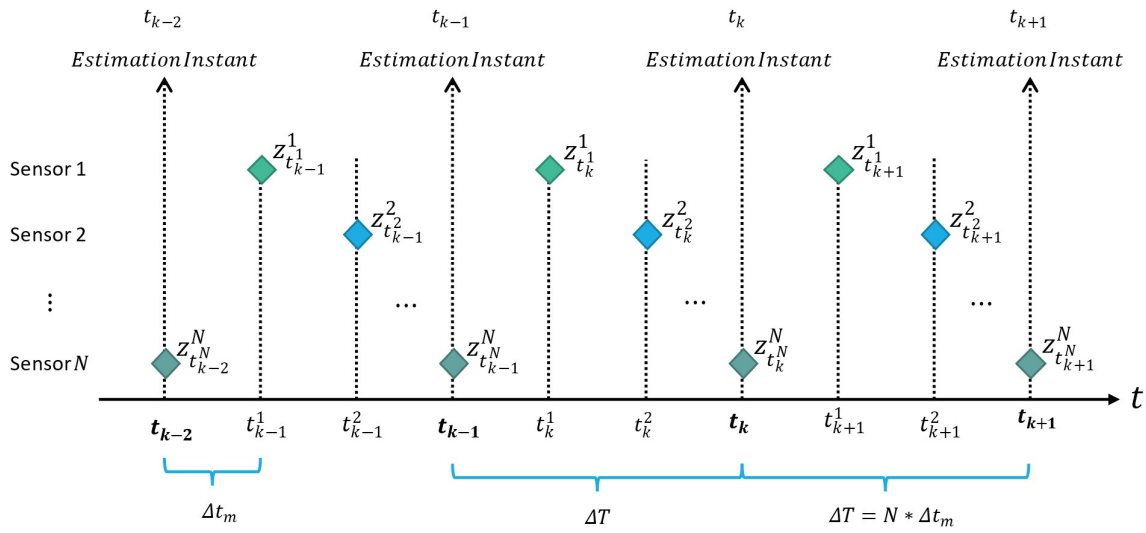

Figure 5.2 - Sequential sampling scenario and relationships between variables.

5.3 Inter-Measurement Latency (IML) Noise Component

Within the problem statement described in the previous section, the considered scenario is simplified in two keyways:

- Firstly, the sensors are sampled periodically with a constant time difference between them, known as the IML value.
- Secondly, the data fusion is carried out on the instant of the $N'th$ measurement.

These simplifications are given to highlight the relationships more easily between values and to reduce variability in the potential outcomes.

As previously stated, the asynchronous sampling is produced by the delay between consecutive measurements as given by the IML. The positioning estimation errors within the asynchronous sampling system occur when measurements are fused from different points in time and, under a dynamic scenario, describe the state of the target at different points in space. For this problem statement scenario, this takes place at the end of every sample period, where N measurements are fused together at the fusion instance to generate an estimate. The error within the individual measurements, caused by the IML, contributes towards the resultant position error. To gain further insight into the effects of asynchronous sampling on localisation techniques, the influencing factors and magnitude of measurement errors that arise from IML are explored within this section.

Firstly, consider the individual sensor measurements discussed throughout this thesis, which are nonlinear observations of the targets state at the measurement instant [132]:

$$z_{t_k^i}^i = h\left(S_{t_k^i}^0, S^i\right) + v_{t_k^i}^i. \tag{5.5}$$

Where $v_{t_k^i}^i$ is additive white zero-mean Gaussian noise such that $v_{t_k^i}^i \sim N(0, \sigma_z)$ with covariance matrix R. S^i represents the $i'th$ sensor position given by 2D coordinates $S^i = \left[x^i, y^i\right]^T$ where x^i and y^i denote the Cartesian coordinates in the x and y axis of the $i'th$ sensor respectively. $S_{t_k^i}^0$ with superscript of zero, represents the target position, given by $S_{t_k^i}^0 = \left[x_{t_k^i}^0, y_{t_k^i}^0\right]$, at timepoint t_k^i, which refers to the $i'th$ sensor's measurement instant within the $[t_k, t_{k-1})$ sampling period. Where x^0 and y^0 denote the Cartesian coordinates in the x and y axis of the target respectively. The nonlinear measurement function h is given by [36]:

$$h\left(S_{t_k^i}^0, S^i\right) = \sqrt{\left(x_{t_k^i}^0 - x^i\right)^2 + \left(y_{t_k^i}^0 - y^i\right)^2}. \tag{5.6}$$

By means of fusing the sensor measurement at the Fusion Centre (FC), one can consider the effects of the IML as an additional error component $\varepsilon_{t_k^i}^{IML,i}$. The error component of each measurement pertains to the range difference between the measurement instant t_k^i and the estimation instant t_k. The range measurement for the $i'th$ sensor at the estimation instant is therefore represented in the following form:

$$z_{t_k}^i = h\left(S_{t_k^i}^0, S^i\right) + v_{t_k}^i + \varepsilon_{t_k^i}^{IML,i}. \tag{5.7}$$

Where $\varepsilon_{t_k^i}^{IML,i}$ represents the IML noise component, which has a complex relationship within the dynamic scenario that is explored throughout this chapter.

To better understand the effect the IML has on the localisation performance, this section initially evaluates the IML noise component $\varepsilon_{t_k^i}^{IML,i}$ for a single sensor. To isolate the IML noise component, the sensor measurement noise $v_{t_k}^i$ is initially set to zero. Consider the $i'th$ sensor, from the network of N sensors, located on a 2D plane. The target to be tracked is assumed to travel along a linear path with constant velocity $V = [v^x, v^y]^T$ where v^x and v^y denote the velocity in the x and y axis respectively.

Sensor i obtains a noise free distance measurement $d_{t_k^i}^i$ of the target at time point t_k^i. The FC performs location estimation at timepoint t_k^N where the time difference between t_k^i and t_k^N is referred to as the Measurement Latency (MLa), denoted by Δt_i. The Cartesian coordinates of the target at the

measurement instant and the estimation instant are given by $S^0_{t^i_k} = \left[x^0_{t^i_k}, y^0_{t^i_k}\right]$ and $S^0_{t^N_k} = \left[x^0_{t^N_k}, y^0_{t^N_k}\right]$ respectively. The true distance between the target and the $i'th$ sensor at the estimation point t^N_k is denoted by $d^i_{t^N_k}$. Under the constant IML scenario, the MLa can be described by a multiple of the IML such that:

$$\Delta t_i = t^N_k - t^i_k = (N - i)\Delta t_m. \tag{5.8}$$

This is illustrated in Figure 5.3.

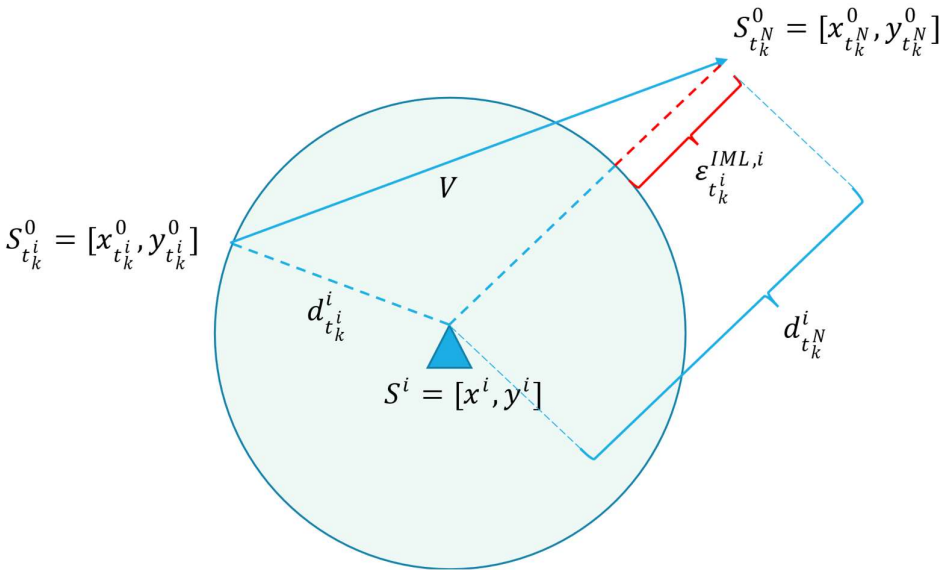

Figure 5.3 - 2D Cartesian representation of the IML Noise Component for a single sensor

The measurement error in this scenario is brought on by the target's movement during the interval Δt_i, in which the distance between the target described by the measurement at time point t^i_k is no longer equivalent to the distance at the estimation instant t^N_k. As such, the magnitude of the IML noise component refers to the absolute difference between the measured range $d^i_{t^i_k}$ and the non-measured true range of the target at t^N_k. Using the relationships described, the magnitude of the IML noise component for a single sensor can be presented as:

$$\varepsilon^{IML,i}_{t^i_k} = \left|d^i_{t^N_k} - d^i_{t^i_k}\right|. \tag{5.9}$$

Furthermore, representing the distances as the Euclidian distance between their respective positions gives:

$$\varepsilon_{t_k^i}^{IML,i} = \left|\left\|S_{t_k^i}^0 - S^i\right\| - \left\|S_{t_k^N}^0 - S^i\right\|\right|. \tag{5.10}$$

Lastly, under the constant velocity assumption, the position of the target at the estimation instant can be represented by the position of the target at the measurement instant and displacement over Δt_i:

$$\varepsilon_{t_k^i}^{IML,i} = \left|\left\|S_{t_k^i}^0 - S^i\right\| - \left\|\left(S_{t_k^i}^0 + V(N-i)\Delta t_m\right) - S^i\right\|\right|. \tag{5.11}$$

From (5.11), the IML noise component can be regarded as a complex function of the target's position relative to the sensor, the velocity of the target and the Measurement Latency (MLa) component. The MLa component here, as per equation (5.8), refers to the IML and the multiplier derived from the sequencing of the specific sensor. From this analysis the IML error component can be regarded as a systematic error which can be quantified.

5.3.1 Single Sensor IML Error Analysis

To provide an initial overview of the IML error component as a function of the variables presented in (5.11), a brief simulation study is carried out for a single sensor system. For the purposes of this simulation, the sensor is assumed to be noiseless in order to isolate the IML effects. The simulation is carried out under three scenarios where the velocity of the target is different in each, with respect to the tangent of the circle formed from the radius of the measurement $d_{t_k^i}^i$. Within each scenario three individual targets A, B & C are considered, in which the initial positions $S_{t_k^i}^0$ are varied. Targets A and C reflect different initial positions with an equal initial measurement value $d_{t_1^i}^i$, such that $d_{t_1^i}^i$(A) is equivalent to $d_{t_1^i}^i$(C). While B, indicates a greater initial range measurement $d_{t_1^i}^i$(B). Considering a 2D model, each range measurement forms a circle about the sensor position S^i with a radius equivalent to the respective range measurement. To evaluate the effects of the IML, the MLa between the measurement instant t_k^i and the estimation instant t_k is increased. While the sensor position is a variable within the IML Error function (5.11), the sensor position is relative to the targets' initial location and therefore the adjustment of the initial target coordinates is sufficient to indicate this change.

It should be noted that the following analysis of the simulation study is a simplification under a constant velocity assumption. The IML error component is calculated as per equation (5.9), and the geometry and target trajectories for each scenario are illustrated in Figure 5.4, with the respective IML

Error components provided in the bottom row of graphs. The analysis of the results presented for each scenario, as shown in Figure 42, is below.

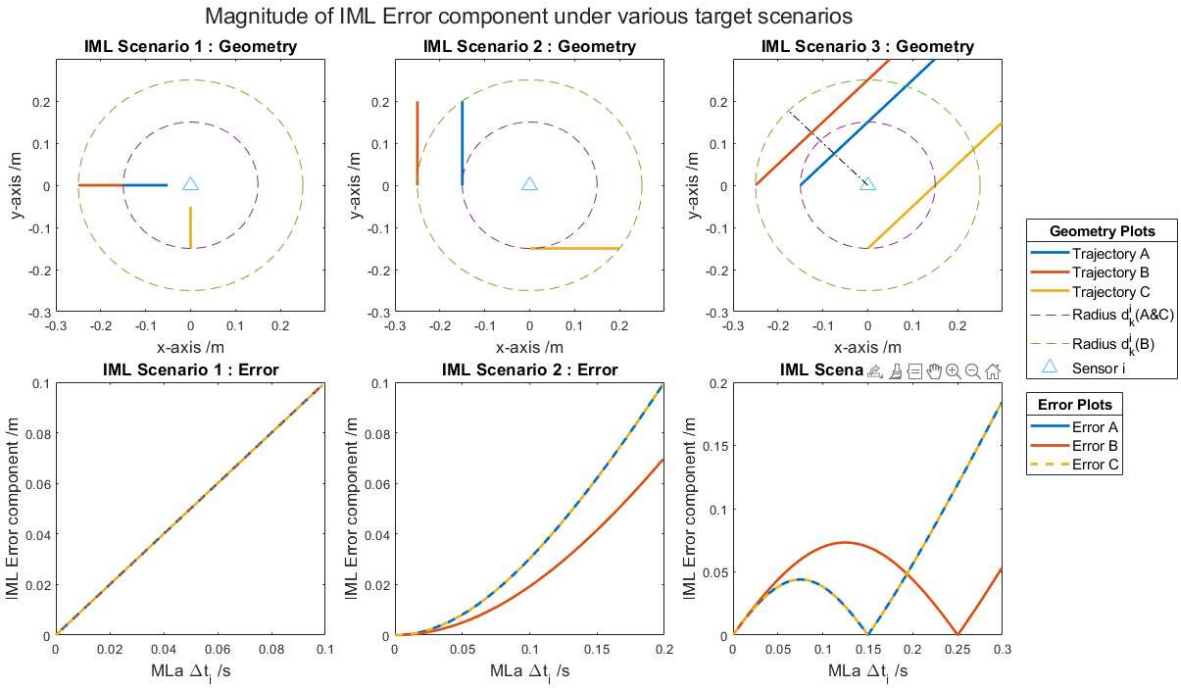

Figure 5.4 - IML error component under three varied trajectory scenarios

Scenario 1

Within Scenario 1, the velocity vector for each target is perpendicular to the tangent of the circle, which is generated by the measurement at t_k^i . As a result, the IML Errors are linearly related to the MLa, and are directly correlated across all the targets. This path generates the greatest possible amount of range error between the measurement instant t_k^i and the later fusion instant t_k.

Scenario 2

For Scenario 2, the target velocity vectors are at a tangent to the circle formed by the measurement at t_k^i. The resulting error that occurs is nonlinear with MLa, and forms an exponential relationship. Notably, targets A and C obtain an identical error, whilst target B, which is at a greater initial distance from the sensor, incurs a smaller relative error. This difference is caused by the nonlinear relationship between the target position and the distance to the sensor.

Scenario 3

The velocity within Scenario 3 reflects an arbitrary vector between the vector values described in Scenario 1 and 2. Interestingly, as the target velocity vector creates a chord through the circle, which

is formed by the measurement, the error increases nonlinearly towards an initial maxima. This maxima coincides with the centre point of the chord. In other words, the error decreases the closer the estimated distance is to the measured distance. Evidently, the error is zero when the target's estimation position is equal to the measured distance. As the IML exceeds this value the errors continue to increase nonlinearly. In this respect, depending on the velocity component, a greater amount of IML does not necessarily dictate a higher level of IML Error. The same observation could be made for scenario 1 however, under the Constant Velocity (CV) assumption, the target would have to pass through the sensor, and this is impossible in practice.

The above analysis of the simulation study provides reasonable insight into the magnitude of the IML error component, which has been evaluated for different scenarios, such that the variables are altered to highlight their individual impact.

5.3.2 Single Sensor IML Error Effects Under Measurement Noise

Having analysed, in the previous section, data collected under ideal noiseless conditions, the following section considers the effects of measurement noise on asynchronously sampled measurements. The IML Error component remains systematic however, when combined with random measurement noise, the resulting effects can be both constructive and deconstructive. This effect is represented by Figure 5.5 below, illustrates how measurement noise may exacerbate or otherwise reduce the effects of IML in comparison to noise free asynchronous measurements. In Figure 5.5A, the black arrow represents a nonlinear target trajectory. The black dots along the trajectory path identify the targets' position at various sensor sampling instances where the last is the estimation instant. Individual sensor range measurements are compared to the true sensor range at the estimation instant and the Range Error (RE) is visualised in red. Figure 5.5B includes measurement noise for each sensor range measurement. The green node illustrates where negative noise decreases the measured range and increases the overall RE. The yellow node shows where positive noise increases the range yet further increases the RE. The blue sensor shows where a positive noise element increases the measured range and corrects for the error attributed to the IML therefore improving the RE. Lastly, the purple node has no IML error but is negatively affected by measurement noise.

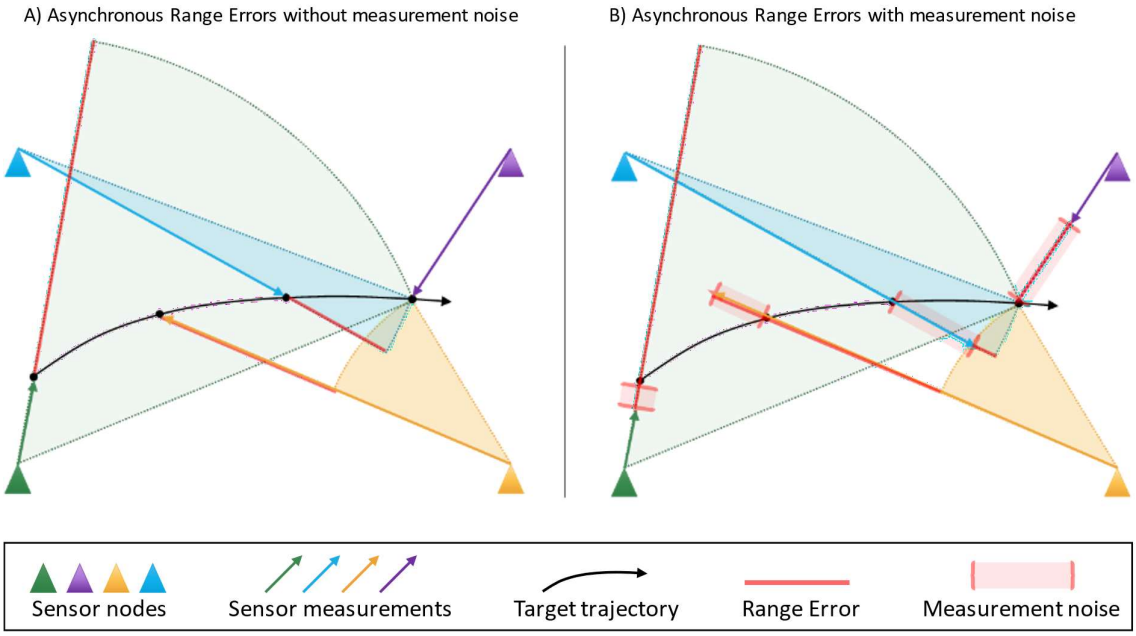

Figure 5.5 - Illustrative comparison of sensor Range Errors for asynchronous sampling, with and without measurement noise

To better understand the effects of IML on range errors under measurement noise, a brief study is presented for the same single sensor measurements as in Section 5.3.1. For this study, only Scenario 1A is observed, as scenario 1 generates the greatest amount of IML Error, and targets B and C within it provided no additional information. Furthermore, for more comparative results across the different scenarios within this thesis, the range of the latency component is set to its maximum as generally considered within this body of work, where $\Delta t_m = 0.1$ s and $N = 4$ and therefore the maximum latency observed is 0.3 s. Figure 5.7 illustrates the magnitude of the error of scenario 1A under variable measurement noise, comparing both a single iteration and an averaged response of 1000 iterations. With the addition of measurement noise, the Range Error (RE) $\varepsilon_{t_k}^{R,i}$ is taken to be the difference between the noisy sensor range measurement $\hat{d}_{t_k^i}^i$ and the true distance between the target and the $i'th$ sensor at the fusion instant $d_{t_k^N}^i$. The RE is the sum of both the AWGN and IML Error component.

$$\varepsilon_{t_k}^{R,i} = \varepsilon_{t_k^i}^{IML,i} + v_{t_k^i}^i = d_{t_k^N}^i - \hat{d}_{t_k^i}^i \tag{5.12}$$

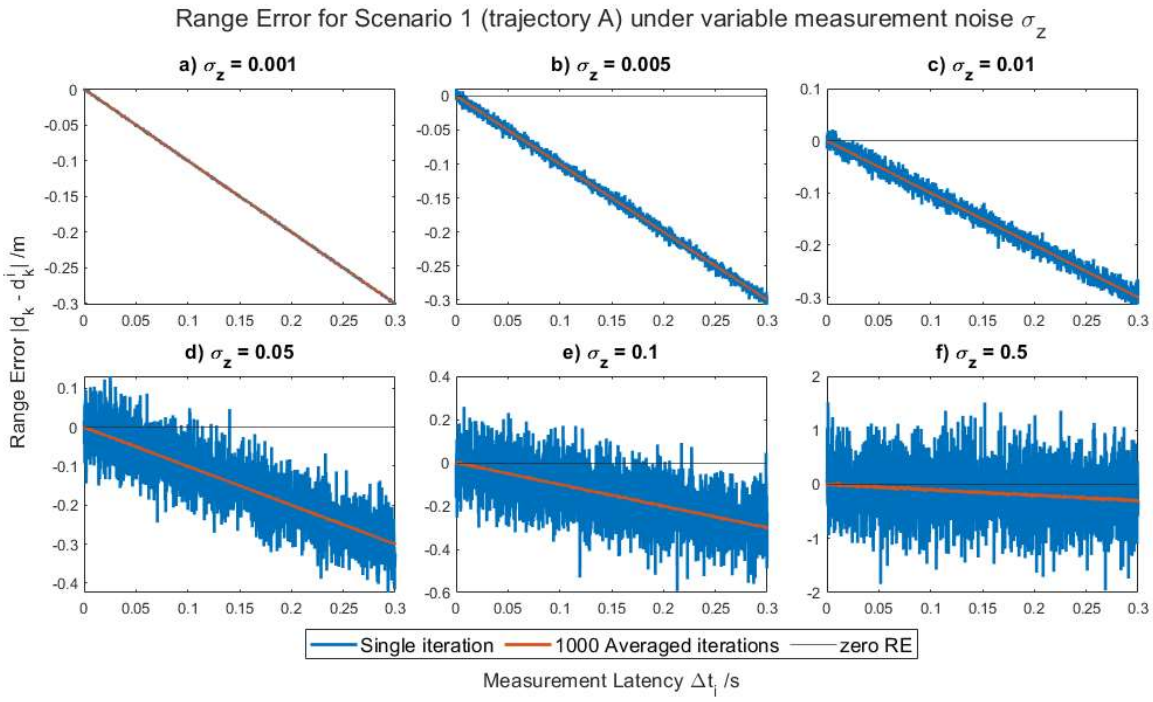

Figure 5.7 - IML error under variable measurement noise values for scenario 1A

The following analysis pertains to Figure 5.7. The Range Error, unlike the IML error component, is given as a non-absolute; therefore, the negative range error describes the true distance at the fusion instance $d^i_{t_k^N}$ being less than the measured distance $\hat{d}^i_{t_k^i}$, which is logical given the target trajectory in Scenario 1A. Given the linear relationship between the Measurement Latency and IML Error component, with consideration given to the scenario IML and sensor numbers, the maximum possible range error accrued by MLa alone is given by a target travelling perpendicular to the tangent of the circle formed by the measurement, with a constant velocity of 1 m/s. Under these conditions, the maximum range error that can be attributed to the IML alone, for a single measurement, is 0.3 m.

Due to its zero-mean nature, averaging the response of over 1000 iterations effectively removes the measurement noise; therefore, the orange line in Figure 5.7, representing the averaged result, illustrates the IML error component. A single iteration is also given to highlight the constructive and deconstructive nature between the two constituents of noise. Where the noises interact and the Range Error is reduced, one can observe the deconstructive qualities of both the MLa and Measurement noise combined. The opposite can also be observed where the measurement noise exaggerates the IML error component, producing a greater level of error.

From Figure 5.7a - Figure 5.7c, which reflect the additive noise range of $\sigma_z = 1$ mm-1 cm, the effects of measurement noise within the scenario are relatively slight. This highlights the significance of the Measurement Latency (MLa), and where it supersedes the effects of measurement

noise. Furthermore, it indicates that the errors due to IML for values within this thesis are not negligible and should not be ignored.

As measurement noise increases in Figure 5.7d - Figure 5.7f, the errors due to the MLa component remain constant, however, the magnitude of the measurement noise dominates the system and the IML error component is less distinguished.

5.3.3 IML Section Summary

Within this section, the principle of IML has been introduced and a function for the IML error component has been derived for range-based estimation under a constant velocity assumption. Subsequently the single sensor RE's caused by IML in both noiseless and noisy conditions has been evaluated. From this work, it is evident that the IML noise component is a highly systematic error with many time varying factors. The introduction of measurement noise within the system is shown to be either constructive or deconstructive.

While it is possible to average out the random measurement noise, identifying the IML noise component is far more complex. This is due to the variability of the parameters within the IML error, and the fact that the error is only present in dynamic scenarios. It should also be noted that in practical scenarios the target's velocity may not be constant and as such, further complexity is added to the scenario. The author, of this thesis, therefore considers primitive methods to calculate the IML component, in order to mitigate its effects, ineffective and costly for real-time tracking solutions.

Under measurement noise, the effects of IML are relatively less significant, however, they are still significant and therefore cannot be disregarded. With this in consideration, the following research investigates the effects of IML on location estimation using a multi-sensor system.

5.4 Existing Tracking Under IML

Whilst the effects of the IML component for a single sensor have been established, analysis of multisensor tracking, with existing nonlinear positioning methods has yet to be evaluated for varied path nonlinearities and levels of IML. Through a series of simulation studies, this section first analyses the effects of IML on conventional tracking solutions in which IML is not acknowledged by the estimation algorithms. This analysis will provide a fundamental understanding of the effects of IML on standard localisation techniques and will further establish the control studies for the remainder of this work. This will allow for improved comparison of the suitability of asynchronous solutions under variable degrees of asynchronous sampling. The nonlinear tracking solutions considered within this section, are the common Least Squares Solution (LSS) Multilateration and the Unscented Kalman Filter (UKF) approach. Both are batch processes conducted once N measurements have been received

sequentially, in accordance with the scenario described in Section 5.2. Later in this section adaptations of the LSS and UKF processes, proposed for asynchronous sampling, are evaluated to assess their overall suitability, under variable conditions. The remainder of this chapter considers the 2D sequentially asynchronous problem statement provided earlier in Section 5.2.

5.4.1 Non-Asynchronous Tracking Solutions

To ascertain the effects of IML on tracking solutions and further explore the necessity of asynchronous solutions, common non-asynchronous localisation techniques are explored under asynchronous sampling conditions. As previously stated, the techniques considered are the Multilateration LSS and the UKF.

The target is set on a given trajectory and at every Δt_m timestep a measurement of the distance between the $i'th$ sensor and the target is taken. For notational convenience the $i'th$ sensor measurement obtained in the sampling period $[t_k, t_{k-1})$ is denoted as $z^i_{t^i_k}$.

5.4.1.1 Multilateration Process Summary

Due to the homogenous nature of the considered sensors, the multilateration approach using the LSS is considered in place of the WLS multilateration approach as described in Section 2.1.3.1.5.1. For readability the general formula and matrices are given for the multilateration approach as [199][12]:

$$\hat{\vartheta} = (G^T G)^{-1} G^T \hat{b}. \tag{5.13}$$

In which,

$$\hat{\vartheta} = \begin{bmatrix} x \\ y \\ (x)^2 + (y)^2 \end{bmatrix}, G = \begin{bmatrix} -2x^1 & -2y^1 & 1 \\ -2x^2 & -2y^2 & 1 \\ -2x^3 & -2y^3 & 1 \\ -2x^4 & -2y^4 & 1 \end{bmatrix}, \hat{b} = \begin{bmatrix} \left(z^1_{t^1_k}\right)^2 - (x^1)^2 - (y^1)^2 \\ \left(z^2_{t^2_k}\right)^2 - (x^2)^2 - (y^2)^2 \\ \left(z^3_{t^3_k}\right)^2 - (x^3)^2 - (y^3)^2 \\ \left(z^4_{t^4_k}\right)^2 - (x^4)^2 - (y^4)^2 \end{bmatrix}. \tag{5.14}$$

The batch process for each multilateration estimate at the estimation instant is given by Algorithm 9 below, where k_{max} represents the maximum number of estimation instants carried out.

[12] The notation of the equation taken from the reference has been altered for consistency with the notation throughout this thesis.

Algorithm 9: LSS Multilateration[13]

For $k = (1{:}\, k_{max})$
  Collect set of N range measurements $z_{t_k}^{i}$ from N sensors $i = (1, \dots, N)$
  Input set of N range measurements and known sensor coordinates into (5.14)
  Compute Target coordinates using (5.13), excluding $\hat{\vartheta}(3)$
End

5.4.1.2 UKF Process Summary

In a general sense, the recursive process of the batch UKF solution generally requires the determination of the sigma points and their respective weights to appropriately define the state distribution. A nonlinear process model is then applied to these sigma points to determine a set of transformed sigma points which are further transformed through the nonlinear observation model. The resulting data is assimilated, and an output is formulated. The process is then repeated.

The process considers a single step, estimating across the entire estimation interval ΔT [136].

$$X_{t_k} = f\left(X_{t_{k-1}}, \Delta T\right) + w_{t_k}. \tag{5.15}$$

Where the state is given by $X_{t_k} = [x^0, y^0, v^x, v^y]^T$ and the process model f considered for this implementation is a linear Constant Velocity (CV) 2D model [137]:

$$f\left(X_{t_{k-1}}, \Delta T\right) = \begin{bmatrix} 1 & 0 & \Delta T & 0 \\ 0 & 1 & 0 & \Delta T \\ 0 & 0 & 1 & 0 \\ 0 & 0 & 0 & 1 \end{bmatrix}. \tag{5.16}$$

w_{t_k} is modelled as a zero-mean white Gaussian noise with covariance matrix Q which is a fixed matrix given by the Discrete-Time Nearly Constant Velocity structure, as discussed in Section 2.1.3.2.1.6, for a two dimension system [133], [141]:

$$Q = \begin{bmatrix} \Delta T^4/4 & 0 & \Delta T^3/3 & 0 \\ 0 & \Delta T^4/4 & 0 & \Delta T^3/3 \\ \Delta T^3/3 & 0 & \Delta T^2 & 0 \\ 0 & \Delta T^3/3 & 0 & \Delta T^2 \end{bmatrix} * \sigma_a^2. \tag{5.17}$$

[13] Ranges of values are represented in the following manner: (initial value : incremental value : end value) and may, in some cases, be assigned equivalent to a variable. Where an incremental value is not given, the increments are defaulted to integers of one. When used as part of a '*For'* loop, each value in the given range is applied individually within a single loop.

Where σ_a is the acceleration noise magnitude and must be determined empirically. The $i'th$ sensor measurement is given by [126]:

$$z_{t_k^i}^i = h^i\left(X_{t_k^i}\right) + v_{t_k^i}^i. \tag{5.18}$$

In which the nonlinear measurement function h^i is given by [126]:

$$h^i\left(X_{t_k^i}, S^i\right) = \sqrt{\left(x^i - x_{t_k^i}^0\right)^2 + \left(y^i - y_{t_k^i}^0\right)^2}. \tag{5.19}$$

Where the sensor noise $v_{t_k^i}^i$ in each measurement is modelled as a normally distributed random variable with zero mean and standard deviation σ_z:

$$v_{t_k^i}^i = N(0, \sigma_z). \tag{5.20}$$

For UKF initialisation, where $k = 1$, the initial state X_{t_1} is given by the least square estimates for $x_{t_1}^0$ and $y_{t_1}^0$, calculated using initial measurements acquired in the first sampling period, and velocity components given as 1. The initial state covariance matrix P_{t_1} is given as an identity matrix. The complete description of UKF equations and process can be reviewed in Section 2.1.3.2.1.3 but are summarised as follows for the readers convenience [136].

Prediction

$$\chi_{t_k}^j = f\left(\chi_{t_{k-1}}^j\right), \qquad (j = 0, \cdots, 2n) \tag{2.53}$$

$$\hat{X}_{t_k}^- = \sum_{j=0}^{2\hat{n}} W^{j,m} \chi_{t_k}^j, \tag{2.54}$$

$$P_{t_k}^- = \sum_{j=0}^{2\hat{n}} W^{j,c}\left(\chi_{t_k}^j - \hat{X}_{t_k}^-\right)\left(\chi_{t_k}^j - \hat{X}_{t_k}^-\right)^T + Q_{t_{k-1}}. \tag{2.55}$$

Measurement update

$$\mathrm{Z}_{t_k}^j = h\left(\chi_{t_k}^j\right), \tag{2.56}$$

$$\hat{z}_{t_k} = \sum_{j=0}^{2\hat{n}} W^{j,m} \mathrm{Z}_{t_k}^j, \tag{2.57}$$

$$P_{t_k}^{zz} = \sum_{j=0}^{2\hat{n}} W^{j,c}\left(\mathrm{Z}_{t_k}^{j} - \hat{z}_{t_k}\right)\left(\mathrm{Z}_{t_k}^{j} - \hat{z}_{t_k}\right)^{T} + R, \tag{2.58}$$

$$P_{t_k}^{xz} = \sum_{j=0}^{2\hat{n}} W^{j,c}\left(\chi_{t_k}^{j} - \hat{X}_{t_k}^{-}\right)\left(\mathrm{Z}_{t_k}^{j} - \hat{z}_{t_k}\right)^{T}, \tag{2.59}$$

$$K_{t_k} = P_{t_k}^{xz}(P_{t_k}^{zz})^{-1}, \tag{2.60}$$

$$\hat{X}_{t_k} = \hat{X}_{t_k}^{-} + K_{t_k}\left(z_{t_k} - \hat{z}_{t_k}\right), \tag{2.61}$$

$$P_{t_k} = P_{t_k}^{\gamma} - K_{t_k} P_{t_k}^{zz} K_{t_k}^{T}. \tag{2.62}$$

The scaling parameter λ presented in (2.52) and used in determining of the sigma point distribution is given by [111]:

$$\lambda = \zeta^2(L + \hat{n}) - \hat{n}. \tag{2.52}$$

Where $\hat{n}$ is the dimension of the state matrix, equal to four.

Within this thesis the sequential fusion approach is used where the measurement update is repeated sequentially for each measurement. For each measurement fused, the distribution must be passed through the nonlinear measurement function h^i as a sigma point distribution. In the initial measurement update $(i = 1)$ the sigma point distribution is already provided from the prediction stage (2.53) and can be applied through the measurement function (2.56) directly. While some literature notes that the distribution of sigma points can be re-evaluated prior to the measurement function, this is not the approach taken in this thesis, to avoid additional computation. For the following measurement updates $(i \geq 2)$ the fused distribution is provided as a mean and covariance and as such, a new set of resampled sigma points are required. This set of sigma points are computed using the same calculations given in (2.45) - (2.52) but where $\hat{X}_{t_{k+1}} \rightarrow X_{t_k}$ and $\hat{P}_{t_{k+1}} \rightarrow P_{t_k}$. For clarification, the resampled sigma points are denoted by $\chi_{t_k}^{j}$ and are applied to the nonlinear measurement function as:

$$\mathrm{Z}_{t_k}^{j} = h^i\left(\chi_{t_k}^{j}, S^i\right) \tag{5.21}$$

The batch UKF algorithm is summarised in Algorithm 10.

Algorithm 10: Batch UKF[14]

For $k = (1: k_{max})$
  Collect N range measurements $z^{i}_{t^{i}_{k}}$ from N sensors $i = (1: N)$
  Determine sigma point set using (2.45) - (2.52)
  Propagate sigma points using process model (2.53)
  Calculate transformed predicted mean and covariance using (2.54) and (2.55) respectively
  Initial Measurement Update
  Transform the predicted sigma point distribution using the measurement function h^{i} (2.56)
  Compute the mean, measurement covariance and the cross covariance (2.57) - (2.59)
  Determine the Kalman gain using (2.60)
  Using $z^{1}_{t^{1}_{k}}$ generate the state estimate and covariance matrix with (2.61) and (2.62) respectively
  Subsequent Measurement Updates
  For $i = (2: N)$ measurements
    Resample the sigma points set using (2.45) - (2.52)
    Transform the resampled sigma point distribution using the measurement function h^{i} (5.21)
    Compute the mean, measurement covariance and the cross covariance (2.57) - (2.59)
    Determine the Kalman gain using (2.60)
    Using $z^{i}_{t^{i}_{k}}$ generate the state estimate and covariance matrix from (2.61) & (2.62) respectively
  End
End

5.4.2 Reference Simulation Scenario

Within this section, the simulation parameters are presented for the study on synchronous localisation solutions. For the sake of equal comparison throughout this and subsequent chapters, the following described tracking simulation scenario will be referred to as the 'Reference Simulation Scenario'. The Reference Simulation Scenario is implemented to evaluate the performance of various localisation solutions under variable degrees of asynchronous sampling, measurement noise and target trajectories. The measurement sampling sequence follows the description given in the Sequentially Asynchronous Sampling problem described at the beginning of this chapter. This states that the IML is constant, and estimation is carried out on the reception of the last sensor measurement. Additionally, transmission times are assumed negligible and the reception of data is not corrupted by potential errors.

[14] Ranges of values are represented in the following manner: (initial value : incremental value : end value) and may, in some cases, be assigned equivalent to a variable. Where an incremental value is not given, the increments are defaulted to integers of one. When used as part of a '*For'* loop, each value in the given range is applied individually within a single loop.

The Reference Simulation Scenarios describe a range of IML values, from 1 ms to 100 ms, and measurement noise with a normal distribution and standard deviation σ_z, ranging from 1 mm to 1 m. Both ranges are implemented with a logarithmic scale where 15 and 10 points are evaluated for the IML range and measurement noise respectively.

5.4.2.1 Physical Layout

The scenario considers a 2D space, where four sensors ($N = 4$) are distributed in an equilateral square configuration. The length of the sides in this square are referred to as the Baseline Distance (BD). Therefore, the x and y coordinates of each sensor are denoted by $S^i = \left[x^i, y^i\right]^T$ such that S^1 to S^4 is given by $[0,0]^T$, $[BD, 0]^T$, $[0, BD]^T$ and $[BD, BD]^T$ respectively.

5.4.2.2 Target Trajectory

The variable trajectory considered throughout the Reference Simulation Scenario is equivalent to the circular path trajectories applied in Section 4.5.2, but on a larger scale. In this scenario, the centre point of the circle is designated at $\left[\frac{BD}{2}, \frac{BD}{2}\right]^T$ and the BD = 10 m. The path angles evaluated range between 0.2 rad and 1 rad, where applying (4.10) the equivalent range of circular path radii is 5 m and 1 m respectively. The target also maintains a constant angular velocity equivalent to 1 m/s along the path circumference. An example of the target trajectories for various θ_{path} values at a $BD = 10$ m is given in Figure 5.8.

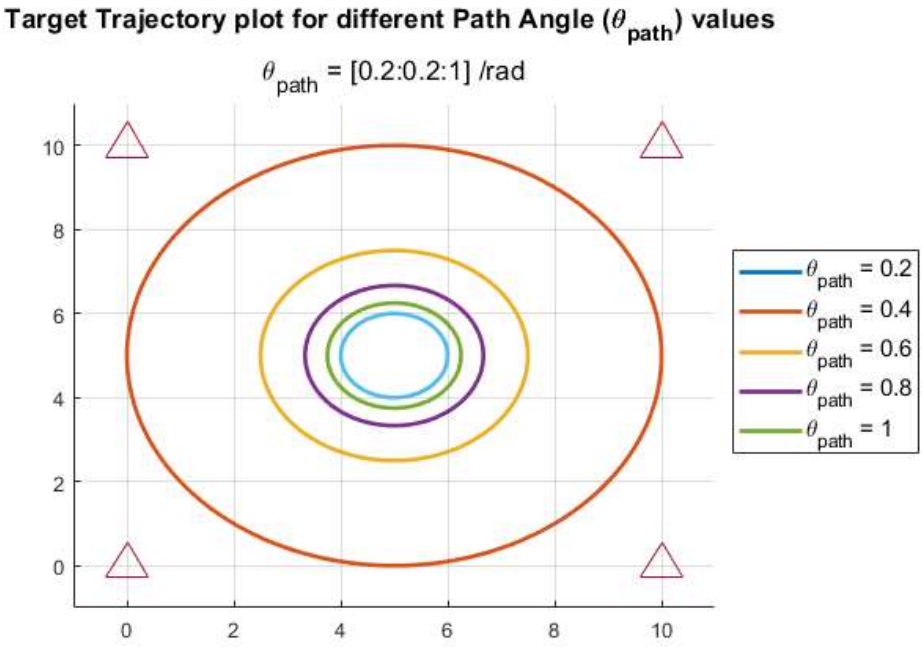

Figure 5.8 - Various target trajectories ranging from 0.2 rad to 1 rad.

As with the similar structured simulations conducted in Section 4.5.2, the circumference of the path changes for each path angle. To obtain equivalent evaluations of the tracking response at different path angles, it is imperative that the number of points evaluated is consistent. The number of position estimations considered is given by (4.11). With a maximum radius of 5 m, minimum IML of 1 ms and 4 sensors, the target is evaluated at 7854 individual points around the given path. To maintain this across all possible path angles and values of IML, the target is set to continue travelling along its circular trajectory until 7854 positions have been evaluated. Once the target travels the full length of the path circumference, the target is deemed to have completed a single '*cycle*'.

5.4.2.3 Performance Metrics

The following performance metrics are obtained throughout the simulation. Both Position Error (PE) and Mean Point Error (MPE) are equivalent to those presented in Section 4.5.3, but are repeated for the readers clarity.

The PE for each position estimate, is taken to be the Euclidian distance between the estimated location $\hat{S}_{t_k}^0$, and the true targets position $S_{t_k}^0$ at t_k:

$$\varepsilon_{t_k}^{PE} = \left\| S_{t_k}^0 - \hat{S}_{t_k}^0 \right\|. \tag{5.22}$$

Once all 7854 estimations have been provided this concludes a single simulation iteration, denoted with subscript It. The simulation is repeated $N_{Iterations}$ times for each variable combination of IML, measurement noise and θ_{path}. Once position errors have been obtained for all iterations the average error for each estimation interval is calculated as the Mean Point Error (MPE):

$$\hat{\varepsilon}_{t_k}^{MPE} = \frac{1}{N_{Iterations}} \sum_{It=1}^{N_{Iterations}} \varepsilon_{t_k,It}^{PE}. \tag{5.23}$$

The Root Mean Square Error (RMSE) is then used to determine the overall error across all estimations and iterations:

$$RMSE = \sqrt{\frac{1}{7854} \sum_{k=1}^{k=7854} \hat{\varepsilon}_{t_k}^{MPE}}. \tag{5.24}$$

The Estimation Runtime (ER) describes the average time it takes the processor to complete a single estimation. This is used to provide insight into the computational complexity of a solution. The simulation runtime is calculated using the inbuilt 'tic/toc' function in MATLAB software which, as documented [259], is unreliable for times less than 10 ms. The individual localisation techniques are therefore looped N_L times over and the total recorded runtime $\left(\Delta T_{N_L}\right)$ is averaged to obtain the individual Estimation Runtime:

$$ER = \frac{1}{N_{Iterations}} \sum_{It=1}^{N_{Iterations}} \left(\frac{\Delta T_{N_L}}{7854 * N_L}\right). \tag{5.25}$$

5.4.2.4 Simulation Algorithm Overview

To evaluate the performance of Multilateration and UKF under variable changes, a variable loop is considered which iterates through a range of values, for the selected variable. Furthermore, an iteration loop is introduced to repeat each simulation for $N_{Iterations}$ iterations, to deliver a more reliable averaged result. Simulations are conducted using a MATLAB script on a DELL G7 7790 Intel(R) Core(TM) i7-9750H CPU @ 2.60GHz, 6 Cores, 12 Logical Processors.

The UKF sigma point scaling parameters using in determining the sigma point values and weightings as well as the simulation parameters are given in Table 5.1.

Table 5.1 - Simulated UKF parameter values

Parameter	Value
$\boldsymbol{\zeta}$	1e-3
$\boldsymbol{L}$	0
$\boldsymbol{\beta}$	2
IML Δt_m (s)	[1e-3,1e-1]
Measurement Noise σ_z (m)	[1e-3, 1e0]
Path Angle θ_{path} (rad)	[0.2:0.2:1]

The executed simulation is summarised in Algorithm 11 below. Due to the repeated use of this Simulation format for evaluating various solutions, Algorithm 11 is generalised and the considered solution algorithms, such as LSS Multilateration and UKF, are applied within line 8 of Algorithm 11. This is identified throughout the thesis as '*Algorithm X is evaluated under the Reference Simulation given in Algorithm 11*' where '*X*' *per*tains to the localisation solution being tested. Therefore within this section, both Algorithm **9** *and* Algorithm **10** are evaluated under the Reference Simulation given in Algorithm 11.

Algorithm 11: Reference Simulation[15]

```
For Δt_m = logspace(1e-3:15:1e-1)
    For σ_z = logspace(1e-3: 6: 1e1)
        For θ_path = (0.2: 0.2: 1)
            For It = (1: N_Iterations)
                Generate set of target measurement positions
                Generate sequence of noisy measurements for each target measurement position using
                additive noise v^i_{t_k^i}
                For loop = (1:N_L)
                    Insert respective Algorithm to be evaluated
                    Calculate respective estimation errors (5.22) across all estimation instants
                End
            End
            Calculate Mean point Error for No. of Iterations (5.23)
            Determine RMSE values for No. of Iterations (5.24)
            Determine Estimation Runtime (5.25)
        End
    End
End
```

As reviewed in Section 2.1.3.2.1.6, the process noise within a Kalman Filter (KF), such as the UKF being applied, must be tuned to suit the system. The following section considers the optimal KF process noise where the acceleration noise magnitude σ_a is the scaling quantity that must be determined to optimise the performance of the UKF.

5.4.2.5 Kalman Filter System Identification - Determining the Acceleration Component of the UKF Process Noise

The process noise of a KF is a critical tuning value and leads to drastic changes in performance. For this study the Discreet Nearly Constant Velocity (DNCV) process noise model as referred to in Section 2.1.3.2.1.6, is most suitable. However, the process noise acceleration component σ_a must be determined empirically within a system, prior to operation [133].

[15] Ranges of values are represented in the following manner: (initial value : incremental value : end value) and may, in some cases, be assigned equivalent to a variable. Where an incremental value is not given, the increments are defaulted to integers of one. When used as part of a '*For'* loop, each value in the given range is applied individually within a single loop. If a range of values are incremented logarithmically the following representation is used: *logspace*(initial value: number of equally logarithmically spaced elements: end value).

A reasonable assumption can be made that, in practice, the KF designer is able to obtain a measure of the measurement noise σ_z^2 variance by recording several measurements in an offline calibration phase. Furthermore, while the localisation processes within this scenario make no attempt to resolve the effects of IML, the system designer is likely to be aware of the IML and its magnitude. As such, the optimal process noise can be configured to obtain a best response for a specifically known IML and measurement noise combination. Alternatively, the targets path nonlinearity may be variable throughout a typical dynamic scenario and as such the optimal process noise cannot be determined for specific path angle values. Optimising for a specific path angle value may lead to overfitting, where the system responds optimally to the individual path angle value and worse to others. Therefore, the process noise acceleration component must be selected to perform admirably over a broad range of path angles. We denote the process noise acceleration component value that is specific to a given scenarios' IML and Measurement noise as $\sigma_a(\Delta t_m, \sigma_z)$.

A simple and decisive manner to determine the correct process noise value for KFs does not yet exist [132] and the optimisation process is therefore conducted by a brute force trial and error process.

5.4.2.5.1 Trial and Error Process

Throughout this thesis, the methodology adopted to determine the optimal process noise acceleration component for any KF is trial-and-error simulations. This entails a set of simulations, where the acceleration noise magnitude is iterated, tried and tested for each combination of sensor measurement noise and IML value. From this data, the optimal process noise acceleration component value is chosen to give the lowest overall RMSE for a variety of path angles.

The trial-and-error process, described below in Algorithm 12, considers iterating Algorithm 11 one hundred times for a suitable range of σ_a values. However, only the two extreme path angles $(\theta_{path} = 0.2 \,\&\, 1)$ are considered. The range of σ_a values chosen are described by q_a^{min}, q_a^{max} and $q_a^{spacing}$ which denotes the lower bound, the upper bound and the interval spacing respectively. In general, the bounds are set to different orders of magnitude and the spacing is logarithmically set to 10 intervals per order of magnitude difference between the upper and lower bounds. The bounds are selected through an initial test to reduce the number of computations carried out. The RMSE of the solution under every value of σ_a is attained and forms an array of σ_a specific RMSE values $RMSE(\Delta t_m, \sigma_z, \theta_{path}, \sigma_a)$. Both the minimum and maximum path angles are evaluated in Algorithm 12, and the two arrays produced are averaged together. The σ_a value that produces the minimum RMSE of the averaged response is selected. In this way, the RMSE results obtained can be used to

identify the optimal σ_a value for each combination of IML and measurement noise at a high and low path nonlinearity.

Algorithm 12: Optimal Acceleration Noise Component [16]

1: *For* Δt_m = *logspace(1e-3: 15: 1e-1)*
2: *For* σ_z = *logspace(1e-3: 6: 1e)*
3: *For* $\theta_{path} = (0.2: 0.2: 1)$
4: *For* $\sigma_a = logspace(q_a^{min} : q_a^{spacing} : q_a^{max})$
5: *For* It = *(1:* $N_{Iterations}$*)*
6: Generate set of target measurement positions
7: Generate sequence of noisy measurements for each target measurement position using additive noise $v_{t_k}^{i}{}_{i}$
8: *Insert respective Algorithm to be evaluated*
9: Calculate respective estimation errors (5.22) across all estimation instants
12: *End*
13: Calculate Mean point Error for $N_{Iterations}$(5.23)
14: Determine RMSE values for $N_{Iterations}$(5.24)
15: *End*
16: Store array of $RMSE(\Delta t_m, \sigma_z, \theta_{path}, \sigma_a)$
17: *End*
18: Average $RMSE(\Delta t_m, \sigma_z, 0.2, \sigma_a)$ & $RMSE(\Delta t_m, \sigma_z, 1, \sigma_a)$
19: Linearly interpolate, attain minimum RMSE and corresponding σ_a value
20: *End*
21: *End*

The resultant $\sigma_a(\Delta t_m, \sigma_z)$ values are stored in a database such that the optimal value can be appointed for each IML and measurement noise scenario. As for the Reference Simulation Scenario, the system identification process is the same for all applied KFs throughout this body of work. In this respect Algorithm 12 is generalised with the inclusion of line 8, where the respective KF-based solution is applied.

[16] Ranges of values are represented in the following manner: (initial value : incremental value : end value) and may, in some cases, be assigned equivalent to a variable. Where an incremental value is not given, the increments are defaulted to integers of one. When used as part of a '*For'* loop, each value in the given range is applied individually within a single loop. If a range of values are incremented logarithmically the following representation is used: *logspace*(initial value: number of equally logarithmically spaced elements: end value).

Figure 5.9 below, illustrates the selection of optimal $\sigma_a(\Delta t_m, \sigma_z)$ for all IML, sensor measurement noise scenarios.

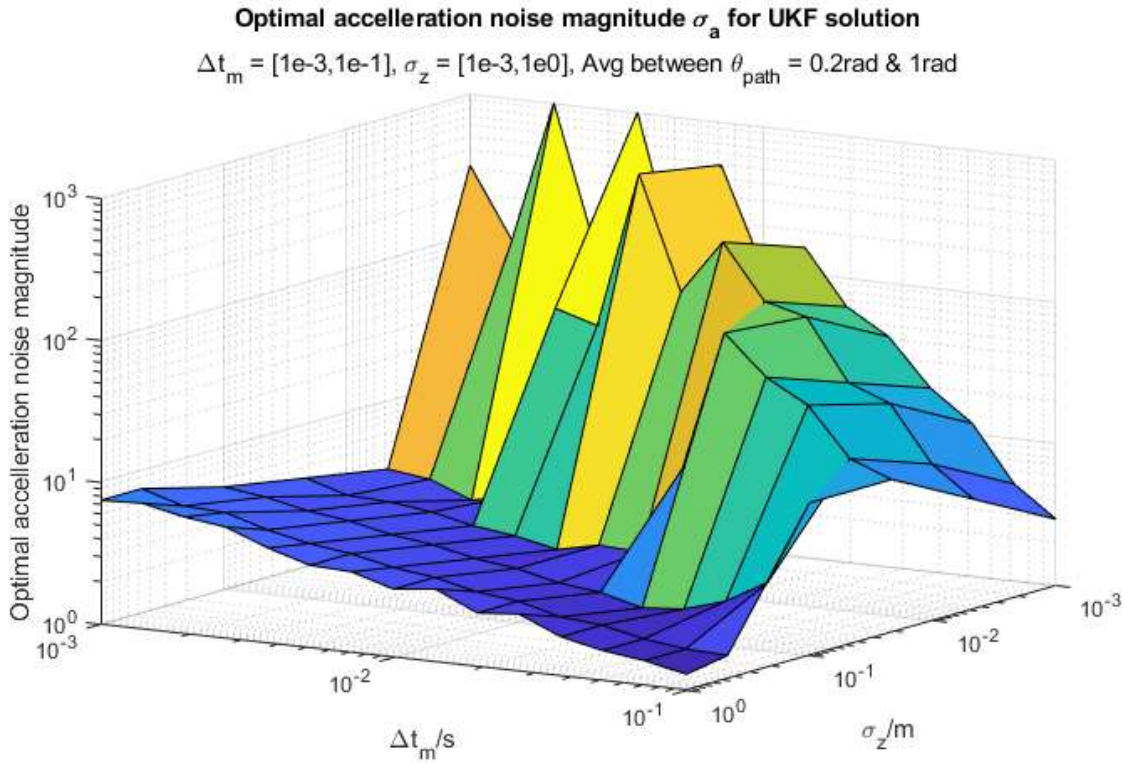

Figure 5.9 - 3D plot of optimal q values for UKF with IML

In analysing the σ_a obtained within Figure 5.9, above, the following observations can be made about the process noise study. It is important to note that the axis scales within Figure 5.9 are inverted for clarity in the image.

The process noise of a system can be considered a measure of the process model's uncertainty; therefore, a greater optimal $\sigma_a(\Delta t_m, \sigma_z)$ value suggests the system performs best, because the measurements are favourable against the predictions formed by the system model. One can also use the optimal acceleration noise magnitudes to infer the response of the UKF when subjected to an asynchronous dataset.

Where measurement noise is high within the study, It is shown to be the more prominent constituent, compared to IML, with regard to their cumulative effects on error and therefore the effects of IML are consequently less prominent. Here, the plot in Figure 5.9 indicates a consistent trend in optimal acceleration noise, where a greater level of measurement noise leads to a slightly higher σ_a value, avoiding potential divergence and overconfidence in the process model.

Conversely, for these higher sensor measurement noises, as the IML increases, the process noise visibly decreases, effectively suggesting that weighting the process estimates more heavily

improves the response. This effect reflects the fact that the state estimate covariance matrix P is influenced by both the state transition matrix A and the process noise covariance matrix Q, as per (5.17). Both A and Q are time dependant, in that they contain the variable ΔT. From the structure of the IML sampling, ΔT is related to the IML from (5.4). What one can obtain from this is that where the IML is greater, the estimation period is also greater, and the weighting in the process model is lower. Therefore, the reduction in σ_a can be expected to compensate for the lower process weighting to avoid complete reliance on the measurements alone.

As shown in Figure 5.9, for most considered values of measurement noise, once the IML is increased above a certain threshold, there is a significant increase in the optimal σ_a value. In this instance the UKF solution performs best when weighting the measurements more heavily. It should be noted that this sharp increase is also the region at which the $RMSE\left(\Delta t_m, \sigma_z, \frac{0.2+1}{2}, \sigma_a\right)$ plateaus and the optimal value can be given by a range of values, hence the sharp fluctuations at the lower region of both IML and measurement noise scales. The amount of IML at which this significant rise in optimal σ_a value appears is correlated with the level of measurement noise and reduces in intensity as the measurement noise increases. This reinforces the idea that the influence of the IML is dampened as Measurement noise is increased.

From the optimal process noise plot and the surge in values, it can be observed that the UKF solution is not designed for handling of the IML effects and suffers irregularities in attempts to compensate. This is made clearer in later comparisons.

5.4.3 Simulation Study of Non-Asynchronous Tracking Solutions Under Variable IML Effects and Various Scenarios

Within this section, the simulation results of the UKF and LSS techniques under variable IML and measurement noise are presented and discussed. The previously described optimal σ_a values are included.

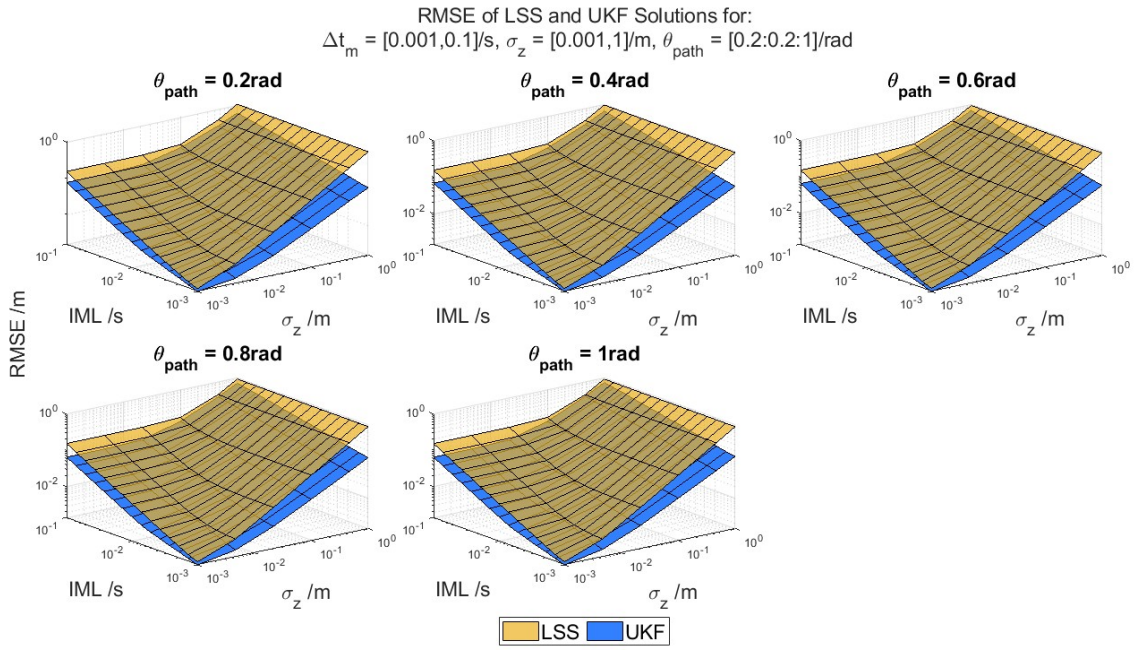

Figure 5.10 - RMSE for LSS and UKF under variable scenario parameters

From Figure 5.10, which displays the RMSE for LSS and UKF under variable scenario parameters, the following initial observations can be made about the RMSE.

Firstly, the UKF technique benefits from its predictive qualities, as it is more successful in reducing the error than the LSS technique. This is evident from the consistently lower RMSE displayed for all considered scenarios. However, for low measurement noise values, both solutions suffer very linear increases in error as IML increases. Similarly, for low IML values, the solutions again experience very linear increases in error as Measurement noise increases

On the other end of the scale, at higher IML values, the effects of Measurement noise become much smaller and are in fact almost negligible. Comparatively, the LSS RMSE remains constant under increasing measurement noise for much longer, which suggests that the MN has less effect on the LSS at higher IML values. Therefore, while the UKF response is generally better than the LSS response, the disparity between the two distinctly reduces as the IML increases.

The same observation can be made for high measurement noises, where the effects of IML are somewhat less prominent than at lower measurement noise values. This is more applicable to the LSS solution, which appears to suffer more from measurement noise. As both sources of error increase the difference between the UKF RMSE and LSS RMSE is greatly reduced indicating that while the UKF exhibits a significantly improved response it does not perform best under both sources of error combined.

The following analysis considers the influence of path angles as presented in Figure 48, for measurement noise standard deviations of 1 mm, 10 cm and 1 m.

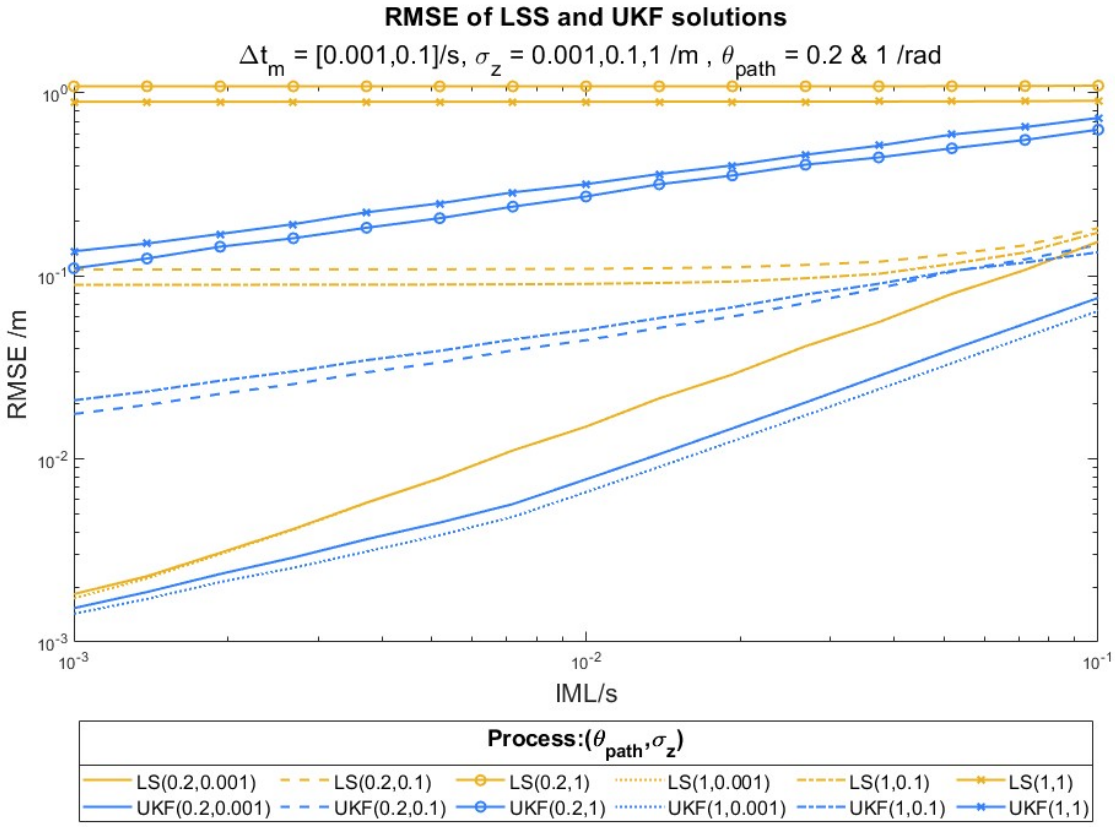

Figure 5.11 - RMSE of position estimation using UKF and LSS for different path trajectories and measurement noises under variable IML

For the LSS, under low measurement noise the path angles are shown to have almost no effect on the resultant RMSE. However, as the Measurement noise increases, increase in path angle is shown to consistently produce a lower RMSE. This is most likely due to the points not being as widely dispersed as they would be within a more linear trajectory.

For the UKF, under low measurement noise values the system responds positively to a higher path angle, however, for higher measurement noise values this effect is reversed. Interestingly, this change in path angle effect for higher measurement noise values is delayed with increasing IML values. This change in response to path nonlinearity can be attributed to the KFs response to a higher measurement noise. This response necessitates more reliance on the CV process model which is known to be less accurate at higher path angles.

Relevant tabulated data for the UKF and LSS is provided in Appendix B of this thesis.

5.4.3.1 Additional Testing

Following the initial observations above, the subsequent simulations were conducted in order to highlight the effects of both sensor sequencing, which relates to sensor positions, and the potential bias of estimation frequency within KF-based solutions.

5.4.3.1.1 Errors due to Sequencing and RRLH Positioning

Multisensor systems used for target tracking require consideration of the sequence of the sensor sampling and the respective sensor position. From the IML single sensor study conducted in Section 5.3.1, the effects of IML are shown to be reduced at greater distances for certain trajectories. It is also known that respective sensor positioning can have great influence on the performance of a system [17], [99], [160], [261], [262]. The same model parameters applied in the aforementioned study were applied to the following simulations, where sensors maintain a standard equilateral square arrangement, but variability is introduced within the sampling sequence.

Figure 5.12 illustrates four considered sensor sampling sequences for a four-sensor system. Both Sequence 1 and 2 follow a zig-zag pattern whereas 3 and 4 are clockwise and counter-clockwise sequences.

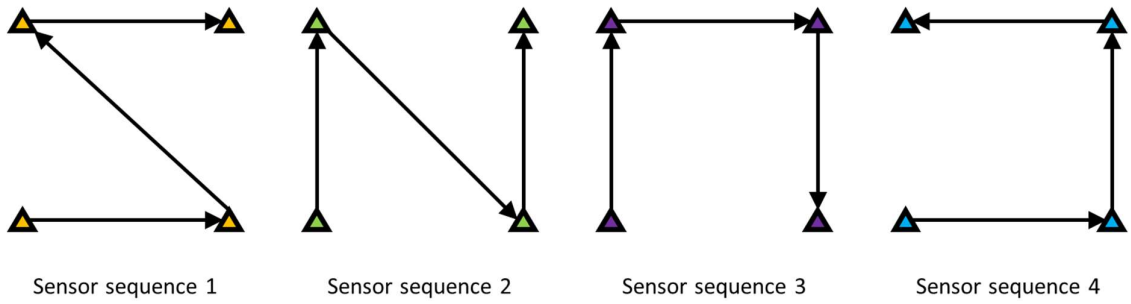

Figure 5.12 - Sampling sequence variations for N = 4

The first sensor within each sequence would generally be expected to obtain a greater level of IML error as due to the sampling sequence, it has a greater overall MLa, however, understanding the effects of target trajectories relative to the sensor position, this cannot be assumed to be true for all cases. To evaluate the change that the sampling sequence has on the resulting estimation, the highest IML value (0.1 s) and a path angle of 0.4 rad is evaluated at various measurement noise values. The results are provided in Figure 5.13 where the MPEs for a 1000 iterations are plotted for a single cycle around the circular trajectory.

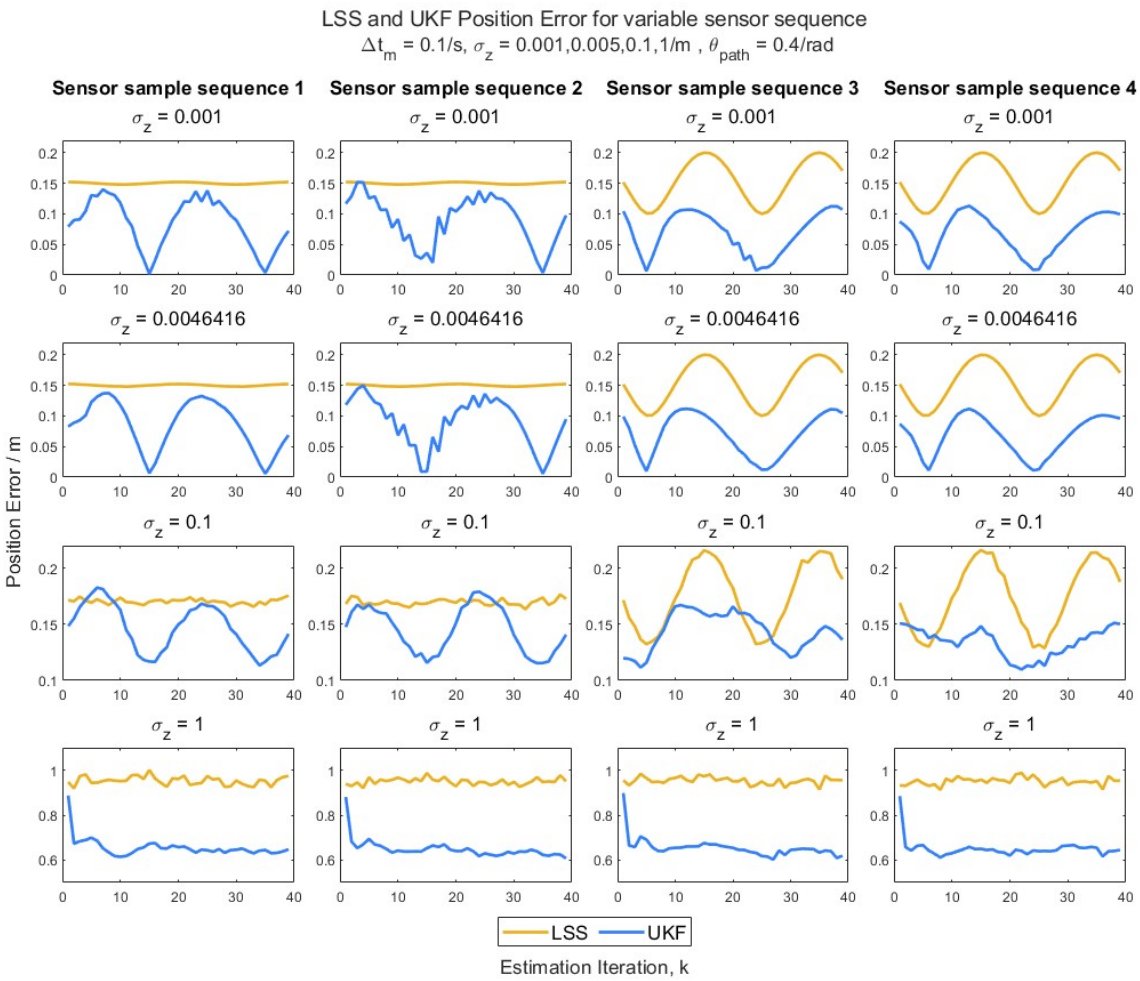

Figure 5.13 - Mean errors for LSS and UKF tracking for different sensor sampling sequences.

One observation that can be made from Figure 5.13, above, is that across most plots the UKF error is shown to exhibit a cyclic error pattern. This is because the KF does not reach a steady state as the Constant Velocity trajectory model applied is not describing the true target motion. The LSS also exhibits a sinusoidal pattern, which is amplified for sensor sequences 3 and 4.

A more pertinent observation from Figure 5.13, is that when comparing Sensor Sequence 1 and 2, it appears as though the sensor sequence effects the stability of the UKF estimation process. This is distinctly indicated by the increased fluctuation in MPE. For Sensor Sequence 3 and 4, the increase in measurement noise results in a large deviation of the somewhat cyclic error pattern. From this brief study, insight is given into the variability of the sampling sequence between four sensors and attention is drawn to the effects this may have on the system response. While variations in sensor sequence exhibit consistent RMSE, due to the stability of the response, sensor sequence 1 was employed throughout the remainder of the studies within this thesis.

5.4.3.1.2 Sampling Time Errors

The Asynchronous sampling scenario assessed within this thesis considers a sampling structure in which the estimation latency ΔT is dictated by the number of sensors and the IML equation (5.4). Naturally, due to the variability of a target's trajectory over time, tracking solutions such as the UKF which rely on predictive models, suffer under increased estimation periods. With this in consideration, it is reasonable to suggest that the errors observed by the increased IML scenarios are primarily a matter of larger estimation intervals. To evaluate this, one can consider the equivalent estimation interval but with no IML and as a result, no temporal or spatial misalignment between measurements. By comparing errors resulting from synchronous measurements of equivalent estimation periods to those of delayed measurements, considered within this thesis, it is possible to assess the contributions of error from the estimation periods and the latency components individually.

To do so, the Reference Simulation Scenario is considered for the UKF solution and the average MPE over 1000 iterations for a single path cycle. The results are displayed in Figure 5.14. To isolate the effects of IML more effectively, the minimum value of measurement noise ($\sigma_z = 1$ mm) is applied to a path angle of 0.4 rad for three different values of Estimation Period ΔT. The three values of ΔT applied are consistent with a $N = 4$ sensor system and IML values of 1e-3 s, 7.2e-3 s, 1e-1 s. From Figure 5.14, the evidence clearly indicates the majority of error arises from the asynchronous measurements and the IML error component.

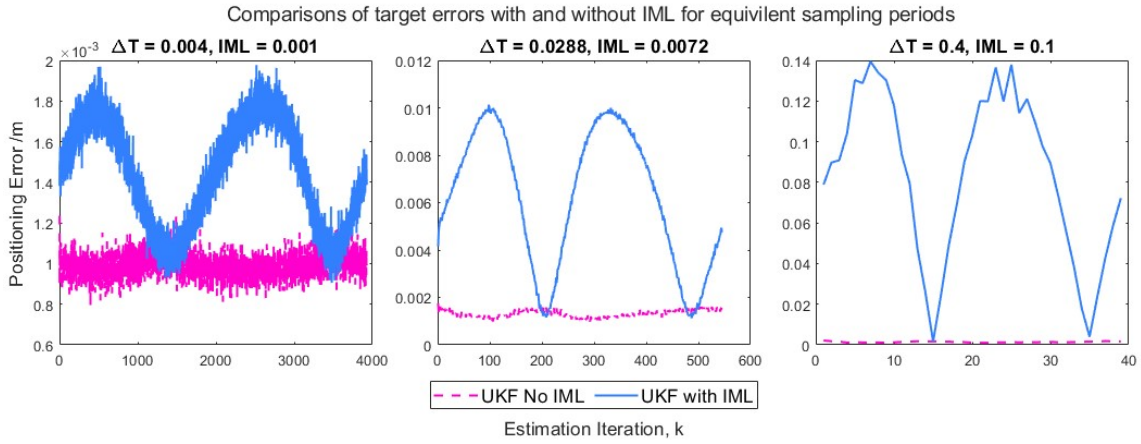

Figure 5.14 - Comparison of UKF estimation errors for variable IML vs No IML for equivalent sampling periods

The optimal acceleration noise magnitude values for the asynchronous sampled measurements, as obtained in Section 5.4.2.5, are applied to the UKF solution under both asynchronous and non-asynchronous measurements. While these are not the optimal σ_a values for the non-asynchronous

case, one can only expect the response to improve under correct tuning which further reinforces the argument that the majority of errors are inflicted by the asynchronous sampling.

5.4.4 Evaluating Existing Asynchronous Localisation Techniques

This section has so far considered the effects of IML errors on single sensor range estimates and used this analysis to draw observations for conventional multisensor tracking systems where asynchronous sampling is applied. The following section presents recent solutions to the asynchronous sampling problem for nonlinear measurements and assesses them against non-asynchronous sampling techniques.

5.4.4.1 Shi's Solution

From the literature review the author, of this thesis, notes the solution presented by Shi *et al.* [44], where the scenario considers sequential sampling and therefore in line with the one studied throughout this thesis. The presented solution considers the time between individual samples to be constructive data, that can be utilised under a CV target trajectory assumption to infer the target velocity. However, the simulated study presented by Shi *et al.* is limited to an idealised constant velocity target trajectory.

To evaluate the solution further, this section first puts forward a reduced form of the solution presented in Shi *et al.* that does not consider clock offsets and anchor node positioning error. The simplified solution is then evaluated under various system parameters against the SUKF, LSS and UKF techniques, that both do and do not consider the effects of IML. Finally, a modified solution based on the principles of the approach presented by Shi *et al.* is proposed and evaluated. The following describes the reduced and general form of the batch solution presented by Shi *et al.*

Consider the estimation interval $[t_k, t_{k-1}]$ where the target state vector to be estimated at the end of the sequential sequence (t_k) is given by $X_{t_k} = \left[\left(S^0_{t_{k-1}}\right)^T, \left(V_{t_k}\right)^T\right]^T$, where $S^0_{t_{k-1}} = \left[x^0_{t_{k-1}}, y^0_{t_{k-1}}\right]^T$ describes the target's position at the start of the sampling period and the target's velocity is given by $V_{t_k} = \left[v^x_{t_k}, v^y_{t_k}\right]^T$. The target is observed by N individual sensors which are set to obtain range measurements in sequence such $t_{k-1} < t^i_k < \cdots < t^i_k < \cdots < t_k$. The range measurement from sensor i is given by [44]:

$$\hat{d}^i_{t^i_k} = d^i_{t^i_k} + n^i_{t^i_k}, \tag{5.26}$$

$$d_{t_k^i}^i = \left\| S_{t_{k-1}}^0 + V_{t_k} \Delta t_s - S^i \right\|. \tag{5.27}$$

Where $n_{t_k^i}^i$ is the independent measurement noise, S^i is the $i'th$ sensors position and Δt_s is the time difference between the $i'th$ sensor measurement and the start of the estimation interval $\Delta t_s = t_k^i - t_{k-1}$. Within the constant IML scenario explored within this thesis the interval Δt_s can also be expressed as an integer multiple of the IML:

$$\Delta t_s = i * \Delta t_m. \tag{5.28}$$

The retrieved range measurements are collected into $\tilde{d}_{t_k} = \left[\hat{d}_{t_k}^1, \hat{d}_{t_k}^2, \cdots \hat{d}_{t_k}^N\right]^T$ which gives the following [44]:

$$\tilde{d}_{t_k} = \bar{d}_{t_k} + \bar{n}_{t_k}. \tag{5.29}$$

Where $\bar{d}_{t_k}$ represents the vector of true sensor-to-target distances and $\bar{n}_{t_k}$ is a zero mean Gaussian random vector with a diagonal covariance matrix C_d.

The process and relationships are illustrated below in Figure 5.15:

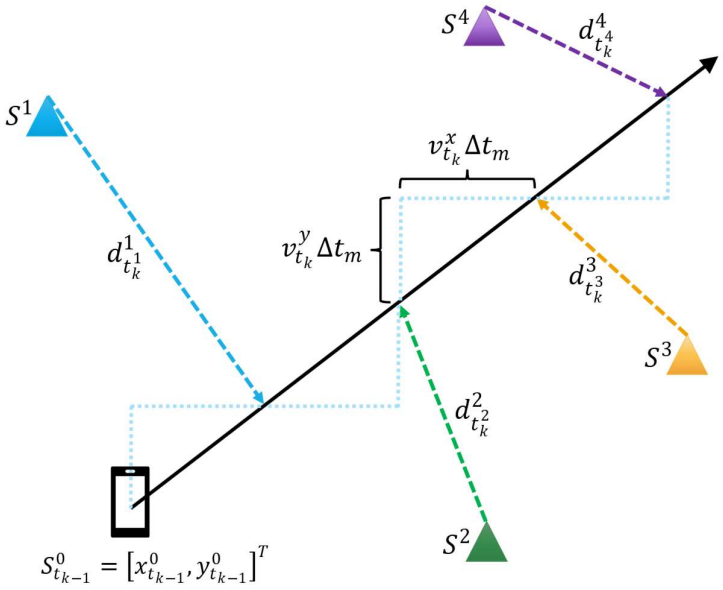

Figure 5.15 - Illustration of sequential sampling structure for four sensors and a target with a constant velocity trajectory

The following describes the formulation of the reduced Shi solution presented and carried out in [44]: Re-arranging (5.26) and squaring both sides gives [44]:

$$\left(\hat{d}_{t_k^i}^i - n_{t_k^i}^i\right)^2 = \left\|S_{t_{k-1}}^0 + V_{t_k}\Delta t_s - S^i\right\|^2. \tag{5.30}$$

Taking $\left\|S_{t_{k-1}}^0 + V_{t_k}\Delta t_s - S^i\right\|^2 = \left(S_{t_{k-1}}^0 + V_{t_k}\Delta t_s - S^i\right)^T\left(S_{t_{k-1}}^0 + V_{t_k}\Delta t_s - S^i\right)$ as in Wang *et al.* [263] and Shi *et al.* [44].

$$\begin{aligned}\left(\hat{d}_{t_k^i}^i\right)^2 - 2\hat{d}_{t_k^i}^i n_{t_k^i}^i + \left(n_{t_k^i}^i\right)^2 \\ = \left\|S_{t_{k-1}}^0\right\|^2 + 2\left(S_{t_{k-1}}^0\right)^T V_{t_k}\Delta t_s - 2\left(S_{t_{k-1}}^0\right)^T S^0 + \Delta t_s^2\left\|V_{t_k}\right\|^2 \\ - 2\left(S^i\right)^T V_{t_k}\Delta t_s + \left\|S^i\right\|^2.\end{aligned} \tag{5.31}$$

Re-arranging (5.31) to give:

$$\begin{aligned}2\left(S^i\right)^T S_{t_{k-1}}^0 + 2\left(S^i\right)^T V_{t_k}\Delta t_s - \left\|S_{t_{k-1}}^0\right\|^2 - \Delta t_s^2\left\|V_{t_k}\right\|^2 - 2\left(S_{t_{k-1}}^0\right)^T V_{t_k}\Delta t_s \\ = \left\|S^i\right\|^2 - \left(\hat{d}_{t_k^i}^i\right)^2 - 2\hat{d}_{t_k^i}^i n_{t_k^i}^i + \left(n_{t_k^i}^i\right)^2.\end{aligned} \tag{5.32}$$

Under the small noise assumption, the second order error term is ignored. The reparametrized vector is given by $\theta_{t_k}^{shi} = \left[X_{t_k}^T, \hat{\theta}_{t_k}^1, \hat{\theta}_{t_k}^2, \hat{\theta}_{t_k}^3\right]^T \in \mathbb{R}^7$, where $\hat{\theta}_{t_k}^1 = -\left\|S^i\right\|^2, \hat{\theta}_{t_k}^2 = -\left\|V_{t_k}\right\|^2$ and $\hat{\theta}_{t_k}^3 = -\left(S_{t_{k-1}}^0\right)^T V_{t_k}$. (5.32) is then given in matrix form as [44]:

$$A_{t_k}^{shi}\theta_{t_k}^{shi} = b_{t_k}^{shi} + \varepsilon_{t_k}^{shi}. \tag{5.33}$$

Where $A_{t_k}^{shi} = \left[\left(a_{t_k}^1\right)^T, \left(a_{t_k}^2\right)^T, \cdots, \left(a_{t_k}^N\right)^T\right]^T$, $b_{t_k}^{shi} = \left[b_{t_k}^1, b_{t_k}^2, \cdots, b_{t_k}^N\right]^T$ and $\varepsilon_{t_k}^{shi} = D_{t_k}\bar{n}_{t_k}$ with the following matrices:

$$\begin{aligned}a_{t_k}^i &= \left[2\left(S^i\right)^T, 2(S^i)^T\Delta t_s, 1, \Delta t_s^2, 2\Delta t_s\right], \\ b_{t_k}^i &= \left[\left\|S^i\right\|^2 - \left(\hat{d}_{t_k}^i\right)^2\right], \\ D_{t_k} &= 2 * diag\left(\left[\hat{d}_{t_k}^1, \hat{d}_{t_k}^2, \cdots, \hat{d}_{t_k}^N\right]\right).\end{aligned} \tag{5.34}$$

The covariance matrix of the error vector $\varepsilon_{t_k}^{shi}$ is then given as [44]:

$$C_{t_k}^{\varepsilon} = D_{t_k}C_d D_{t_k}^T. \tag{5.35}$$

The final WLS solution for (5.33) and its covariance matrix is finally given by (5.36) and (5.37) respectively [44]:

$$\hat{\theta}_{t_k}^{shi} = \left(\left(A_{t_k}^{shi}\right)^T {C_{t_k}^{\varepsilon}}^{-1} A_{t_k}^{shi}\right)^{-1} \left(A_{t_k}^{shi}\right)^T {C_{t_k}^{\varepsilon}}^{-1} b_{t_k}^{shi}, \tag{5.36}$$

$$C_{t_k}^{\hat{\theta}} = \left(\left(A_{t_k}^{shi}\right)^T {C_{t_k}^{\varepsilon}}^{-1} A_{t_k}^{shi}\right)^{-1}. \tag{5.37}$$

During the first stage, the relationship between X_{t_k} and the nuisance variables $(\hat{\theta}_{t_k}^1, \hat{\theta}_{t_k}^2, \hat{\theta}_{t_k}^3)$ is ignored. During the second stage, this relationship is exploited in order to refine the estimates of X_{t_k}. While Shi *et al.* propose a Gauss Newton iterative solution with a stopping criteria function, considering the covariance of the positioning errors they present, the approach taken in this thesis is a single second stage iteration. This more closely reflects the Two Step Weighted Least Squares (TSWLS) work from Wang *et al.* [263] which much of Shi *et al.*'s work can be derived from. The derivation of the second stage can be considered through the explanation therein.

Taking the initial estimate of X_{t_k} produced within the first stage result of $\hat{\theta}_k^{shi}$ to be $\hat{X}_{t_k}$, the error ΔX_{t_k} increment is given and estimated as $\widehat{\Delta X}_{t_k}$ in (5.38) and (5.39) respectively [44]:

$$\Delta X_{t_k} = X_{t_k} - \hat{X}_{t_k}, \tag{5.38}$$

$$\widehat{\Delta X}_{t_k} = \left(J_{t_k}^T \left(C_{t_k}^{\hat{\theta}}\right)^{-1} J_{t_k}\right)^{-1} J_{t_k}^T \left(C_{t_k}^{\hat{\theta}}\right)^{-1} \tilde{r}_{t_k}. \tag{5.39}$$

Where the respective matrices are given by [44]:

$$\tilde{r}_{t_k} = \hat{\theta}_{t_k}^{shi} - \left[\hat{X}_{t_k}^T, -\left\|\hat{S}^i\right\|^2, -\left\|\hat{V}_{t_k}\right\|^2, -\left(\hat{S}_{t_{k-1}}^0\right)^T \hat{V}_{t_k}\right]^T, \quad J_{t_k} = \begin{bmatrix} I_{4*4} \\ \hat{J}_{t_k} \end{bmatrix},$$

and

$$\hat{J}_{t_k} = \begin{bmatrix} -2\hat{x}_{t_{k-1}}^0 & -2\hat{y}_{t_{k-1}}^0 & 0 & 0 \\ 0 & 0 & -2\hat{v}_{t_k}^x & -2\hat{v}_{t_k}^y \\ -\hat{v}_{t_k}^x & -\hat{v}_{t_k}^y & -\hat{x}_{t_{k-1}}^0 & -\hat{y}_{t_{k-1}}^0 \end{bmatrix}. \tag{5.40}$$

The solution of (5.39) is then added to the initial estimate of $\hat{X}_{t_k}$ to refine the final estimate of X_{t_k}. The reduced form of the solution presented by Shi *et al.* summarised in Algorithm 13 ignores the

sensor position uncertainties, clock offset and clock skew which are irrelevant to the work within this thesis.

Algorithm 13: The Shi solution[17] [44]

Initialisation

1: Under a static sensor and constant IML scenario, Preconfigure matrix A^{shi} (5.34) and (5.28)

2: Preconfigure matrix C_d

Estimation Loop

3: *For k = (1: k_{max})*

> ***Initial Estimate***
>
> ***4:*** Collect N range measurements $z_{t_k^i}^i$ from N sensors $i = (1:N)$
>
> ***5:*** Use measurements to populate $b_{t_k}^{shi}$ and D_{t_k} as in (5.34)
>
> ***6:*** Determine $C_{t_k}^{\varepsilon}$ as in (5.35)
>
> ***7:*** Compute the initial solution $\hat{\theta}_{t_k}^{shi}$ and covariance matrix $C_{t_k}^{\hat{\theta}}$ from (5.36) and (5.37) respectively
>
> ***Second Step***
>
> ***8:*** Populate $\tilde{r}_{t_k}$ and J_{t_k} using the initial estimate $\hat{\theta}_{t_k}^{shi}$ as given in
>
> (5.40)
>
> ***9:*** Compute error estimate $\widehat{\Delta X}_{t_k}$ as in (5.39)
>
> ***10:*** Correct initial state estimate $\hat{X}_{t_k}$ with error estimate $\widehat{\Delta X}_{t_k}$ using (5.38)
>
> ***11:*** Obtain $S_{t_{k-1}}^0$ from $\hat{X}_{t_k}$

12: *End*

5.4.4.2 Modified Backward Propagation Model

The linear solution proposed by Shi *et al.* [44] is a straightforward technique that relies upon the constant velocity principle of the target trajectory. An initial observation of the solution is that within the arrangement of the timing sequence, the estimated position $\hat{S}_{t_{k-1}}^0$ refers to the start of the sampling frame. As such, two sources of error can be expected.

Firstly, in conventional real-time tracking solutions, the objective is to attain the target position at the most recent instant. With this in consideration, the solution proposed by Shi *et al.* is therefore counter intuitive. Secondly, the measurements in the sequence are all considered to refer

[17] Ranges of values are represented in the following manner: (initial value : incremental value : end value) and may, in some cases, be assigned equivalent to a variable. Where an incremental value is not given, the increments are defaulted to integers of one. When used as part of a '*For'* loop, each value in the given range is applied individually within a single loop.

to the estimated position with a partial influence of the velocity component. Within a typically non-constant velocity scenario this invokes a partial error into each measurement value.

Based on these observations, the author, of this thesis, proposes an adaptation of the Shi solution in a reversed propagation format, where the target position to be obtained within the interval $[t_k, t_{k-1})$, is $S_{t_k}^0$, such that $X_{t_k} = \left[\left(S_{t_k}^0\right)^T, \left(V_{t_k}\right)^T\right]^T$.While this acquires a more recent and therefore more accurate result when compared to the targets latest position, this formulation additionally utilises the most recent measurement without any added velocity assumptions. To reflect this change, the proposed solution of (5.27) becomes:

$$d_{t_k}^i = \left\| S_{t_k}^0 - V_{t_k}\Delta t_i - S^i \right\|. \tag{5.41}$$

Where instead of Δt_s, one now considers the Measurement Latency (Δt_i) which represents the time difference between the sensor i measurement $\left(t_k^i\right)$ and the estimation instant (t_k). As before, this can also be expressed as an integer multiple of the IML:

$$\Delta t_i = t_k - t_k^i = (N - i) * \Delta t_m. \tag{5.42}$$

Repeating the same processes described in (5.30) - (5.32) produces a similar result to that of (5.33) where:

$$\begin{aligned} \hat{\theta}_{t_k}^3 &= \left(S_{t_k}^0\right)^T V_{t_k}, \\ a_{t_k}^i &= \left[2(S^i)^T, -2(S^i)^T\Delta t_i, 1, \Delta t_i^2, 2\Delta t_i\right]. \end{aligned} \tag{5.43}$$

For the refinement in the second stage the matricies $\tilde{r}_{t_k}$ and $\hat{J}_{t_k}$ are now given by:

$$\tilde{r}_{t_k} = \hat{\theta}_{t_k}^{shi} - \left[\hat{X}_{t_k}^T, -\left\|\hat{S}^i\right\|^2, -\left\|\hat{V}_{t_k}\right\|^2, \left(\hat{S}_{t_k}^0\right)^T \hat{V}_{t_k}\right]^T, \tag{5.44}$$

$$\hat{J}_{t_k} = \begin{bmatrix} -2\hat{x}_{t_k}^0 & -2\hat{y}_{t_k}^0 & 0 & 0 \\ 0 & 0 & -2\hat{v}_{t_k}^x & -2\hat{v}_{t_k}^y \\ \hat{v}_{t_k}^x & \hat{v}_{t_k}^y & \hat{x}_{t_k}^0 & \hat{y}_{t_k}^0 \end{bmatrix}.$$

The resultant second stage estimates obtained from the simplified and proposed modified approach of Shi *et al.*'s technique are denoted as $\hat{X}_{shi}$ and $\hat{X}_{mod}$ respectively.

The Algorithm for the Modified backward propagation solution, given by Algorithm **14**, follows the same process as that of the Shi solution but with the relevant changes made to the matrices.

Algorithm 14: The Modified backward propagation Shi solution[18]

Initialisation

1: Under a static sensor and constant IML scenario, Preconfigure matrix A^{shi} from (5.43) and (5.42)

2: Preconfigure matrix C_d

Estimation Loop

3: *For k = (1: k_{max})*

> ***Initial Estimate***
>
> ***4:*** Collect N range measurements $z_{t_k}^{i}$ from N sensors $i = (1:N)$
>
> ***5:*** Use measurements to populate $b_{t_k}^{shi}$ and D_{t_k} as in (5.34)
>
> ***6:*** Determine $C_{t_k}^{\varepsilon}$ as in (5.35)
>
> ***7:*** Compute the initial solution $\hat{\theta}_{t_k}^{shi}$ and covariance matrix $C_{t_k}^{\hat{\theta}}$ from (5.36) and (5.37) respectively
>
> ***Second Step***
>
> ***8:*** Populate $\tilde{r}_{t_k}$ and J_{t_k} using the initial estimate $\hat{\theta}_{t_k}^{shi}$ as given in
>
> (5.40) with $\hat{J}_k$ calculated from (5.44)
>
> ***9:*** Compute error estimate $\widehat{\Delta X}_{t_{k-1}}$ as in (5.39)
>
> ***10:*** Correct initial state estimate $\hat{X}_{t_{k-1}}$ with error estimate $\widehat{\Delta X}_{t_{k-1}}$ using (5.38)
>
> ***11:*** Obtain $S_{t_k}^{0}$ from $\hat{X}_{t_k}$

12: *End*

Figure 5.16 is provided to further illustrate the variation between Algorithm 13 and Algorithm **14**.

[18] Ranges of values are represented in the following manner: (initial value : incremental value : end value) and may, in some cases, be assigned equivalent to a variable. Where an incremental value is not given, the increments are defaulted to integers of one. When used as part of a '*For'* loop, each value in the given range is applied individually within a single loop.

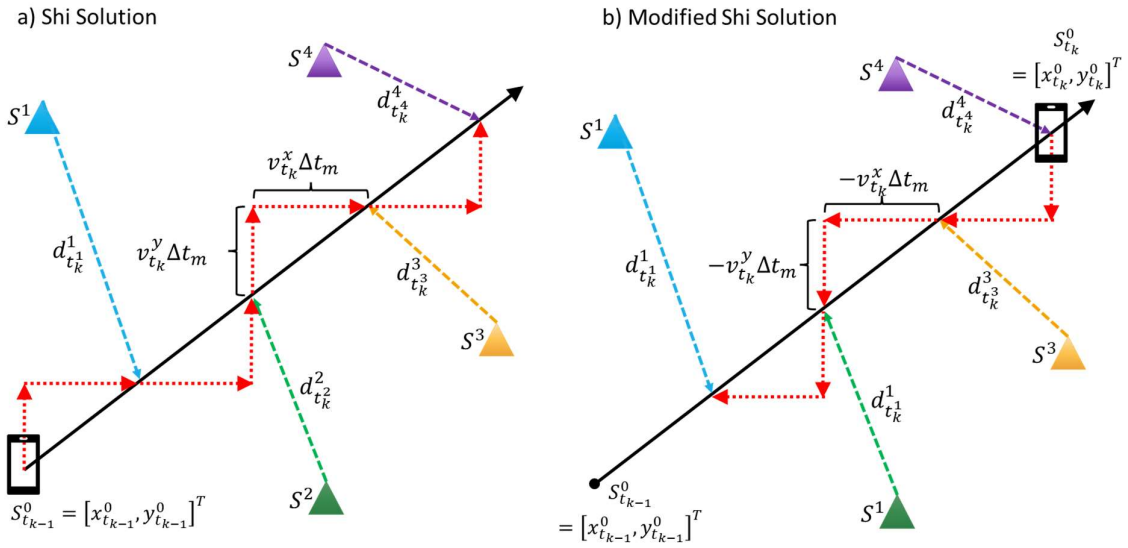

Figure 5.16 - Comparison between principles of a) Algorithm 13 and b) Algorithm **14**

Notably, as illustrated by the placement of the mobile device in Figure 5.16, the principle of the Modified Shi algorithm is to obtain the position of the UE at the most recent timepoint t_k within each sampling interval $[t_k, t_{k-1})$, as opposed to the Shi solution which identifies the previous estimation instant t_{k-1}. To reflect these changes forward in time the relationship between distance measurements, time and the estimation instant of interest are reversed as indicated by the red dotted lines in Figure 5.16. As such, the sensor distance measurements in Algorithm 14 are no longer related to the previous estimation instant by (5.27) and (5.28) but to the most recent estimation instant by (5.41) and (5.42). Consequently matrix A^{shi} must be updated on initialisation as reflected in step *1)* of Algorithm **14** and $\hat{j}_{t_k}$ is modified in step *8)*.

5.4.4.2.1 Simulation Results

Prior to comparison with the UKF and LSS solutions under the Reference Simulation Scenario, a comparison is made for the reduced Shi solution and the modified backward propagation model presented by the author of this thesis. These are henceforth referred to as the 'Shi' and 'Modified-Shi' solution respectively.

The initial scenario considered here follows the same sampling protocol and model parameters as the Reference Simulation Scenario however, the scenario considers a completely linear target trajectory, as described in the studies conducted by Shi *et al.* [44] and Pu *et al.* [190]. The sensors Baseline distance is maintained at 10 m.

The target trajectory starts from the coordinates (0,5) and then travels with a velocity of 1 m/s across the x-axis only. The simulation concludes once the target reaches the boundary formed

by the square formation of sensors at coordinates (10,5). For the $k'th$ estimation step, the Position Error (PE), denoted by $\varepsilon_{t_k}^{PE}$, is taken as the Euclidian distance of the targets true position at the estimation instant and position estimate provided by the respective technique:

$$\varepsilon_{t_k}^{PE} = \left\| S_{t_k}^0 - \hat{S}_{t_k}^0 \right\|. \tag{5.45}$$

From the formulation of the Shi solution, it is known that the estimate for the targets position at the previous estimation instant is provided, such that $\hat{S}_{t_k}^0$ describes $S_{t_{k-1}}^0$. The metrics are therefore also provided for the accuracy of the Shi solution, considering the prior target position:

$$\varepsilon_{t_k}^{PE} = \left\| S_{t_{k-1}}^0 - \hat{S}_{t_k}^0 \right\|. \tag{5.46}$$

In this manner, the errors owing to the time delay from estimating the previous estimation instant are eliminated, and the solutions accuracy alone can be identified. These Time-Corrected (TC) Shi solution metrics are henceforth referred to as 'Shi-TC'. The average PE for each estimation instant is given for the linear trajectory scenario and displayed in Figure 5.17[19]. Within this scenario, 500 iterations of all three variations of the Shi solution and LSS estimate are compared. The LSS estimate is provided here as a control metric, given its lack of response to the IML or Measurement noise. The simulation is considered for five different IML values (columns) and four different Measurement noise standard deviation values (rows).

[19] Notably, y-axis data is varied according to the number of estimations carried out along a set path length for different sampling latencies. Additionally, attention should be paid to the inconsistent x-axis values which are included for readability.

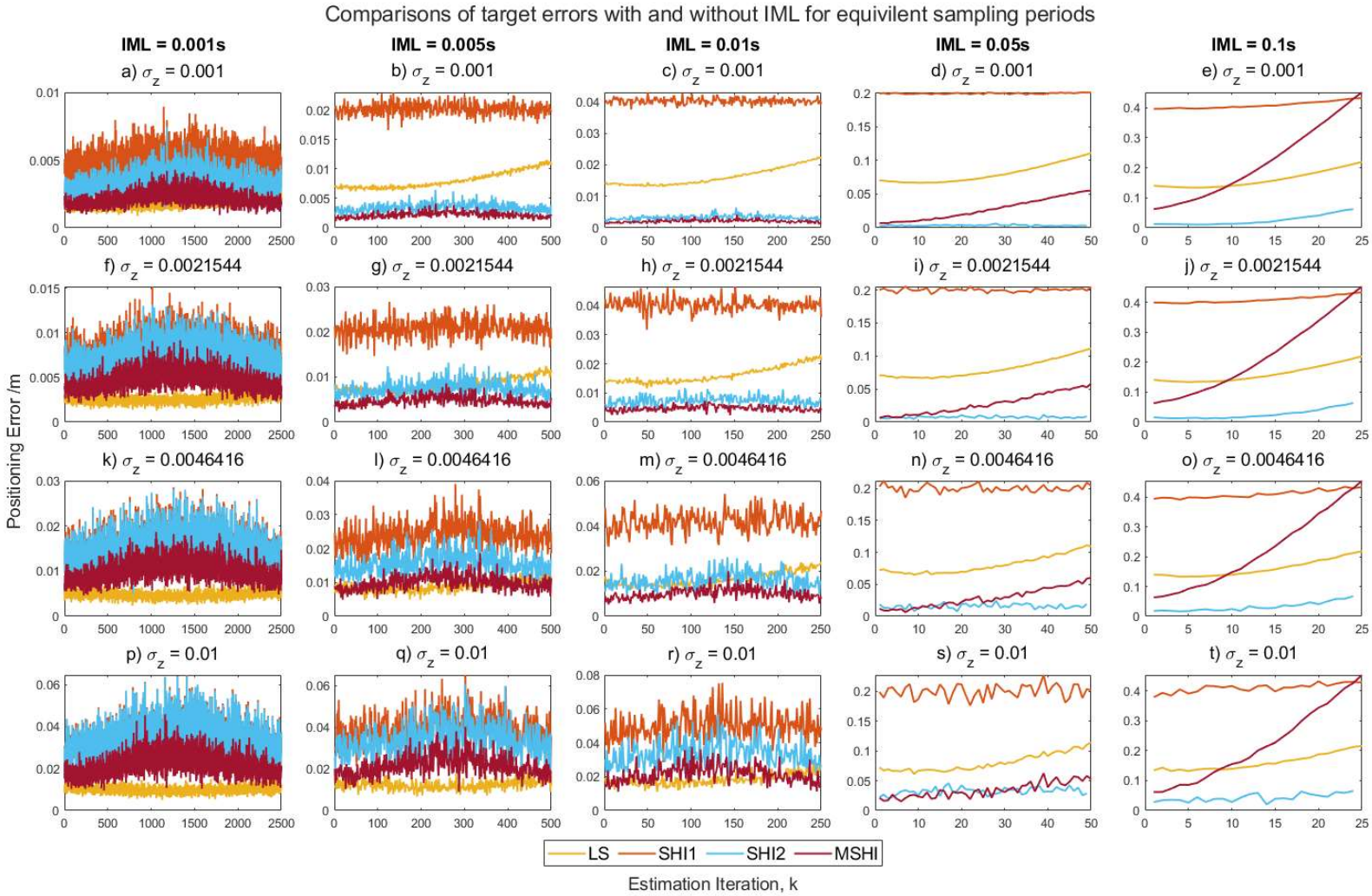

Figure 5.17 - Shi solution, Shi-TC solution and modified Shi solution positioning errors given for the linear trajectory scenario for different magnitudes of measurement noise and IML.

From Figure 5.17 one can observe that, when not correcting for the time delay, the Shi solution performs significantly worse than all other solutions considered. Comparing the Shi solution results to those of the Shi-TC solution highlights the magnitude of error which is simply established by the estimation latency.

Generally, the variations of the Shi solution do not prove to withstand measurement noise adequately, which is evident from the considerably lower error produced by the LSS. With respect to measurement noise, the proposed modified Shi approach is consistently the most resilient, which can be attributed to the reduction in applied velocity estimations. It is also worth noting that due to the poor performance under measurement noise, the measurement noise values considered within this scenario are far less than those considered previously within this section, at a maximum of 1 cm and 1 m respectively.

Another observation that can be made from the results presented in Figure 5.17, is that as IML increases from 0.005 s to 0.01 s, the modified Shi solution presents the best performance for both latency and noise. Comparing the modified Shi approach against the Shi-TC solution highlights the improvements to the position estimation when disregarding the latency error of the Shi solution. In these cases, the modified solutions performance is therefore improved because of the lack of the additional velocity assumptions. However, for IML that surpasses 0.05 s, the modified Shi approach begins to diverge from the path, which creates large instabilities and positioning errors. In these cases where the IML is higher, the Shi-TC solution demonstrates a much more stable performance.

From this study, one can conclude that the adaptations made to the Shi solution in the proposed modified approach improves the resilience to noise but at the cost of poorer performance at higher IML values. However, one can also ascertain that the Shi solution variants generally do not provide a great deal of improvement against the standard LSS solution. While the Shi-TC solution is more impressive at higher IML values, the solution may only be beneficial for non-realtime tracking, where improved accuracy is needed in a sequential scenario. Due to the demands of real time tracking considered within this thesis, the Modified Shi solution is considered going forward, with the Shi-TC solution provided for reference.

5.4.4.3 The Sequential Unscented Kalman Filter - SUKF

The Sequential Unscented Kalman Filter (SUKF) is fundamentally a sequential version of the Unscented Kalman Filter (UKF). For this reason, the equations are identical to those presented in literature review Section 2.2.4.1, and are therefore not repeated within this section.

The only variation between the UKF and SUKF solutions is that for the SUKF solution, the estimations are carried out across Δt_m and not ΔT. Each received measurement is thereby fused to the time it was

attained at the sensor or equivalently, the FC under the zero-transmission delay assumption. The SUKF approach is summarised in algorithm 12, below.

Algorithm 15: SUKF[20]

Initialisation

1: Initial state vector $X_{t_1} = \left[x_{t_1}^0, y_{t_1}^0, v_{t_1}^x, v_{t_1}^y\right]$ given coordinates from initial LSS estimate and velocities of 1 m/s for both axes.

2: State covariance matrix P_{t_1} given as identity matrix

3: Under constant IML scenario populate Q matrix (5.17) and apply empirically tuned acceleration noise magnitude multiplier dependant on the IML and Measurement noise values.

Estimation Loop

4: *For k = (2: k_{max})*

5: *For $i = (1:N)$ range measurements*

Prediction

6: Compute the sigma points $\chi_{t_k^{i-1}}$ and respective weightings W^m and W^c(2.45) -(2.52) *(where i=1, $\chi_{t_k^{i-1}}$ refers to $\chi_{t_{k-1}^N}$)*

7: Propagate the sigma points through the nonlinear process function (2.53), where $\Delta t = \Delta t_m$, to obtain the transformed set $\chi_{t_k^i}^i$

8: Compute the transformed state $\hat{X}_{t_k^i}^-$ and covariance $P_{t_k^i}^-$ with (2.54) and (2.55) respectively

Update

9: Propagate the transformed set of sigma points through the nonlinear measurement function (2.56)

10: Determine the estimated measurement mean $\hat{z}_{t_k^i}^i$ and respective innovation covariance matrix $P_{t_k^i}^{zz}$ from (2.57) and (2.58) respectively

11: Calculate the cross covariance $P_{t_k^i}^{xz}$ as given by (2.59)

12: Compute the Kalman gain $K_{t_k^i}$ with (2.60)

13: Determine the updated state $\hat{X}_{t_k^i}$ and state covariance matrix $\hat{P}_{t_k^i}$ using (2.61) and (2.62) respectively

14: *End*

15: *End*

In contrast to the batch process of both the Shi and Modified Shi solutions, presented in Algorithm 13 and Algorithm **14**, the SUKF solution sequentially estimates the UE position at each sensor sampling

[20] Ranges of values are represented in the following manner: (initial value : incremental value : end value) and may, in some cases, be assigned equivalent to a variable. Where an incremental value is not given, the increments are defaulted to integers of one. When used as part of a '*For'* loop, each value in the given range is applied individually within a single loop.

instant. This is reflected in Figure 5.18 by the multiple sensor-coloured UE's along the trajectory. As described in steps *6-8* of Algorithm **15**, for each sensor measurement a prediction of the UE position, illustrated by a red UE within Figure 5.18, is initially generated using a trajectory model. Similarly to the Shi and Modified Shi process, the CV trajectory model illustrated in Figure 5.18 applies an assumed velocity component V for a known period of time Δt_m to the previously estimated target position. The SUKF solution however offers more flexibility with regards to the applied trajectory model. Subsequently, the prediction and sensor measurement are then fused to produce a state estimate as described in steps *9-13* of Algorithm **15**, and the process is repeated.

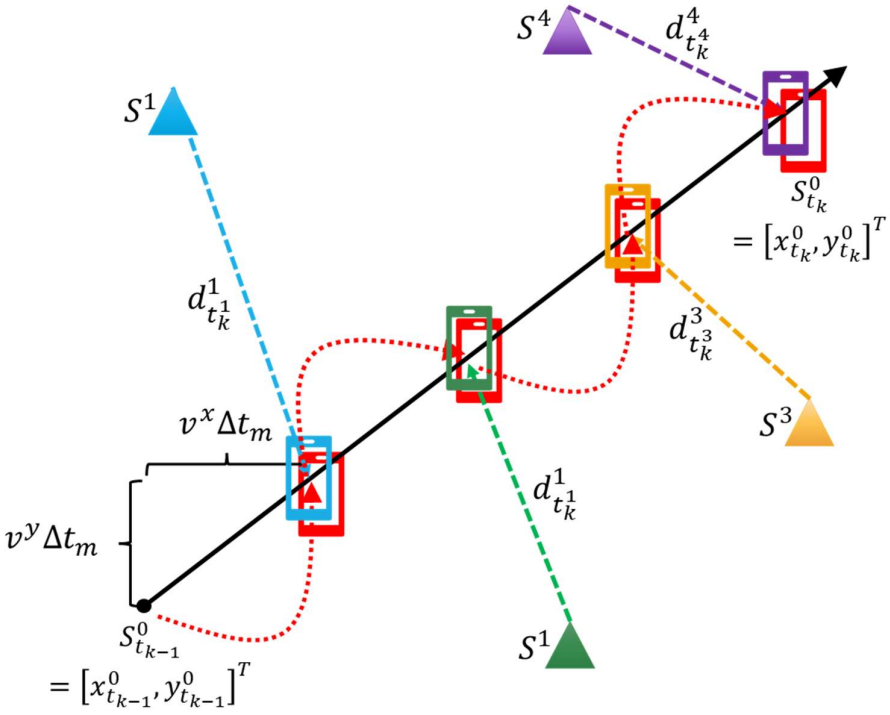

Figure 5.18 - Illustration of SUKF process

While other SUKF studies presented in the literature review introduced fading factors [36], [126], [189] and other constraints, this thesis considers a constant IML, where there is therefore no unknown stochastic noise parameter. This deterministic error component can be estimated using empirical data, following the KF trial and error system identification process as described in Section 5.4.2.5 and summarised in Algorithm 12.

Due to the influence that the process noise covariance matrix Q and the measurement noise covariance matrix R have on the response of the KF, the optimal acceleration noise magnitude, which directly effects Q, provides significant insight into the behaviour of the KFs. Figure 5.19 below

illustrates the optimal acceleration noise magnitude values for the SUKF and UKF systems, implementing the aforementioned trial and error system identification process.

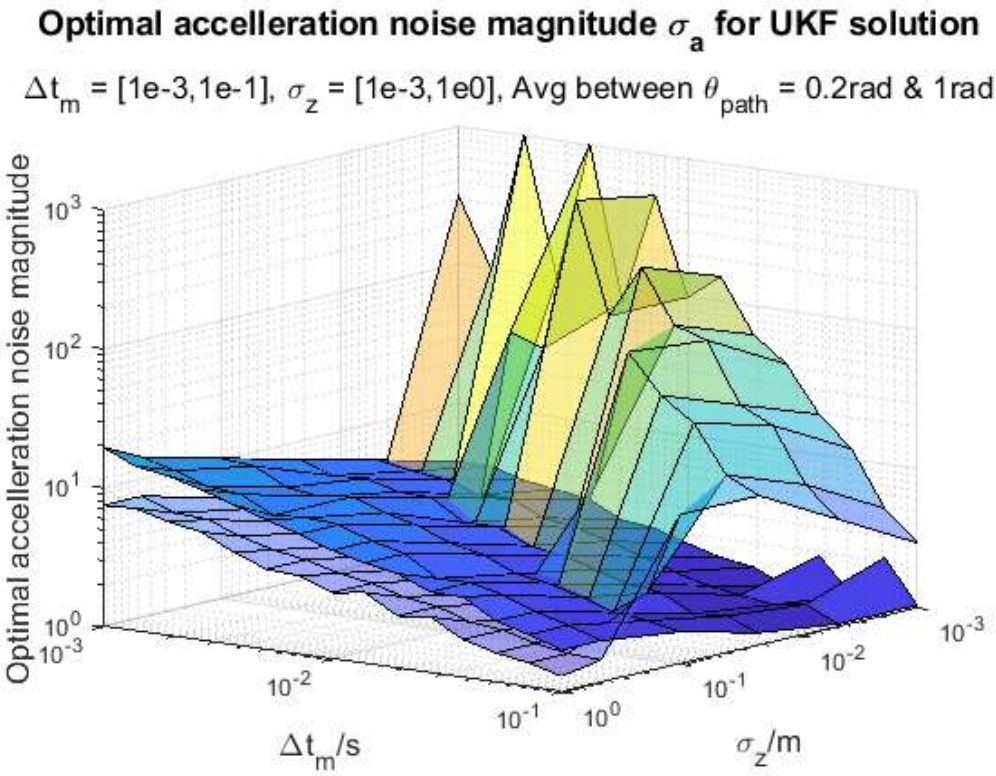

Figure 5.19 - Optimal Acceleration noise magnitude values for both SUKF (opaque) and UKF (translucent) solutions at different IML and Measurement noise scenarios.

Figure 5.19 demonstrates that generally, compared to the UKF optimal acceleration noise magnitude, the SUKF solution presents a vastly more linear response. This can be attributed to the fact that the IML errors do not exist when measurements are processed for the time they are acquired. As such, the SUKF response is not affected by IML in the same manner as the UKF response.

The SUKF does however rely strictly on single sensor measurements, which makes it far more susceptible to individual sensor errors. The result of this is that as the IML increases, the estimation periods also increase as shown by the IML to estimation period relationship given in (5.4). As the process noise is time dependant, as indicated by (5.17), this therefore increases with greater IML values. In response to larger IML, the magnitude of the acceleration component decreases to some extent, in order to improve stability and avoid overdependence on the measurements.

Conversely, as the measurement noise increases, the optimal acceleration noise magnitude also increases, in order to avoid over-reliance in the process noise which can lead to divergence. In

this respect, the tuning effect that Q and R have within the KF is apparent and one can ascertain that an optimal balance must be maintained in order to provide a smooth but stable response.

5.4.4.4 Simulation Results

Within this section Algorithm **13**, Algorithm **14** and Algorithm **15** are evaluated under the Reference Simulation given in Algorithm 11 for 500 iterations. The results are then compared against those obtained for the UKF and LSS in Section 5.4.3 as control studies. Figure 5.20 illustrates the RMSE for each considered location estimation technique, across all considered IML and Measurement noise values. Within this figure, the solutions are individually included as 'layers' for illustrative purposes and the two rows of graphs reflect the results obtained from a path angle of 0.2rad and 1rad respectively. Tabulated data for Figure 5.20 is provided in Appendix B of this thesis.

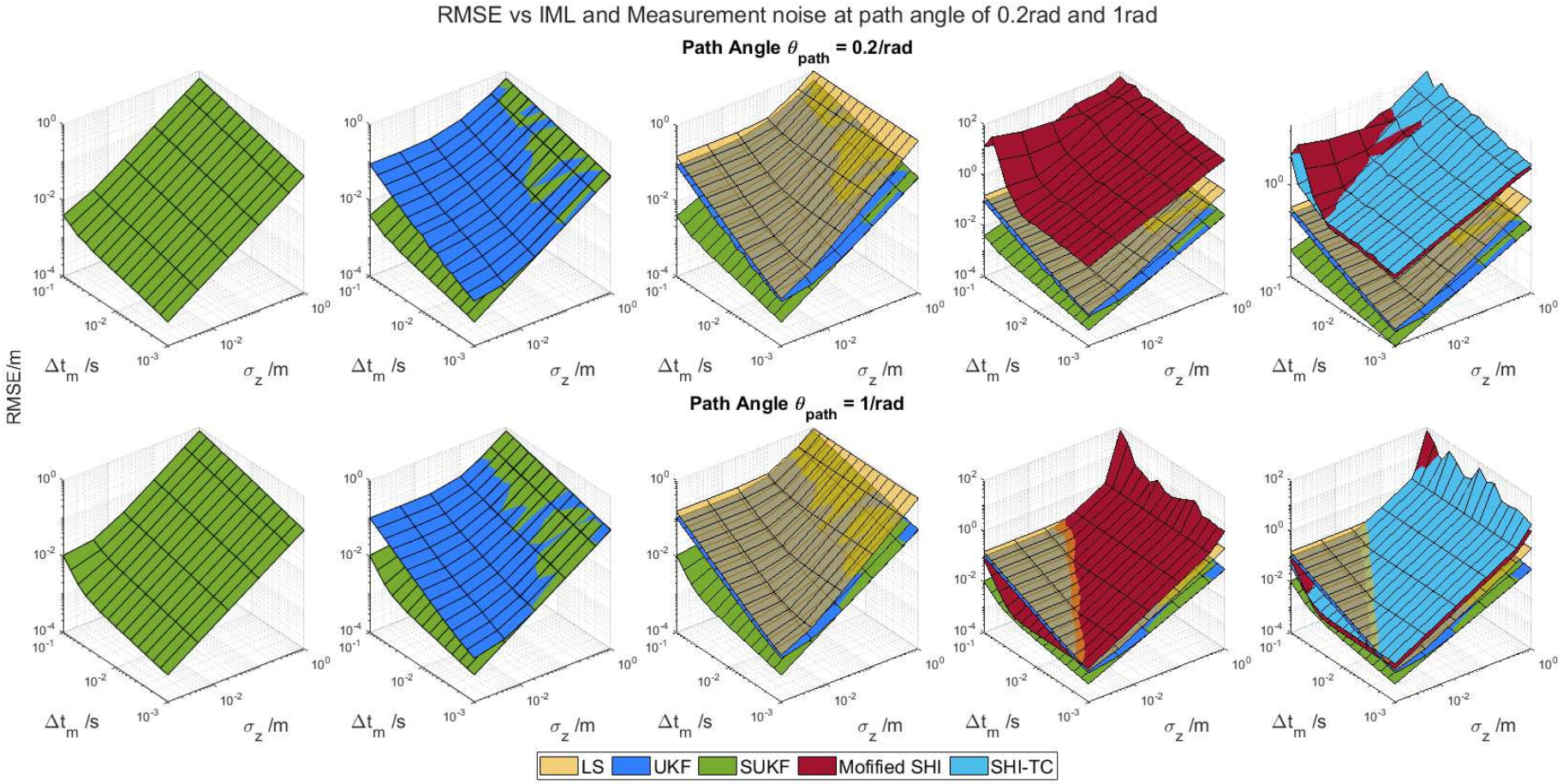

Figure 5.20 - 3D RMSE plots for all considered IML and Measurement noise values at path angles of 0.2rad and 1rad

From Figure 5.20 , it is clear that SUKF displays the best overall performance, as it exhibits significantly lower RMSE for all scenarios considered. The results for the Shi solutions reflect observations of the results obtained from the earlier linear trajectory test. With the minimum level of measurement noise, the Shi-TC and Modified Shi Solution do reduce the error compared to the LSS and the UKF solutions. Again the Modified Shi solution shows a prominent improvement against the Shi-TC solution which is notably time corrected and does not illustrate the Shi solution errors for realtime tracking. However, as IML increases, the linear velocity assumption clearly fails under a circular trajectory and both Shi-TC and Modified Shi approaches illustrate gradual increases in error. As with the Linear trajectory test, given by Figure 5.17, the proposed Modified Shi approach is not as suitable for higher IML values. Regardless, due to the small noise assumption involved in the Shi solutions, the noise quickly corrupts all estimates, further deeming the Shi solutions highly unsuitable for most considered scenarios.

For the top row of data displayed in Figure 55, where the path angle is 0.2 rad, the circumference of the path trajectory forms a tangent along the boundary formed by the four sensors. At this path angle the Shi solution and Modified Shi solution both exhibit sudden high positioning errors at specific estimation instants, which results in an increased RMSE. This is attributed to flip ambiguities and can be resolved in one of two ways. The first is through the inclusion of an additional sensor somewhere not on the circumference of the circle that the other existing sensors lie along. Alternatively, this can be achieved by moving a single sensor to ensure that it does not lie on the plane on which the other sensors are positioned.

Overall, the modified Shi process provides consistently superior results than even the Time corrected Shi (Shi-TC) process, which illustrates its dominant resilience to measurement noise. However, the performance in contrast to the alternative solutions remains highly unattractive for all applications considered within this thesis.

Figure 5.21, below, presents a more quantifiable comparison of the various location estimation methods. The results presented are for all considered IML values at measurement noises of both 1 mm and 1 m and path angles of both 0.2 and 1 rad.

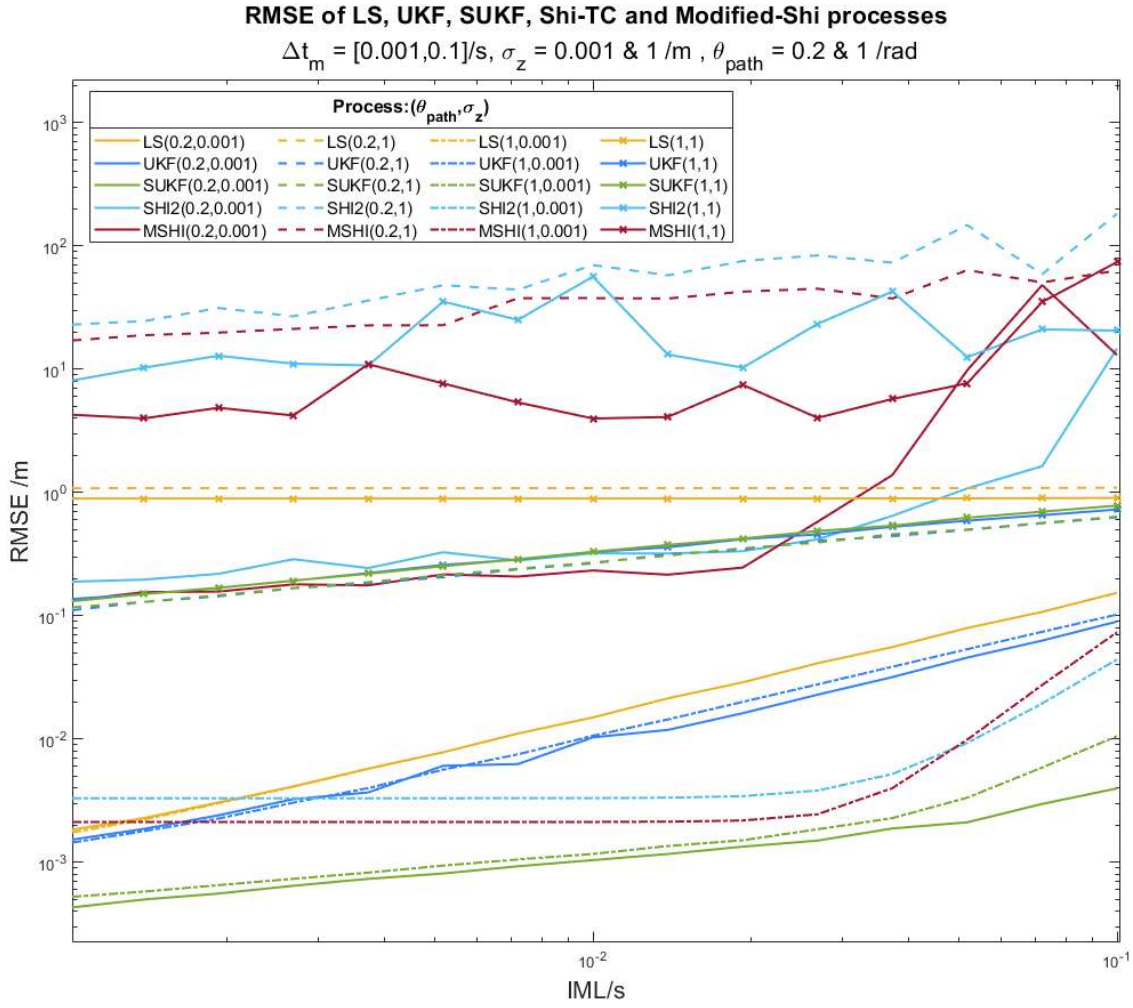

Figure 5.21 - RMSE for all IML values at different measurement noises and path angles

Initially, when comparing the SUKF and UKF approaches, the sequential processing is proven to successfully reduce the effects of IML and sequential measurement acquisition. As the random measurement noise dominates over the IML error, and the effects of IML are therefore dampened, one can observe the performance of the UKF and SUKF become nearly identical to one another. This relationship is evident from the indistinguishable lines within Figure 5.21.

To provide a clearer visual representation of the difference in RMSE between the SUKF and UKF solutions, Figure 5.22 presents the percentage difference in RMSE performance between them as given by (5.47):

$$RMSE\%_{diff} = 100 * \frac{\left(SUKF_{RMSE}(\Delta t_m, \sigma_z, \theta_{path}) - UKF_{RMSE}(\Delta t_m, \sigma_z, \theta_{path})\right)}{UKF_{RMSE}(\Delta t_m, \sigma_z, \theta_{path})}. \quad (5.47)$$

Within this figure, the effects of path angle are also distinctly more visible. As path angle increases, the UKF approach performance degrades under greater IML, however, as measurement noise increases, the UKF is shown to be far more resilient. This is because as the measurement noise increases and the IML effects are minimised, the SUKF solution is more susceptible to single sensor errors whereas the UKF is able to combine multiple measurements and consequently produce more stable results.

As with the UKF solution, an increase in the nonlinearity of the target trajectory leads to an increase in the estimation error, which can be attributed to the CV model and increased prediction intervals. More significantly, when the path angle is increased, the SUKF solution does indicate a more prominent increase in error at higher IML values.

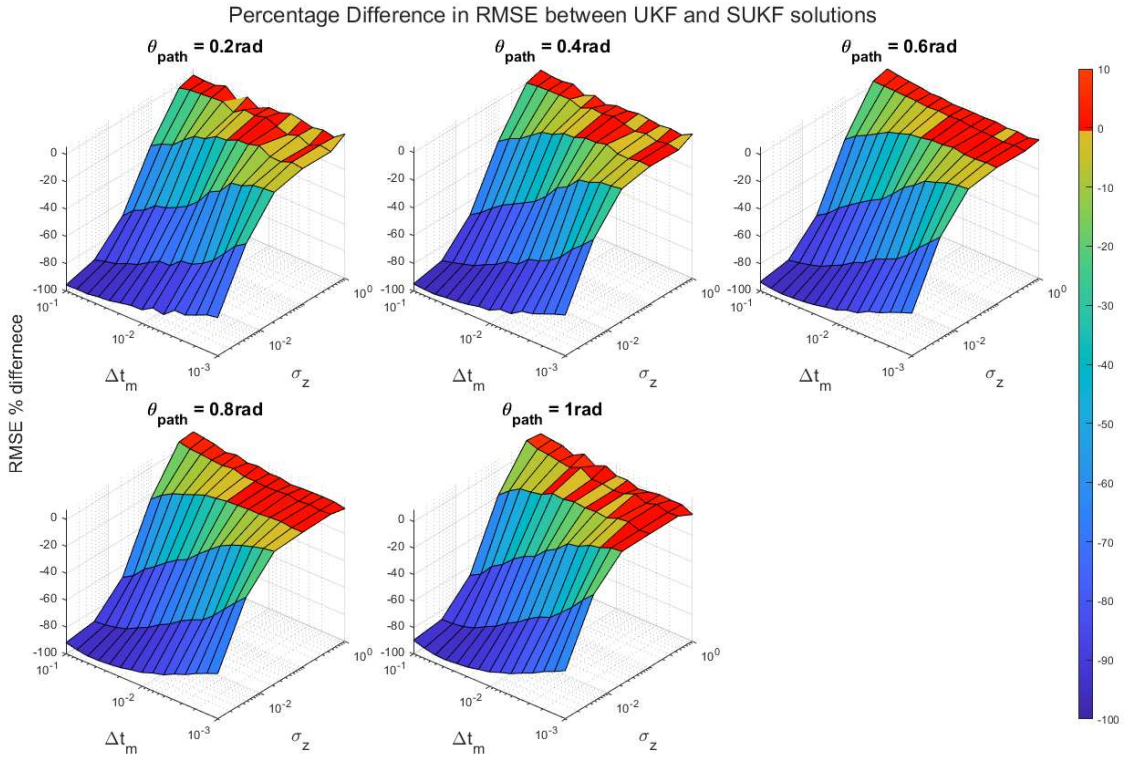

Figure 5.22 - RMSE positioning error performance comparison between UKF and SUKF for all considered path angles

To evaluate the computational complexity and energy required by each solution, the computation times are evaluated according to (5.25), where $N_L = 50$ and each loop resolves all 7854 estimations. This is repeated for 50 iterations. The Estimation Runtimes (ER) are given in Table 5.2 for IML, σ_z and path angle set to 1e-3 s, 1e-3 m and 0.2 rad respectively. Both Shi and Shi-TC solutions are computed in the same manner and are therefore represented by a singular ER value.

Table 5.2 - Comparative table of computation runtimes for each evaluated solution under the same test parameters

Solution	LSS	UKF	Shi	MShi	SUKF
Estimation Runtime /s	8.87e-6	6.03e-5	6.78e-5	6.81e-5	7.37e-5

Table 22 demonstrates that LSS obtains the fastest time by far, due to its simplicity and low matrix dimensions. The UKF follows with the second-fastest time, due to the computationally intensive Unscented Transforms utilised. The Shi and MShi solutions then obtain similar times, as there is a considerable lack of variation between them. Notably, while these solutions are extensions of the LSS, the matrix dimensions and two-stage process require far more computations than that of the LSS. Finally, the SUKF process incurs the most significant time to compute and, therefore demands the highest computational effort.

5.5 Chapter Summary

While it has been recognised within literature [44], [264] that the effects of asynchronous sampling have negative impacts on nonlinear location estimation, this chapter has expanded on that understanding by evaluating the degree to which asynchronous range estimates affect both single sensor range estimates and multi-sensor position estimates. Comprehensive simulations were conducted on various existing processes that do and do not consider asynchronous measurements to assess their response under variable degrees of asynchronous sampling, sensor measurement noise and path nonlinearity.

Results highlight that while some solutions perform better than others in general, asynchronous sampling solutions do entail additional computation costs, as shown by the significantly greater computation times of the Shi variant solutions and the SUKF solution.

The proposed Modified Shi solution is shown to be more effective at resisting the effects of sensor measurement noise while improving on the latency of the original Shi solution [44]. For low sensor measurement noise and higher IML values, the Shi-TC and Modified Shi solutions are evidently effective at reducing estimation error brought on by IML. However under low IML and increased sensor measurement noises both Shi solutions exhibit greater errors than conventional sysnchronous solutions while being more susceptible to ambiguities. Considering the poor resistance to measurement noise, coupled with the increased complexity and computation time, the Shi solutions are not considered to be a highly effective solution for asynchronous sampling.

The SUKF is shown to be the optimal solution with regards to accuracy and reliability for most cases at a much greater computational cost which dictates a more extensive energy demand. This presents a trade-off between complexity and precision that can be used to suit the requirements of a positioning system. It is shown that for substantial measurement noise, the effects of IML are less prominent, and the performance of the optimal SUKF solution degrades such that it becomes comparable, if not, worse than the UKF solution. Within these cases, the author of this thesis encourages the use of the less demanding UKF solution, which is not so reliant on single sensor performance. Regardless, a system designer should account for the more frequent estimation updates enabled by sequential filtering.

Building on this research, the following chapter considers the computational demand of asynchronous sampling solutions coupled with the understanding of efficient localisation processes to develop a more computationally efficient solution.

6 A computationally Efficient Approach to Asynchronous Localisation under Nonlinear Measurements

6.1 Introduction

6.1.1 Key Insights So Far in this Area

Chapter 5 highlighted the negative impacts or errors that asynchronous sampling can have on localisation performance and, using a variety of parameters, assessed the effectiveness of specific asynchronous localisation solutions in reducing the accumulated error. While these showed improved accuracy and reliability over non-asynchronous localisation solutions, for certain degrees of measurement noise and asynchronous sampling, the greater complexity of these solutions resulted in increased latency. Latency reflects computational complexity and therefore the energy required by these processes. For mobile device applications that operate using battery power the energy efficiency of functions must be minimised to lengthen battery life, reduce processor demands and decrease maintenance costs for the user. The importance of energy efficiency and reduced latency has been extensively addressed in wireless localisation techniques and processes [14], [15], [89], [90], [142], [170], [173], [175], [182], [265]–[267], and highlighted by 3GPP specifications [202].

Consequently, whilst asynchronous solutions are required to achieve good positioning accuracy, the computational efficiency of these solutions need to be reduced. To this end, a novel and more efficient solution to the tracking problem of asynchronously sampled nonlinear range measurements, referred to as the Kalman Extrapolated Least Squares (KELS) solution is proposed.

6.1.2 Chapter Contributions

Within this chapter the author of this thesis proposes a novel and more computationally efficient solution for target localisation under asynchronous sampling for nonlinear range measurements. This is done by utilising existing low complexity localisation solutions.

6.1.3 Overview of Chapter

This chapter presents the underlying principles of the proposed KELS solution and then evaluates the solution against existing non-asynchronous localisation methods. Following analysis of the results additional processes are then reasoned and applied to improve the performance resulting in an improved KELS solution.

6.2 Development of the Proposed Asynchronous Nonlinear Localisation Solution

6.2.1 Extrapolating Range Measurements

Chapter 5 showed the optimality of the Least Squares Solution (LSS) with regards to latency and is therefore considered for efficient position estimation within the proposed IoRL approach. Multilateration within an asynchronously sampled system means each sensor describes the target at a different point in space and time. The high sensitivity of Lateration schemes, to inaccuracies in distance measurements, is shown to cause high errors within the asynchronous scenario. A common principle observed in the LSS [44], Measurement Augmentation (MA) [184] and Extrapolation [191] techniques is the development of a set of pseudo measurements that relate to a single point in time, simulating synchronised measurements and thereby mitigating the errors attributed to IML. Once artificially synchronised, conventional synchronous estimation techniques can then be applied.

In the previous chapter both sequential nonlinear KFs and linear constant velocity solutions were evaluated with regards to SUKF and the Shi solution. As introduced in chapter 2, the concept of extrapolation has been used throughout the literature to time align measurements established from asynchronous sensors. This process to date has been limited to linear extrapolations of target positions (poses) or IMU and bearing measurements. The author of this thesis recognises that to the best of their knowledge the extrapolation approach has not previously been applied directly to range estimates for use within asynchronous localisations. Due to its simplicity, and hence computational efficiency, the principle of extrapolation is therefore considered for time alignment of measurements in the proposed KELS approach.

The initial principle for the proposed asynchronous solution is to extrapolate range measurements linearly to a common point in time, where they can be processed as synchronous measurements using efficient synchronous position estimation techniques.

The extrapolation process itself is suboptimal as it is based on the assumption of a linear change in measurement value across a sampling period. Therefore, to reduce the number of adjustments required the measurements are all extrapolated to the known timepoint of the most recent measurement. Under a homogenous sensor network, it is reasonable to assume this most recent measurement is the most accurate, and within a sequential sampling scenario suffers no Inter Measurement Latency (IML) error. In this case the final sensor measurement is not extrapolated. A geometrical illustration of this concept is presented for four sensors in Figure 6.1. In which measurements sampled sequentially are represented by the respective colour of the mobile device and sensor. Solid and dotted lines represent the initial range measurements and extrapolated measurements respectivly. Dotted arrows represent the extrapolation of each measurment and colours are used to relate datasets to the individual sensor.

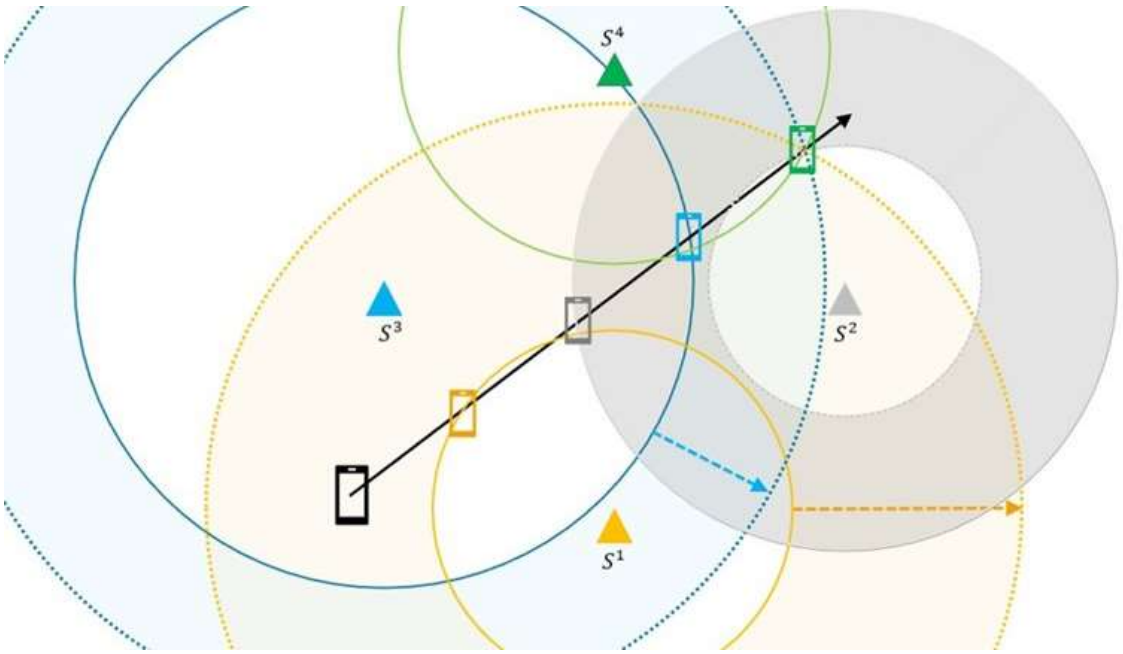

Figure 6.1 - Graphical representation of the extrapolation of range based sensor measurements.

6.2.1.1 Direct Linear Extrapolation for Multilateration

The proposed approach applies extrapolation techniques directly to the range measurements and is referred to as Direct Extrapolation (DE) further in this thesis. The following section outlines the DE process for the asynchronous sampling scenario described in Section 5.2. A denotation change is applied to avoid confusion later in the chapter. General range measurements sampled by the $i'th$ sensor within the Fusion Centre (FC) sampling period of $[t_k, t_{k-1})$, are denoted as $\hat{d}^i_{t^i_k}$. The estimation instant or point in time the measurement is to be extrapolated to, is denoted by t_k alone. The solution requires that the FC can store the range estimates from the previous estimation interval $[t_{k-1}, t_{k-2})$. A simple linear extrapolation for sensor i during the sampling period $[t_k, t_{k-1})$, is given as follows:

$$\alpha^i_{t_k} = \left(\frac{t_k - t^i_k}{t^i_k - t^i_{k-1}}\right) \Delta\hat{d}^i_{t^i_k, t^i_{k-1}}, \tag{6.1}$$

In which,

$$\Delta\hat{d}^i_{t^i_k, t^i_{k-1}} = \hat{d}^i_{t^i_k} - \hat{d}^i_{t^i_{k-1}}. \tag{6.2}$$

Here $\alpha_{t_k}^i$ denotes the sensor measurement extrapolation value, for the time t_k^i. $\Delta\hat{d}_{t_k^i,t_{k-1}^i}^i$ representing the change in distance value between the two consecutive measurements $\hat{d}_{t_k^i}^i$ and $\hat{d}_{t_{k-1}^i}^i$, received at times t_k^i and t_{k-1}^i respectively. Measurements are received periodically at the $i'th$ sensor at times t_k^i and t_{k-1}^i, therefore:

$$\Delta T^i = t_k^i - t_{k-1}^i. \tag{6.3}$$

In which ΔT^i represents the constant sampling period of the sensor. Following on from the extrapolation, the pseudo measurement considered at the estimation instant is given by the combination of the most recent measurement and the additional calculated extrapolated value:

$$\hat{d}_{t_{k,est}}^i = \hat{d}_{t_k^i}^i + \alpha_{t_k}^i \tag{6.4}$$

A single extrapolation period, concerning two FC sampling periods, is illustrated in Figure 6.2. for a four sensor system with a constant IML (Δt_m) value and a sensor sequence such that $t_k^1 < t_k^2 < \cdots t_k^N$. Given the constant IML and fixed sequence, the following relationship can be derived for the $i'th$ sensor measurement during the $k'th$ sampling period $\hat{d}_{t_k^i}^i$ which is received at time t_k^i:

$$t_k^i = t_{k-1} + (i * \Delta t_m). \tag{6.5}$$

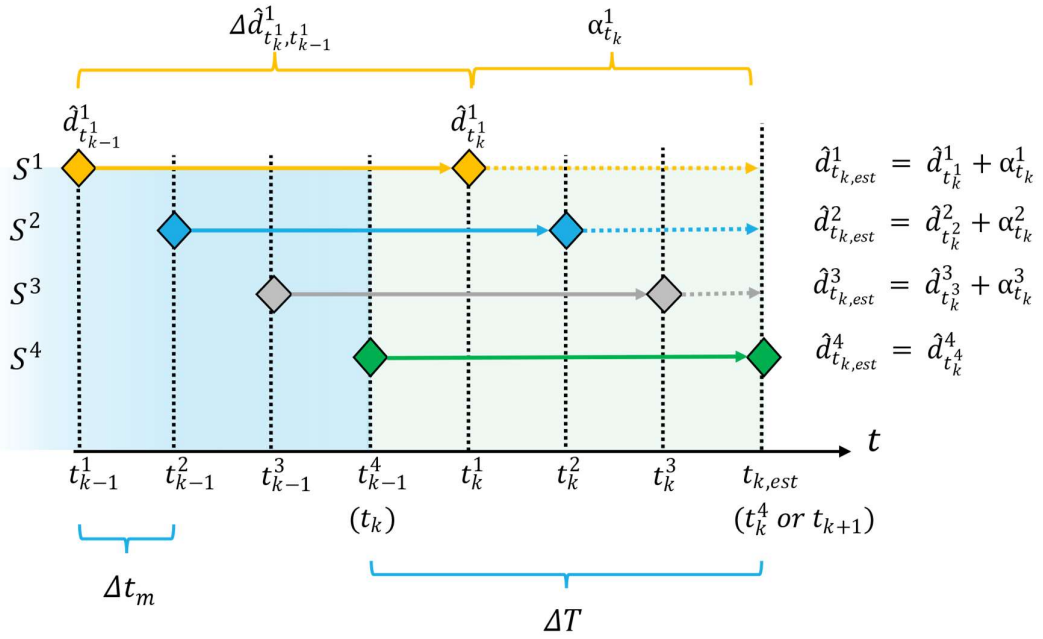

Figure 6.2 – Extrapolation process for a $N = 4$ sensor system across two estimation intervals. (Highlighted by different background colours)

Notably, the IML is set to be a constant and the sensors all have the same sampling period (ΔT) such that:

$$\Delta T = \Delta T^i \; for \; all \; i = (1 \cdots N). \tag{6.6}$$

Due to the sequential nature of the system, the Sampling period (ΔT) is defined by the number of sensors and the IML such that:

$$\Delta T = N * \Delta t_m. \tag{6.7}$$

Since a previous measurement is required for extrapolation in (6.1), the initial set of measurements retrieved within $[t_1, t_0)$ cannot be extrapolated upon. Because of this, the first provided state estimate cannot be computed until $k > 1$. The Estimation instant t_k is set to the same time as when the fourth sensor measurement is received such that:

$$t_{k-1}^N = t_k \; for \; all \; integers \; of \; k \geq 1. \tag{6.8}$$

The period of the $i'th$ sensors extrapolation component is given by the Measurement Latency (MLa) given again as:

$$\Delta t_i = t_k - t_k^i. \tag{6.9}$$

Therefore using equations (6.4), (6.6) and (6.7) one can simplify (6.1) to:

$$\alpha_{t_k}^i = \left(\frac{\Delta t_i}{N * \Delta t_m}\right) \Delta \hat{d}^i_{t_k^i, t_{k-1}^i}. \tag{6.10}$$

Using (6.8), Δt_i is also equivalent to $t_k^N - t_k^i$. Substitution of (6.5) into (6.9) obtains:

$$\Delta t_i = t_k^N - t_k^i = \left(t_k + (N * \Delta t_m)\right) - (t_k + (i * \Delta t_m)) = (N - i) * \Delta t_m. \tag{6.11}$$

Therefore, substituting (6.11) into (6.10) and simplifying:

$$\alpha_{t_k}^i = \left(\frac{N - i}{N}\right) \Delta \hat{d}^i_{t_k^i, t_{k-1}^i}. \tag{6.12}$$

From here one can retrieve the $N-1$ individual extrapolated and the $N'th$ non-extrapolated measurement from (6.12) and (6.4) to give:

$$\hat{d}^i_{t_{k,est}} = \hat{d}^i_{t^i_k} + \left(\frac{N-i}{N}\right)\Delta\hat{d}^i_{t^i_k,t^i_{k-1}}. \tag{6.13}$$

These are then entered into the LSS Multilateration algorithm, as described in Section 0, using the matrix form $G\hat{\vartheta} = \hat{b}$ as follows [91]:

$$\begin{bmatrix} 2x^1 & 2y^1 & 1 \\ \vdots & \vdots & \vdots \\ 2x^N & 2y^N & 1 \end{bmatrix}\begin{bmatrix} x^0 \\ y^0 \\ (x^0)^2+(y^0)^2 \end{bmatrix} = \begin{bmatrix} (\hat{d}^1_{t_{k,est}})^2 & -(x^1)^2 & -(y^1)^2 \\ \vdots & \vdots & \vdots \\ (\hat{d}^N_{t_{k,est}})^2 & -(x^N)^2 & -(y^N)^2 \end{bmatrix}. \tag{6.14}$$

The LSS is calculated using [91]:

$$\hat{\vartheta} = (G^T W^{-1} G)^{-1} G^T W^{-1} \hat{b}. \tag{6.15}$$

This process is repeated for each sampling instant as a batch process. This concludes the explanation of the Direct Extrapolation (DE) approach, which is summarised in Algorithm 16.

Algorithm 16: Direct Extrapolation[21]

INPUT: **Sensor coordinates S^i *for* $i = (1, \cdots, N)$**

1. *For* $k = (2: k_{max})$

2. *For* $i = (1: N)$

3. Retrieve sensor distance measurement $\hat{d}^i_{t^i_k}$ and previous sampling period measurement $\hat{d}^i_{t^i_{k-1}}$

4. Determine measurement difference $\Delta\hat{d}^i_{t^i_k, t^i_{k-1}}$ using (6.2)

5. Calculate the extrapolated measurement estimate $\hat{d}^i_{t_k, est}$ from (6.13)

6. *End*

7. Compute Target coordinates using (6.14) and (6.15). Exclude last component of $\hat{\vartheta}$

8. *End*

6.2.1.1.1 DE Simulation Analysis

Referring back to Chapter 5, to evaluate the response of the DE approach in comparison to existing solutions, Algorithm **16** *is evaluated under the Reference Simulation given in Algorithm 11 for 500 iterations*. The RMSE results for different sensor measurement noises, Inter Measurement Latency (IML) and path angle (PA) values are compared to the results obtained by the UKF and LSS approaches in Section 5.4.3 and presented in Figure 6.3.

In chapter 5 IML was introduced and the effects of Measurement Latency (MLa) were evaluated for asynchronous measurements, when related to a later estimation instant. In this chapter, the MLa error is mitigated using extrapolation techniques. Since the proposed DE approach is an adaptation of the LSS it is important to note that the difference in errors, between the DE and LSS, shown in Figure 6.3 are related to the pseudo measurements and the linear extrapolations applied. Figure 6.3 shows that, in contrast to the LSS (orange) and UKF (blue) techniques, the DE (purple) approach is highly effective in reducing IML effects under low levels of measurement noise. Although, the DE technique does well to supress the effects of IML for low values of measurement noise, there is a sudden and significant increase in error for higher measurement noise values. This effect is exaggerated under a greater path angle, due to the applied linear extrapolation not being ideal under greater path non-linearity. Relevant tabulated RMSE data for the DE solution is provided in Appendix C of this thesis.

[21] Ranges of values are represented in the following manner: (initial value : incremental value : end value) and may, in some cases, be assigned equivalent to a variable. Where an incremental value is not given, the increments are defaulted to integers of one. When used as part of a '*For'* loop, each value in the given range is applied individually within a single loop.

While the DE solution is effective against most considered levels of IML, the effects of measurement noise are clearly apparent and show a drastic increase in error, quickly surpassing both the LSS and UKF with increased noise. This can be explained by the extrapolation process simultaneously exacerbating both the measurement and the noise component.

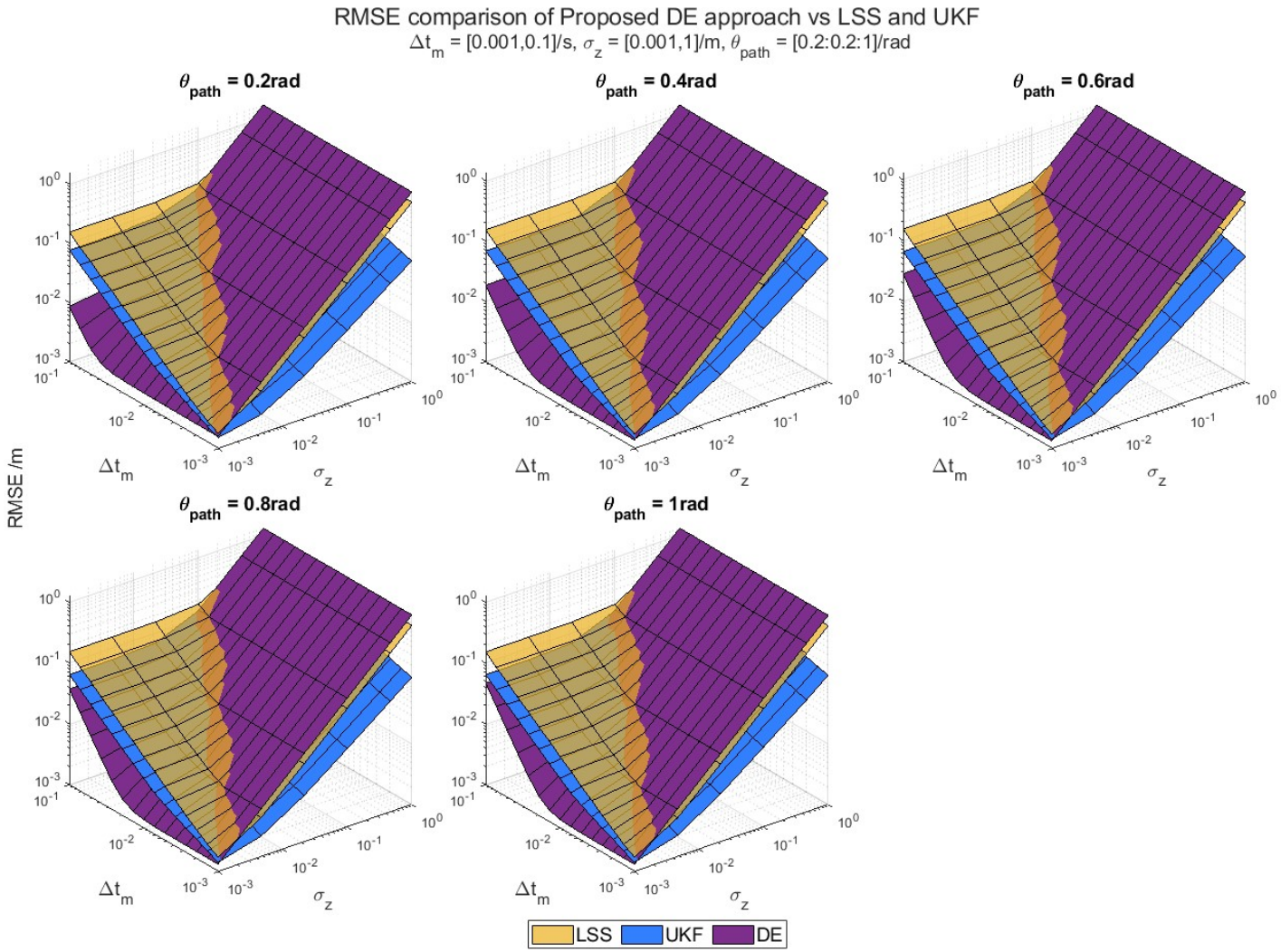

Figure 6.3 - Result plot from comparing LSS, UKF and proposed Direct Extrapolation method

While Figure 6.3 provides an overview of the system performance, to further assess the proposed DE solution, the following section evaluates the DE response at the sensor level. Specific parameters are isolated and adjusted as defined in Table 6.1. With a focus on IML throughout this thesis, the range of parameter values are selected to highlight the IML effects on sensor Range Error (RE), both regarding the obtained measurement error $\varepsilon_{t_k}^{R,i}$, as in (5.12), and the extrapolated estimate error $\varepsilon_{t_k}^{R,DE,i}$ obtained by the DE process. These are referred to as the Measurement Range Error (MRE) and the Extrapolated Range Error (ERE) respectively:

$$\varepsilon_{t_k}^{R,i} = d_{t_k}^i - \hat{d}_{t_k^i}^i, \tag{6.16}$$

$$\varepsilon_{t_k}^{R,DE,i} = d_{t_k}^i - \hat{d}_{t_k,est}^i. \tag{6.17}$$

Where $d_{t_k}^i$ is the true distance between the $i'th$ sensor position and the target's true position at the $k'th$ estimation instant, $\hat{d}_{t_k^i}^i$ is the sensor measurement obtained within the sampling period $[t_k, t_{k-1})$ and $\hat{d}_{t_k,est}^i$ is the extrapolated estimate generated by the DE process (6.13).

In addition, for further insight, the rate of change between consecutive measurements $\Delta\hat{d}_{t_k^i,t_{k-1}^i}^i$ is also given in the following plotted results. Due to the scale of $\Delta\hat{d}_{t_k^i,t_{k-1}^i}^i$ values in relation to the RE components the $\Delta\hat{d}_{t_k^i,t_{k-1}^i}^i$ value is halved to allow for better comparison on a single axis.

Table 6.1 - Values evaluated for the Sensor level study on DE response

Test	IML ($\boldsymbol{\Delta t_m}$) /s	Measurement noise $\boldsymbol{\sigma_z}$ /m	Path angle $\boldsymbol{\theta_{path}}$ /rad
1	0.1	[0.1,0.01,0.001]	0.2
2	[0.1,0.0518,0.01]	0.001	0.2
3	0.1	0.001	[0.2,0.6,1]

Throughout the following studies, Algorithm **16** is evaluated under the Reference Simulation given in Algorithm 11 but for the fixed values given in Table 6.1. To avoid eliminating the random sensor measurement noise, the simulation is iterated only once. Additionally, to clearly indicate the cyclic pattern of error only a single path cycle is presented in the following plots. Figure 6.4 is provided for reference throughout the following analysis.

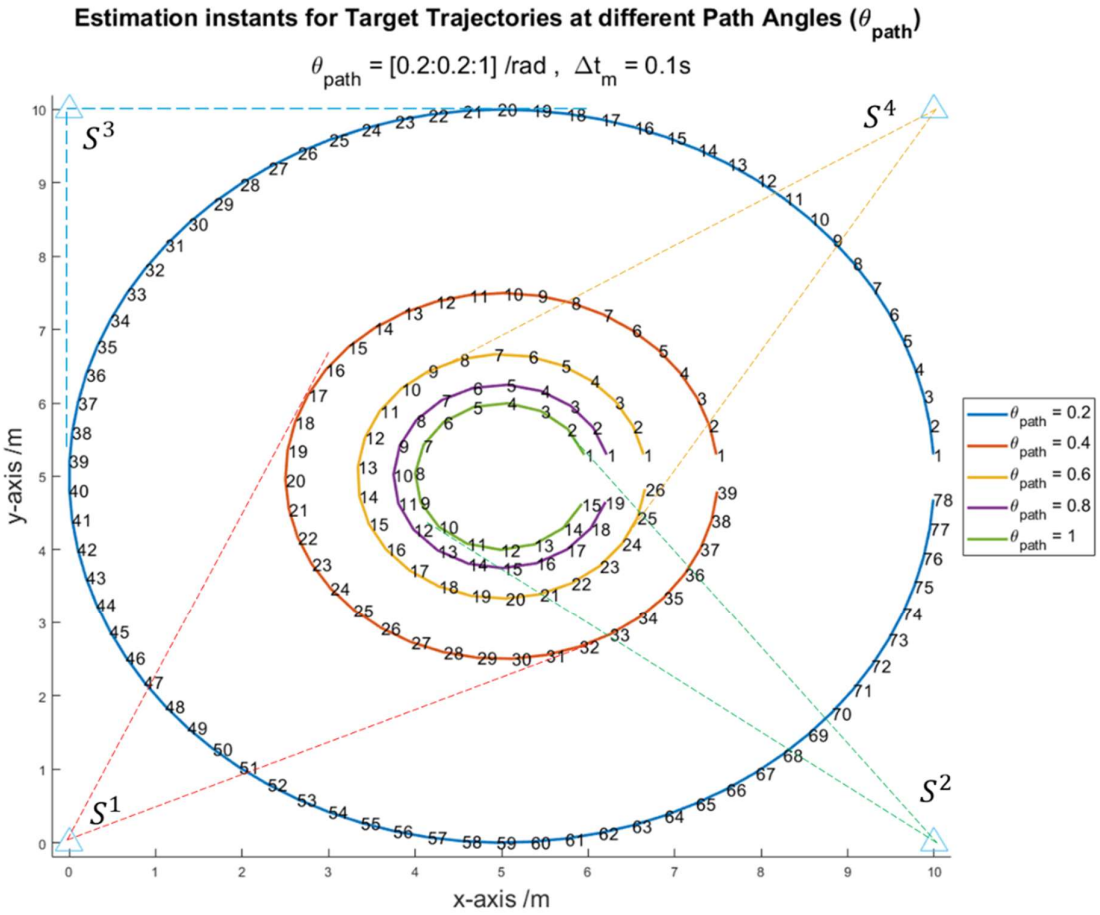

Figure 6.4 - Target trajectories and labelled estimation intervals for simulated scenario. Numbers indicate the iteration of the estimation instants. Triangles mark the sensor positions, numbered according to their identifier and subsequent sequence. Dashed lines used to illustrate the points at which the target exhibits a constant change in measurement value respective to the sensor.

6.2.1.1.1.1 DE Sensor Response Under Variable Measurement Noise

The individual sensor responses under Test 1 conditions are illustrated in Figure 6.5 which highlight the effects of sensor measurement noise on the extrapolated Range Errors (REs).

In accordance with the RMSE results from Figure 6.3, under low sensor measurement noise, as shown in Figure 6.5a- Figure 6.5d, the proposed DE approach significantly reduces the overall error as illustrated by the MRE and lower ERE values.

The extrapolation process however incurs errors due to the linear change assumption. This is because the linear extrapolations do not correctly describe the true change between consecutive distance measurements. This is identified more easily using the plotted $\Delta\hat{d}^{i}_{t^{i}_{k},t^{i}_{k-1}}$ values, where the

extrapolated errors are shown to be greatest when the rate of change is at a maximum. Similarly, the EREs are negated where the rate of change is zero and the linear assumption is satisfied.

Moreover, using the plotted trajectories given in Figure 6.4, the estimation instant at which the peak occurs for each sensor can be identified. This occurrence of peak ERE correlates to the target's trajectory relative to the sensor, as discussed in the previous IML studies in chapter 5. The scenario observations in Figure 5.4 indicate how the target's trajectory, relative to the sensor, effects the IML error. This can also be perceived as the change in the true measurement value over time. In these scenarios, the change in measurement values were seen to follow a linear relationship, or a highly non-linear relationship, depending on the target's velocity relative to the sensor position. From this, the most non-linear change in measurements occurs when the target travels along the tangent path off the circle formed by the previous measurement. This correlates to the nearest and furthest points on the circular path relative to the sensor. The linear extrapolations fail to accurately describe the true rate of change in measurements in these highly non-linear instances, resulting in greater EREs. Additionally, as shown in Figure 5.4 Scenario 2, the higher non-linearity was observed for shorter distances. Hence why the linear extrapolations exhibit more significant REs as the target passes closest to the respective sensor. At these instances, relative changes in range measurements are more abrupt. In short, where the change in measurements is least consistent, the linear extrapolations lead to the highest extrapolated REs. This is evaluated further in later test results. Observing the increase in sensor measurement noise in Figure 6.5, the noise quickly corrupts the EREs. This is where the extrapolation method is sensitive to noise since the process augments not only the measurement but the noise component too.

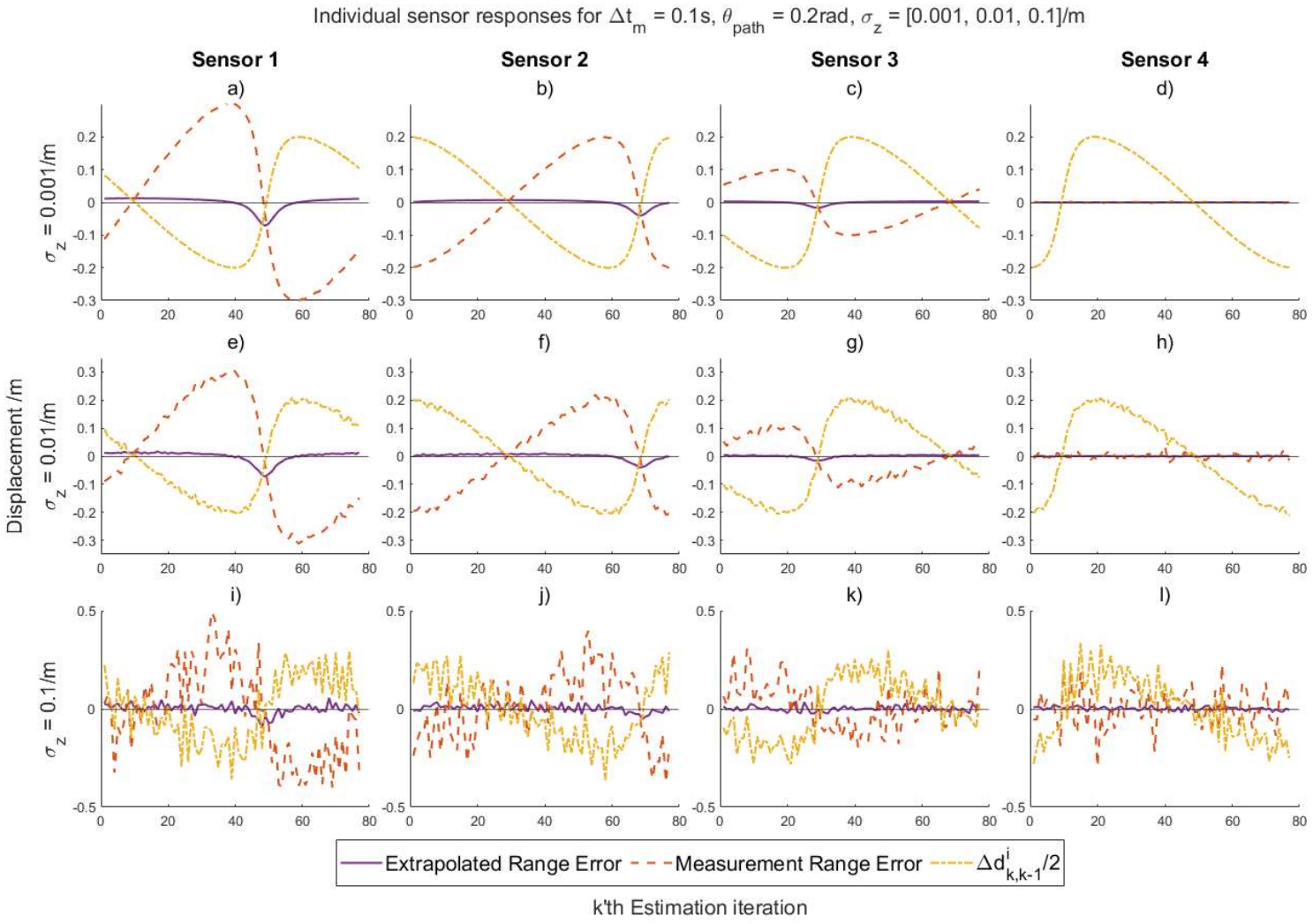

Figure 6.5 - DE sensor Range errors under variable sensor measurement noise σ_z , Path angle = 0.2 rad, IML = 0.1 s

DE Sensor Response Under Variable IML

The individual sensor responses under Test 2 conditions are illustrated in Figure 6.6, where to identify the EREs more easily, the measurement RE and $\Delta\hat{d}^{i}_{t^{i}_{k},t^{i}_{k-1}}$ plots are omitted. Most noticeably the IML is seen to exacerbate the EREs across all sensors.

As established in the analysis of Test 1 results, given in Section 6.2.1.1.1.1, the linear extrapolations are prone to errors. The magnitude of these extrapolation errors correlates to the sensor sequence, such that sensor one and sensor four exhibit the greatest and least ERE respectively. This effect is attributed to the extended period of required extrapolation to compensate for the greater MLa. Since the estimation is carried out at the instant of the most recent $(i = 4)$ measurement, there is no MLa for the last measurement and therefore no need for extrapolation. In this case the resultant ERE is purely measurement noise. This is highlighted in Figure 6.5 where the REs are equivalent.

Test 2 results also reflect the observations made for Test 1. Whereas the IML increases, the error becomes more systematic, and the errors become less random.

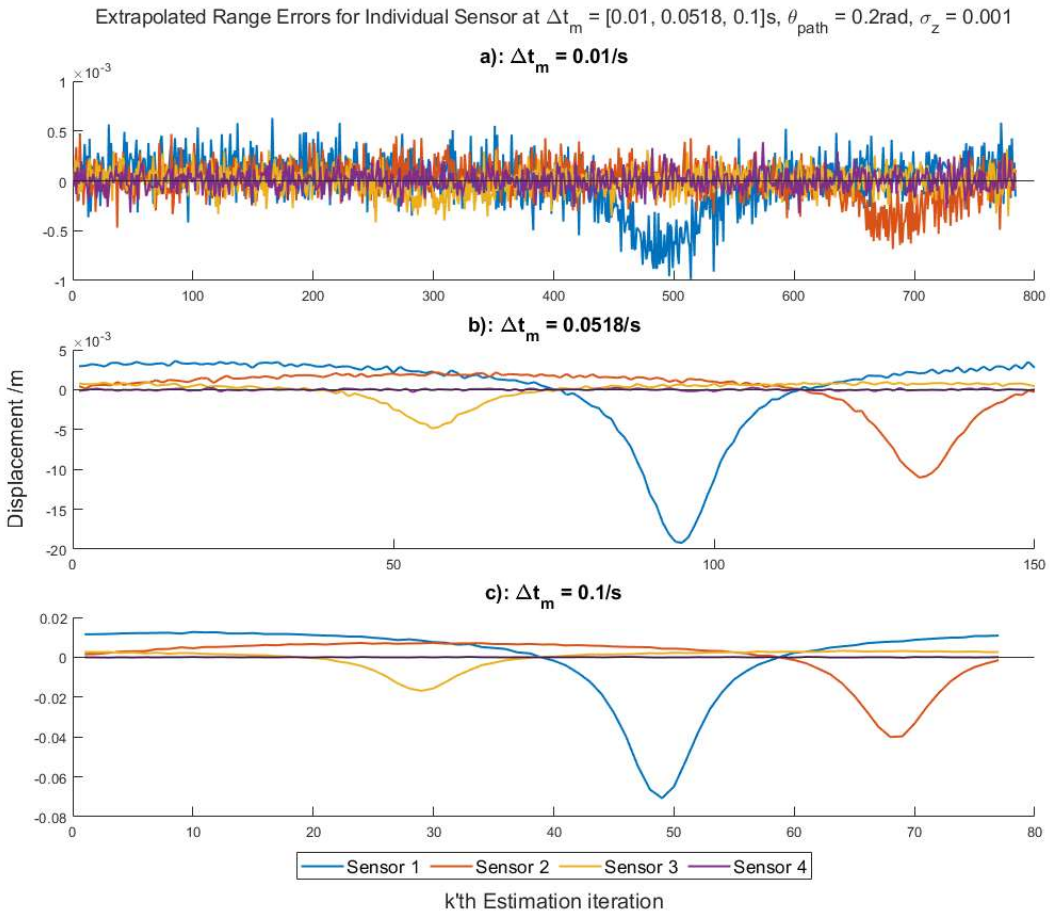

Figure 6.6 - Direct Extrapolation Sensor errors for variable IML. Path angle = 0.4 rad and Measurement noise =1 mm.

6.2.1.1.1.2 DE Sensor Response Under Variable Path Angle

The individual sensor responses under Test 3 conditions are illustrated in Figure 6.7, where it can be observed that the larger Path Angle (PA) leads to an increase in RE but a more evenly distributed error.

Firstly, the PA impacts the linear change assumption. As the target's trajectory becomes more non-linear, the change in measurement is more significant. Therefore, the ERE increases due to the applied linear extrapolation assumption failing to correctly describe a less constant change in distance. While it is not fairly represented in Figure 6.7, as the x-axis scales are not equivalent, it should be noted that for greater PA, the same change in measurement value is carried out over significantly less estimation intervals.

Secondly, where the PA is increased, the radius of the trajectory path is reduced. The radius of the circular path affects the relative distances from the sensor to the nearside and the far-side of the circular path. Consequently, the rate of change in measurements is more evenly distributed resulting in a higher positive to negative error ratio.

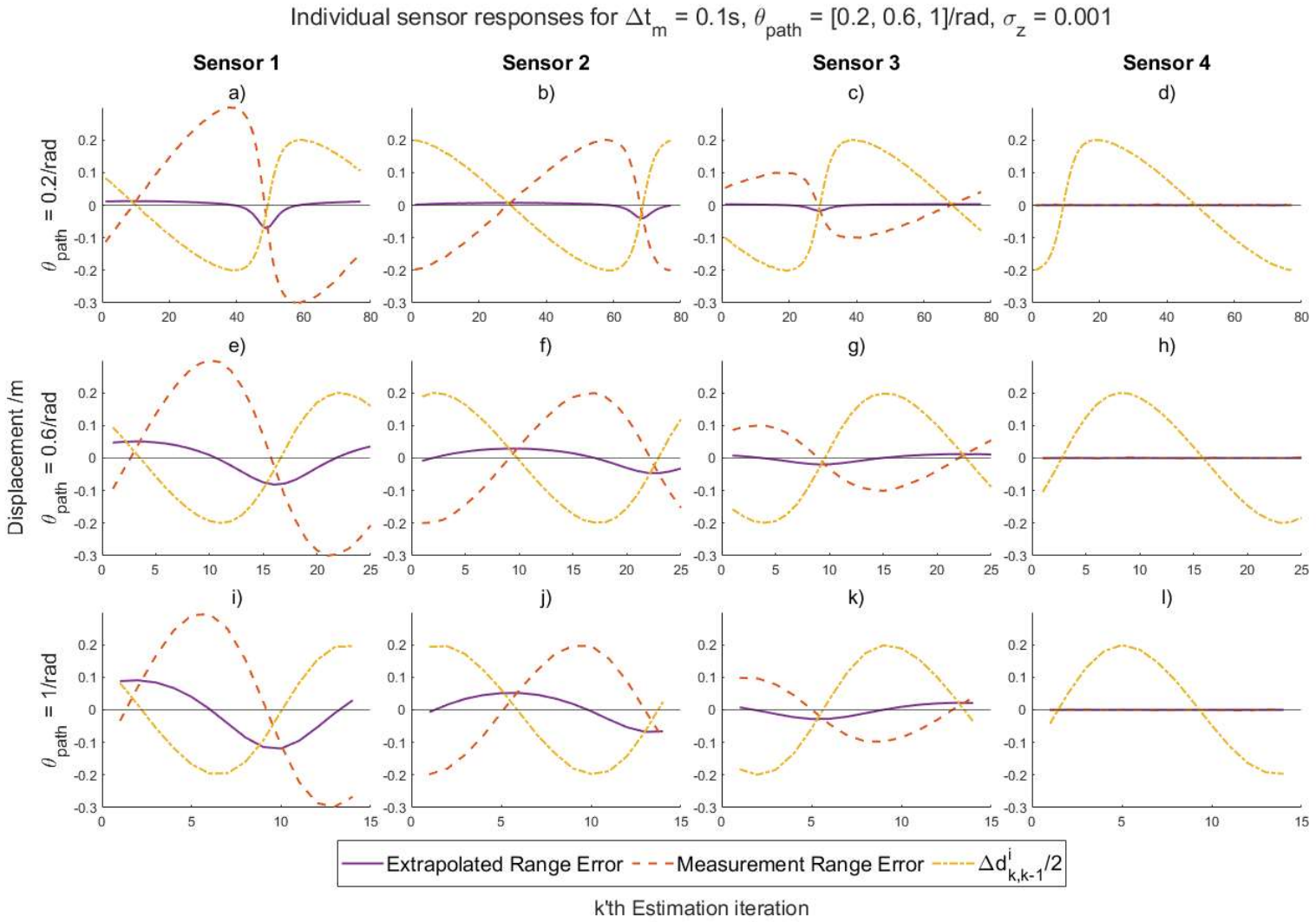

Figure 6.7 - DE Sensor range errors under variable Path angle for IML = 0.1 s and Measurement noise = 1 mm.

From the sensor level study conducted in Tests 1, 2 and 3, it is evident that the EREs, much like the IML error component, are a function of the random sensor measurement noise. The true change in measurement values is attributed to the target's velocity vector and position of the target relative to the sensor as well as the IML which affects the extent of extrapolations and consequently exaggerates the extrapolation error.

The results highlight that the principle of the DE approach works well to counter the effects of asynchronous measurements. However, small sensor measurement noise values reduce the effectiveness of the solution considerably and present the greatest challenge. This occurs because the extrapolation process exacerbates both the measurement and the noise component of the observation. Additionally, the rate of change described by the linear extrapolation process suffers lag under the nonlinear scenario. Critically, to attain a better response from the proposed solution the measurement noise must first be reduced. The following section considers noise reduction using Kalman Filter (KF) techniques.

6.2.1.2 The Proposed Kalman Extrapolated Least Squares (KELS) Solution

Linear Kalman Filters (LKFs) can be effectively applied to each sensor measurement for noise reduction and prediction. LKFs, unlike non-linear Kalman filters present a much lower computational burden, therefore should not significantly increase the complexity of the proposed approach. The less noisy output of the LKF is extrapolated to form a set of pseudo measurements which are applied to the LSS multilateration approach for state estimation. The following section describes the proposed KELS method.

6.2.1.2.1 The Linear Kalman Filter Model

Within the Fusion Centre (FC) sampling period $[t_k, t_{k-1})$, the proposed KELS solution employs a LKF for all sensor measurements. During the prediction phase the LKF must initially predict the measurement value $\hat{d}^i_{t^i_k}$ for $i = (1, \cdots, N)$. These predicted measurements are subsequently fused with sensor observations $z^i_{t^i_k}$ for $i = (1, \cdots, N)$ to determine the optimal measurement values. The $i'th$ sensor measurement at t^i_k can be predicted using a Constant Velocity (CV) model:

$$\hat{d}^i_{t^i_k} = \hat{d}^i_{t^i_{k-1}} + \Delta T^i_{t^i_k, t^i_{k-1}} * V^i_{t^i_{k-1}, t^i_{k-2}}. \tag{6.18}$$

Where $\hat{d}^i_{t^i_{k-1}}$ is the obtained range measurement received in the previous estimation period $[t_{k-1}, t_{k-2})$, $\Delta T^i_{t^i_k, t^i_{k-1}}$ is the estimation period given by $t^i_k - t^i_{k-1}$ and $V^i_{t^i_{k-1}, t^i_{k-2}}$ is the velocity, given by the range displacement over time:

$$V^i_{t^i_{k-1}, t^i_{k-2}} = \frac{\hat{d}^i_{t^i_{k-1}} - \hat{d}^i_{t^i_{k-2}}}{t^i_{k-1} - t^i_{k-2}} = \frac{\Delta \hat{d}^i_{t^i_{k-1}, t^i_{k-2}}}{\Delta T^i_{t^i_k, t^i_{k-1}}}. \tag{6.19}$$

For a generalized asynchronous scenario, the process equation is given in the matrix form $X^i_{t^i_k} = A^i_{t^i_k} X^i_{t^i_{k-1}}$ as:

$$\begin{bmatrix} \hat{d}^i_{t^i_k} \\ V^i_{t^i_k, t^i_{k-1}} \end{bmatrix} = \begin{bmatrix} 1 & \Delta T^i_{t^i_k, t^i_{k-1}} \\ 0 & 1 \end{bmatrix} \begin{bmatrix} \hat{d}^i_{t^i_{k-1}} \\ V^i_{t^i_{k-1}, t^i_{k-2}} \end{bmatrix}. \tag{6.20}$$

Where $\begin{bmatrix} \hat{d}^i_{t^i_k} \\ V^i_{t^i_k, t^i_{k-1}} \end{bmatrix}$ is the state $X^i_{t^i_{k-1}}$ to be determined and $\begin{bmatrix} 1 & \Delta T^i_{t^i_k, t^i_{k-1}} \\ 0 & 1 \end{bmatrix}$ is the state transition matrix $A^i_{t^i_k}$.

Throughout runtime, the timestamps of the received data are compared to establish the estimation period $\Delta T^i_{t^i_k, t^i_{k-1}} = t^i_k - t^i_{k-1}$. For initialisation the first two measurements $\hat{d}^i_{t^i_2}$ *and* $\hat{d}^i_{t^i_1}$ and their respective timestamps t^i_2 *and* t^i_1 would be applied within (6.19) to establish the initial velocity value of $V^i_{t^i_2, t^i_1}$. Due to this initialisation process, the proposed solution does not produce an estimate until the third estimation interval, consequently the initialised state vector is $X^i_{t^i_2}$.

6.2.1.2.2 Batch vs Sequential Approach

Noticeably the matrix dimensions for a single sensor as shown above are very low, allowing for high computational efficiency. However, for a sensor network of N sensors applying this to a batch process equation for the system would be as follows:

$$\begin{bmatrix} \hat{d}^1_{t^1_k} \\ V^1_{t^1_k, t^1_{k-1}} \\ \vdots \\ \hat{d}^N_{t^N_k} \\ V^N_{t^N_k, t^N_{k-1}} \end{bmatrix} = \begin{bmatrix} 1 & \Delta T^1_{t^1_k, t^1_{k-1}} & \cdots & 0 & 0 \\ 0 & 1 & \cdots & 0 & 0 \\ \vdots & \vdots & \ddots & \vdots & \vdots \\ 0 & 0 & \cdots & 1 & \Delta T^N_{t^N_k, t^N_{k-1}} \\ 0 & 0 & \cdots & 0 & 1 \end{bmatrix} \begin{bmatrix} \hat{d}^1_{t^1_{k-1}} \\ V^1_{t^1_{k-1}, t^1_{k-2}} \\ \vdots \\ \hat{d}^N_{t^N_{k-1}} \\ V^N_{t^N_{k-1}, t^N_{k-2}} \end{bmatrix}. \tag{6.21}$$

Where the given state dimensions are $2N * 1$, the KF process is expected to suffer from dimensionality in which the expansion of the KF dimensions, due to higher sensor numbers, will lead to a reduced performance as high dimension matrix multiplication is computationally costly.

Furthermore, in a batch process the computation cannot begin until the $N'th$ sensor measurement is received by the FC, resultantly the Kalman filtering, extrapolation and multilateration processes will only commence at the end of the sampling period. Consequently, a batch approach is expected to lead to an increase in estimation latency and a surge in processing power.

Alternatively, drawing inspiration from sequential KF approaches [175], [188], the use of multiple lower dimension LKFs (6.31) may be employed sequentially.

The proposed KELS process uses an individual Linear Kalman filter (LKF^i) for each sensor. Each sensor specific LKF can be executed the instant a measurement is received, thereby spreading the computations throughout the sampling period. This results in a lower overall estimation latency and even distribution of processing demands. Furthermore, the sequential approach reduces the dimension of the KF matrices and thus redundant calculations.

For each sensor, once a measurement is obtained, the prediction stage for the $i'th$ sensor KF LKF^i is computed [133]:

$$\hat{X}^{i-}_{t^i_k} = A^i_{t^i_k} \hat{X}^i_{t^i_{k-1}}, \tag{6.22}$$

$$P^{i-}_{t^i_k} = A^i_{t^i_k} P^i_{t^i_{k-1}} \left(A^i_{t^i_k}\right)^T + Q^i_{t^i_k, t^i_{k-1}}. \tag{6.23}$$

The predicted sensor range estimate is then compared in the measurement update stage [133]:

$$K_{t^i_k} = P^{i-}_{t^i_k} H^T \left(H P^{i-}_{t^i_k} H^T + R\right)^{-1}, \tag{6.24}$$

$$\hat{X}^i_{t^i_k} = \hat{X}^{i-}_{t^i_k} + K_{t^i_k} \left(z^i_{t^i_k} - H\hat{X}^{i-}_{t^i_k}\right), \tag{6.25}$$

$$P^i_{t^i_k} = \left(I - K_{t^i_k} H\right) P^{i-}_{t^i_k}. \tag{6.26}$$

In which,

$$P^i_{t^i_k} = \begin{bmatrix} \sigma_d^2 & \sigma_d \sigma_V \\ \sigma_d \sigma_V & \sigma_V^2 \end{bmatrix}, H = \begin{bmatrix} 1 & 0 \end{bmatrix}, R = \sigma_z^2. \tag{6.27}$$

In which, σ_d is the standard deviation of the range estimate, σ_V is the standard deviation of the estimated velocity and σ_z^2 is the variance of the sensor measurement noise which is assumed to be known and derived from empirical measurements. As the process employs a CV model, the applied process noise covariance matrix $Q^i_{t^i_k, t^i_{k-1}}$ is given by the Discrete-time Nearly Constant Velocity (DNCV) matrix structure [142]:

$$Q^i_{t^i_k, t^i_{k-1}} = \begin{bmatrix} (\Delta T^i_{t^i_k, t^i_{k-1}}/4 & (\Delta T^i_{t^i_k, t^i_{k-1}})^3/2 \\ (\Delta T^i_{t^i_k, t^i_{k-1}})^3/2 & (\Delta T^i_{t^i_k, t^i_{k-1}})^2 \end{bmatrix} \sigma_a^2. \tag{6.28}$$

Note that matrices $H\ and\ R$ are fixed values and therefore not denoted with a time subscript.

6.2.1.2.3 Kalman Filter Prediction for Extrapolation

The KELS solution so far employs Kalman filtering to reduce measurement noise, extrapolation for pseudo-measurement synchronization and the LSS for state estimation. Applying the predictive ability of KFs, like the SUKF solutions presented by Zhang *et al.* [188] and similar to predictive tracking for latency reduction [7], [124], [125], the sensor KFs can be used to carry out an additional prediction stage. This is referred to as the 'synch prediction', to attain the estimate of the sensor measurement at the fusion instant.

The synch prediction stage is conducted to synchronise each sensor measurement to the estimation instant. Due to the differing magnitudes of MLa for each sensor the synch prediction is carried out over the MLa period. For a general asynchronous sensor network, where the IML is not constant, the MLa is variable and given for the $k'th$ estimation instant by:

$$\Delta t_{i,k} = t_k - t_k^i. \tag{6.29}$$

Taking the generalized set of equations, given by (6.20), the prediction stage is repeated where $\Delta T^i_{t_k^i, t_{k-1}^i}$ is given by $\Delta t_{i,k}$.

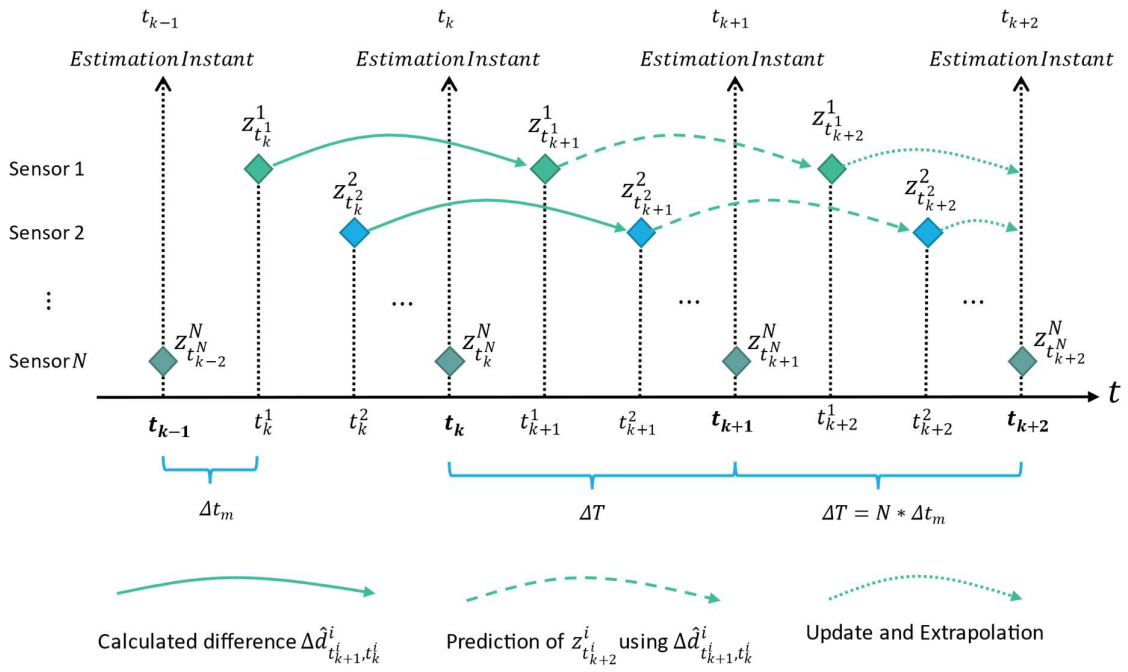

Figure 6.8 -Timing sequence of estimates and processes for KF range smoothing and extrapolation

Figure 6.8 illustrates the timing process and predictive nature of the individual KFs approach for extrapolation. Measurements are obtained during the $[t_k, t_{k-1})$ and $[t_{k-1}, t_{k-2})$ estimation periods.

6.2.1.2.4 Sequential Sampling Adjustment of KELS Algorithm

The proposed solution presented above is given for a generalised asynchronous solution where the IML may not be constant through each estimation period.

Throughout this thesis the considered sampling scenario given in Section 5.2 regards sequential sampling with constant IML values. As such the sampling rate of each sensor $\Delta T^{i}_{t^{i}_{k},t^{i}_{k-1}}$ is assumed constant and equal to ΔT. One can simplify the discrete time process of the range measurements to a Constant Change (CC) model in which the range measurement at the next time instance is equivalent to the sum of the previous measurements and the rate of change in measurement distance per sampling period:

$$\hat{d}^{i}_{t^{i}_{k}} = \hat{d}^{i}_{t^{i}_{k-1}} + \Delta T * \frac{\hat{d}^{i}_{t^{i}_{k-1}} - \hat{d}^{i}_{t^{i}_{k-2}}}{\Delta T} = \hat{d}^{i}_{t^{i}_{k-1}} + \Delta\hat{d}^{i}_{t^{i}_{k-1},t^{i}_{k-2}}. \tag{6.30}$$

The CC model involves initialising $\Delta\hat{d}^{i}_{t^{i}_{k-1},t^{i}_{k-2}}$ at the start of the process, where $k = 2$. The CC process equation for the $i'th$ sensor LKF (LKF^{i}) therefore can be simply represented in the following matrix form $X^{i}_{t^{i}_{k}} = AX^{i}_{t^{i}_{k-1}}$:

$$\begin{bmatrix} \hat{d}^{i}_{t^{i}_{k}} \\ \Delta\hat{d}^{i}_{t^{i}_{k},t^{i}_{k-1}} \end{bmatrix} = \begin{bmatrix} 1 & 1 \\ 0 & 1 \end{bmatrix} \begin{bmatrix} \hat{d}^{i}_{t^{i}_{k-1}} \\ \Delta\hat{d}^{i}_{t^{i}_{k-1},t^{i}_{k-2}} \end{bmatrix}. \tag{6.31}$$

Where $\begin{bmatrix} \hat{d}^{i}_{t^{i}_{k}} \\ \Delta\hat{d}^{i}_{t^{i}_{k},t^{i}_{k-1}} \end{bmatrix}$ is the state $X^{i}_{t^{i}_{k}}$ to be determined and $\begin{bmatrix} 1 & 1 \\ 0 & 1 \end{bmatrix}$ is the state transition matrix A. The synch prediction stage is then given by a repeated prediction step with a sensor specific state transition matrix A^{i}_{sync} and process noise covariance matrix Q^{i}_{synch} [142]:

$$A^{i}_{synch} = \begin{bmatrix} 1 & \Delta t_i \\ 0 & 1 \end{bmatrix}, \quad Q^{i}_{synch} = \begin{bmatrix} (\Delta t_i)^4/4 & (\Delta t_i)^3/2 \\ (\Delta t_i)^3/2 & (\Delta t_i)^2 \end{bmatrix} \sigma_a^2 \tag{6.32}$$

In which the MLa is fixed and given by:

$$\Delta t_i = \frac{\Delta t_m (N - i)}{N}. \tag{6.33}$$

6.2.1.2.5 The Kalman Extrapolated Weighted Least Squares Solution

The consideration of applied weightings is evaluated in the next part of this chapter. In general, for a homogenous system of sensors, the sensor measurement errors are equivalent. Therefore, the use of evenly distributed errors provides no additional information to the solution. Where sensors present

different measurement errors, these differences can be proportionally weighted. The weighted estimates are then considered within the WLS solution given in Section 2.1.3.1.5.1. leading to the Kalman Extrapolated Weighted Least Squares (KEWLS) solution.

So far, the proposed KELS solution has only considered the LSS since the sensors are homogenous. However, the extrapolated pseudo measurements no longer retain equivalent error distributions. This can be seen by the distribution of sensor EREs shown in the three previous DE test results. In the simulated scenario due to the AWGN, the sensor measurement noise is evenly applied to all sensors. In contrast, the sensor sequence dictates a variability of MLa between all sensors, which results in a greater distribution of errors for the earlier sensors in the sequence. Due to the equidistant sensor separations, sampling configuration and target trajectory considered, the PA affects the sensor errors of those that experience MLa evenly. There is a slight disparity when considering the $N'th$ sensor under variable PA, as this is not subjected to any MLa and therefore no additional extrapolation errors arise in the $N'th$ sensor from a change in PA. As such, while the PA varies all sensors except the last experience a change in error. This is observable in the results of the DE scenario for Test 3 as shown in Figure 6.7. While this may be explored in greater detail in further work, this PA disparity only effects a single sensor. Therefore, during this study, only the disparity between sensor error distributions due to MLa effects, which effect all sensors and are considered to have a more prominent effect, are considered.

The effects of MLa can be clearly seen in the results of the DE scenario for Test 2 as shown in Figure 6.6. To compensate for this, the more recently obtained measurement should be weighted higher than earlier measurements. However, this generalized assumption does not hold true for all time instances because EREs are dependent on both the velocity vector and the sensor position relative to the sensor. The simulated scenario considered throughout this thesis highlights the fluctuations in EREs with peaks of errors visible at distinct estimation intervals. Therefore, at a given estimation instant the errors may not correlate with the sensor sequence.

Whilst this is acknowledged, the adaptive identification of the error magnitude, at distinct instances respective of the targets position and dynamics relative to each sensor, presents additional complexity to the solution which is not in line with the scope of this chapter.

When assessing computational efficiency, the assumption applied is that the sensors weightings are relative to the sensor sequence. This can be neatly extracted from state estimate covariance matrix provided by the individual KFs after the synch prediction. These measurement variances can be applied to a WLS solution as measurement weightings. The inclusion of weightings within the KELS process is referred to as the KEWLS solution. The weightings approach and how it is applied is described below.

6.2.1.2.5.1 Weighting approach

The respective variances $\sigma^2_{\hat{d}^i_{t_k,est}}$ of each pseudo-measurement $\hat{d}^i_{t_k,est}$ are extracted from the state estimate covariance matrix as $P^i_{t_k}(1,1)$. These are then applied as weightings using a Weighted Least Squares (WLS) approach [44].

$$\bar{\vartheta} = (G^T W^{-1} G)^{-1} G^T W^{-1} \hat{b}. \tag{6.34}$$

Where W is given as in (2.17).

$$W = DC_d D. \tag{2.17}$$

In which, D and C_d are diagonal matrices of the extracted pseudo-measurements and the variances respectively.

$$D = -2 * diag([\hat{d}^1_{t_k,est}, \hat{d}^2_{t_k,est}, \cdots, \hat{d}^N_{t_k,est}]), \tag{6.35}$$

$$C_d = diag\left(\left[\sigma^2_{\hat{d}^1_{t_k,est}}, \sigma^2_{\hat{d}^2_{t_k,est}}, \cdots, \sigma^2_{\hat{d}^3_{t_k,est}}\right]\right). \tag{6.36}$$

The Proposed KELS and KEWLS solution is summarised in Algorithm **17**. The author of this thesis notes that the state and covariance estimates generated from the synch prediction may be applied directly to generate the following state and state covariance within the subsequent prediction stage. For ease of explanation, this alternative approach is not reflected in this thesis. Alternatively, the results of the synch prediction step are utilised for multilateration and then subsequently ignored.

Algorithm 17: The Proposed KELS and KEWLS Solution[22]

***INPUT*:** Sensor positions $\boldsymbol{S^i = [x^i, y^i]^T}$ *for* $\boldsymbol{i = (1: N)}$

Initialisation: Under the given static sensor and constant IML scenario:

1: Establish ΔT from (6.7)

Compute each sensors fixed Kalman filters

2: *For* $i = (1: N)$

Determine initial matrices

3: $P^i_{t^i_2}$ initialised as an identity matrix

4: *For k = (1:2)*

5: Compute $\Delta\hat{d}^i_{t_2,t_1}$ from (6.2) using $z^i_{t^i_k} \rightarrow d^i_{t^i_k}$

6: Initialise $X^i_{t^i_2} = \left[\hat{d}^i_{t^i_2}, \Delta\hat{d}^i_{t^i_2,t^i_1}\right]^T$

7: *End*

Determine synch matrices

8: Determine Δt_i from (6.33)

9: Compute A^i_{synch} and Q^i_{synch} as per (6.32)

10: *End*

11: Generate $H = [1\ 0\ ]$ *&* $A = [10; 01]$ as per (6.31)

12: Compute $Q^i_{t_2,t_1}$ using (6.28) where $\Delta T \rightarrow \Delta T^i_{k,k-1}$

Estimation Loop

13: *For k = (3: Number of estimation intervals)*

14: *For* $i = (1: N)$

15: Execute LKF^i prediction (6.22) *&* (6.23) using $i'th$ sensor filter matrices $X^i_{t^i_{k-1}}$ & $P^i_{t^i_{k-1}}$

16: Obtain $i'th$ sensor observation $z^i_{t^i_k}$ and respective covariance matrix R

17: Execute LKF^i update (6.24) - (6.26) using $i'th$ sensor filter matrices $X^{-i}_{t^i_k}$ & $P^{-i}_{t^i_k}$

18: ***Perform synch prediction***

19: Obtain $X^i_{t_k}, P^i_{t_k}$ by executing LKF^i prediction (6.22) *&* (6.23) using updated $i'th$ sensor filter matrices $X^i_{t^i_k}, P^i_{t^i_k}$ and the $i'th$ sensor synch prediction matrices A^i_{synch} and Q^i_{synch}.

20: *End*

21: *If performing KELS computation*

22: Extract predicted measurements from $X^i_{t_k}$ for $i = (1, \cdots, N)$

23: Using sensor position data formulate the LSS matrices (6.14)

24: Compute position estimate from LSS using (6.15)

25: *Else If performing KEWLS computation*

[22] Ranges of values are represented in the following manner: (initial value : incremental value : end value) and may, in some cases, be assigned equivalent to a variable. Where an incremental value is not given, the increments are defaulted to integers of one. When used as part of a '*For'* loop, each value in the given range is applied individually within a single loop.

26: | | Compute D and C_d *from* (6.35) and (6.36) respectively

27: | | Determine W from (2.7)

28: | | Carry out WLS using (6.34)

29: | *End*

30: *End*

6.3 Simulation Study Against Existing Techniques

The following sections compare the proposed KELS and KEWLS solutions against the DE and SUKF methods. *Within this section the proposed KELS and KEWLS methods, given by Algorithm 17 are evaluated under the Reference Simulation given in Algorithm 11 for 500 iterations*.

6.3.1 System Identification of KELS

The system identification process employed throughout this thesis is applied again to the proposed KELS solution where the optimal acceleration noise magnitude is equivalent for all sensor LKFs and selected to give the lowest average RMSE for both the highest and lowest PA values. The optimal values of the acceleration noise magnitude for all evaluated IML and measurement noise values are shown in Figure 6.9. Noticeably this exhibits an extremely linear and steady change in optimal acceleration noise magnitude across most scenarios. The sudden peaks visible at the higher IML values represent a region where the optimal acceleration noise magnitude reaches a plateau. At this point, the change in acceleration noise magnitude, across a region of values has a negligible effect on the response of the filter. While these peaks may be removed, they are the product of the utilised codes attempt to find a minimum and are kept for observation purposes and due to their lack of influence. *The difference between KELS and KEWLS is only the use of weightings in the final estimation stage, therefore the optimal process noise values are equivalent in both solutions.*

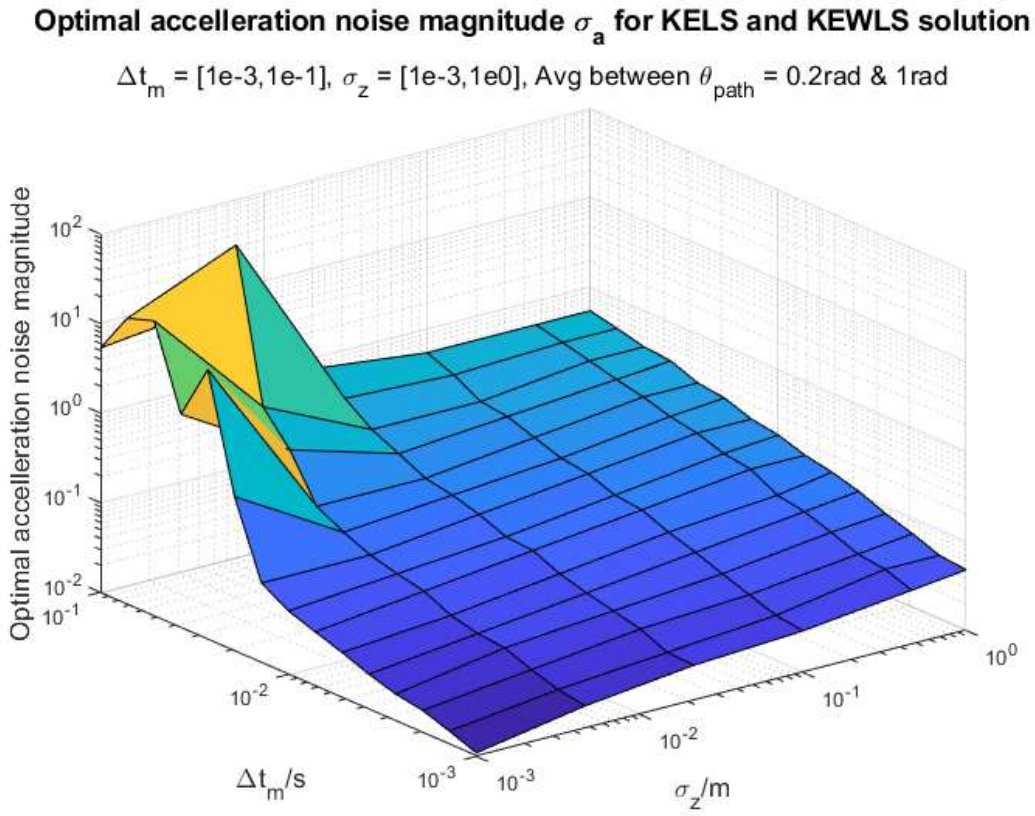

Figure 6.9 - Optimal acceleration noise magnitudes for the proposed KELS and KEWLS solutions at each considered scenario value.

6.3.2 Simulation Results & Analysis

Due to the superior accuracy performance of the SUKF solution demonstrated in chapter 5, the KELS and KEWLS approaches are evaluated against the SUKF alone. The results highlight only a slight difference and are illustrated in Figure 6.10 below as the Percentage difference between each SUKF and KELS RMSE value for the given IML (Δt_m), Sensor measurement noise (σ_z) and PA (θ_{path}) as given in:

$$RMSE\%_{diff} = 100 * \frac{\left(KE(W)LS_{RMSE}(\Delta t_m, \sigma_z, \theta_{path}) - SUKF_{RMSE}(\Delta t_m, \sigma_z, \theta_{path})\right)}{SUKF_{RMSE}(\Delta t_m, \sigma_z, \theta_{path})} \quad (6.37)$$

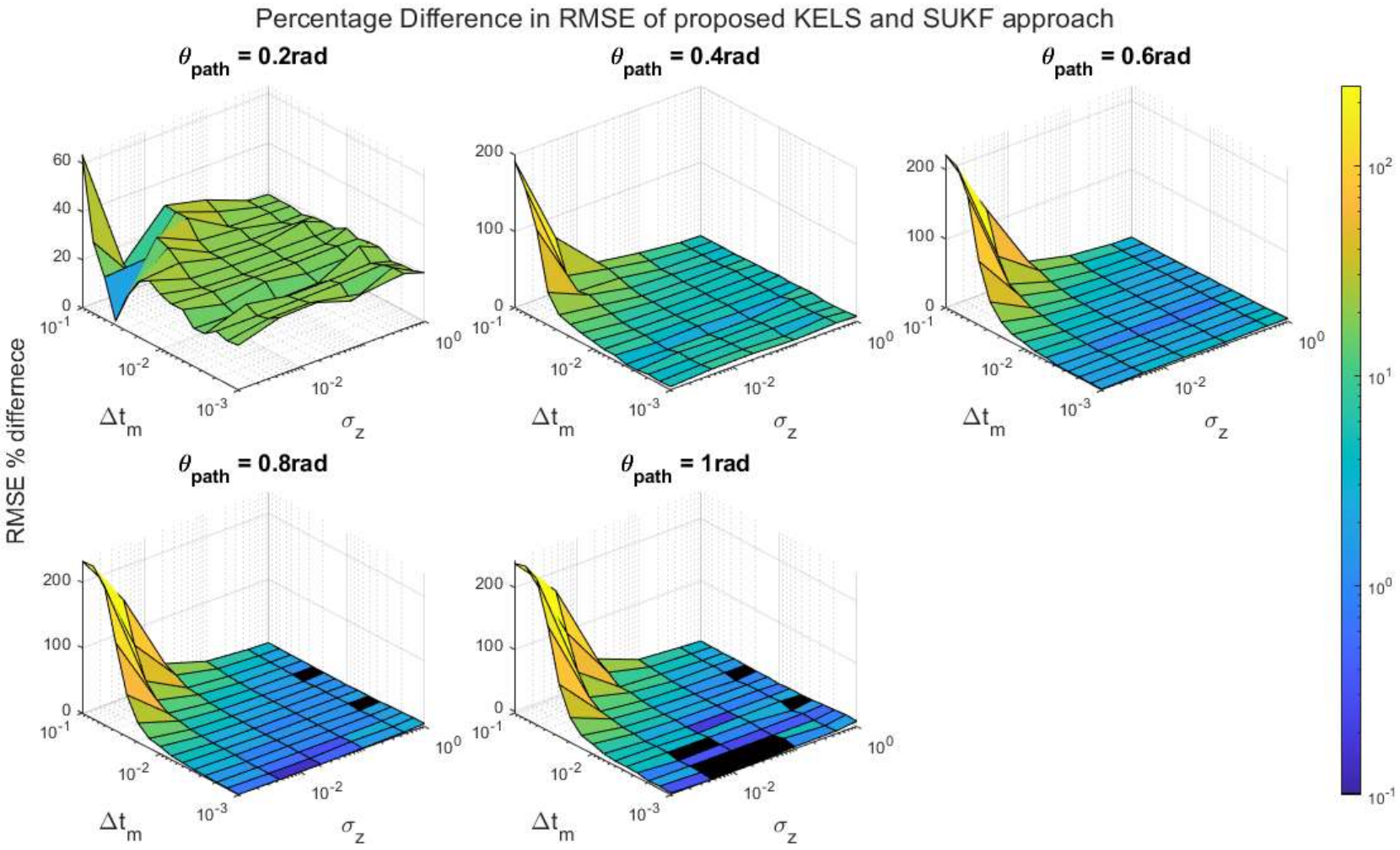

Figure 6.10 - RMSE Positioning error difference between the optimal SUKF and proposed KELS approach

The KEWLS and KELS approaches are highly similar in their relationship to SUKF therefore only the KELS % errors with respect to SUKF are shown in Figure 6.10. With the exception of only a few instances, indicated by the black regions in Figure 6.10, the SUKF obtains a higher accuracy than the KELS solution across all cases as shown by the positive difference. For the more non-linear trajectories, this improvement is very slight across most cases, as the SUKF solution suffers under the CV process model assumption.

Relevant tabulated RMSE data for KELS-CV and KEWLS-CV is provided in Appendix C of this thesis and comparative tabulated data for KELS-CV and KEWLS-CV vs SUKF is provided in Appendix D. The average percentage difference for both the KELS and KEWLS solutions are provided in Table 6.2, from which the average percentage error for the KELS solution are shown to range from 20.51-13.31%.

The KEWLS solution performance is considerably improved with lower minimum, average and maximum percentage errors. In the majority of cases, the KEWLS solution proves superior compared to the SUKF solution. It is important to note that the proposed approaches all suffer significantly at greater IML values where the linear extrapolations fail to accurately respond to changes in measurements. This is observed and analysed in Figure 6.6. However, under scenarios with measurement noise both KELS and KEWLS solutions perform comparably with the SUKF with no significant trends.

For the more linear trajectories, given by $\theta_{path} = 0.2$, the SUKF approach performs significantly better on average than either KELS or KEWLS. This is to be expected as the more linear trajectory is ideally suited to the process model of the SUKF. However, as the PA increases the proposed approaches KELS and KEWLS show significant improvements across a majority of scenarios. Nevertheless, the greater PA amplifies the errors at higher IML where linear extrapolations perform poorly.

In cases where the IML is higher the shortcomings of the proposed solutions, which decrease performance over greater angles, are clearly seen. In general, the proposed approaches KELS and KEWLS perform best across the midrange of angles and show comparable performance to the SUKF solution for a wide range of scenarios.

Table 6.2 – Percentage difference of KELS and KEWLS vs SUKF

Path Angle $\boldsymbol{\theta_{path}}$ (**rad**)	0.2	0.4	0.6	0.8	1
			KELS - SUKF		
Min. % diff	1.85	2.30	0.81	-0.25	-3.18
Avg. % diff	20.51	13.31	14.56	16.49	18.31
Max. % diff	63.61	192.29	221.35	233.92	243.62
			KEWLS - SUKF		
Min. % diff	-10.49	-2.37	-1.68	-1.55	-3.76
Avg. % diff	5.33	4.48	6.35	7.76	8.89
Max. % diff	29.86	107.63	121.26	129.60	135.54

6.3.2.1 KELS vs KEWLS

To compare the proposed approaches, Figure 6.11 below illustrates the percentage error difference between the KELS and KEWLS approach given by:

$$RMSE\%_{diff} = 100 * \frac{\left(KEWLS_{RMSE}(\Delta t_m, \sigma_z, \theta_{path}) - KELS_{RMSE}(\Delta t_m, \sigma_z, \theta_{path})\right)}{KELS_{RMSE}(\Delta t_m, \sigma_z, \theta_{path})} \quad (6.38)$$

The SUKF comparison above, detailed in Table 23, shows that the addition of the assumed weightings in the proposed KEWLS solution provides a consistent benefit across most scenarios. Considerable improvements are seen at lower PAs. As the PA increases the general improvements provided by the weightings have less impact. However, the opposite is true for larger IML scenarios where the weightings provide a markedly superior performance.

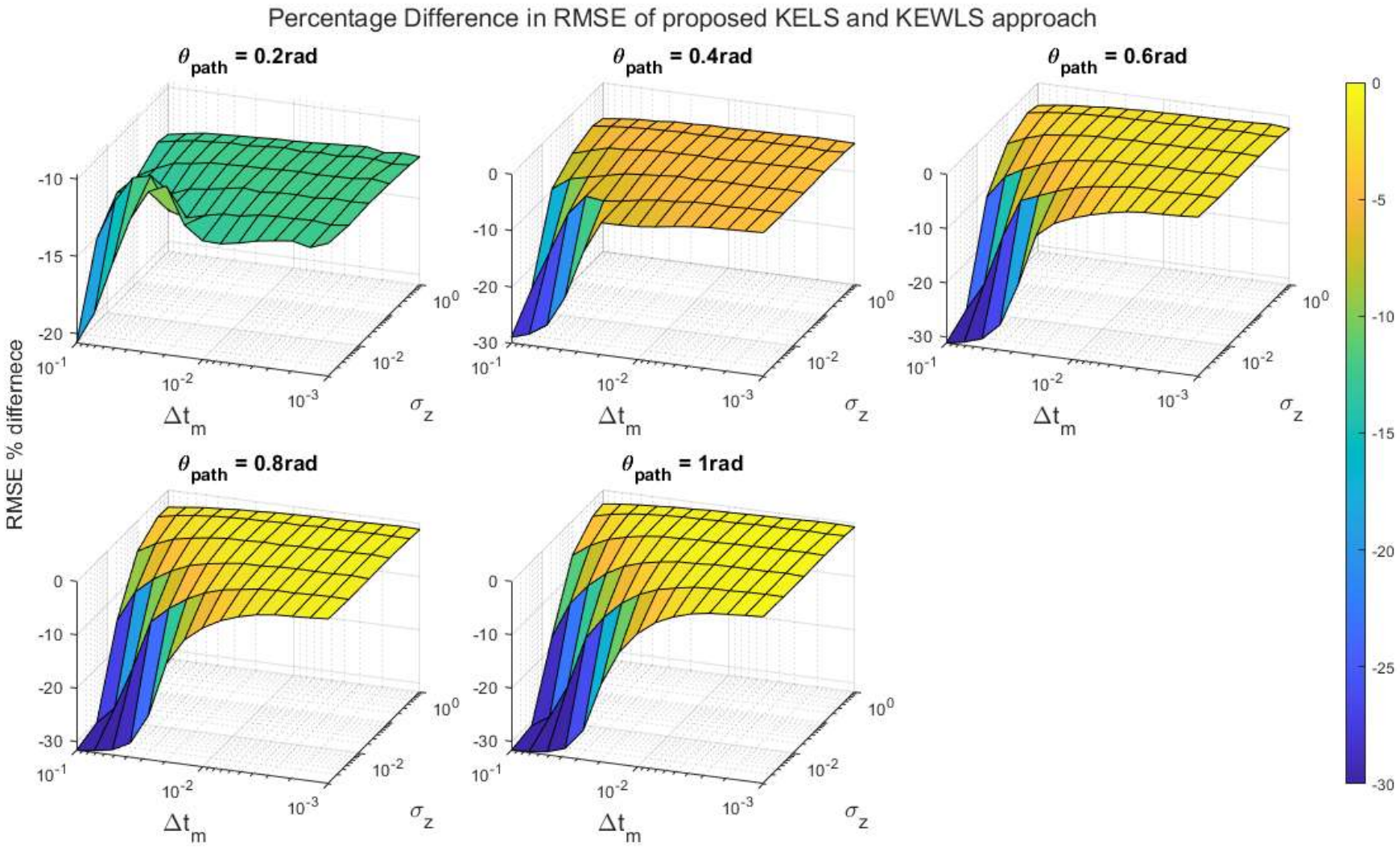

Figure 6.11 - Comparison of proposed KELS and KEWLS approaches

While the weighting is shown to be effective, the convenience of the simplified scenario under which this is tested cannot be dismissed. Given the equidistant sensor positions and circular trajectory each sensor is subjected to an equal distribution of range measurements. However, it can be reasoned that if the target were to favour a single region of the tracking area, the errors received by each sensor would not be equivalent. The sensor measurement noise is also assumed homogenous, which from the data in chapter 1 is evidently not the case, even for sensors of the same type. Furthermore, in practical scenarios measurement noise may fluctuate due to increased distances as is typical of RSS measurements which are worse at greater ranges, or multipath or noises exhibited at different areas within the environment. The IML within this simple scenario is also considered constant, whereas variations in IML between consecutive sensors may differ however the amount of MLa. For these reasons discussed the weightings applied to the KEWLS solution may be idealised to the given scenario and further testing, under non-idealised conditions, should be considered.

6.3.2.2 Timing Performance

The accuracy of the proposed solutions is shown to achieve comparable results to the optimal SUKF solution however the complexity of the proposed solutions are far less. This is tested by calculating the Estimation Runtime (ER) for both KELS and KEWLS in the same manner as previous chapters. The ER describes the average time it takes the processor to complete a single estimation. This is used to provide insight into the computational complexity of a solution. The simulation runtime is calculated using the inbuilt 'tic/toc' function in MATLAB software which, as documented [259], is unreliable for runtimes less than 10 ms. The individual localisation techniques are therefore looped N_L times within the Reference Simulation Scenario, given by Algorithm 11, and later averaged out. The calculation is repeated below for clarity.

$$ER = \frac{1}{N_{Iterations}} \sum_{I=1}^{N_{Iterations}} \left(\frac{Recorded_{runtime}}{7854 * N_{loops}} \right) \tag{5.25}$$

For this test $N_L = 50$, each loop computing all 7854 estimations and repeating the test for 50 iterations. The ER as computed in (5.25) for IML, σ_z and PA set to 1e-3s, 1e-3m and 0.2rad respectively. The KELS and KEWLS solution obtain ER values of 2.35e-5s and 3.31e-5s respectively.

Comparing these ER values to the alternative approaches presented in Table 5.2, KELS and KEWLS are the second and third fastest solutions, only slower than the LSS solution which gives substantially reduced accuracy. In comparison to the optimal SUKF approach the KELS and KEWLS ERs present

68.11% and 55.1% improvements respectively. This shows that the proposed solutions, KELS and KEWLS, require one third and less than half of the time and energy to achieve highly similar results, respectively. The computational complexity of the SUKF is instigated from the repeated use of complex nonlinear Unscented Transforms. While the KELS and KEWLS approach apply more efficient LKFs, prediction and LSS techniques.

Furthermore, the solutions presented throughout this thesis are given for 2D systems. In contrast to the SUKF and UKF approaches, for three-dimension systems, the computation improvements of KELS and KEWLS can be expected to increase further. This is due to the fact the dimension of the LKFs within KELS and KEWLS remains constant for all dimensions and only the dimension of the multilateration state matrix is required to increase. Whereas the SUKF and UKF techniques will require a state dimension increase of two states, pertaining to the third axis coordinates and its velocity component.

6.3.2.3 Summary

The SUKF solution is optimal with regards to accuracy but computationally costly whereas the proposed KELS and KEWLS solution are shown to be far more computationally efficient while performing comparably to the optimal SUKF solution in most of the considered scenarios. Naturally, this presents a compromise that must be made between energy efficiency and accuracy. While the decision is subjective to the application demands, the difference in accuracy between the proposed solutions and the SUKF solution is so slight that the proposed solutions can be argued to present a more significant advantage. Regardless the following work considers adaptations to further improve the accuracy of KELS and KEWLS.

6.4 Further Development of KELS and KEWLS

While the performance of the proposed KELS and KEWLS solutions are comparable to the optimal SUKF, but at a much lower computation cost, there is scope to improve the techniques further. This section further develops the KELS and KEWLS approach to improve accuracy, while attempting not to compromise latency and energy benefits.

6.4.1 Analysis of the KELS/KEWLS Constant Change Model

From the comparable response to the SUKF solution, the KEWLS and KELS approach is indirectly shown to have significantly improved performance compared to the earlier DE approach. The application of KFs has shown to greatly reduce the noise within the sensor measurements and therefore improve the accuracy of the LSS estimates. However, the performance of the LKFs relies heavily on the model used to predict and accurately smooth the errors. It should be noted that prior to the LSS estimation,

the KELS and KEWLS solutions follow the same process and exhibit identical range estimates. Therefore, the following section refers to both KELS and KEWLS equally but for ease of reading is described using KELS.

To highlight the KF response the KELS approach is compared to the DE solution at a sensor level. Figure 6.12 below provides the average EREs over 5000 iterations given by the Reference Simulation Scenario, for $\Delta t_m = [0.0193, 0.0373]/s$ and $\sigma_z = [0.0046, 0.022]/m$ over a single path cycle. The IML and sensor measurement noise values are selected to highlight the trends in the KELS solution

The averaging process lessens the effects of the random sensor measurement error component, isolating the systematic error brought on by the linear extrapolations. The LKF process model effectively applies a linear extrapolation to reduce noise in the estimates and this process increases the systematic extrapolation error. The DE RE appears lower than the KELS RE in most cases.

This is highlighted at the fourth sensor, where the DE approach applies no extrapolation and the RE is entirely due to sensor measurement noise. For the fourth sensor the KELS process applied no synch prediction step, however the KF process can be observed to introduce a systematic error component as indicated by the generally higher error and noticeable peak, in Figure 6.12. This peak correlates to where the constant change model is shown to be least applicable, as discussed in the previous DE studies.

Figure 6.12 is constructed of 16 sensor level RE plots from four scenarios. Going from the left column to the right column illustrates an increase in sensor measurement noise while observing the top four plots against the bottom four plots shows a decrease in IML.

Observing first the effects of an increase in sensor measurement noise across both levels of IML, as shown from the left to right columns of Figure 6.12, a greater level of RE for the KELS solution is observed. While not evident from the scaling, the systematic component of the DE RE is unaffected by the measurement noise since the DE solution ignores measurement noise and therefore this is averaged out. As discussed in Section 2.1.3.2.1.1, the response of the KF is heavily dictated by the noise parameters. Within this scenario, the increase in sensor measurement noise increases the KF weighting towards the predictions which are generated using the constant change model. Therefore, the response increases the systematic extrapolation error. This is more prominent for lower IML values where the random noise is dominant.

For decreased IML, as shown from the top four figures against the bottom four figures in Figure 6.12, systematic error is reduced for both the DE and KELS solution due to a reduced estimation period. Comparatively, this reduction is less prominent within the KELS solution due to the dual use of linear assumptions within the initial prediction and the synch prediction.

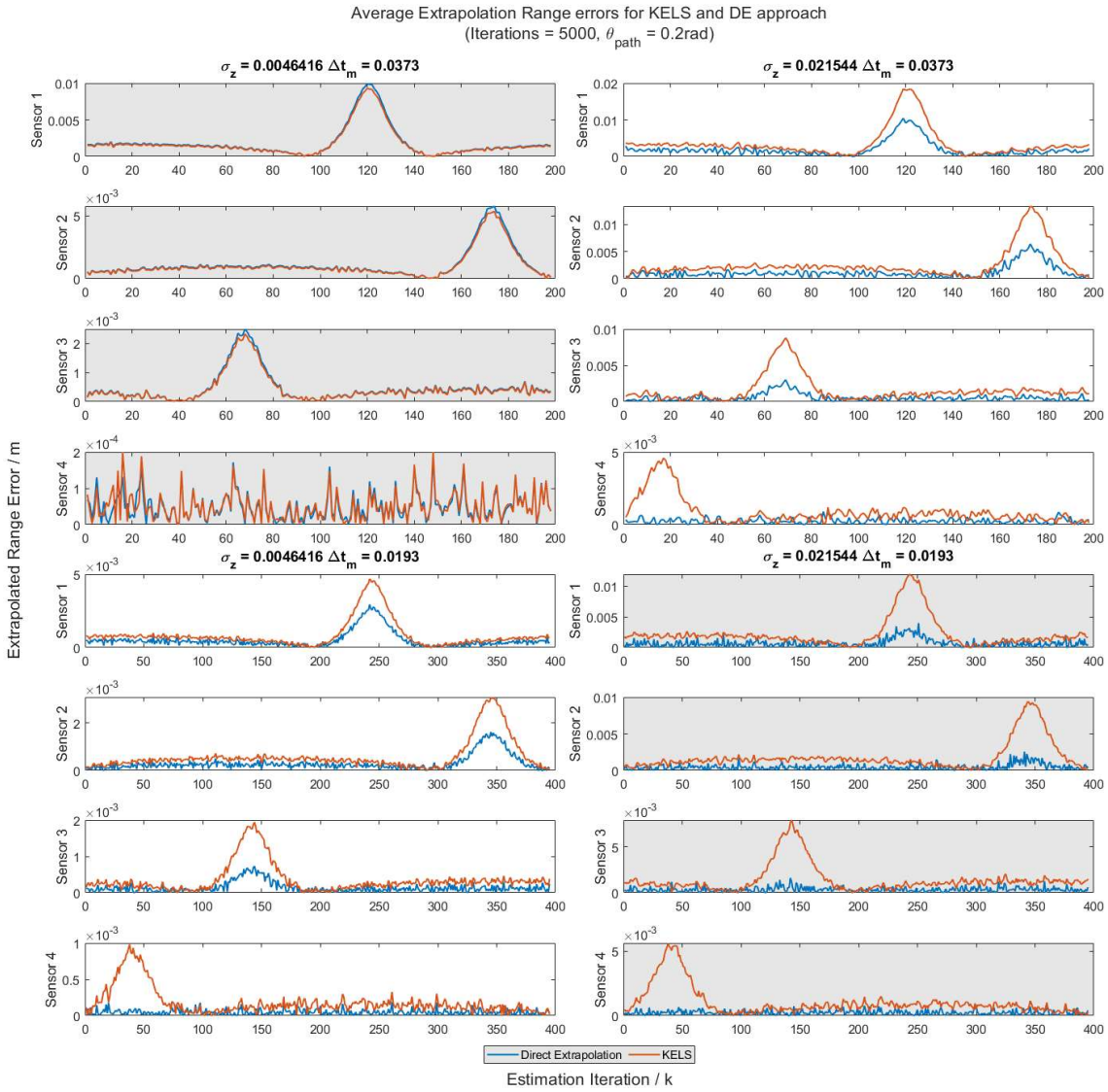

Figure 6.12 - Sensor range errors for KELS and Direct Extrapolation Approaches for a single path trajectory cycle.

Figure 6.12 presents four different scenarios of parameter sets which are given to be the four quadrants of the figure and differnetiated by darker or lighter backgrounds. For each scenario, the average Extrapolation Range Error for the DE and KELS techniques are given for the four individual sensors in separate graphs, or rows of Figure 6.12. The right column shows an increase in sensor measurement noise ($\sigma_z = 0.022$ m) compared to the left column ($\sigma_z = 0.005$ m), while the top four plots present a greater level of IML ($\Delta t_m = 0.04$ s) than the bottom four ($\Delta t_m = 0.02$ s). KFs are shown to be effective in reducing the random sensor measurement noise, however when isolating systematic error, it is clear that the Constant Velocity (CV) process model used in the proposed KELS approach is not optimal for describing the change in measurements. This is evident from the high systematic errors attributed to the KFing in Figure 6.12. This is also the case for the various

observations made throughout the DE analysis in Section 6.2.1.1.1. Even for a target travelling on a constant velocity trajectory, the change in distance relative to the sensor is not always constant and as such suggests the need for higher order filtering. This will therefore be applied in the following section.

Remark 7 - The process model described here refers to the estimation of distances and not the trajectory of the target. The error within the simulations carried out can be expected to lessen if a solution describing the trajectory of the model, such as the UKF or SUKF, were to apply a constant acceleration model as opposed to a constant velocity model. Nevertheless, the study conducted in Section 5.3.1 describes constant velocity trajectories where the range estimates are best described by a constant rate of change model. From this, one can state that the KEWLS approach does not provide any overfitting advantage when compared to a CV SUKF or CV UKF approach, under the premise that the constant rate of change (CA solution) is more applicable, for estimating range measurements, under both linear and nonlinear target trajectories.

Constant Acceleration Process model

The application of a higher order, Constant Acceleration (CA), model within the KELS and KEWLS solution is discussed in this section. The CV and CA processes are differentiated through the suffix '-CV' or '-CA' respectively.

The process for the KELS-CA and KEWLS-CA solutions is identical, except for the modifications required to the KF matrices and initialisation process.

6.4.1.1 Generalised Solution

For a general asynchronous scenario, where IML values may not be constant, the LKFs are adjusted to a CA process where the state to be estimated is given by:

$$X^i_{t^i_k} = \left[\hat{d}^i_{t^i_k}, V^i_{t^i_k,t^i_{k-1}}, a^i_{t^i_k,t^i_{k-1},t^i_{k-2}}\right]^T. \tag{6.39}$$

In which a^i is the acceleration component of measurement displacement for the $i'th$ sensor, given by:

$$a^i_{t^i_k,t^i_{k-1},t^i_{k-2}} = \frac{V^i_{t^i_k,t^i_{k-1}} - V^i_{t^i_{k-1},t^i_{k-2}}}{t^i_k - t^i_{k-1}} = \frac{\left(\frac{\Delta\hat{d}^i_{t^i_k,t^i_{k-1}}}{\Delta T^i_{t^i_k,t^i_{k-1}}} - \frac{\Delta d^i_{t^i_{k-1},t^i_{k-2}}}{\Delta T^i_{t^i_{k-1},t^i_{k-2}}}\right)}{\Delta T^i_{t^i_k,t^i_{k-1}}}. \tag{6.40}$$

Where $\Delta T^i_{t^i_k,t^i_{k-1}}$ is the period between measurements given by timestamps $t^i_k - t^i_{k-1}$. $V^i_{t^i_k,t^i_{k-1}}$ is given by (6.19). On initialisation, due to the intervals required to establish an initial estimate of $a^i_{t^i_k,t^i_{k-1},t^i_{k-2}}$ the proposed approach does not provide an estimate until the fourth estimation interval. The respective CA state transition matrix is given by [141]:

$$A^i_{t^i_k} = \begin{bmatrix} 1 & \Delta T^i_{t^i_k,t^i_{k-1}} & (\Delta T^i_{t^i_k,t^i_{k-1}})^2/2 \\ 0 & 1 & 1 \\ 0 & 0 & 1 \end{bmatrix}. \tag{6.41}$$

The process noise covariance matrix, presented in Section 2.1.3.2.1.6, is given by the Discrete-time Nearly Constant Velocity (DNCV) matrix structure [141]:

$$Q = FF^T\sigma_a^2 = \begin{bmatrix} \frac{(\Delta T^i_{t^i_k,t^i_{k-1}})^4}{4} & \frac{(\Delta T^i_{t^i_k,t^i_{k-1}})^3}{2} & \frac{(\Delta T^i_{t^i_k,t^i_{k-1}})^2}{2} \\ \frac{(\Delta T^i_{t^i_k,t^i_{k-1}})^3}{2} & (\Delta T^i_{t^i_k,t^i_{k-1}})^2 & \Delta T^i_{t^i_k,t^i_{k-1}} \\ \frac{(\Delta T^i_{t^i_k,t^i_{k-1}})^2}{2} & \Delta T^i_{t^i_k,t^i_{k-1}} & 1 \end{bmatrix}\sigma_a^2. \tag{6.42}$$

Where $F = \left[\frac{(\Delta T^i_{t^i_k,t^i_{k-1}})^2}{2}, \Delta T^i_{t^i_k,t^i_{k-1}}, 1\right]$ is from Section 2.1.3.2.1.6. The covariance matrix $P^i_{t^i_3}$ is initiated as an identity matrix and the Measurement Matrix $H = [1\ 0\ 0]$. The synch prediction stage is carried out over the Measurement Latency value in the same manner as before where $\Delta t_{i,k} = t_k - t^i_k$.

6.4.1.2 Thesis Applied Solution

Following the simplified sequential sampling scenario considered throughout this thesis, in accordance with the proposed demonstration IoRL sampling scheme, the above process and matrices are applied as follows in the later simulations:

Due to a constant sensor sampling period, $\Delta T^i_{t^i_k,t^i_{k-1}} = t^i_k - t^i_{k-1}$, for all k>2, the subscript and superscript can be omitted, and the state transition matrix and process noise covariance matrix are given as fixed values. Substituting ΔT for all the different instances of ΔT^i in (6.40) the acceleration component $a^i_{t^i_k,t^i_{k-1},t^i_{k-2}}$ is defined by:

$$a^i_{t^i_k,t^i_{k-1},t^i_{k-2}} = \frac{\Delta d^i_{t^i_k,t^i_{k-1}} - \Delta d^i_{t^i_{k-1},t^i_{k-2}}}{\Delta T^2}. \tag{6.43}$$

Therefore, the process equation $X^i_{t^i_k} = AX^i_{t^i_{k-1}}$ can more simply be represented as:

$$\begin{bmatrix} \hat{d}^i_{t^i_k} \\ \Delta\hat{d}^i_{t^i_k,t^i_{k-1}} \\ \Delta\Delta\hat{d}^i_{t^i_k,t^i_{k-1},t^i_{k-2}} \end{bmatrix} = \begin{bmatrix} 1 & 1 & 1/2 \\ 0 & 1 & 1 \\ 0 & 0 & 1 \end{bmatrix} \begin{bmatrix} \hat{d}^i_{t^i_{k-1}} \\ \Delta\hat{d}^i_{t^i_{k-1},t^i_{k-2}} \\ \Delta\Delta\hat{d}^i_{t^i_{k-1},t^i_{k-2},t^i_{k-3}} \end{bmatrix}. \tag{6.44}$$

In which,

$$\Delta\Delta\hat{d}^i_{t^i_k,t^i_{k-1},t^i_{k-2}} = \Delta\hat{d}^i_{t^i_k,t^i_{k-1}} - \Delta\hat{d}^i_{t^i_{k-1},t^i_{k-2}}. \tag{6.45}$$

The process noise covariance matrix Q is given by [141]:

$$Q = FF^T\sigma_a^2 = \begin{bmatrix} \frac{\Delta T^4}{4} & \frac{\Delta T^3}{2} & \frac{\Delta T^2}{2} \\ \frac{\Delta T^3}{2} & \Delta T^2 & \Delta T \\ \frac{\Delta T^2}{2} & \Delta T & 1 \end{bmatrix}\sigma_a^2. \tag{6.46}$$

The covariance matrix $P^i_{t^i_3}$ is initiated as an identity matrix and the Measurement Matrix $H = [1\ 0\ 0]$. The Synch prediction step carries out a repeated prediction stage with a sensor specific state transition matrix A^i_{sync} and process noise covariance matrix Q^i_{synch} [141]:

$$\begin{aligned} A^i_{synch} &= \begin{bmatrix} 1 & \Delta t_i & \frac{\Delta t^i}{2} \\ 0 & 1 & \Delta t_i \\ 0 & 0 & 1 \end{bmatrix}, \\ Q^i_{synch} &= \begin{bmatrix} (\Delta t_i)^4/4 & (\Delta t_i)^3/2 & (\Delta t_i)^2/2 \\ (\Delta t_i)^3/2 & (\Delta t_i)^2 & \Delta t_i \\ (\Delta t_i)^2/2 & \Delta t_i & 1 \end{bmatrix}\sigma_a^2. \end{aligned} \tag{6.47}$$

In which the MLa is fixed and given by:

$$\Delta t_i = \Delta t_m * (N - i). \tag{6.48}$$

A summary of the proposed KELS-CA solution is given in Algorithm **18** below.

Algorithm 18: The Proposed KELS-CA Solution[23]

INPUT: **Sensor positions $S^i = [x^i, y^i]^T$ for $i = (1{:}N)$**

***Initialisation*: *Under the given static sensor and constant IML scenario*:**

1: Establish ΔT from (6.7)

Compute each sensors fixed Kalman filters

2: *For* $i = (1{:}N)$

Determine initial matrices

3: $P^i_{t^i_3}$ initialised as an identity matrix

4: *For* $k = 3$

5: Compute $\Delta\hat{d}^i_{t^i_2,t^i_1}$ and $\Delta\hat{d}^i_{t^i_3,t^i_2}$ from (6.2) using $z^i_{t^i_k} \rightarrow d^i_{t^i_k}$

6: Compute $\Delta\Delta\hat{d}^i_{t^i_3,t^i_2,t^i_1}$ from (6.45)

7: Initialise $X^i_{t^i_3} = \left[\hat{d}^i_{t^i_3}, \Delta\hat{d}^i_{t^i_3,t^i_2}, \Delta\Delta\hat{d}^i_{t^i_3,t^i_2,t^i_1}\right]^T$

8: *End*

Determine synch matrices

9: Determine Δt_i from (6.48)

10: Compute A^i_{synch} and Q^i_{synch} as per (6.47)

11: *End*

12: Generate $H = [1\ 0\ 0\ ]$ & A as per (6.44)

13: Compute Q using (6.46)

Estimation Loop

14: *For* $k = (4{:}\ k_{max})$

15: *For* $i = (1{:}N)$

16: Execute LKF^i prediction (6.22) & (6.23) using $i'th$ sensor filter matrices $X^i_{t^i_{k-1}}$ & $P^i_{t^i_{k-1}}$

17: Obtain $i'th$ sensor observation $z^i_{t^i_k}$ and respective covariance matrix R

18: Execute LKF^i update (6.24) - (6.26) using $i'th$ sensor filter matrices $X^{-i}_{t^i_k}$ *and* $P^{-i}_{t^i_k}$

19: ***Perform synch prediction***

20: Obtain $X^i_{t_k}, P^i_{t_k}$ by executing LKF^i prediction (6.22) & (6.23) using updated $i'th$ sensor filter matrices $X^{-i}_{t^i_k}, P^{-i}_{t^i_k}$ and the $i'th$ sensor synch prediction matrices A^i_{synch} *and* Q^i_{synch}.

21: *End*

22: *If performing KELS computation*

23: Extract predicted measurements from $X^i_{t_k}$ for $i = (1, \cdots, N)$

24: Using sensor position data formulate the LSS matrices (6.14)

25: Compute position estimate from LSS using (6.15)

[23] Ranges of values are represented in the following manner: (initial value : incremental value : end value) and may, in some cases, be assigned equivalent to a variable. Where an incremental value is not given, the increments are defaulted to integers of one. When used as part of a '*For'* loop, each value in the given range is applied individually within a single loop.

26: *Else If performing KEWLS computation*

27: Compute D and C_d from (6.35) and (6.36) respectively

28: Determine W from (2.7)

29: Carry out WLS using (6.34)

30: *End*

31: *End*

6.5 Simulation Study

The following sections compare the proposed KELS and KEWLS solutions against the DE and SUKF methods. *Within this section the proposed KELS-CA method given by* Algorithm 18 *and KEWLS-CA method given by the described substitutions to* Algorithm 18*, are evaluated under the Reference Simulation given in Algorithm 11 for 500 iterations*.

6.5.1 KELS-CA System Identification

The system identification process employed throughout this thesis is applied again to the proposed KELS-CA solution where the optimal acceleration noise magnitude is equivalent for all sensor LKFs and selected to give the lowest average RMSE for both the highest and lowest PA (θ_{path}) values. The optimal values of the acceleration noise magnitude for all evaluated IML and Measurement noise values are shown in Figure 6.13. The optimal acceleration noise magnitude values for the KELS-CV approach are given for comparison. *As with the KELS-CV and KEWLS-CV solutions, the difference between KELS-CA and KEWLS-CA is in the final estimation stage therefore the optimal process noise values are equivalent*

With the understanding that the σ_a value scales the process noise covariance Q, and therefore affects the weightings of the measurements and process equations within the KFs, a lower σ_a indicates optimal performance due to a greater reliance on the process model. Visual comparison between the optimal values for KELS-CV and KELS-CA indicates a clear improvement in the suitability of the CA process model.

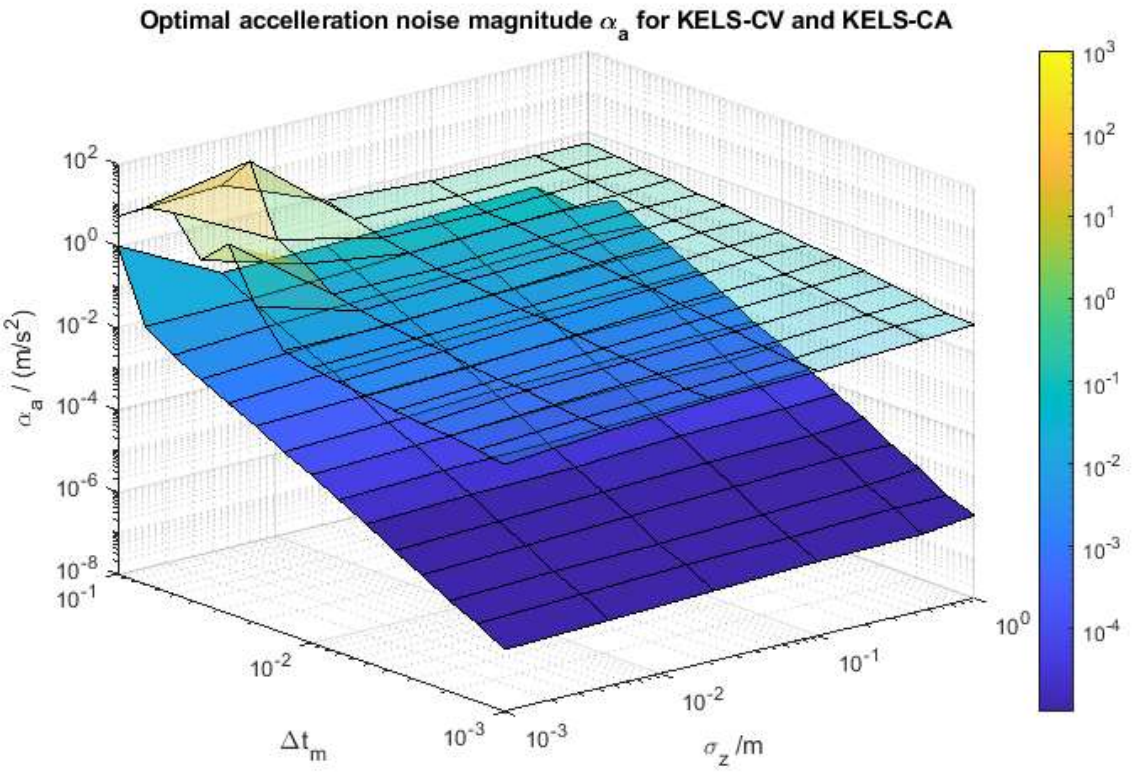

Figure 6.13 - Optimal Acceleration noise magnitude for the proposed KELS-CA (opaque) solution, and KELS-CV (translucent) for reference

6.5.2 RMSE Results

The RMSE results of both the proposed KELS-CA method given by Algorithm 18*, evaluated under the Reference Simulation given in Algorithm 11 for 500 iterations*, are presented in Figure 6.14 for all considered scenarios as a percentage difference between the proposed KELS-CA and SUKF approach calculated using (6.37). Relevant tabulated RMSE data for KELS-CA and KEWLS-CA is provided in Appendix C of this thesis and comparative tabulated data for KELS-CA and KEWLS-CA vs SUKF is provided in Appendix E of this thesis.

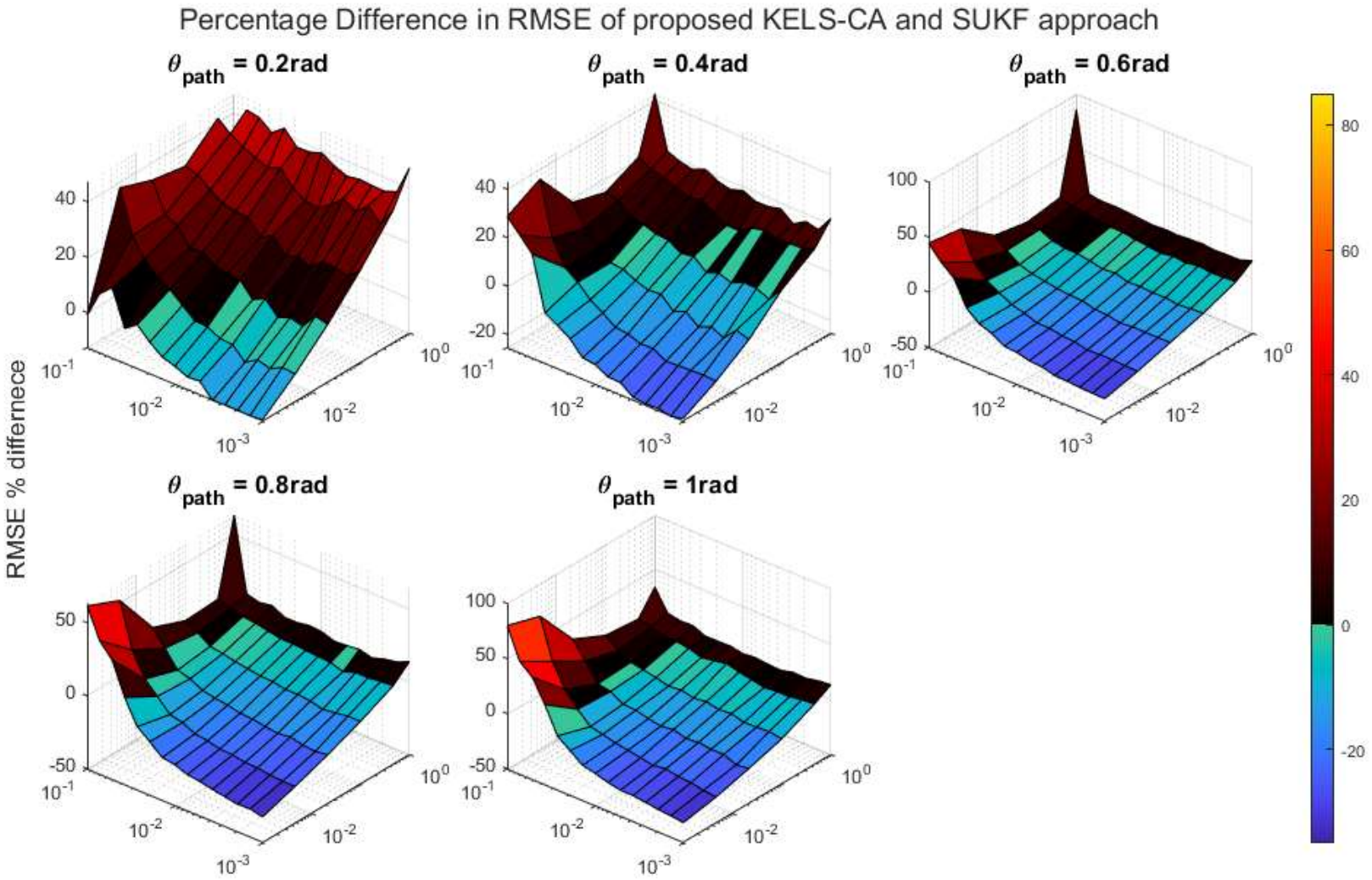

Figure 6.14 – RMSE percentage difference between the SUKF and proposed KELS-CA solution

A summary of the RMSE percentage differences for both the KELS-CA and KEWLS-CA solutions is given below in Table 6.3.

Table 6.3 – Percentage difference of KELS-CA and KEWLS-CA vs SUKF

Path Angle $\boldsymbol{\theta_{path}}$/ $\boldsymbol{rad}$	0.2	0.4	0.6	0.8	1
			KELS-CA - SUKF		
Min. % diff	-13.88	-25.51	-30.12	-32.84	-33.02
Avg. % diff	15.30	1.36	-2.40	-3.41	-1.01
Max. % diff	40.96	32.13	75.06	62.56	81.68
			KEWLS-CA - SUKF		
Min. % diff	-24.61	-29.39	-31.82	-33.52	-33.13
Avg. % diff	-0.33	-5.35	-6.40	-6.57	-4.15
Max. % diff	22.93	19.74	65.54	55.36	57.77

Position estimation performance of the KELS-CA solution is significantly more accurate than the KELS-CV solution, as indicated by lower percentage differences for all cases. These results are further improved through the weighted KEWLS-CA approach, where again, the weighting proves highly effective. As indicated by the blue region in Figure 6.14 and the negative average values in Table 6.3, the proposed KELS-CA and KEWLS-CA solutions provide substantial accuracy improvements, in most considered cases, compared to the optimal SUKF approach.

It can be seen that the SUKF solution is better suited to more linear trajectories that better satisfy the CV process model applied. However, as the path nonlinearity increases, the KELS-CA and KEWLS-CA solutions achieve higher accuracy for lower IML scenarios. As observed for the KELS-CV and KEWLS-CV solutions, the extrapolations lead to more significant errors for greater IML values; however, the CA model reduces these negative impacts considerably.

It should be noted that for substantially high IML and sensor measurement noise, the proposed solutions can be seen to obtain a poorer performance than the optimal SUKF solution.

However, drawing on observations from chapter 5, the high measurement noise region, in which the KELS-CA and KEWLS-CA solutions diminishes in comparable accuracy to the SUKF, the SUKF performance is similar to that of the more computationally efficient UKF.

The author of this thesis, therefore, argues that within these high sensor measurement noise regions, where the SUKF solution is dominant over the proposed approach, the need for an asynchronous solution is redundant. The noise is so great that the more computationally efficient UKF solution should be appointed due to its comparable performance. This is illustrated in Figure 6.15,

where the optimal RMSE obtained between the KELS-CA, SUKF and UKF solutions are presented for all considered scenarios. In summary, the proposed KELS-CA and KEWLS-CA solution are shown to achieve optimal accuracy across the majority of evaluated strategies, for high IML values, the SUKF is still optimal in regards to accuracy while the more efficient UKF solution should be applied for higher measurement noise cases.

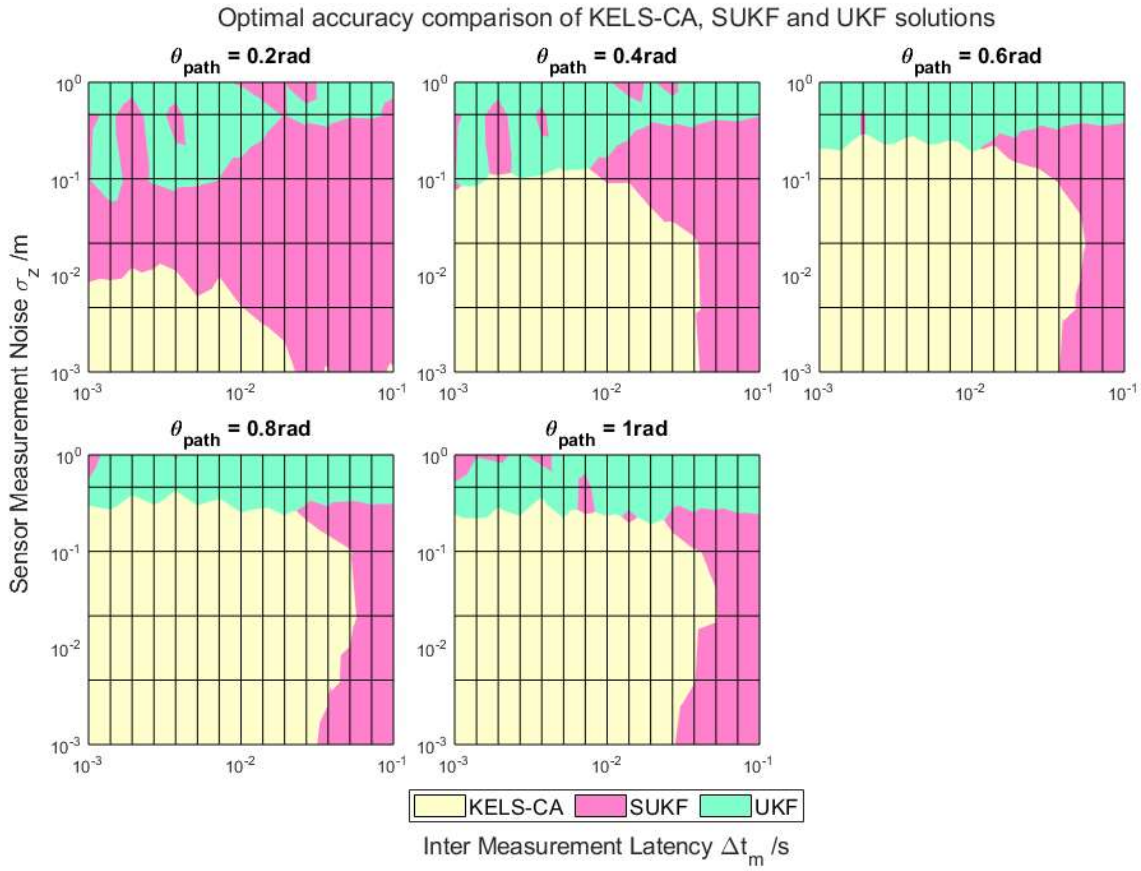

Figure 6.15 - Accuracy comparison of KELS-CA, SUKF and UKF solutions under various scenarios

6.5.3 Sensor Level Performance

The improved performance of the KELS-CA solution can be attributed to it being a better-suited process model to the scenario, correctly capturing that the change in measurements are typically not constant. To illustrate this point, Figure 6.16 presents the ERE from the DE, KELS-CV and KELS-CA solutions for the same simulated parameters considered in Section 6.4.1 and shown in Figure 6.12. The author of this thesis notes that the ERE values are equivalent for both the KELS and KEWLS solutions therefore, only the KELS solution is referred to in the following analysis.

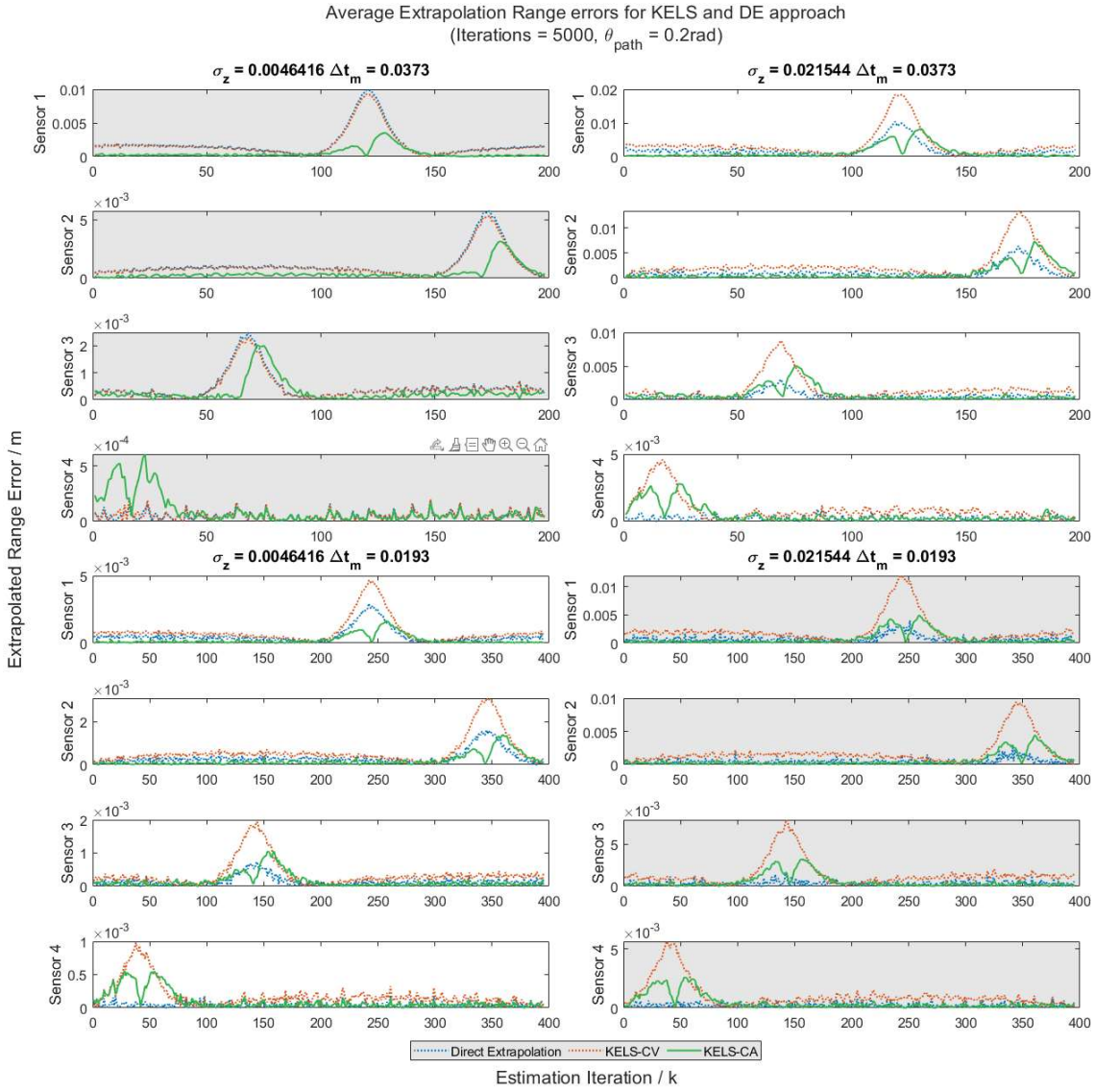

Figure 6.16 - Sensor Range Errors over 1000 iterations for the DE, KELS-CV and KELS-CA solutions.

Figure 6.16 presents four different scenarios of parameter sets which are given to be the four quadrants of the figure and differnetiated by darker or lighter backgrounds. For each scenario the average Extrapolation Range Error for the DE, KELS-CV and KELS-CA techniques are given for the four individual sensors in separate graphs, or rows of Figure 6.16. The right column shows an increase in sensor measurement noise ($\sigma_z = 0.022$ m) compared to the left column ($\sigma_z = 0.005$ m), while the top four plots present a greater level of IML ($\Delta t_m = 0.04$ s) than the bottom four ($\Delta t_m = 0.02$ s). The CA process model still introduces more systematic noise than the DE approach; however, from Figure 6.16, the systematic errors produced by the extrapolation estimations are shown to visibly reduce, in most cases, when comparing the CA to the previous CV model. This is evident in the peaks and across the range of estimates throughout the path cycle in all plots of Figure 6.16. Additionally,

each CA response during the sharper change in measurement values is seen to overshoot, producing two peaks in the absolute value.

Otherwise, similar trends regarding the Kalman filtering response with regards to the IML and sensor measurement noise are observed for both the CA and CV models as discussed in Section 6.4.1.

6.5.4 Energy Efficiency

To evaluate the complexity of the proposed KELS-CA and KEWLS-CA solutions the Estimation Runtime (ER) is calculated, this is taken to reflect the energy demand of the solutions and therefore the energy efficiency.

As in Section 6.3.2.2, $N_L = 50$ where each loop computes all 7854 estimations and repeats the test for 50 iterations. The Average Estimation Runtime (ER) as computed in (5.25) for IML, σ_z and PA set to 1e-3s, 1e-3m and 0.2rad respectively. The ER values obtained for the proposed KELS-CA and KEWLS-CA solutions are 2.51e-5s and 3.5e-5s respectively. For comparison, the computation time of all proposed variations of the proposed solutions are presented in Table 6.4. Compared to the CV based solutions the proposed CA based solution results in a slightly higher increase in computational complexity due to the greater state dimensions. Regardless of this, the proposed KELS-CA and KEWLS-CA solutions are 65.94% and 52.21% more efficient than the SUKF solution respectively.

Table 6.4 – Performance summary of existing and proposed localisation solutions

Solution	**LSS**	**KELS-CV**	**KEWLS-CV**	**KELS-CA**	**KEWLS-CA**	**UKF**	**SHI**	**MSHI**	**SUKF**
Estimation Runtime /s	8.87e-6	2.35e-5	3.31e-5	2.51e-5	3.50e-5	6.03e-5	6.78e-5	6.81e-5	7.37e-5

To better visualise the magnitude of the difference the average runtime for all 50 iterations is presented in Figure 6.17 below. From Figure 6.17 it is evident that the weighting process in the KEWLS solutions is more demanding than the additional state dimensions required of the CA model.

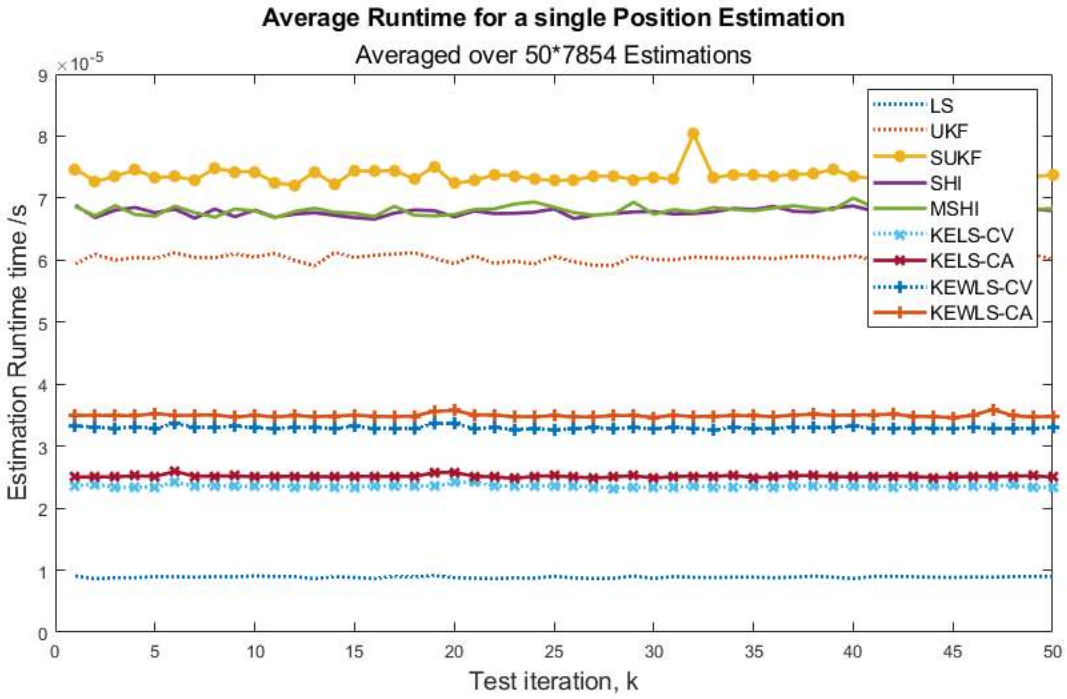

Figure 6.17 - Comparison of Average Estimation Runtime for various localisation methods

6.6 Chapter 6 Conclusions

Throughout this chapter, a simple and effective novel solution has been proposed to achieve accurate and computationally more efficient localisation when considering a system using nonlinear range measurements that are sequentially sampled. Through various simulation studies and analysis, the proposed solution is shown to outperform the optimal Sequential Unscented Kalman Filter (SUKF) significantly in regard to computational efficiency while obtaining superior accuracy and reliability for most considered values of IML, sensor measurement noise and path nonlinearity. The Proposed KELS and KEWLS solution enables energy savings of over 50% and can be applied to any range-based localisation technique. However, one must also consider the estimation frequency advantage provided by the SUKF.

With regards to the IoRL project, where sequential measurement sampling is shown to be present, the VLC RSSI accuracies presented within Chapter 3 are within the centimetre range, and the IML values are given to be 1ms. Therefore, given these values, the proposed KELS and KEWLS methods are the optimal solutions for VLC position estimation within the IoRL project. The mmWave accuracies are undetermined within the IoRL project and cannot be commented on.

While the proposed solutions show strong promise, the simplified scenario considered throughout this thesis should be extended to assess the proposed solutions further and evaluate the use of weightings applied in the KEWLS solution within a more general sense. This is discussed in further works.

7 Thesis Conclusions and Further Work

7.1 Conclusions

This digital era, needs high accuracy and low latency communications and positioning to support emerging markets and Location Based Services (LBS) for more densely populated and challenging environments. To satisfy these requirements, novel Radio Access Networks (RAN) and software solutions will be implemented within the latest and fifth generation of networks. Financed by Horizon 2020, the Internet of Radio Light (IoRL) is an example of one such international research venture into 5G networks for buildings using mmWaves and Visible Light Communications (VLC) technology. The research presented in this thesis explores the communication protocols and performance of the IoRL Indoor Positioning System (IPS) using measured and simulated data. The author of this thesis identifies the challenges within Visible Light Positioning (VLP) due to the use of light sources with non-Lambertian emission patterns and the computational burden of existing techniques to resolve asynchronous sampling of non-linear range measurements.

7.1.1 Visible Light Positioning

For the widespread deployment of 5G networks, VLC technology is an immensely viable and exciting potential solution due to the minimal required adaptations to existing infrastructure, illumination, and cost benefits. With demands for improved communication and localisation, VLC sources should be expected in all manner of existing lighting systems. As such, the necessary measures need to be taken to ensure that the potential localisation performance is not hindered despite the lens or source structure. In an initial evaluation of the VLC data obtained through the IoRL measurement campaign, the author of this thesis, identifies the negative implications of directly applying the widely adopted Lambertian assumptions to a non-Lambertian source for traditional 2D multilateration techniques.

This thesis then presents a novel calibration method and modification of the Lambertian range estimation, identifying and correcting the non-Lambertian region of the given light source. The proposed Halo-Lens Compensation (HLC) method significantly reduces Lambertian modelling errors by 50% when using average datasets and 39% for individual datasets. While this work evaluates a particular Total Internal Reflection (TIR) lens with a centrally frosted diffuser, it highlights the negative implications of applying Lambertian channel models to non-Lambertian sources for Visible Light Positioning (VLP) and the need for suitable calibration of channel parameters. This also demonstrates the potential for using non-Lambertian sources to achieve high positioning accuracy comparable to existing solutions using Lambertian sources. This principle can be applied to more varied lens structures, widening the suitable range of light fittings for VLP solutions.

7.1.2 Internet of Radio Light Data Fusion

The thesis then considers the proposed IoRL architecture for achieving high quality and low latency localisation by fusing both mmWave and VLC data. The HCL method and obtained results are then combined through simulations with modelled mmWave data, where 2D tracking shows promising centimetre to millimetre levels of accuracy across a range of mmWave noise levels. This study highlights the potential of the IoRL architecture and provides preliminary insight into further system developments.

7.1.3 Efficient Localisation for Asynchronously Sampled Non-Linear Range Measurements

Within the IoRL architecture, different degrees of asynchronous sampling of range measurements are identified. While localisation solutions exist for asynchronous sampling of non-linear measurements, this thesis aims to understand better the effects of asynchronous measurements and the necessity of these solutions for various levels of sensor measurement noise, target trajectory and asynchronous sampling latencies. Through comprehensive simulations and analysis, the author of this thesis, identifies the latency effects of single and multi-sensor systems with and without sensor measurement noise. Collected data shows that while the performance of asynchronous techniques can vary, the optimal solution of the Sequential Unscented Kalman Filter (SUKF) provides a significant accuracy advantage over non-asynchronous localisation techniques at lower sensor measurement noise levels but at a greater computational cost. This highlights the trade-off between accuracy and cost, which is subject to individual application requirements. However, where sensor measurement noise is higher, the accuracy advantage presented by SUKF is reduced and even negated.

As localisation performance improves, sensor measurement noise within wireless sensor networks will expectedly reduce. Therefore, the benefits of asynchronous solutions to achieve greater accuracy will be emphasised. However, the computational demand is not suitable for mobile applications where battery life and functionality are hindered. Therefore, the author of this thesis proposes a novel localisation solution for asynchronously sampled non-linear measurements by implementing low-cost linear techniques. In doing so, a weighted and non-weighted solution referred to as KEWLS-CA and KELS-CA are shown to achieve comparable, if not superior, results to that of the optimal SUKF solution with 52% and 66% energy reduction, respectively.

These presented solutions indicate substantial energy savings that can support a range of scenarios and prove to be optimal for use within the IoRL project, which exhibits 1 ms Inter Measurement Latencies (IML) and centimetre level accuracies.

In conclusion, this work demonstrates both the capability for high-performance VLP from non-Lambertian sources and the potential for energy-efficient localisation for sequentially sampled range measurements without compromising accuracy.

7.2 Further Work

7.2.1 Non-Lambertian Sources

In the later chapters of this thesis, a key emphasis is placed on the accuracy versus the cost of positioning systems. However, this was not the case in earlier work regarding the proposed HLC method. While the additional HLC process is slight, the computational demand of it should be considered against the accuracy benefits.

Building on this notion of energy, the workload required for fingerprinting solutions is a significant negative factor in why scene analysis is not widely adopted. While the author of this thesis uses the data available to avoid the same challenges as Fingerprinting, the dimension of both the dataset required for the proposed calibration and the number of measurements within each dataset should be evaluated. While existing literature specifies that as little as two points may define a Lambertian distribution, this is not the case for non-Lambertian scenarios.

This thesis explicitly considers the non-Lambertian lenses used within the IoRL Remote Radio Light Heads (RRLHs). While results prove the efficacy of non-Lambertian sources for high accuracy VLP, to support wider adoption of VLC technology, further analysis should be conducted on various lens structures.

Despite the brief discussion and application of subcarrier influence within chapter 3, the conventional notion of using the highest subcarrier power was not absolute, and further analysis should be considered for optimising performance as specific subcarriers.

Overall, the results of the IoRL VLP system are promising, however insight into 3D positioning solutions and angles of incidence should be conducted for non-Lambertian sources.

7.2.2 Internet of Radio Light (IoRL) Data Fusion Modelling

Chapter 4 presents an improved IoRL model than those previously developed by the author of this thesis. However, various developments should be considered to provide a more comprehensive overview of the performance of the IoRL solution.

While the VLC errors suitably fit a normal distribution and are modelled as additive white Gaussian noise, the errors are not expected to be uniform throughout the tracking area.

Modelling of individual range errors should be performed to reflect the noise parameters of respective light sources more appropriately. Regarding mmWave modelling, more sophisticated techniques such as raytracing, that consider the environment's geometry, signal frequency, system bandwidth, and multipath effects can be expected to provide a more accurate response.

Further measurements, particularly in the case of mmWave, will aid in correctly describing the response of the system. More extensive data collection will enable proper 3D modelling, where the existing system is limited to a 2D plane. Additionally, the solution should be tried on more realistic and challenging trajectories where more sophisticated process models can be used. The Location Server structure could also be improved to facilitate multiple users and reduce the overall latency, thereby enhancing the system response and properly utilising each dataset.

7.2.3 Survey of Asynchronous Sampling Techniques

Chapter 5 presents an evaluation of existing localisation solutions that both do and do not consider asynchronous sampling. While the conducted study provides critical insight into sequential sampling, as is experienced within the IoRL system, the modelled parameters are strongly simplified for preliminary evaluation. Further considerations could give a more comprehensive overview of these solutions for Indoor Positioning System (IPS) designers.

Regarding the sampling protocol, the sequential sampling structure doesn't account for the delay between sampling intervals. These would be expected from the IoRL sampling during the first N subframes of the transmission block. Moreover, the current solution ignores transmission delays, which are evident within the IoRL IPS as tested in chapter 3. In this case, the final sensor measurements would not be free from extrapolation and may incur additional errors. For a wider approach, a more generally asynchronous system could be considered, in which the sampling periods of individual sensors is not equivalent, measurements might suffer delays and might arrive out of sequence.

Regarding the system parameters, the system should be extended to evaluate a more significant number of parameters. Such as for a varied number of sensors, arbitrary placement of sensors, and different target trajectories. Additionally, analysis of the localisation techniques for 3D positioning could be more effective, where specific solutions may be less accurate or suffer more significant latencies.

7.2.4 Further Evaluation of KELS and KEWLS

The work presented in chapter 6 offers novel solutions to the asynchronous sampling problem however faces many of the same criticisms regarding the oversimplifications made in chapter 5. A

more comprehensive study might highlight necessary changes or potential limitations within the proposed solutions. Most notably, the KELS and KEWLS solutions are presented in a generalised manner. However, in keeping with the IoRL protocol, the conducted simulations consider the simplified sequential scenario. Furthermore, while measurement noise is considered and therefore system reliability is evaluated, consideration of corrupt or missing data sets would be of interest for application in practical systems.

The series of tests conducted throughout this thesis are limited to 2D tracking, and while the processes can be easily extended to 3D space; the exact effects remain unknown. The KELS and KEWLS approaches strictly utilise single dimension KFs; therefore, applications within 3D positioning would only require modifications within the Least Squares Solution (LSS) multilateration process at the end. However, for the SUKF and UKF approaches, the state vector increases by two variables for each dimension and these additional calculations are carried through the computationally extensive Unscented Transforms (UT). Therefore, it is suggested that for 3D solutions, the proposed KELS and KEWLS solutions may provide an even greater computational advantage over the UKF and SUKF approaches, but this is yet to be tested.

One key advantage of the SUKF approach remains the estimation update frequency, which considerably reduces estimation latency. This is a critical advantage when considering larger sensor networks in which batch process solutions present greater overall delays. Additionally, this might lead to extended extrapolation errors within the proposed solutions. To further increase the suitability of the proposed KELS and KEWLS solutions above existing systems, additional methods could be considered which would increase the estimation frequency and explore more extensive sensor networks.

As discussed in chapter 6, the proposed weighted solution KEWLS utilises a simplified assumption of sensor error distributions concerning the sampling sequence. Despite this assumption proving consistently beneficial within the considered scenario, one must consider the simplifications made to the trajectory, sensor placement, noise distribution and sequencing. To this end, the author of this thesis proposes that further testing is required to explore the suitable extent of this weighted approach in a broader setting.

8 References

[1] N. Bonnor, “A brief history of global navigation satellite systems,” *J. Navig.*, vol. 65, no. 1, pp. 1–14, 2012, doi: 10.1017/S0373463311000506.

[2] J. M. Kizza, “Internet of Things (IoT): Growth, Challenges, and Security,” pp. 517–531, 2017, doi: 10.1007/978-3-319-55606-2_24.

[3] 3GPP, “TR 21.916 V16.0.0 (2021-06) Technical Specification Group Services and System Aspects; Release 16 Description; Summary of Rel-16 Work Items (Release 16),” vol. 0, no. Release 16, 2021.

[4] L. Mainetti, L. Patrono, and I. Sergi, “A survey on indoor positioning systems,” *2014 22nd Int. Conf. Software, Telecommun. Comput. Networks, SoftCOM 2014*, pp. 111–120, 2014, doi: 10.1109/SOFTCOM.2014.7039067.

[5] A. Basiri *et al.*, “Indoor location based services challenges, requirements and usability of current solutions,” *Comput. Sci. Rev.*, vol. 24, no. July, pp. 1–12, 2017, doi: 10.1016/j.cosrev.2017.03.002.

[6] R. Want, A. Hopper, V. Falcão, and J. Gibbons, “The Active Badge Location System,” *ACM Trans. Inf. Syst.*, vol. 10, no. 1, pp. 91–102, 1992, doi: 10.1145/128756.128759.

[7] G. F. Welch, “HISTORY: The use of the Kalman filter for human motion tracking in virtual reality,” *Presence Teleoperators Virtual Environ.*, vol. 18, no. 1, pp. 72–91, 2009, doi: 10.1162/pres.18.1.72.

[8] A. Yassin *et al.*, “Recent Advances in Indoor Localization: A Survey on Theoretical Approaches and Applications,” *IEEE Commun. Surv. Tutorials*, vol. 19, no. 2, pp. 1327–1346, 2017, doi: 10.1109/COMST.2016.2632427.

[9] S. Jobs, “Introduction to Wireless,” *Nature*, vol. 162, no. 4128, pp. 911–911, 2005, doi: 10.1038/162911c0.

[10] X. Liu, L. Guo, and X. Wei, “Indoor visible light applications for communication, positioning, and security,” *Wirel. Commun. Mob. Comput.*, vol. 2021, 2021, doi: 10.1155/2021/1730655.

[11] A. M. Youssef and M. Youssef, “A Taxonomy of Localization Schemes for Wireless Sensor Networks.,” *Icwn*, no. January 2014, pp. 444–450, 2007.

[12] L. Zhu, A. Yang, D. Wu, and L. Liu, “Survey of indoor positioning technologies and systems,” *Commun. Comput. Inf. Sci.*, vol. 461, pp. 400–409, 2014, doi: 10.1007/978-3-662-45283-7_41.

[13] X. Guo, N. Ansari, F. Hu, Y. Shao, N. R. Elikplim, and L. Li, “A survey on fusion-based indoor positioning,” *IEEE Commun. Surv. Tutorials*, vol. 22, no. 1, pp. 566–594, 2020, doi: 10.1109/COMST.2019.2951036.

[14] G. Oguntala, R. Abd-Alhameed, S. Jones, J. Noras, M. Patwary, and J. Rodriguez, “Indoor location identification technologies for real-time IoT-based applications: An inclusive survey,” *Comput. Sci. Rev.*, vol. 30, pp. 55–79, 2018, doi: 10.1016/j.cosrev.2018.09.001.

[15] F. Zafari, A. Gkelias, and K. K. Leung, “A Survey of Indoor Localization Systems and Technologies,” *IEEE Commun. Surv. Tutorials*, vol. 21, no. 3, pp. 2568–2599, 2019, doi: 10.1109/COMST.2019.2911558.

[16] P. Z. Sotenga, K. Djouani, A. M. Kurien, and M. M. Mwila, “Indoor Localisation of Wireless Sensor Nodes Towards Internet of Things,” *Procedia Comput. Sci.*, vol. 109, pp. 92–99, 2017, doi: 10.1016/j.procs.2017.05.299.

[17] D. Plets, Y. Almadani, S. Bastiaens, M. Ijaz, L. Martens, and W. Joseph, “Efficient 3D trilateration algorithm for visible light positioning,” *J. Opt. (United Kingdom)*, vol. 21, no. 5, pp. 20–22, 2019, doi: 10.1088/2040-8986/ab1389.

[18] H. X. Zhao and J. T. Wang, “A Novel Three-Dimensional Algorithm Based on Practical Indoor Visible Light Positioning,” *IEEE Photonics J.*, vol. 11, no. 3, pp. 1–8, 2019, doi: 10.1109/JPHOT.2019.2911738.

[19] O. Kanhere and T. S. Rappaport, “Position Locationing for Millimeter Wave Systems,” *2018 IEEE Glob. Commun. Conf. GLOBECOM 2018 - Proc.*, pp. 1–6, 2018, doi: 10.1109/GLOCOM.2018.8647983.

[20] J. Yang, S. Jin, C.-K. Wen, J. Guo, and M. Matthaiou, “3-D Positioning and Environment Mapping for mmWave Communication Systems,” pp. 1–30, 2019, [Online]. Available: http://arxiv.org/abs/1908.04142.

[21] Z. Xiao and Y. Zeng, “An Overview on Integrated Localization and Communication Towards 6G,” *arXiv*, pp. 1–35, 2020.

[22] A. Journal, “The European 5G Annual Journal 2021,” *Eur. 5G Annu. J. 2021*, p. 107, 2021.

[23] M. Liu, J. Du, Q. Zhou, Z. Cao, and Y. Liu, “Eyeloc: Smartphone vision-enabled plug-n-play indoor localization in large shopping malls,” *IEEE Internet Things J.*, vol. 8, no. 7, pp. 5585–5596, 2021, doi: 10.1109/JIOT.2020.3031285.

[24] S. Zeb *et al.*, “On TOA-based Ranging over mmWave 5G for Indoor Industrial IoT Networks,” *2020 IEEE Globecom Work. GC Wkshps 2020 - Proc.*, pp. 5–10, 2020, doi: 10.1109/GCWkshps50303.2020.9367555.
[25] X. R. Li and V. P.Jilkov, “Survey of Maneuvering Target Tracking. Part I: Dynamic Models X.,” *Ieee Trans. Aerosp. Electron. Syst.*, vol. 39, no. 4, pp. 1333–1364, 2003.
[26] C. Wang, H. Wu, and N. F. Tzeng, “RFID-based 3-D positioning schemes,” *Proc. - IEEE INFOCOM*, pp. 1235–1243, 2007, doi: 10.1109/INFCOM.2007.147.
[27] G. Deak, K. Curran, and J. Condell, “A survey of active and passive indoor localisation systems,” *Comput. Commun.*, vol. 35, no. 16, pp. 1939–1954, 2012, doi: 10.1016/j.comcom.2012.06.004.
[28] J. Yan, H. Zhao, X. Luo, Y. Wang, C. Chen, and X. Guan, “Asynchronous Localization of Underwater Target Using Consensus-Based Unscented Kalman Filtering,” *IEEE J. Ocean. Eng.*, vol. 45, no. 4, pp. 1466–1481, 2020, doi: 10.1109/JOE.2019.2923826.
[29] A. G. Ferreira, D. Fernandes, A. P. Catarino, and J. L. Monteiro, “Performance analysis of ToA-based positioning algorithms for static and dynamic targets with low ranging measurements,” *Sensors (Switzerland)*, 2017, doi: 10.3390/s17081915.
[30] J. Barnes, C. Rizos, and J. Wang, “Locata : the positioning technology of the future ?,” *6th Int. Symp. Present. SatNav 2003 Satell. Navig. Technol. Incl. Mob. Position. Locat. Serv.*, vol. 49, no. May 2014, pp. 1–14, 2003.
[31] B. N. Priyantha, A. Chakraborty, and H. Balakrishnan, “The Cricket Location-Support System,” 2000.
[32] 5G PPP Technology Board, “Delivery of 5G Services to Indoors – the wireless wire challenge and solutions,” 2021, doi: 10.5281/zenodo.4280750.
[33] T. Komine and M. Nakagawa, “Fundamental analysis for visible-light communication system using LED lights,” *IEEE Trans. Consum. Electron.*, vol. 50, no. 1, pp. 100–107, 2004, doi: 10.1109/TCE.2004.1277847.
[34] Y. Golovachev, A. Etinger, G. A. Pinhasi, and Y. Pinhasi, “Propagation properties of sub-millimeter waves in foggy conditions,” *J. Appl. Phys.*, vol. 125, no. 15, pp. 1–7, 2019, doi: 10.1063/1.5083711.
[35] T. Mogi and T. Ohtsuki, “TOA localization using RSS weight with path loss exponents estimation in NLOS environments,” *2008 14th Asia-Pacific Conf. Commun. APCC 2008*, no. c, 2008.
[36] W. A. Zhang, X. Yang, L. Yu, and S. Liu, “Sequential Fusion Estimation for RSS-Based Mobile Robots Localization with Event-Driven WSNs,” *IEEE Trans. Ind. Informatics*, vol. 12, no. 4, pp. 1519–1528, 2016, doi: 10.1109/TII.2016.2585350.
[37] M. A. Elkarim, N. A. Mohammed, and M. H. Aly, “Exploring the performance of indoor localization systems based on VLC-RSSI, including the effect of NLOS components using two light-emitting diode lighting systems,” *Opt. Eng.*, vol. 54, no. 10, p. 105110, 2015, doi: 10.1117/1.oe.54.10.105110.
[38] Y. Almadani, M. Ijaz, S. Bastiaens, S. Rajbhandari, W. Joseph, and D. Plets, “An Experimental Analysis of the Effect of Reflections on the Performance of Visible Light Positioning Systems in Warehouses,” *2019 IEEE 2nd Br. Irish Conf. Opt. Photonics, BICOP 2019*, no. Cmd, pp. 1–4, 2019, doi: 10.1109/BICOP48819.2019.9059580.
[39] G. Bellusci, G. J. M. Janssen, J. Yan, and C. C. J. M. Tiberius, “Modeling Distance and Bandwidth Dependency of TOA-Based UWB Ranging Error for Positioning,” *Res. Lett. Commun.*, vol. 2009, pp. 1–4, 2009, doi: 10.1155/2009/468597.
[40] S. Zeb *et al.*, “On TOA-based Ranging over mmWave 5G for Indoor Industrial IoT Networks,” pp. 5–10.
[41] N. Garcia, A. M. Haimovich, M. Coulon, and J. A. Dabin, “High Precision TOA-based Direct Localization of Multiple Sources in Multipath,” vol. 15, pp. 1–17, 2015, [Online]. Available: http://arxiv.org/abs/1505.03193.
[42] X. Sun, J. Duan, Y. Zou, and A. Shi, “Impact of multipath effects on theoretical accuracy of TOA-based indoor VLC positioning system,” *Photonics Res.*, vol. 3, no. 6, p. 296, 2015, doi: 10.1364/prj.3.000296.
[43] M. Dashti, M. Ghoraishi, K. Haneda, and J. I. Takada, “Sources of ToA estimation error in LoS scenario,” *2010 IEEE Int. Conf. Ultra-Wideband, ICUWB2010 - Proc.*, vol. 2, pp. 643–646, 2010, doi: 10.1109/ICUWB.2010.5614046.
[44] Q. Shi, X. Cui, S. Zhao, and M. Lu, “Sequential TOA-Based Moving Target Localization in Multi-Agent Networks,” *IEEE Commun. Lett.*, vol. 24, no. 8, pp. 1719–1723, 2020, doi: 10.1109/LCOMM.2020.2993894.
[45] X. Li, J. He, L. Xu, and Q. Wang, “The effect of multipath and NLOS on TOA ranging error and energy based on UWB,” *2016 IEEE Int. Conf. Consum. Electron. ICCE-TW 2016*, pp. 16–17, 2016, doi: 10.1109/ICCE-TW.2016.7520939.
[46] R. Kaune, “Accuracy studies for TDOA and TOA localization,” *15th Int. Conf. Inf. Fusion, FUSION 2012*, pp. 408–415, 2012.
[47] S. M. Prasad, T. Panigrahi, M. Hassan, and M. Ding, “Sampling Free TDOA Localization in Millimeter Wave Networks,” in *IEEE Wireless Communications and Networking Conference, WCNC*, 2019, vol. 2019-April, doi:

10.1109/WCNC.2019.8886011.
[48] J. Y. Chen, Y. Zhao, C. Zhao, and Y. Zhao, “Improved two-step weighted least squares algorithm for TDOA-based source localization,” *Proc. Int. Radar Symp.*, vol. 2018-June, pp. 1–6, 2018, doi: 10.23919/IRS.2018.8448149.
[49] S. Potluri, “HYPERBOLIC POSITION LOCATION ESTIMATOR WITH TDOAS FROM FOUR STATIONS,” *Public Health*, p. 125, 2007, [Online]. Available: http://scholar.google.com/scholar?hl=en&btnG=Search&q=intitle:Some+Contributions+on+MIMO+Radar#0.
[50] P. Wu, S. Su, Z. Zuo, X. Guo, B. Sun, and X. Wen, “Time difference of arrival (TDOA) localization combining weighted least squares and firefly algorithm,” *Sensors (Switzerland)*, vol. 19, no. 11, 2019, doi: 10.3390/s19112554.
[51] X. Wen and J. Wang, “TDOA Location Accuracy Experiment,” *J. Phys. Conf. Ser.*, vol. 1237, no. 3, 2019, doi: 10.1088/1742-6596/1237/3/032031.
[52] G. Shen, R. Zetik, and R. S. Thomä, “Performance comparison of TOA and TDOA based location estimation algorithms in LOS environment,” *5th Work. Positioning, Navig. Commun. 2008, WPNC’08*, vol. 2008, pp. 71–78, 2008, doi: 10.1109/WPNC.2008.4510359.
[53] F. Lemic *et al.*, “Localization as a feature of mmWave communication,” *2016 Int. Wirel. Commun. Mob. Comput. Conf. IWCMC 2016*, pp. 1033–1038, 2016, doi: 10.1109/IWCMC.2016.7577201.
[54] O. A. Oumar, M. F. Siyau, and T. P. Sattar, “Comparison between MUSIC and ESPRIT direction of arrival estimation algorithms for wireless communication systems,” *1st Int. Conf. Futur. Gener. Commun. Technol. FGCT 2012*, pp. 99–103, 2012, doi: 10.1109/FGCT.2012.6476563.
[55] G. B. Prince and T. D. C. Little, “A two phase hybrid RSS/AoA algorithm for indoor device localization using visible light,” *GLOBECOM - IEEE Glob. Telecommun. Conf.*, pp. 3347–3352, 2012, doi: 10.1109/GLOCOM.2012.6503631.
[56] Y. Jia, H. Tian, S. Fan, and B. Liu, “Motion Feature and Millimeter Wave Multi-path AoA-ToA Based 3D Indoor Positioning,” *IEEE Int. Symp. Pers. Indoor Mob. Radio Commun. PIMRC*, vol. 2018-Septe, pp. 1–7, 2018, doi: 10.1109/PIMRC.2018.8580805.
[57] W. Mao, “Approaches for Angle of Arrival Estimation Angle of Arrival (AoA),” 2019.
[58] X. Li and K. Pahlavan, “Super-Resolution TOA Estimation With Diversity for Indoor Geolocation,” *IEEE Trans. Wirel. Commun.*, vol. 3, no. 1, pp. 224–234, 2004, doi: 10.1109/TWC.2003.819035.
[59] J. Y. Do, M. Rabinowitz, and P. Enge, “Linear time-of-arrival estimation in a multipath environment by inverse correlation method,” *Proc. Annu. Meet. - Inst. Navig.*, no. June, pp. 720–725, 2005.
[60] Z. Naseem, I. Nausheen, and Z. Mirza, “Propagation Models for Wireless Communication System,” *Int. Res. J. Eng. Technol.*, vol. 9001, pp. 237–242, 2008, [Online]. Available: www.irjet.net.
[61] H. Liu, H. Darabi, P. Banerjee, and J. Liu, “Survey of wireless indoor positioning techniques and systems,” *IEEE Transactions on Systems, Man and Cybernetics Part C: Applications and Reviews*, vol. 37, no. 6. pp. 1067–1080, Nov. 2007, doi: 10.1109/TSMCC.2007.905750.
[62] A. Jafari, “New TDOA based localization method for HDR systems,” Université Pierre et Marie Curie, 2015.
[63] Y. Zhuang *et al.*, “A survey of positioning systems using visible LED lights,” *IEEE Commun. Surv. Tutorials*, vol. 20, no. 3, pp. 1963–1988, 2018, doi: 10.1109/COMST.2018.2806558.
[64] N. Maletic, V. Sark, M. Ehrig, J. Gutierrez, and E. Grass, “Experimental Evaluation of Round-Trip ToF-based Localization in the 60 GHz Band,” *2019 Int. Conf. Indoor Position. Indoor Navig. IPIN 2019*, no. 761329, 2019, doi: 10.1109/IPIN.2019.8911743.
[65] E. V. Carrera, E. Mena, P. Arciniega, A. Padilla, and M. Paredes, “Analysis and evaluation of sound-based positioning techniques for short distances,” *2020 Ieee Andescon, Andescon 2020*, no. October, 2020, doi: 10.1109/ANDESCON50619.2020.9272155.
[66] K. Nur, S. Feng, C. Ling, and W. Ochieng, “Integration of GPS with a WiFi high accuracy ranging functionality,” *Geo-Spatial Inf. Sci.*, vol. 16, no. 3, pp. 155–168, 2013, doi: 10.1080/10095020.2013.817106.
[67] H. Obeidat, W. Shuaieb, O. Obeidat, and R. Abd-Alhameed, *A Review of Indoor Localization Techniques and Wireless Technologies*, vol. 119, no. 1. Springer US, 2021.
[68] H. El-Sayed, G. Athanasiou, and C. Fischione, “Evaluation of localization methods in millimeter-wave wireless systems,” *2014 IEEE 19th Int. Work. Comput. Aided Model. Des. Commun. Links Networks, CAMAD 2014*, pp. 345–349, 2014, doi: 10.1109/CAMAD.2014.7033263.
[69] H. I. Ahmed, P. Wei, I. Memon, Y. Du, and W. Xie, “Estimation of Time Difference of Arrival (TDOA) for the Source Radiates BPSK Signal,” *IJCSI Int. J. Compuer Sci.*, vol. 10, no. 3, pp. 164–171, 2013.

[70] S. M. Prasad, T. Panigrahi, M. Hassan, and M. Ding, “Sampling Free TDOA Localization in Millimeter Wave Networks,” *IEEE Wirel. Commun. Netw. Conf. WCNC*, vol. 2019-April, no. Vcd, pp. 1–6, 2019, doi: 10.1109/WCNC.2019.8886011.
[71] X.-L. Liang, H. Zhang, T.-T. Lu, T. A. Gulliver, and X. Cui, “A Novel TOA Estimation Algorithm Based on Kurtosis and Standard Slope in the 60GHz Sensor Network,” *Int. J. Futur. Gener. Commun. Netw.*, vol. 9, no. 3, pp. 123–138, 2016, doi: 10.14257/ijfgcn.2016.9.3.12.
[72] X. Cui, T. A. Gulliver, H. Song, and J. Li, “Real-Time Positioning Based on Millimeter Wave Device to Device Communications,” *IEEE Access*, vol. 4, pp. 5520–5530, 2016, doi: 10.1109/ACCESS.2016.2604360.
[73] O. Kanhere and T. S. Rappaport, “Position Locationing for Millimeter Wave Systems,” *2018 IEEE Glob. Commun. Conf. GLOBECOM 2018 - Proc.*, pp. 206–212, 2018, doi: 10.1109/GLOCOM.2018.8647983.
[74] B. Alavi and K. Pahlavan, “Bandwidth effect on distance error modeling for indoor geolocation,” *IEEE Int. Symp. Pers. Indoor Mob. Radio Commun. PIMRC*, vol. 3, pp. 2198–2202, 2003, doi: 10.1109/PIMRC.2003.1259106.
[75] J. Luo, L. Fan, and H. Li, “Indoor Positioning Systems Based on Visible Light Communication: State of the Art,” *IEEE Commun. Surv. Tutorials*, vol. 19, no. 4, pp. 2871–2893, 2017, doi: 10.1109/COMST.2017.2743228.
[76] E. Soltanaghaei, A. Kalyanaraman, and K. Whitehouse, “Multipath Triangulation: Decimeter-level WiFi Localization and Orientation with a Single Unaided Receiver,” pp. 376–388, 2018, doi: 10.1145/3210240.3210347.
[77] L. Lu, G. Y. Li, A. L. Swindlehurst, A. Ashikhmin, and R. Zhang, “An overview of massive MIMO: Benefits and challenges,” *IEEE J. Sel. Top. Signal Process.*, vol. 8, no. 5, pp. 742–758, 2014, doi: 10.1109/JSTSP.2014.2317671.
[78] S. Singh and A. Aggarwal, “Survey on Localization Techniques of RFID for IOT,” *Int. J. Comput. Appl.*, vol. 137, no. 12, pp. 23–27, 2016, doi: 10.5120/ijca2016908989.
[79] M. Kok, J. D. Hol, and T. B. Schön, “Using inertial sensors for position and orientation estimation,” *Found. Trends Signal Process.*, vol. 11, no. 1–2, pp. 1–153, 2017, doi: 10.1561/2000000094.
[80] R. Harle, “A Survey of Indoor Inertial Positioning Systems for Pedestrians,” *IEEE Commun. Surv. Tutorials*, vol. 15, no. 3, pp. 1281–1293, 2013, doi: 10.1109/SURV.2012.121912.00075.
[81] D. C. Niehorster, L. Li, and M. Lappe, “The accuracy and precision of position and orientation tracking in the HTC vive virtual reality system for scientific research,” *Iperception.*, vol. 8, no. 3, pp. 1–23, 2017, doi: 10.1177/2041669517708205.
[82] L. Chot Hun, O. Lee Yeng, L. Tien Sze, and K. Voon Chet, “Kalman Filtering and Its Real-Time Applications,” 2016, doi: 10.5772/62352.
[83] Y. Wu, F. Tang, and H. Li, “Image-based camera localization: an overview,” *Vis. Comput. Ind. Biomed. Art*, vol. 1, no. 1, pp. 1–13, 2018, doi: 10.1186/s42492-018-0008-z.
[84] V. Osa, J. Matamales, J. F. Monserrat, and J. López, “Localization in wireless networks: The potential of triangulation techniques,” *Wirel. Pers. Commun.*, vol. 68, no. 4, pp. 1525–1538, 2013, doi: 10.1007/s11277-012-0537-2.
[85] G. Félix, M. Siller, and E. N. Álvarez, “A fingerprinting indoor localization algorithm based deep learning,” *Int. Conf. Ubiquitous Futur. Networks, ICUFN*, vol. 2016-Augus, no. July, pp. 1006–1011, 2016, doi: 10.1109/ICUFN.2016.7536949.
[86] Y. Gu, A. Lo, and I. Niemegeers, “A Survey of Indoor Positioning Systems for Wireless Personal Networks,” *Yanying Gu, Anthony Lo*, vol. 337, no. 1, pp. 13–32, 2008, doi: 10.1136/bmj.a928.
[87] K. Nguyen and Z. Luo, “Evaluation of bluetooth properties for indoor localisation,” *Lect. Notes Geoinf. Cartogr.*, vol. 0, no. 9783642342028, pp. 127–149, 2013, doi: 10.1007/978-3-642-34203-5_8.
[88] E. Elnahrawy, X. Li, and R. P. Martin, “The limits of localization using signal strength: A comparative study,” *2004 First Annu. IEEE Commun. Soc. Conf. Sens. Ad Hoc Commun. Networks, IEEE SECON 2004*, pp. 406–414, 2004, doi: 10.1109/sahcn.2004.1381942.
[89] A. Olivier, G. Bielsa, I. Tejado, M. Zorzi, J. Widmer, and P. Casari, “Lightweight indoor localization for 60-GHz millimeter wave systems,” *2016 13th Annu. IEEE Int. Conf. Sensing, Commun. Networking, SECON 2016*, 2016, doi: 10.1109/SAHCN.2016.7732999.
[90] J. Xiao, Z. Zhou, Y. Yi, and L. M. Ni, “A survey on wireless indoor localization from the device perspective,” *ACM Comput. Surv.*, vol. 49, no. 2, 2016, doi: 10.1145/2933232.
[91] A. Norrdine, “An Algebraic Solution to the Multilateration Problem,” 2012.
[92] K. W. Cheung, H. C. So, W. –. Ma, and Y. T. Chan, “Least Squares Algorithms for Time-of-Arrival-Based Mobile

Location," vol. 47, no. 2, pp. 10–13, 2013.
[93] C. H. Park and J. H. Chang, "Closed-form two-step weighted-leastsquares-based time-of-arrival source localisation using invariance property of maximum likelihood estimator in multiplesample environment," *IET Commun.*, vol. 10, no. 10, pp. 1206–1213, 2016, doi: 10.1049/iet-com.2015.0952.
[94] D. WANG, J. YIN, T. TANG, R. LIU, and Z. WU, "A two-step weighted least-squares method for joint estimation of source and sensor locations: A general framework," *Chinese J. Aeronaut.*, vol. 32, no. 2, pp. 417–443, 2019, doi: 10.1016/j.cja.2018.12.027.
[95] A. Olivier, G. Bielsa, I. Tejado, M. Zorzi, J. Widmer, and P. Casari, "Lightweight indoor localization for 60-GHz millimeter wave systems," *2016 13th Annu. IEEE Int. Conf. Sensing, Commun. Networking, SECON 2016*, 2016, doi: 10.1109/SAHCN.2016.7732999.
[96] S. Bai and H. Qi, "Tackling the flip ambiguity in wireless sensor network localization and beyond," *Digit. Signal Process. A Rev. J.*, vol. 55, pp. 85–97, 2016, doi: 10.1016/j.dsp.2016.05.006.
[97] K. Park, J. Kang, Z. Arjmandi, M. Shahbazi, and G. Sohn, "Multilateration under Flip Ambiguity for Uav Positioning Using Ultrawide-Band," *ISPRS Ann. Photogramm. Remote Sens. Spat. Inf. Sci.*, vol. 5, no. 1, pp. 317–323, 2020, doi: 10.5194/isprs-annals-V-1-2020-317-2020.
[98] Y. Almadani *et al.*, "An experimental evaluation of a 3D visible light positioning system in an industrial environment with receiver tilt and multipath reflections," *Opt. Commun.*, vol. 483, no. June 2020, p. 126654, 2021, doi: 10.1016/j.optcom.2020.126654.
[99] Y. Almadani *et al.*, "A novel 3D visible light positioning method using received signal strength for industrial applications," *Electron.*, vol. 8, no. 11, pp. 0–15, 2019, doi: 10.3390/electronics8111311.
[100] Y. Cheng and T. Zhou, "UWB indoor positioning algorithm based on TDOA technology," *Proc. - 10th Int. Conf. Inf. Technol. Med. Educ. ITME 2019*, pp. 777–782, 2019, doi: 10.1109/ITME.2019.00177.
[101] Y. T. Chan and K. C. Ho, "A Simple and Efficient Estimator for Hyperbolic Location," *IEEE Trans. Signal Process.*, vol. 42, no. 8, pp. 1905–1915, 1994, doi: 10.1109/78.301830.
[102] K. Lee, W. Hwang, H. Ryu, and H. J. Choi, "New TDOA-based three-dimensional positioning method for 3GPP LTE system," *ETRI J.*, vol. 39, no. 2, pp. 264–274, 2017, doi: 10.4218/etrij.17.0116.0554.
[103] R. Blumrich and J. Altmann, "Medium-range localization of aircraft via triangulation," *Appl. Acoust.*, vol. 61, no. 1, pp. 65–82, 2000, doi: 10.1016/S0003-682X(99)00066-3.
[104] D. L. Hall and J. Llinas, "An introduction to multisensor data fusion," *Proc. IEEE*, vol. 85, no. 1, pp. 6–23, 1997, doi: 10.1109/5.554205.
[105] M. Laaraiedh, L. Yu, S. Avrillon, and B. Uguen, "Comparison of hybrid localization schemes using RSSI, TOA, and TDOA," *17th Eur. Wirel. Conf. 2011, EW 2011*, pp. 626–630, 2011.
[106] B. Khaleghi, A. Khamis, F. O. Karray, and S. N. Razavi, "Multisensor data fusion: A review of the state-of-the-art," *Inf. Fusion*, vol. 14, no. 1, pp. 28–44, 2013, doi: 10.1016/j.inffus.2011.08.001.
[107] M. Kozlowski, "Robust and Efficient Residential Indoor Localisation for Healthcare."
[108] F. Castanedo, "A review of data fusion techniques," *Sci. World J.*, vol. 2013, 2013, doi: 10.1155/2013/704504.
[109] L. Kong, X. Peng, Y. Chen, P. Wang, and M. Xu, "Multi-sensor measurement and data fusion technology for manufacturing process monitoring: A literature review," *Int. J. Extrem. Manuf.*, vol. 2, no. 2, 2020, doi: 10.1088/2631-7990/ab7ae6.
[110] R. E. Kalman, "A new approach to linear filtering and prediction problems," *J. Fluids Eng. Trans. ASME*, vol. 82, no. 1, pp. 35–45, 1960, doi: 10.1115/1.3662552.
[111] Z. Cai and D. Zhao, "Unscented Kalman filter for non-linear estimation," *Geomatics Inf. Sci. Wuhan Univ.*, vol. 31, no. 2, pp. 180–183, 2006.
[112] F. E. Ababsa, M. Mallem, and D. Roussel, "Comparison between particle filter approach and Kalman filter-based technique for head tracking in augmented reality systems," *Proc. - IEEE Int. Conf. Robot. Autom.*, vol. 2004, no. 1, pp. 1021–1026, 2004, doi: 10.1109/robot.2004.1307284.
[113] A. B. L. Larsen, S. Hauberg, and K. S. Pedersen, "Unscented kalman filtering for articulated human tracking," *Lect. Notes Comput. Sci. (including Subser. Lect. Notes Artif. Intell. Lect. Notes Bioinformatics)*, vol. 6688 LNCS, pp. 228–237, 2011, doi: 10.1007/978-3-642-21227-7_22.
[114] J. Elfring, E. Torta, and R. Van De Molengraft, "Particle Filters : A Hands-On Tutorial," pp. 1–28, 2021.
[115] Z. X. Liu, "A sequential GM-based PHD filter for a linear Gaussian system," *Sci. China Inf. Sci.*, vol. 56, no. 10, pp. 1–10, 2013, doi: 10.1007/s11432-013-4901-y.
[116] Z. Liu, Q. Zhang, and Y. Zou, "Sequential measurement-driven multi-target Bayesian filter for nonlinear multi-target models," *Int. Conf. Signal Process. Proceedings, ICSP*, vol. 0, pp. 1524–1528, 2016, doi:

10.1109/ICSP.2016.7878081.
[117] Q. Li, R. Li, K. Ji, and W. Dai, “Kalman Filter and Its Application,” *2015 8th Int. Conf. Intell. Networks Intell. Syst.*, no. 10, pp. 74–77, 2015, doi: 10.1109/ICINIS.2015.35.
[118] P. H. Abreu, J. Xavier, D. Castro Silva, L. P. Reis, and M. Petry, “Using Kalman filters to reduce noise from RFID location system,” *Sci. World J.*, vol. 2014, pp. 1–10, 2014, doi: 10.1155/2014/796279.
[119] P. R. Cis *et al.*, “Application of Kalman filtering to noise reduction on microsensor signals Application de filtres de Kalman à la réduction de bruit,” no. October, pp. 443–450, 2000.
[120] G. Welch and G. Bishop, “An Introduction to the Kalman Filter,” *In Pract.*, vol. 7, no. 1, pp. 1–16, 2006, doi: 10.1.1.117.6808.
[121] R. Singh, R. Mehra, and L. Sharma, “Design of Kalman filter for wireless sensor network,” *2016 Int. Conf. Internet Things Appl. IOTA 2016*, pp. 63–67, 2016, doi: 10.1109/IOTA.2016.7562696.
[122] H. Lui, R. Zhangl, and Y. W. Chenl, “Head detection and tracking by mean-shift and Kalman filter,” *3rd Int. Conf. Innov. Comput. Inf. Control. ICICIC’08*, pp. 3–6, 2008, doi: 10.1109/ICICIC.2008.302.
[123] P. Ernesto, “Human Tracking Using Kalman Filter.”
[124] A. Kiruluta, M. Eizenman, and S. Pasupathy, “Predictive head movement tracking using a Kalman filter,” *IEEE Trans. Syst. Man, Cybern. Part B Cybern.*, vol. 27, no. 2, pp. 326–331, 1997, doi: 10.1109/3477.558841.
[125] R. T. Azuma, “Predictive Tracking for Augmented Reality,” no. February, p. 262, 1995, [Online]. Available: http://www.cs.unc.edu/techreports/95-007.pdf.
[126] X. Yang, W. A. Zhang, M. Z. Q. Chen, and L. Yu, “Hybrid sequential fusion estimation for asynchronous sensor network-based target tracking,” *IEEE Trans. Control Syst. Technol.*, vol. 25, no. 2, pp. 669–676, 2017, doi: 10.1109/TCST.2016.2558632.
[127] H. Qi and J. B. Moore, “Direct Kalman filtering approach for GPS/INS integration,” *IEEE Trans. Aerosp. Electron. Syst.*, 2002, doi: 10.1109/TAES.2002.1008998.
[128] G. Nützi, S. Weiss, D. Scaramuzza, and R. Siegwart, “Fusion of IMU and vision for absolute scale estimation in monocular SLAM,” *J. Intell. Robot. Syst. Theory Appl.*, vol. 61, no. 1–4, pp. 287–299, 2011, doi: 10.1007/s10846-010-9490-z.
[129] X. Yang, W. A. Zhang, L. Yu, and K. Xing, “Sequential fusion estimations for asynchronous sensor networks,” *Chinese Control Conf. CCC*, vol. 2015-Septe, no. 1, pp. 7692–7696, 2015, doi: 10.1109/ChiCC.2015.7260861.
[130] J. A. Corrales, F. A. Candelas, and F. Torres, “Hybrid tracking of human operators using IMU/UWB data fusion by a Kalman filter,” *HRI 2008 - Proc. 3rd ACM/IEEE Int. Conf. Human-Robot Interact. Living with Robot.*, pp. 193–200, 2008, doi: 10.1145/1349822.1349848.
[131] P. S. Maybeck and G. M. Siouris, “Stochastic Models, Estimation, and Control, Volume I,” *IEEE Transactions on Systems, Man and Cybernetics*. 1980, doi: 10.1109/TSMC.1980.4308494.
[132] A. G. Gelen and A. Atasoy, “A New Method for Kalman Filter Tuning,” *2018 Int. Conf. Artif. Intell. Data Process. IDAP 2018*, 2019, doi: 10.1109/IDAP.2018.8620863.
[133] K. Saho, “Kalman Filter for Moving Object Tracking: Performance Analysis and Filter Design,” in *Kalman Filters - Theory for Advanced Applications*, 2018.
[134] J. S. Gutmann and D. Fox, “An experimental comparison of localization methods continued,” in *IEEE International Conference on Intelligent Robots and Systems*, 2002, vol. 1, pp. 454–459, doi: 10.1109/irds.2002.1041432.
[135] X. Wang, M. Fu, and H. Zhang, “Target tracking in wireless sensor networks based on the combination of KF and MLE using distance measurements,” *IEEE Trans. Mob. Comput.*, vol. 11, no. 4, pp. 567–576, 2012, doi: 10.1109/TMC.2011.59.
[136] G. A. Terejanu, “Unscented Kalman filter tutorial,” *Univ. Buffalo, Dep. Comput. Sci. Eng. NY*, no. 1, pp. 1–6, 2011.
[137] H. Qasem and L. Reindl, “Unscented and extended kalman estimators for non linear indoor tracking using distance measurements,” *4th Work. Positioning, Navig. Commun. 2007, WPNC’07 - Work. Proc.*, vol. 2007, pp. 177–181, 2007, doi: 10.1109/wpnc.2007.353631.
[138] R. Van Der Merwe and E. A. Wan, “The square-root unscented Kalman filter for state and parameter-estimation,” *ICASSP, IEEE Int. Conf. Acoust. Speech Signal Process. - Proc.*, vol. 6, no. February 2001, pp. 3461–3464, 2001, doi: 10.1109/icassp.2001.940586.
[139] G. J. Liu, X. L. Tang, J. H. Huang, J. F. Liu, and D. Sun, “Hierarchical model-based human motion tracking via unscented Kalman filter,” *Proc. IEEE Int. Conf. Comput. Vis.*, no. 92, 2007, doi: 10.1109/ICCV.2007.4408941.
[140] B. D. R. Stenger, P. R. S. Mendonca, and R. Cipolla, “Model-Based Hand Tracking Using an Unscented Kalman

Filter," pp. 8.1-8.10, 2013, doi: 10.5244/c.15.8.
[141] B. Ekstrand, "Some aspects on filter design for target tracking," *Journal of Control Science and Engineering*, vol. 2012. 2012, doi: 10.1155/2012/870890.
[142] G. F. Basso, T. Guilherme Silva De Amorim, A. V. Brito, and T. P. Nascimento, "Kalman Filter with Dynamical Setting of Optimal Process Noise Covariance," *IEEE Access*, vol. 5, pp. 8385–8393, 2017, doi: 10.1109/ACCESS.2017.2697072.
[143] L. Elling, "Performance Analysis of Interacting Multiple Model - Extended Kalman Filters at High Update Rates," vol. 4, no. 4, pp. 1–79, 2016.
[144] K. Saho and M. Masugi, "Automatic Parameter Setting Method for an Accurate Kalman Filter Tracker Using an Analytical Steady-State Performance Index," *IEEE Access*, vol. 3, pp. 1919–1930, 2015, doi: 10.1109/ACCESS.2015.2486766.
[145] R. Labbe, "Kalman-and-Bayesian-Filters-in-Python (/github/rlabbe/Kalman-and-Bayesian-Filters-in-Python/tree/master)," pp. 1–24, 2021.
[146] H. Koyuncu, "Indoor Localisation By Using Wireless Sensor Nodes A Doctoral Thesis," 2014, [Online]. Available: https://dspace.lboro.ac.uk/2134/18044.
[147] F. Van Diggelen and C. Abraham, "Indoor GPS technology," *CTIA Wireless-Agenda, Dallas*, no. May, pp. 1–10, 2001, [Online]. Available: http://d1.ourdev.cn/bbs_upload782111/files_35/ourdev_607138GSZQOV.pdf.
[148] J. Chung, M. Donahoe, C. Schmandt, I. J. Kim, P. Razavai, and M. Wiseman, "Indoor location sensing using geo-magnetism," *MobiSys'11 - Compil. Proc. 9th Int. Conf. Mob. Syst. Appl. Serv. Co-located Work.*, pp. 141–154, 2011, doi: 10.1145/1999995.2000010.
[149] K. P. Subbu, B. Gozick, and R. Dantu, "LocateMe: Magnetic-fields-based indoor localization using smartphones," *ACM Trans. Intell. Syst. Technol.*, vol. 4, no. 4, 2013, doi: 10.1145/2508037.2508054.
[150] O. Woodman, "An introduction to inertial navigation," 2007.
[151] Y.-S. Kuo, P. Pannuto, K.-J. Hsiao, and P. Dutta, "Luxapose," pp. 447–458, 2014, doi: 10.1145/2639108.2639109.
[152] D. Eger Passos and B. Jung, *Measuring the Accuracy of Inside-Out Tracking in XR Devices Using a High-Precision Robotic Arm*, vol. 1224 CCIS. Springer International Publishing, 2020.
[153] A. Mandai, C. V. Lopes, T. Givargis, A. Haghighat, R. Jurdak, and P. Baldi, "Beep: 3D indoor positioning using audible sound," *2005 2nd IEEE Consum. Commun. Netw. Conf. CCNC2005*, vol. 2005, no. May 2014, pp. 348–353, 2005, doi: 10.1109/ccnc.2005.1405195.
[154] B. Xu, R. Yu, G. Sun, and Z. Yang, "Whistle: Synchronization-free TDOA for localization," *Proc. - Int. Conf. Distrib. Comput. Syst.*, pp. 760–769, 2011, doi: 10.1109/ICDCS.2011.30.
[155] Y. C. Tung and K. G. Shin, "EchoTag: Accurate infrastructure-free indoor location tagging with smartphones," *Proc. Annu. Int. Conf. Mob. Comput. Networking, MOBICOM*, vol. 2015-Septe, pp. 525–536, 2015, doi: 10.1145/2789168.2790102.
[156] A. Harter, A. Hopper, P. Steggles, A. Ward, and P. Webster, "The anatomy of a context-aware application," *Wirel. Networks*, vol. 8, no. 2–3, pp. 187–197, 2002, doi: 10.1023/A:1013767926256.
[157] Y. Fukuju, M. Minami, H. Morikawa, and T. Aoyama, "DOLPHIN: An autonomous indoor positioning system in ubiquitous computing environment," *Proc. - IEEE Work. Softw. Technol. Futur. Embed. Syst. WSTFES 2003*, pp. 53–56, 2003, doi: 10.1109/WSTFES.2003.1201360.
[158] E. Luckett, "A Quantitative Evaluation of the HTC Vive for Virtual Reality Research," no. May, 2018, [Online]. Available: http://thesis.honors.olemiss.edu/1122/7/Luckett Thesis.pdf%0Ahttp://thesis.honors.olemiss.edu/1122/%0Afile:///Users/momma/Dropbox (個人)/Library.papers3/Files/50/500D2813-C25B-4414-AE17-802A93AF21E4.pdf%0Apapers3://publication/uuid/D186C232-A717-4E2E-9142-0.
[159] M. Borges, A. Symington, B. Coltin, T. Smith, and R. Ventura, "HTC Vive: Analysis and Accuracy Improvement," *IEEE Int. Conf. Intell. Robot. Syst.*, pp. 2610–2615, 2018, doi: 10.1109/IROS.2018.8593707.
[160] L. Li, P. Hu, C. Peng, G. Shen, and F. Zhao, "Epsilon: A visible light based positioning system," *Proc. 11th USENIX Symp. Networked Syst. Des. Implementation, NSDI 2014*, pp. 331–343, 2014.
[161] B. Paramvir and V. Padmanabhan, "RADAR: An In-Building RF-based User Location and Tracking System," *Biomed. Res.*, vol. 2016, no. Special Issue 1, pp. S400–S406, 2016.
[162] P. Bahl and V. N. Padmanabhan, "Enhancements to the RADAR User Location and Tracking System," 2000.
[163] N. Hernández *et al.*, "WiFiNet: WiFi-based indoor localisation using CNNs," *Expert Syst. Appl.*, vol. 177, no. October 2019, 2021, doi: 10.1016/j.eswa.2021.114906.

[164] R. Faragher and R. Harle, “Location fingerprinting with bluetooth low energy beacons,” *IEEE J. Sel. Areas Commun.*, vol. 33, no. 11, pp. 2418–2428, 2015, doi: 10.1109/JSAC.2015.2430281.
[165] J. Niu, B. Wang, L. Shu, T. Q. Duong, and Y. Chen, “ZIL: An Energy-Efficient Indoor Localization System Using ZigBee Radio to Detect WiFi Fingerprints,” *IEEE J. Sel. Areas Commun.*, vol. 33, no. 7, pp. 1431–1442, 2015, doi: 10.1109/JSAC.2015.2430171.
[166] J. Hightower, G. Borriello, and R. Want, “SpotON: An indoor 3D location sensing technology based on RF signal strength,” *Uw Cse*, no. March 2000, p. 16, 2000, [Online]. Available: http://scholar.google.com/scholar?hl=en&btnG=Search&q=intitle:SpotON+:+An+Indoor+3D+Location+Sensing+Technology+Based+on+RF+Signal+Strength#0.
[167] A. Papapostolou and H. Chaouchi, “Considerations for RFID-based indoor simultaneous tracking,” *IFIP Adv. Inf. Commun. Technol.*, vol. 308, pp. 309–320, 2009, doi: 10.1007/978-3-642-03841-9_28.
[168] A. R. J. Ruiz and F. S. Granja, “Comparing Ubisense, BeSpoon, and DecaWave UWB Location Systems: Indoor Performance Analysis,” *IEEE Trans. Instrum. Meas.*, vol. 66, no. 8, pp. 2106–2117, 2017, doi: 10.1109/TIM.2017.2681398.
[169] L. Yan, X. Rong Li, Y. Xia, and M. Fu, “Optimal sequential and distributed fusion for state estimation in cross-correlated noise,” *Automatica*, vol. 49, no. 12, pp. 3607–3612, 2013, doi: 10.1016/j.automatica.2013.09.013.
[170] A. T. Alouani, J. E. Gray, and D. H. McCabe, “Theory of distributed estimation using multiple asynchronous sensors,” *IEEE Trans. Aerosp. Electron. Syst.*, vol. 41, no. 2, pp. 717–722, 2005, doi: 10.1109/TAES.2005.1468761.
[171] L. Yan, Y. Xia, and M. Fu, “Optimal fusion estimation for stochastic systems with cross-correlated sensor noises,” *Sci. China Inf. Sci.*, vol. 60, no. 12, pp. 1–14, 2017, doi: 10.1007/s11432-017-9140-x.
[172] M. E. Liggins *et al.*, “Distributed fusion architectures and algorithms for target tracking,” *Proc. IEEE*, vol. 85, no. 1, pp. 95–106, 1997, doi: 10.1109/jproc.1997.554211.
[173] W. A. Zhang, B. Chen, and M. Z. Q. Chen, “Hierarchical fusion estimation for clustered asynchronous sensor networks,” *IEEE Trans. Automat. Contr.*, vol. 61, no. 10, pp. 3064–3069, 2016, doi: 10.1109/TAC.2015.2498701.
[174] D. Jeon and Y. Eun, “Distributed asynchronous multiple sensor fusion with nonlinear multiple models,” *Aerosp. Sci. Technol.*, vol. 39, pp. 692–704, 2014, doi: 10.1016/j.ast.2014.08.006.
[175] W. A. Zhang and L. Shi, “Sequential fusion estimation for clustered sensor networks,” *Automatica*, vol. 89, pp. 358–363, 2018, doi: 10.1016/j.automatica.2017.12.038.
[176] H. Xie, J. Xu, and J. Li, “Adaptive localization algorithm in distributed asynchronous wireless sensor network,” *ICALIP 2010 - 2010 Int. Conf. Audio, Lang. Image Process. Proc.*, pp. 1561–1565, 2010, doi: 10.1109/ICALIP.2010.5684508.
[177] T. Li, A. Ekpenyong, and Y. F. Huang, “A location system using asynchronous distributed sensors,” *Proc. - IEEE INFOCOM*, vol. 1, pp. 620–628, 2004, doi: 10.1109/infcom.2004.1354533.
[178] W. D. Blair, T. R. Rice, A. T. Alouani, and P. Xia, “Asynchronous data fusion for target tracking with a multitasking radar and optical sensor,” *Acquis. Tracking, Pointing V*, vol. 1482, no. August 1991, pp. 234–245, 1991, doi: 10.1117/12.45699.
[179] X. J. Shen, Y. T. Luo, Y. M. Zhu, and E. Bin Song, “Globally optimal distributed Kalman filtering fusion,” *Sci. China Inf. Sci.*, vol. 55, no. 3, pp. 512–529, 2012, doi: 10.1007/s11432-011-4538-7.
[180] B. Chen, W. A. Zhang, and L. Yu, “Distributed fusion estimation with missing measurements, random transmission delays and packet dropouts,” *IEEE Trans. Automat. Contr.*, vol. 59, no. 7, pp. 1961–1967, 2014, doi: 10.1109/TAC.2013.2297192.
[181] H. Yanyan, D. Zhansheng, and H. Chongzhao, “Optimal batch asynchronous fusion algorithm,” *2005 IEEE Int. Conf. Veh. Electron. Saf. Proc.*, vol. 2005, no. 1, pp. 237–240, 2005, doi: 10.1109/ICVES.2005.1563648.
[182] W. A. Zhang, M. Z. Q. Chen, A. Liu, and S. Liu, “Aperiodic optimal linear estimation for networked systems with communication uncertainties,” *IEEE Trans. Cybern.*, vol. 47, no. 8, pp. 2256–2265, 2017, doi: 10.1109/TCYB.2017.2684136.
[183] T. D. Larsen, N. A. Andersen, O. Ravn, and N. K. Poulsen, “Incorporation of time delayed measurements in a discrete-time Kalman filter,” *Proc. IEEE Conf. Decis. Control*, vol. 4, no. December, pp. 3972–3977, 1998, doi: 10.1109/cdc.1998.761918.
[184] Y. Hu, Z. Duan, and D. Zhou, “Estimation fusion with general asynchronous multi-rate sensors,” *IEEE Trans. Aerosp. Electron. Syst.*, vol. 46, no. 4, pp. 2090–2102, 2010, doi: 10.1109/TAES.2010.5595618.
[185] L. P. Yan, B. S. Liu, and D. H. Zhou, “The modeling and estimation of asynchronous multirate multisensor

dynamic systems," *Aerosp. Sci. Technol.*, vol. 10, no. 1, pp. 63–71, 2006, doi: 10.1016/j.ast.2005.09.001.
[186] L. P. Yan, B. S. Liu, and D. H. Zhou, "Asynchronous multirate multisensor information fusion algorithm," *IEEE Trans. Aerosp. Electron. Syst.*, vol. 43, no. 3, pp. 1135–1146, 2007, doi: 10.1109/TAES.2007.4383603.
[187] H. Geng, Z. Wang, Y. Liang, Y. Cheng, and F. E. Alsaadi, "State estimation for asynchronous sensor systems with Markov jumps and multiplicative noises," *Inf. Sci. (Ny).*, vol. 417, pp. 1–19, 2017, doi: 10.1016/j.ins.2017.07.001.
[188] W. A. Zhang, K. Zhou, X. Yang, and A. Liu, "Sequential Fusion Estimation for Networked Multisensor Nonlinear Systems," *IEEE Trans. Ind. Electron.*, vol. 67, no. 6, pp. 4991–4999, 2020, doi: 10.1109/TIE.2019.2927191.
[189] H. Zhu and M. Luo, "Hybrid Robust Sequential Fusion Estimation for WSN-Assisted Moving-Target Localization with Sensor-Node-Position Uncertainty," *IEEE Trans. Instrum. Meas.*, vol. 69, no. 9, pp. 6499–6508, 2020, doi: 10.1109/TIM.2020.2967875.
[190] W. Pu, Y. F. Liu, J. Yan, H. Liu, and Z. Q. Luo, "Optimal estimation of sensor biases for asynchronous multi-sensor data fusion," *Math. Program.*, vol. 170, no. 1, pp. 357–386, 2018, doi: 10.1007/s10107-018-1304-2.
[191] P. Geneva, K. Eckenhoff, and G. Huang, "Asynchronous Multi-Sensor Fusion for 3D Mapping and Localization," *Proc. - IEEE Int. Conf. Robot. Autom.*, pp. 5994–5999, 2018, doi: 10.1109/ICRA.2018.8460204.
[192] C. Guo, D. Kottas, R. DuToit, A. Ahmed, R. Li, and S. Roumeliotis, "Efficient Visual-Inertial Navigation using a Rolling-Shutter Camera with Inaccurate Timestamps," 2015, doi: 10.15607/rss.2014.x.057.
[193] A. Patron-Perez, S. Lovegrove, and G. Sibley, "A Spline-Based Trajectory Representation for Sensor Fusion and Rolling Shutter Cameras," *Int. J. Comput. Vis.*, vol. 113, no. 3, pp. 208–219, 2015, doi: 10.1007/s11263-015-0811-3.
[194] R. Tadayoni, A. Henten, and J. Sørensen, "Mobile communications – On standards, classifications and generations," in *28th European Regional Conference of the International Telecommunications Society*, 2017, vol. 42, no. 3, pp. 253–262, doi: 10.1016/j.telpol.2018.01.001.
[195] A. M. Al-Samman, T. A. Rahman, M. H. Azmi, M. N. Hindia, I. Khan, and E. Hanafi, "Statistical modelling and characterization of experimental mm-wave indoor channels for future 5g wireless communication networks," *PLoS One*, vol. 11, no. 9, 2016, doi: 10.1371/journal.pone.0163034.
[196] 3GPP, "(3GPP TS 22.261 V16.14) 5G; Service requirements for next generation new services and markets," vol. 0, no. Release 16, 2021.
[197] A. Gupta and R. K. Jha, "A Survey of 5G Network: Architecture and Emerging Technologies," *IEEE Access*, vol. 3, pp. 1206–1232, 2015, doi: 10.1109/ACCESS.2015.2461602.
[198] G. Liu and D. Jiang, "5G: Vision and Requirements for Mobile Communication System towards Year 2020," *Chinese J. Eng.*, vol. 2016, no. March 2016, 2016, doi: 10.1155/2016/5974586.
[199] L. Shi *et al.*, "5G Internet of Radio Light Positioning System for Indoor Broadcasting Service," *IEEE Trans. Broadcast.*, vol. 66, no. 2, pp. 534–544, 2020, doi: 10.1109/TBC.2020.2981755.
[200] 3GPP, "3GPP TS 22.104 Service requirements for cyber-physical control applications in vertical domains," vol. 0, no. Release 16, pp. 1–55, 2020.
[201] T. Specification and G. Services, "(3GPP TS 22.261 V17.7) 5G; Service requirements for next generation new services and markets," vol. 0, no. Release 17, 2021.
[202] 3GPP, "(3GPP TS 22.261 V15.5.0) 5G; Service requirements for next generation new services and markets," vol. TS 22.261, pp. 0–52, 2018.
[203] R. Tiwari, S. Buse, and C. Herstatt, "The Mobile Commerce Technologies: Generations, Standards and Protocols," *SSRN Electron. J.*, vol. 49, no. 40, 2012, doi: 10.2139/ssrn.1583453.
[204] T. L. Marzetta, "Massive MIMO: An introduction," *Bell Labs Tech. J.*, vol. 20, pp. 11–12, 2015, doi: 10.15325/BLTJ.2015.2407793.
[205] E. G. Larsson, O. Edfors, F. Tufvesson, and T. L. Marzetta, "Massive MIMO for next generation wireless systems," *IEEE Commun. Mag.*, vol. 52, no. 2, pp. 186–195, 2014, doi: 10.1109/MCOM.2014.6736761.
[206] J. Cosmas, Y. Zhang, and X. Zhang, "Internet of Radio-Light: 5G broadband in buildings," 2017.
[207] J. Cosmas *et al.*, "5G Internet of radio light services for supermarkets," 2017, doi: 10.1109/IFWS.2017.8245977.
[208] J. Cosmas *et al.*, "A Scaleable and License Free 5G Internet of Radio Light Architecture for Services in Train Stations," *IEEE Int. Symp. Broadband Multimed. Syst. Broadcast. BMSB*, vol. 2018-June, pp. 168–173, 2018, doi: 10.1109/BMSB.2018.8436938.
[209] J. Cosmas *et al.*, "5G Internet of radio light services for Musée de la Carte à Jouer," 2018, doi: 10.23919/GLC.2018.8319095.

[210] J. Cosmas *et al.*, "A 5G Radio-Light SDN Architecture for Wireless and Mobile Network Access in Buildings," 2018, doi: 10.1109/5GWF.2018.8516970.
[211] J. Cosmas *et al.*, "Network and application layer services for high performance communications in buildings," *IEEE Int. Symp. Broadband Multimed. Syst. Broadcast. BMSB*, vol. 2020-Octob, 2020, doi: 10.1109/BMSB49480.2020.9379769.
[212] Y. Zhang *et al.*, "Internet of radio and light: 5G building network radio and edge architecture," *Intell. Converg. Networks*, vol. 1, no. 1, pp. 37–57, 2020, doi: 10.23919/icn.2020.0002.
[213] I. Iskandar and D. Harinitha, "Simulation and characterization of WLAN indoor channels at 60 GHz," *CTRQ 2011 - 4th Int. Conf. Commun. Theory, Reliab. Qual. Serv.*, no. c, pp. 128–132, 2011.
[214] D. Wang, M. Fattouche, and X. Zhan, "Pursuance of mm-Level Accuracy: Ranging and Positioning in mmWave Systems," *IEEE Syst. J.*, vol. 13, no. 2, pp. 1169–1180, 2019, doi: 10.1109/JSYST.2018.2805879.
[215] P. Gertzell *et al.*, "5G multi-BS positioning with a single-antenna receiver," *IEEE Int. Symp. Pers. Indoor Mob. Radio Commun. PIMRC*, vol. 2020-Augus, 2020, doi: 10.1109/PIMRC48278.2020.9217124.
[216] A. Jafari, J. Sarrazin, D. Lautru, A. Benlarbi-Delaï, L. Petrillo, and P. De Doncker, "NLOS influence on 60 GHz indoor localization based on a new TDOA extraction approach," *Eur. Microw. Week 2013, EuMW 2013 - Conf. Proceedings; EuMC 2013 43rd Eur. Microw. Conf.*, pp. 330–333, 2013, doi: 10.23919/EuMC.2013.6686658.
[217] F. Zhao, T. Huang, and D. Wang, "Fundamental limits of single anchor-based cooperative localization in millimeter wave systems," *EURASIP J. Adv. Signal Process.*, vol. 2020, no. 1, 2020, doi: 10.1186/s13634-020-00683-6.
[218] T. Wei and X. Zhang, "MTrack: High-precision passive tracking using millimeter wave radios," 2015, doi: 10.1145/2789168.2790113.
[219] C. Loyez, M. Bocquet, and K. Haddadi, "Six-Port Technology for 5G Millimeter-Wave Localization Systems," *Proc. 2018 20th Int. Conf. Electromagn. Adv. Appl. ICEAA 2018*, no. 3, pp. 272–275, 2018, doi: 10.1109/ICEAA.2018.8520353.
[220] N. Obeid, M. Heddebaut, F. Boukour, C. Loyez, and N. Rolland, "Millimeter wave ultra wide band short range radar localization accuracy," *IEEE Veh. Technol. Conf.*, pp. 1–5, 2009, doi: 10.1109/VETECS.2009.5073669.
[221] X. Cui, X. Chen, H. Song, and J. Li, "Study on the ranging estimation based on millimeter-wave with raised-cosine carrier," *Proc. - 2016 Int. Conf. Identification, Inf. Knowl. Internet Things, IIKI 2016*, vol. 2018-Janua, no. 2, pp. 223–226, 2018, doi: 10.1109/IIKI.2016.107.
[222] B. Lin, X. Tang, Z. Ghassemlooy, C. Lin, and Y. Li, "Experimental Demonstration of an Indoor VLC Positioning System Based on OFDMA," *IEEE Photonics J.*, vol. 9, no. 2, pp. 1–9, 2017, doi: 10.1109/JPHOT.2017.2672038.
[223] F. Alam, B. Parr, and S. Mander, "Visible Light Positioning Based on Calibrated Propagation Model," *IEEE Sensors Lett.*, vol. 3, no. 2, pp. 1–4, 2019, doi: 10.1109/LSENS.2018.2889270.
[224] S. H. Yang, E. M. Jeong, D. R. Kim, H. S. Kim, Y. H. Son, and S. K. Han, "Indoor three-dimensional location estimation based on LED visible light communication," *Electron. Lett.*, vol. 49, no. 1, pp. 54–56, 2013, doi: 10.1049/el.2012.3167.
[225] M. Yasir, S. W. Ho, and B. N. Vellambi, "Indoor positioning system using visible light and accelerometer," *J. Light. Technol.*, vol. 32, no. 19, pp. 3306–3316, 2014, doi: 10.1109/JLT.2014.2344772.
[226] Y. U. Lee and M. Kavehrad, "Two hybrid positioning system design techniques with lighting LEDs and ad-hoc wireless network," *IEEE Trans. Consum. Electron.*, vol. 58, no. 4, pp. 1176–1184, 2012, doi: 10.1109/TCE.2012.6414983.
[227] A. Hasan, T. Glass, F. Alam, and M. Legg, "Fingerprint-Based Visible Light Positioning using Multiple Photodiode Receiver," *2020 IEEE Sensors Appl. Symp. SAS 2020 - Proc.*, 2020, doi: 10.1109/SAS48726.2020.9220080.
[228] H. Zhang *et al.*, "High-precision indoor visible light positioning using modified momentum back propagation neural network with sparse training point," *Sensors (Switzerland)*, vol. 19, no. 10. 2019, doi: 10.3390/s19102324.
[229] Y. S. Erogluy, I. Guvency, N. Palay, and M. Yukselz, "AOA-based localization and tracking in multi-element VLC systems," *2015 IEEE 16th Annu. Wirel. Microw. Technol. Conf. WAMICON 2015*, pp. 1–5, 2015, doi: 10.1109/WAMICON.2015.7120424.
[230] M. A. Long, P. B. Stretesky, G. Harms, R. Sollund, P. Macmillan, and B. Chapter, "A VLC Smartphone Camera based Indoor Positioning System," vol. 51, no. September, pp. 1–51, 2015.
[231] R. Zhang, W. De Zhong, K. Qian, and D. Wu, "Image Sensor Based Visible Light Positioning System with Improved Positioning Algorithm," *IEEE Access*, vol. 5, pp. 6087–6094, 2017, doi:

10.1109/ACCESS.2017.2693299.
[232] C. Wang, L. Wang, X. Chi, S. Liu, W. Shi, and J. Deng, “The research of indoor positioning based on visible light communication,” *China Commun.*, vol. 12, no. 8, pp. 85–92, 2015, doi: 10.1109/CC.2015.7224709.
[233] M. F. Keskin, E. Gonendik, S. Gezici, and S. Member, “Improved Lower Bounds for Ranging in Synchronous Visible Light Positioning Systems,” no. c, pp. 1–9, 2016.
[234] N. A. Mohammed and M. A. Elkarim, “Exploring the effect of diffuse reflection on indoor localization systems based on RSSI-VLC,” *Opt. Express*, vol. 23, no. 16, p. 20297, 2015, doi: 10.1364/oe.23.020297.
[235] W. Gu, M. Aminikashani, P. Deng, and M. Kavehrad, “Impact of Multipath Reflections on the Performance of Indoor Visible Light Positioning Systems,” *J. Light. Technol.*, vol. 34, no. 10, pp. 2578–2587, 2016, doi: 10.1109/JLT.2016.2541659.
[236] A. J. C. Moreira, R. T. Valadas, and A. M. De Oliveira Duarte, “Optical interference produced by artificial light,” *Wirel. Networks*, vol. 3, no. 2, pp. 131–140, 1997, doi: 10.1023/A:1019140814049.
[237] W. Gu, M. Aminikashani, and M. Kavehrad, “Indoor visible light positioning system with multipath reflection analysis,” *2016 IEEE Int. Conf. Consum. Electron. ICCE 2016*, no. Mmc, pp. 89–92, 2016, doi: 10.1109/ICCE.2016.7430533.
[238] K. Lee, H. Park, and J. R. Barry, “Indoor channel characteristics for visible light communications,” *IEEE Commun. Lett.*, vol. 15, no. 2, pp. 217–219, 2011, doi: 10.1109/LCOMM.2011.010411.101945.
[239] G. Shi, Y. Li, and W. Cheng, “Accuracy analysis of indoor visible light communication localization system based on received signal strength in non-line-of-sight environments by using least squares method,” *Opt. Eng.*, vol. 58, no. 05, p. 1, 2019, doi: 10.1117/1.oe.58.5.056102.
[240] P. Du *et al.*, “Experimental Demonstration of 3D Visible Light Positioning Using Received Signal Strength with Low-Complexity Trilateration Assisted by Deep Learning Technique,” *IEEE Access*, vol. 7, pp. 93986–93997, 2019, doi: 10.1109/ACCESS.2019.2928014.
[241] S. H. Yang, E. M. Jung, and S. K. Han, “Indoor location estimation based on LED visible light communication using multiple optical receivers,” *IEEE Commun. Lett.*, vol. 17, no. 9, pp. 1834–1837, 2013, doi: 10.1109/LCOMM.2013.070913.131120.
[242] S. Xu, Y. Wu, X. Wang, and F. Wei, “Indoor 3D visible light positioning system based on adaptive parameter particle swarm optimisation,” *IET Commun.*, vol. 14, no. 20, pp. 3707–3714, 2020, doi: 10.1049/iet-com.2019.1141.
[243] D. Kim, J. K. Park, and J. T. Kim, “Three-Dimensional VLC Positioning System Model and Method Considering Receiver Tilt,” *IEEE Access*, vol. 7, pp. 132205–132216, 2019, doi: 10.1109/ACCESS.2019.2940759.
[244] C. Jenila and R. K. Jeyachitra, “Illumination, communication and energy efficiency analysis of indoor visible light communication systems under the influence of optical source emission characteristics,” *Photonic Netw. Commun.*, vol. 38, no. 1, pp. 129–141, 2019, doi: 10.1007/s11107-019-00834-2.
[245] H. Q. Nguyen *et al.*, “Effect of LED emission cross-section in indoor visible light communication systems,” *Eurasip J. Wirel. Commun. Netw.*, vol. 2012, pp. 1–11, 2012, doi: 10.1186/1687-1499-2012-286.
[246] H. S. Kim, D. R. Kim, S. H. Yang, Y. H. Son, and S. K. Han, “An indoor visible light communication positioning system using a RF carrier allocation technique,” *J. Light. Technol.*, vol. 31, no. 1, pp. 134–144, 2013, doi: 10.1109/JLT.2012.2225826.
[247] N. Wu, L. Feng, and A. Yang, “Localization Accuracy Improvement of a Visible Light Positioning System Based on the Linear Illumination of LED Sources,” *IEEE Photonics J.*, vol. 9, no. 5, 2017, doi: 10.1109/JPHOT.2017.2727643.
[248] Ali, Kareem *et al.*, “Measurement Campaign on 5G Indoor millimeter Wave and Visible Light Communications Multi Component Carrier System,” 2021.
[249] L. T. Chen and G. Keiser, “Simplified design of a precise freeform TIR lens for LED lighting applications,” *16th Opto-Electronics Commun. Conf. OECC 2011*, pp. 509–510, 2011.
[250] I. Tavakkolnia, D. Cheadle, R. Bian, T. H. Loh, and H. Haas, “High speed millimeter-wave and visible light communication with off-the-shelf components,” *2020 IEEE Globecom Work. GC Wkshps 2020 - Proc.*, vol. 1, pp. 1–6, 2020, doi: 10.1109/GCWkshps50303.2020.9367475.
[251] C. C. Zarakovitis *et al.*, “Three-dimensional Access Point Assignment in Hybrid VLC, mmWave and WiFi Wireless Access Networks,” *IEEE Int. Conf. Commun.*, vol. 2020-June, 2020, doi: 10.1109/ICC40277.2020.9148722.
[252] O. Narmanlioglu and M. Uysal, “Event-Triggered Adaptive Handover for Centralized Hybrid VLC/MMW Networks,” *IEEE Trans. Commun.*, vol. PP, no. c, pp. 1–1, 2021, doi: 10.1109/tcomm.2021.3120719.

[253] P. Botsinis *et al.*, “Quantum-Assisted Indoor Localization for Uplink mm-Wave and Downlink Visible Light Communication Systems,” *IEEE Access*, vol. 5, pp. 23327–23351, 2017, doi: 10.1109/ACCESS.2017.2733557.
[254] A. M. Nor and E. M. Mohamed, “Li-Fi Positioning for Efficient Millimeter Wave Beamforming Training in Indoor Environment,” *Mob. Networks Appl.*, vol. 24, no. 2, pp. 517–531, 2019, doi: 10.1007/s11036-018-1154-4.
[255] C. W. Hsu, S. J. Su, Y. W. Chen, Q. Zhou, Y. Alfadhli, and G. K. Chang, “Real-time Demonstration of 5G MMW Beamforming and Tracking Using Integrated Visible Light Positioning System,” *2021 Opt. Fiber Commun. Conf. Exhib. OFC 2021 - Proc.*, vol. 1, pp. 5–7, 2021, doi: 10.1364/ofc.2021.tu5e.6.
[256] S. M. Sheikholeslami, F. Fazel, J. Abouei, and K. N. Plataniotis, “Sub-Decimeter VLC 3D Indoor Localization with Handover Probability Analysis,” *IEEE Access*, vol. 9, pp. 122236–122253, 2021, doi: 10.1109/ACCESS.2021.3108173.
[257] B. Meunier, J. Cosmas, N. Jawad, and K. Ali, “Realising a new generation of 5G VR systems through Internet of Radio Light,” pp. 1–8, 2019.
[258] B. Meunier and J. Cosmas, “5G Internet of Radio Light Virtual Reality System,” 2018, doi: 10.1109/BMSB.2018.8436602.
[259] MathWorks, “Measure the Performance of Your Code.” https://uk.mathworks.com/help/matlab/matlab_prog/measure-performance-of-your-program.html (accessed Apr. 09, 2021).
[260] F. E. Grubbs, “Sample Criteria for Testing Outlying Observations,” *Ann. Math. Stat.*, vol. 21, no. 1, pp. 27–58, 1950, doi: 10.1214/aoms/1177729885.
[261] R. Amsters, E. Demeester, P. Slaets, D. Holm, J. Joly, and N. Stevens, “Towards automated calibration of visible light positioning systems,” *2019 Int. Conf. Indoor Position. Indoor Navig. IPIN 2019*, pp. 1–8, 2019, doi: 10.1109/IPIN.2019.8911756.
[262] B. Xie *et al.*, “LIPS: A light intensity-based positioning system for indoor environments,” *ACM Trans. Sens. Networks*, vol. 12, no. 4, 2016, doi: 10.1145/2953880.
[263] Y. Wang, J. Huang, L. Yang, and Y. Xue, “TOA-based joint synchronization and source localization with random errors in sensor positions and sensor clock biases,” *Ad Hoc Networks*, vol. 27, pp. 99–111, 2015, doi: 10.1016/j.adhoc.2014.12.001.
[264] V. Fathabadi, M. Shahbazian, K. Salahshour, and L. Jargani, “Comparison of Adaptive Kalman Filter Methods in State Estimation of a Nonlinear System Using Asynchronous Measurements,” *Lect. Notes Eng. Comput. Sci.*, vol. 2179, no. 1, pp. 884–891, 2009.
[265] H. Lin and S. Sun, “Optimal sequential estimation for asynchronous sampling discrete-time systems,” *IEEE Trans. Signal Process.*, vol. 68, pp. 6117–6127, 2020, doi: 10.1109/TSP.2020.3031388.
[266] P. Zhang, W. Qi, and Z. Deng, “Sequential fusion Kalman filter,” *15th Int. Conf. Inf. Fusion, FUSION 2012*, no. 6, pp. 2140–2146, 2012.
[267] T. Wang, X. Wang, W. Shi, Z. Zhao, Z. He, and T. Xia, “Target localization and tracking based on improved Bayesian enhanced least-squares algorithm in wireless sensor networks,” *Comput. Networks*, vol. 167, p. 106968, 2020, doi: 10.1016/j.comnet.2019.106968.

9 Appendix A: Mapped Layout of the Visible Light Positioning Experiment

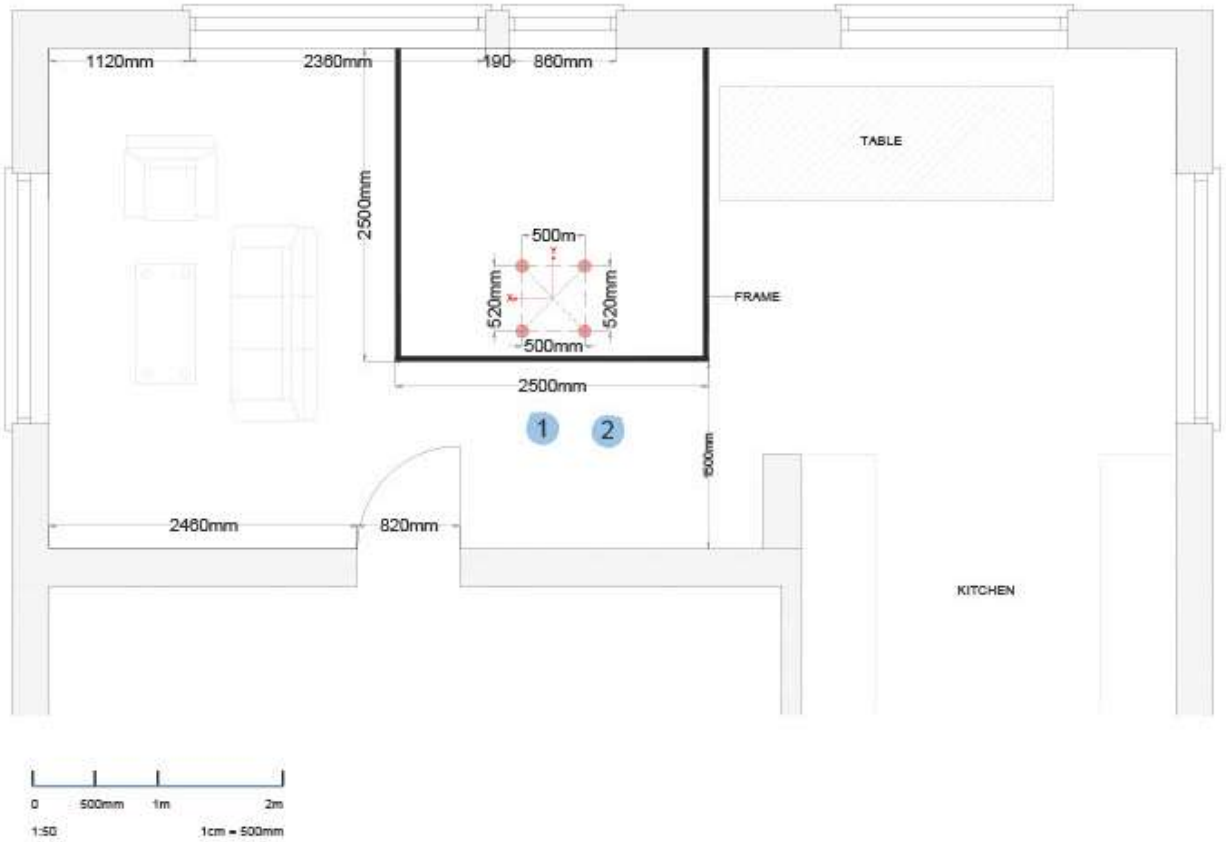

10 Appendix B: Tabulated Data Comparison of Existing Localisation Techniques Under Asynchronous Sampling

Tabulated Data Comparison of Existing Localisation Techniques Under Asynchronous Sampling

RMSE vs IML [1e-3,1e-1] and Measurement noises [1e-3,1e0] at path angle of 0.2 rad and 1 rad

Inter Measurement Latency (IML) (Δt_m) / s	θ_{path}	Sequential Unscented Kalman Filter (SUKF)						Unscented Kalman Filter (UKF)						Least Squares (LS)						Modified Shi (MSHI)						Shi Time-shifted (SHI-TS)					
		0.001	0.0046	0.0215	0.1	0.4642	1	0.001	0.0046	0.0215	0.1	0.4642	1	0.001	0.0046	0.0215	0.1	0.4642	1	0.001	0.0046	0.0215	0.1	0.4642	1	0.001	0.0046	0.0215	0.1	0.4642	1
0.1	0.2	0.004	0.0091	0.0297	0.1042	0.3534	0.6391	0.09	0.0905	0.0997	0.152	0.3597	0.6306	0.1542	0.1542	0.1554	0.1827	0.5233	1.096	13.09	6.712	6.562	24.11	29.56	63.27	14.76	9.572	7.678	15.62	82.96	183.2
0.072	0.2	0.003	0.008	0.0266	0.092	0.3153	0.5686	0.0631	0.0639	0.0716	0.1257	0.315	0.5642	0.108	0.1081	0.1096	0.1471	0.5132	1.091	48.24	27.52	22.32	16.47	25.87	50.73	1.639	2.518	4.701	12.74	70.45	59.1
0.0518	0.2	0.0021	0.0068	0.0228	0.0801	0.2791	0.5023	0.0459	0.0477	0.0559	0.1054	0.2772	0.4986	0.0799	0.08	0.0822	0.1314	0.5093	1.089	9.83	5.448	6.128	17.32	40.05	63.86	1.083	1.377	5.054	32.33	63.55	148
0.0373	0.2	0.0019	0.0059	0.0208	0.0715	0.2499	0.4601	0.0319	0.0333	0.044	0.0863	0.2465	0.4439	0.056	0.0561	0.0592	0.1196	0.5066	1.088	1.389	1.141	3.17	15.64	35.62	37.6	0.6489	0.9677	3.964	9.426	52.59	73.38
0.0268	0.2	0.0015	0.0052	0.0181	0.0633	0.2194	0.3936	0.023	0.0253	0.0368	0.0711	0.2152	0.4063	0.0413	0.0415	0.0462	0.115	0.5055	1.088	0.5805	0.7542	2.791	7.862	29.45	45.15	0.4183	1.017	4.034	19.29	52.62	84.12
0.0193	0.2	0.0013	0.0046	0.0162	0.0552	0.1871	0.3536	0.0162	0.0182	0.0306	0.0609	0.192	0.3457	0.029	0.0292	0.0357	0.1116	0.5047	1.087	0.2467	0.5852	2.297	5.688	31.32	42.71	0.3351	0.9244	2.717	10.2	41.95	75.71
0.0139	0.2	0.0012	0.0041	0.0144	0.0498	0.1723	0.3086	0.0119	0.0139	0.025	0.0521	0.1678	0.3164	0.0215	0.0218	0.0308	0.1103	0.5043	1.087	0.216	0.5058	1.837	5.322	31.97	37.53	0.3212	0.807	3.16	9.013	35.23	58.01
0.01	0.2	0.001	0.0037	0.0125	0.0437	0.1516	0.2711	0.0104	0.0123	0.0195	0.0453	0.1489	0.2674	0.015	0.0155	0.027	0.1094	0.5043	1.087	0.2337	0.6209	1.494	5.406	21.86	37.86	0.3219	0.9742	2.61	8.406	38.02	70.15
0.0072	0.2	0.0009	0.0033	0.0113	0.0391	0.135	0.2416	0.0063	0.0089	0.0152	0.0392	0.1299	0.2391	0.0111	0.0119	0.0255	0.109	0.5041	1.087	0.2087	0.5868	1.976	5.15	18.74	37.83	0.2819	0.8166	2.786	7.189	32	44.36
0.0052	0.2	0.0008	0.0029	0.0097	0.0345	0.1162	0.2143	0.0061	0.0076	0.0123	0.0344	0.1152	0.2066	0.0078	0.0089	0.0244	0.1088	0.5041	1.087	0.2173	0.5433	1.563	4.712	15.89	22.82	0.3286	0.7996	2.31	6.464	25.34	48.15
0.0037	0.2	0.0007	0.0026	0.0089	0.0306	0.0979	0.1882	0.0037	0.0061	0.0101	0.0298	0.0999	0.1839	0.0058	0.0074	0.024	0.1087	0.5042	1.087	0.1771	0.5123	1.617	4.334	15.91	22.74	0.2446	0.7516	2.221	6.114	22.54	36.18
0.0027	0.2	0.0006	0.0022	0.0076	0.0258	0.0895	0.1685	0.0033	0.0047	0.0086	0.0264	0.0887	0.1678	0.0041	0.0062	0.0237	0.1087	0.5043	1.087	0.1804	0.4701	1.553	4.868	14.05	21.32	0.2883	0.7117	2.218	6.48	20.27	26.94
0.0019	0.2	0.0006	0.0019	0.0067	0.0222	0.0765	0.1471	0.0024	0.0035	0.0072	0.0227	0.0788	0.1444	0.0031	0.0057	0.0235	0.1086	0.5041	1.087	0.1577	0.4737	1.451	4.046	13.98	19.87	0.2196	0.6771	2.141	5.805	17.93	31.47
0.0014	0.2	0.0005	0.0017	0.0057	0.0204	0.069	0.13	0.0019	0.0026	0.0061	0.0202	0.0685	0.1297	0.0023	0.0054	0.0235	0.1086	0.5041	1.087	0.156	0.496	1.491	3.978	13.74	18.94	0.197	0.6065	1.835	5.203	17.17	24.62
0.001	0.2	0.0004	0.0015	0.0051	0.0176	0.0606	0.1169	0.0015	0.0021	0.0054	0.0177	0.0611	0.1103	0.0018	0.0052	0.0234	0.1086	0.5041	1.087	0.1325	0.4117	1.197	3.398	10.57	17.08	0.1891	0.582	1.758	4.922	15.86	23.03
0.1	1	0.0106	0.0134	0.035	0.1193	0.4266	0.7862	0.1026	0.1025	0.1048	0.1475	0.3908	0.7301	0.1537	0.1537	0.1545	0.1728	0.4388	0.9072	0.0737	0.0739	0.0833	0.2314	1.053	74.19	0.0444	0.0459	0.0812	0.3324	1.556	20.65
0.072	1	0.0059	0.0099	0.0294	0.1051	0.3752	0.7005	0.0744	0.0745	0.0779	0.12	0.3533	0.6567	0.1079	0.1079	0.1089	0.1345	0.4268	0.9014	0.0275	0.0285	0.0527	0.2193	1.027	35.23	0.0195	0.0236	0.0733	0.3317	1.561	21.08
0.0518	1	0.0034	0.0079	0.0274	0.0963	0.3335	0.626	0.0537	0.0539	0.0581	0.1039	0.3163	0.5924	0.0798	0.0799	0.0814	0.1164	0.4219	0.8992	0.0099	0.0134	0.0472	0.216	1.015	7.717	0.0093	0.0173	0.0718	0.3322	1.562	12.58
0.0373	1	0.0023	0.0067	0.0234	0.0842	0.2915	0.5393	0.0387	0.039	0.0448	0.0899	0.2805	0.5281	0.0559	0.056	0.0581	0.1028	0.4185	0.8977	0.004	0.0104	0.0463	0.2145	1.009	5.755	0.0052	0.0159	0.0716	0.332	1.563	42.78
0.0268	1	0.0019	0.0061	0.0214	0.0748	0.2583	0.4886	0.0278	0.0282	0.0359	0.0784	0.2515	0.4593	0.0413	0.0415	0.0445	0.0972	0.4172	0.897	0.0025	0.01	0.0461	0.214	1.006	4.043	0.0038	0.0155	0.0716	0.3321	1.564	23.38
0.0193	1	0.0015	0.0053	0.0187	0.0668	0.2352	0.4241	0.0201	0.0207	0.0287	0.067	0.2213	0.4193	0.029	0.0291	0.0334	0.0932	0.4166	0.8967	0.0022	0.0099	0.046	0.2135	1.003	7.5	0.0035	0.0154	0.0715	0.3321	1.564	10.32
0.0139	1	0.0014	0.0048	0.0167	0.0579	0.1989	0.3767	0.0145	0.0152	0.0243	0.0586	0.197	0.3605	0.0214	0.0217	0.0279	0.0916	0.416	0.8964	0.0021	0.0099	0.0459	0.2134	1.002	4.108	0.0034	0.0154	0.0715	0.3324	1.563	13.2
0.01	1	0.0012	0.0042	0.0148	0.0512	0.1751	0.3315	0.0107	0.0117	0.0194	0.051	0.1734	0.3301	0.015	0.0154	0.0236	0.0905	0.4158	0.8964	0.0021	0.0099	0.0459	0.2131	1.002	3.995	0.0033	0.0154	0.0715	0.332	1.563	56.54
0.0072	1	0.0011	0.0037	0.0129	0.0446	0.153	0.2886	0.0075	0.0089	0.0159	0.0449	0.1538	0.2865	0.0111	0.0116	0.0218	0.0901	0.4159	0.8963	0.0021	0.0099	0.0459	0.2132	1.002	5.391	0.0033	0.0154	0.0716	0.332	1.563	25.22
0.0052	1	0.0009	0.0033	0.0117	0.0393	0.1362	0.2532	0.0057	0.0071	0.0132	0.0393	0.1356	0.2593	0.0078	0.0086	0.0205	0.0898	0.4159	0.8963	0.0021	0.0099	0.0459	0.2131	1.001	7.686	0.0033	0.0154	0.0715	0.3319	1.563	35.44
0.0037	1	0.0008	0.0029	0.01	0.0342	0.1241	0.2201	0.004	0.0058	0.011	0.0347	0.1195	0.2229	0.0058	0.0068	0.02	0.0897	0.4156	0.8962	0.0021	0.0099	0.0459	0.2131	1	11.01	0.0033	0.0154	0.0714	0.3322	1.562	10.76
0.0027	1	0.0007	0.0026	0.0089	0.0311	0.1058	0.1936	0.0031	0.0046	0.0094	0.0305	0.1056	0.193	0.0041	0.0056	0.0196	0.0896	0.4156	0.8963	0.0021	0.0099	0.0459	0.2132	1	4.225	0.0033	0.0154	0.0715	0.3322	1.562	11.12
0.0019	1	0.0007	0.0023	0.0078	0.0275	0.0941	0.1687	0.0023	0.0035	0.0081	0.0268	0.0913	0.1692	0.003	0.005	0.0195	0.0895	0.4157	0.8964	0.0021	0.0099	0.0459	0.2131	1	4.879	0.0033	0.0154	0.0715	0.332	1.56	12.9
0.0014	1	0.0006	0.002	0.0071	0.0237	0.0824	0.1503	0.0018	0.0028	0.0072	0.0237	0.0821	0.1506	0.0022	0.0046	0.0194	0.0895	0.4158	0.8963	0.0021	0.0099	0.0459	0.2131	1	4.002	0.0033	0.0154	0.0715	0.3319	1.563	10.32
0.001	1	0.0005	0.0018	0.0062	0.0211	0.0721	0.1308	0.0014	0.0022	0.0061	0.0209	0.0712	0.1365	0.0017	0.0044	0.0193	0.0895	0.4155	0.8963	0.0021	0.0099	0.0459	0.213	1.001	4.298	0.0033	0.0154	0.0715	0.3318	1.563	8.024

Measurement noise (σ_z) / m

11 Appendix C: Tabulated Data Comparison of Proposed Localisation Techniques Under Asynchronous Sampling

RMSE vs IML [1e-3,1e-1] and Measurement noises [1e-3,1e0] at path angle of 0.2 rad and 1 rad

Inter Measurement Latency (IML) (Δt_m) / s	Direct Extrapolation (DE)						Kalman Extrapolated Least Squares - Constant Velocity (KELS-CV)						Kalman Extrapolated Least Squares - Constant Accelleration (KELS-CA)						Kalman Extrapolated Weighetd Least Squares - Constant Velocity (KEWLS-CV)						Kalman Extrapolated Weighetd Least Squares - Constant Accelleration (KEWLS-CA)					
θ_{path} =0.2																														
0.1	0.0085	0.0108	0.0353	0.16	0.7494	1.619	0.0065	0.0102	0.0385	0.1311	0.421	0.7576	0.0038	0.0122	0.0393	0.1356	0.4938	0.705	0.0052	0.0087	0.0333	0.113	0.3667	0.6587	0.0032	0.0094	0.032	0.115	0.4269	0.6282
0.072	0.0046	0.0084	0.0345	0.1599	0.7459	1.608	0.0039	0.0087	0.0345	0.1134	0.3747	0.6731	0.0032	0.0097	0.0324	0.1161	0.4216	0.8015	0.0032	0.0076	0.03	0.0985	0.3272	0.5866	0.0025	0.0078	0.0271	0.0998	0.367	0.6989
0.0518	0.0027	0.0077	0.0346	0.1599	0.7467	1.618	0.0025	0.008	0.0296	0.0957	0.332	0.5952	0.0024	0.0078	0.0274	0.1006	0.3759	0.7014	0.0021	0.0072	0.0256	0.0836	0.2905	0.5198	0.0019	0.0065	0.0234	0.0872	0.3282	0.6133
0.0373	0.0019	0.0075	0.0344	0.1598	0.7448	1.605	0.0019	0.0077	0.0255	0.0866	0.2933	0.5406	0.0019	0.0065	0.0236	0.0877	0.3289	0.6271	0.0017	0.0069	0.0222	0.0757	0.2569	0.4724	0.0015	0.0055	0.0204	0.0764	0.2876	0.5486
0.0268	0.0017	0.0075	0.0345	0.1611	0.7461	1.608	0.0017	0.0066	0.0218	0.0753	0.2612	0.4676	0.0016	0.0055	0.0205	0.0767	0.2832	0.5497	0.0015	0.0058	0.019	0.0661	0.229	0.4089	0.0013	0.0048	0.0178	0.067	0.248	0.4808
0.0193	0.0016	0.0074	0.0345	0.1606	0.7495	1.604	0.0017	0.0057	0.0195	0.066	0.2295	0.4218	0.0013	0.0048	0.0176	0.0673	0.2483	0.4734	0.0015	0.005	0.017	0.0579	0.2011	0.3691	0.0011	0.0042	0.0153	0.0588	0.2173	0.4142
0.0139	0.0016	0.0074	0.0346	0.1603	0.7435	1.603	0.0015	0.005	0.0172	0.0594	0.2053	0.3671	0.0011	0.0042	0.0154	0.0579	0.2178	0.4228	0.0013	0.0043	0.015	0.0522	0.1801	0.3214	0.001	0.0036	0.0135	0.0507	0.1908	0.3701
0.01	0.0016	0.0075	0.0345	0.1602	0.7453	1.609	0.0013	0.0044	0.0148	0.0516	0.1793	0.3296	0.001	0.0037	0.0138	0.0508	0.1947	0.3717	0.0011	0.0038	0.013	0.0453	0.1574	0.2887	0.0008	0.0032	0.012	0.0445	0.1706	0.3252
0.0072	0.0016	0.0074	0.0345	0.1608	0.7445	1.611	0.0011	0.0039	0.0135	0.0467	0.1616	0.2892	0.0008	0.0031	0.0118	0.0442	0.167	0.3199	0.001	0.0034	0.0119	0.041	0.1418	0.2534	0.0007	0.0027	0.0103	0.0387	0.1462	0.2795
0.0052	0.0016	0.0074	0.0345	0.16	0.7454	1.61	0.001	0.0033	0.0116	0.0404	0.1367	0.2585	0.0007	0.0028	0.0105	0.0383	0.1468	0.2872	0.0009	0.0029	0.0102	0.0355	0.12	0.2268	0.0006	0.0024	0.0092	0.0335	0.1284	0.251
0.0037	0.0016	0.0074	0.0345	0.1602	0.7439	1.608	0.0009	0.003	0.0102	0.0353	0.122	0.2274	0.0006	0.0024	0.0092	0.0343	0.1271	0.2491	0.0007	0.0026	0.009	0.031	0.1071	0.1996	0.0006	0.0021	0.0081	0.03	0.111	0.2178
0.0027	0.0016	0.0074	0.0345	0.1604	0.7433	1.608	0.0008	0.0027	0.0091	0.0308	0.1074	0.1981	0.0006	0.0021	0.0078	0.0297	0.1127	0.218	0.0007	0.0024	0.008	0.0271	0.0943	0.1741	0.0005	0.0018	0.0068	0.0259	0.0985	0.1902
0.0019	0.0016	0.0074	0.0345	0.1602	0.7455	1.61	0.0007	0.0023	0.008	0.0267	0.0932	0.1742	0.0005	0.0018	0.0069	0.0258	0.0988	0.1958	0.0006	0.002	0.007	0.0235	0.0818	0.1526	0.0004	0.0016	0.006	0.0225	0.0862	0.1699
0.0014	0.0016	0.0074	0.0346	0.1605	0.7445	1.611	0.0006	0.0021	0.0069	0.0236	0.0849	0.154	0.0004	0.0016	0.0061	0.0233	0.0885	0.1794	0.0005	0.0018	0.0061	0.0207	0.0745	0.1351	0.0004	0.0014	0.0053	0.0203	0.0769	0.1557
0.001	0.0016	0.0074	0.0345	0.1603	0.7446	1.608	0.0005	0.0018	0.0063	0.0213	0.0745	0.1405	0.0004	0.0014	0.0054	0.0208	0.0784	0.1598	0.0004	0.0016	0.0056	0.0187	0.0654	0.1232	0.0003	0.0012	0.0047	0.0181	0.0681	0.1386
θ_{path} =1																														
0.1	0.0471	0.0474	0.0527	0.14	0.6201	1.319	0.0358	0.0362	0.0473	0.1306	0.4452	0.805	0.0192	0.023	0.0455	0.1381	0.4819	1.054	0.0245	0.0251	0.0388	0.122	0.4314	0.7833	0.0167	0.0196	0.0396	0.128	0.459	1.034
0.072	0.0245	0.0249	0.036	0.1366	0.6129	1.351	0.0203	0.021	0.0361	0.1124	0.3883	0.7153	0.009	0.0132	0.0339	0.1144	0.4227	0.8028	0.0139	0.0149	0.032	0.1076	0.3794	0.699	0.008	0.0115	0.031	0.1093	0.4078	0.7706
0.0518	0.0127	0.0137	0.0306	0.1348	0.6148	1.338	0.0112	0.0124	0.0299	0.1009	0.3407	0.6361	0.0048	0.0089	0.0272	0.0973	0.3589	0.7047	0.0077	0.0096	0.0276	0.0982	0.3348	0.6236	0.0043	0.008	0.0258	0.0945	0.3496	0.6808
0.0373	0.0067	0.0086	0.0297	0.1332	0.6125	1.343	0.0061	0.0085	0.0256	0.0862	0.2994	0.5505	0.0028	0.0067	0.0228	0.0837	0.3118	0.6058	0.0043	0.0074	0.0243	0.0847	0.2952	0.5407	0.0025	0.0062	0.0221	0.0822	0.3053	0.5886
0.0268	0.0036	0.0068	0.0287	0.133	0.6134	1.322	0.0034	0.0069	0.0225	0.0764	0.2618	0.4947	0.0018	0.0054	0.0195	0.0724	0.2758	0.5285	0.0025	0.0063	0.0218	0.0755	0.2588	0.4871	0.0017	0.0052	0.0191	0.0716	0.2709	0.5153
0.0193	0.0021	0.0063	0.0287	0.1316	0.6197	1.336	0.0021	0.0058	0.0194	0.0677	0.2308	0.4276	0.0014	0.0046	0.0171	0.0629	0.2396	0.4696	0.0017	0.0055	0.019	0.0671	0.2286	0.4214	0.0013	0.0045	0.0169	0.0624	0.236	0.4588
0.0139	0.0016	0.0062	0.0284	0.1332	0.6175	1.326	0.0016	0.0051	0.017	0.0585	0.2007	0.3809	0.0011	0.0039	0.0148	0.0555	0.2083	0.402	0.0014	0.0049	0.0168	0.0581	0.1988	0.3763	0.0011	0.0039	0.0147	0.0552	0.2055	0.394
0.01	0.0014	0.0061	0.0284	0.1334	0.6158	1.335	0.0013	0.0044	0.0152	0.052	0.1774	0.3298	0.0009	0.0034	0.0127	0.0482	0.1788	0.3496	0.0012	0.0043	0.0151	0.0517	0.176	0.3259	0.0009	0.0034	0.0126	0.048	0.1768	0.3432
0.0072	0.0013	0.0061	0.0286	0.1324	0.6141	1.325	0.0011	0.0038	0.0131	0.045	0.1542	0.2918	0.0008	0.003	0.0113	0.0423	0.1584	0.3131	0.0011	0.0037	0.013	0.0447	0.153	0.2887	0.0008	0.003	0.0112	0.0421	0.1567	0.3073
0.0052	0.0013	0.0062	0.0286	0.1328	0.6127	1.323	0.001	0.0034	0.0117	0.04	0.1396	0.2548	0.0007	0.0026	0.0097	0.0375	0.1384	0.2691	0.001	0.0034	0.0116	0.0398	0.1388	0.2524	0.0007	0.0026	0.0097	0.0375	0.137	0.2648
0.0037	0.0013	0.0062	0.0284	0.1326	0.615	1.331	0.0009	0.003	0.0102	0.0352	0.1202	0.2232	0.0006	0.0023	0.0084	0.0318	0.1213	0.2371	0.0009	0.003	0.0102	0.035	0.1195	0.2212	0.0006	0.0022	0.0084	0.0317	0.1202	0.2333
0.0027	0.0013	0.0061	0.0285	0.1326	0.6164	1.333	0.0008	0.0026	0.009	0.0314	0.1075	0.2002	0.0005	0.002	0.0076	0.0285	0.1073	0.2127	0.0008	0.0026	0.009	0.0313	0.1068	0.1986	0.0005	0.002	0.0076	0.0284	0.1064	0.2094
0.0019	0.0013	0.0062	0.0286	0.1325	0.6154	1.328	0.0007	0.0023	0.0078	0.0277	0.0946	0.1762	0.0005	0.0017	0.0065	0.0249	0.0939	0.1846	0.0007	0.0023	0.0078	0.0276	0.0941	0.1751	0.0005	0.0017	0.0065	0.0248	0.093	0.1818
0.0014	0.0013	0.0061	0.0285	0.1327	0.6165	1.33	0.0006	0.002	0.0071	0.0249	0.083	0.1597	0.0004	0.0015	0.0058	0.0218	0.0844	0.1639	0.0006	0.002	0.0071	0.0248	0.0825	0.1586	0.0004	0.0015	0.0057	0.0217	0.0836	0.1614
0.001	0.0013	0.0061	0.0285	0.1325	0.6155	1.327	0.0005	0.0018	0.0061	0.0213	0.0734	0.1378	0.0004	0.0013	0.005	0.0191	0.0756	0.1477	0.0005	0.0017	0.006	0.0213	0.073	0.1368	0.0004	0.0013	0.005	0.019	0.0749	0.1451
Measurement noise (σ_z) / m	0.001	0.0046	0.0215	0.1	0.4642	1	0.001	0.0046	0.0215	0.1	0.4642	1	0.001	0.0046	0.0215	0.1	0.4642	1	0.001	0.0046	0.0215	0.1	0.4642	1	0.001	0.0046	0.0215	0.1	0.4642	1

12 Appendix D: Tabulated Data Comparison of Proposed KELS-CV and KEWLS-CV vs SUKF Under Asynchronous Sampling

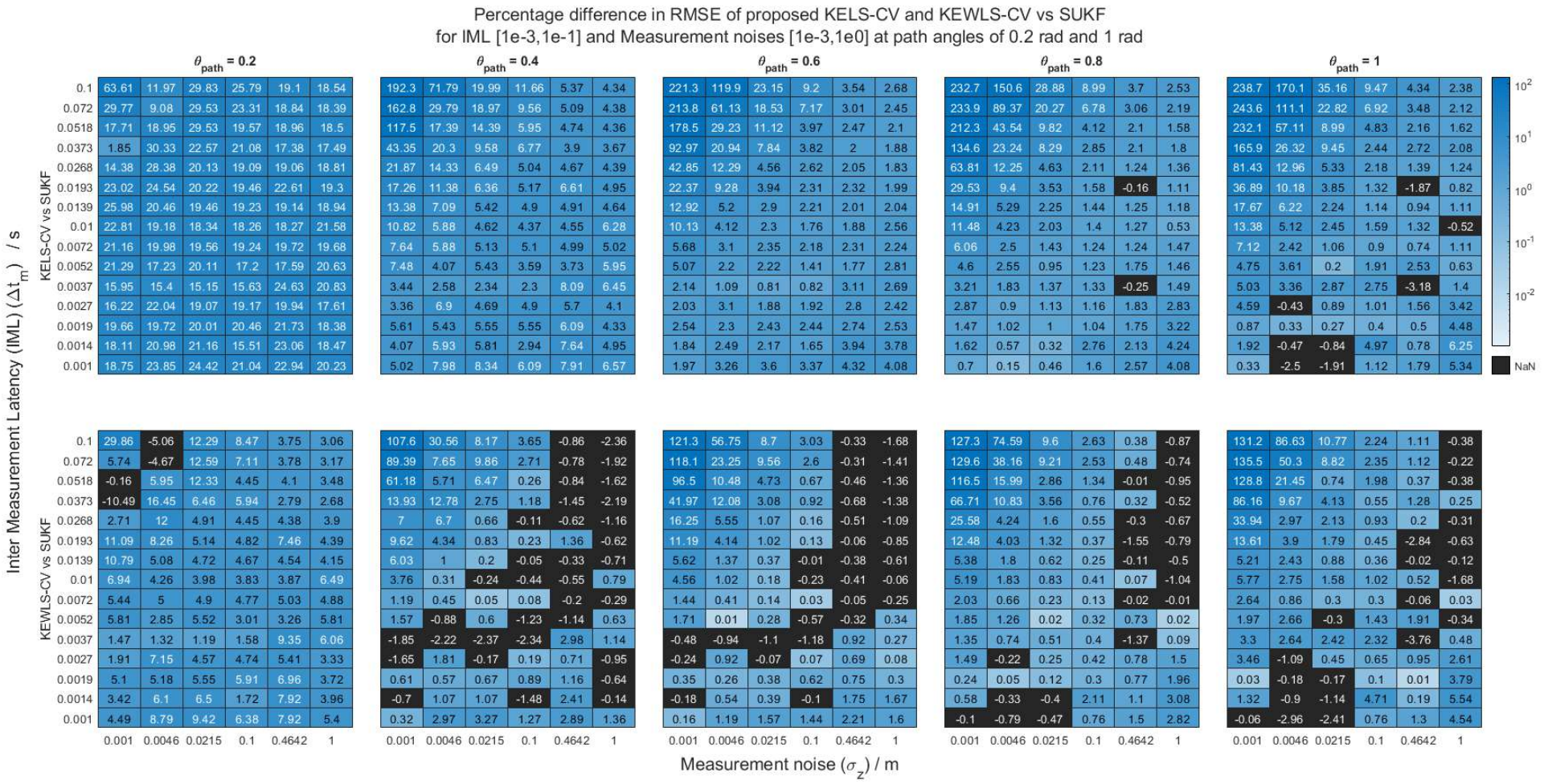

KELS-CV vs SUKF	θ_{path} = 0.2					
0.1	63.61	11.97	29.83	25.79	19.1	18.54
0.072	29.77	9.08	29.53	23.31	18.84	18.39
0.0518	17.71	18.95	29.53	19.57	18.96	18.5
0.0373	1.85	30.33	22.57	21.08	17.38	17.49
0.0268	14.38	28.38	20.13	19.09	19.06	18.81
0.0193	23.02	24.54	20.22	19.46	22.61	19.3
0.0139	25.98	20.46	19.46	19.23	19.14	18.94
0.01	22.81	19.18	18.34	18.26	18.27	21.58
0.0072	21.16	19.98	19.56	19.24	19.72	19.68
0.0052	21.29	17.23	20.11	17.2	17.59	20.63
0.0037	15.95	15.4	15.15	15.63	24.63	20.83
0.0027	16.22	22.04	19.07	19.17	19.94	17.61
0.0019	19.66	19.72	20.01	20.46	21.73	18.38
0.0014	18.11	20.98	21.16	15.51	23.06	18.47
0.001	18.75	23.85	24.42	21.04	22.94	20.23

KELS-CV vs SUKF	θ_{path} = 0.4					
0.1	192.3	71.79	19.99	11.66	5.37	4.34
0.072	162.8	29.79	18.97	9.56	5.09	4.38
0.0518	117.5	17.39	14.39	5.95	4.74	4.36
0.0373	43.35	20.3	9.58	6.77	3.9	3.67
0.0268	21.87	14.33	6.49	5.04	4.67	4.39
0.0193	17.26	11.38	6.36	5.17	6.61	4.95
0.0139	13.38	7.09	5.42	4.9	4.91	4.64
0.01	10.82	5.88	4.62	4.37	4.55	6.28
0.0072	7.64	5.88	5.13	5.1	4.99	5.02
0.0052	7.48	4.07	5.43	3.59	3.73	5.95
0.0037	3.44	2.58	2.34	2.3	8.09	6.45
0.0027	3.36	6.9	4.69	4.9	5.7	4.1
0.0019	5.61	5.43	5.55	5.55	6.09	4.33
0.0014	4.07	5.93	5.81	2.94	7.64	4.95
0.001	5.02	7.98	8.34	6.09	7.91	6.57

KELS-CV vs SUKF	θ_{path} = 0.6					
0.1	221.3	119.9	23.15	9.2	3.54	2.68
0.072	213.8	61.13	18.53	7.17	3.01	2.45
0.0518	178.5	29.23	11.12	3.97	2.47	2.1
0.0373	92.97	20.94	7.84	3.82	2	1.88
0.0268	42.85	12.29	4.56	2.62	2.05	1.83
0.0193	22.37	9.28	3.94	2.31	2.32	1.99
0.0139	12.92	5.2	2.9	2.21	2.01	2.04
0.01	10.13	4.12	2.3	1.76	1.88	2.56
0.0072	5.68	3.1	2.35	2.18	2.31	2.24
0.0052	5.07	2.2	2.22	1.41	1.77	2.81
0.0037	2.14	1.09	0.81	0.82	3.11	2.69
0.0027	2.03	3.1	1.88	1.92	2.8	2.42
0.0019	2.54	2.3	2.43	2.44	2.74	2.53
0.0014	1.84	2.49	2.17	1.65	3.94	3.78
0.001	1.97	3.26	3.6	3.37	4.32	4.08

KELS-CV vs SUKF	θ_{path} = 0.8					
0.1	232.7	150.6	28.88	8.99	3.7	2.53
0.072	233.9	89.37	20.27	6.78	3.06	2.19
0.0518	212.3	43.54	9.82	4.12	2.1	1.58
0.0373	134.6	23.24	8.29	2.85	2.1	1.8
0.0268	63.81	12.25	4.63	2.11	1.24	1.36
0.0193	29.53	9.4	3.53	1.58	-0.16	1.11
0.0139	14.91	5.29	2.25	1.44	1.25	1.18
0.01	11.48	4.23	2.03	1.4	1.27	0.53
0.0072	6.06	2.5	1.43	1.24	1.24	1.47
0.0052	4.6	2.55	0.95	1.23	1.75	1.46
0.0037	3.21	1.83	1.37	1.33	-0.25	1.49
0.0027	2.87	0.9	1.13	1.16	1.83	2.83
0.0019	1.47	1.02	1	1.04	1.75	3.22
0.0014	1.62	0.57	0.32	2.76	2.13	4.24
0.001	0.7	0.15	0.46	1.6	2.57	4.08

KELS-CV vs SUKF	θ_{path} = 1					
0.1	238.7	170.1	35.16	9.47	4.34	2.38
0.072	243.6	111.1	22.82	6.92	3.48	2.12
0.0518	232.1	57.11	8.99	4.83	2.16	1.62
0.0373	165.9	26.32	9.45	2.44	2.72	2.08
0.0268	81.43	12.96	5.33	2.18	1.39	1.24
0.0193	36.89	10.18	3.85	1.32	-1.87	0.82
0.0139	17.67	6.22	2.24	1.14	0.94	1.11
0.01	13.38	5.12	2.45	1.59	1.32	-0.52
0.0072	7.12	2.42	1.06	0.9	0.74	1.11
0.0052	4.75	3.61	0.2	1.91	2.53	0.63
0.0037	5.03	3.36	2.87	2.75	-3.18	1.4
0.0027	4.59	-0.43	0.89	1.01	1.56	3.42
0.0019	0.87	0.33	0.27	0.4	0.5	4.48
0.0014	1.92	-0.47	-0.84	4.97	0.78	6.25
0.001	0.33	-2.5	-1.91	1.12	1.79	5.34

KEWLS-CV vs SUKF	θ_{path} = 0.2					
0.1	29.86	-5.06	12.29	8.47	3.75	3.06
0.072	5.74	-4.67	12.59	7.11	3.78	3.17
0.0518	-0.16	5.95	12.33	4.45	4.1	3.48
0.0373	-10.49	16.45	6.46	5.94	2.79	2.68
0.0268	2.71	12	4.91	4.45	4.38	3.9
0.0193	11.09	8.26	5.14	4.82	7.46	4.39
0.0139	10.79	5.08	4.72	4.67	4.54	4.15
0.01	6.94	4.26	3.98	3.83	3.87	6.49
0.0072	5.44	5	4.9	4.77	5.03	4.88
0.0052	5.81	2.85	5.52	3.01	3.26	5.81
0.0037	1.47	1.32	1.19	1.58	9.35	6.06
0.0027	1.91	7.15	4.57	4.74	5.41	3.33
0.0019	5.1	5.18	5.55	5.91	6.96	3.72
0.0014	3.42	6.1	6.5	1.72	7.92	3.96
0.001	4.49	8.79	9.42	6.38	7.92	5.4

KEWLS-CV vs SUKF	θ_{path} = 0.4					
0.1	107.6	30.56	8.17	3.65	-0.86	-2.36
0.072	89.39	7.65	9.86	2.71	-0.78	-1.92
0.0518	61.18	5.71	6.47	0.26	-0.84	-1.62
0.0373	13.93	12.78	2.75	1.18	-1.45	-2.19
0.0268	7	6.7	0.66	-0.11	-0.62	-1.16
0.0193	9.62	4.34	0.83	0.23	1.36	-0.62
0.0139	6.03	1	0.2	-0.05	-0.33	-0.71
0.01	3.76	0.31	-0.24	-0.44	-0.55	0.79
0.0072	1.19	0.45	0.05	0.08	-0.2	-0.29
0.0052	1.57	-0.88	0.6	-1.23	-1.14	0.63
0.0037	-1.85	-2.22	-2.37	-2.34	2.98	1.14
0.0027	-1.65	1.81	-0.17	0.19	0.71	-0.95
0.0019	0.61	0.57	0.67	0.89	1.16	-0.64
0.0014	-0.7	1.07	1.07	-1.48	2.41	-0.14
0.001	0.32	2.97	3.27	1.27	2.89	1.36

KEWLS-CV vs SUKF	θ_{path} = 0.6					
0.1	121.3	56.75	8.7	3.03	-0.33	-1.68
0.072	118.1	23.25	9.56	2.6	-0.31	-1.41
0.0518	96.5	10.48	4.73	0.67	-0.46	-1.36
0.0373	41.97	12.08	3.08	0.92	-0.68	-1.38
0.0268	16.25	5.55	1.07	0.16	-0.51	-1.09
0.0193	11.19	4.14	1.02	0.13	-0.06	-0.85
0.0139	5.62	1.37	0.37	-0.01	-0.38	-0.61
0.01	4.56	1.02	0.18	-0.23	-0.41	-0.06
0.0072	1.44	0.41	0.14	0.03	-0.05	-0.25
0.0052	1.71	0.01	0.28	-0.57	-0.32	0.34
0.0037	-0.48	-0.94	-1.1	-1.18	0.92	0.27
0.0027	-0.24	0.92	-0.07	0.07	0.69	0.08
0.0019	0.35	0.26	0.38	0.62	0.75	0.3
0.0014	-0.18	0.54	0.39	-0.1	1.75	1.67
0.001	0.16	1.19	1.57	1.44	2.21	1.6

KEWLS-CV vs SUKF	θ_{path} = 0.8					
0.1	127.3	74.59	9.6	2.63	0.38	-0.87
0.072	129.6	38.16	9.21	2.53	0.48	-0.74
0.0518	116.5	15.99	2.86	1.34	-0.01	-0.95
0.0373	66.71	10.83	3.56	0.76	0.32	-0.52
0.0268	25.58	4.24	1.6	0.55	-0.3	-0.67
0.0193	12.48	4.03	1.32	0.37	-1.55	-0.79
0.0139	5.38	1.8	0.62	0.25	-0.11	-0.5
0.01	5.19	1.83	0.83	0.41	0.07	-1.04
0.0072	2.03	0.66	0.23	0.13	-0.02	-0.01
0.0052	1.85	1.26	0.02	0.32	0.73	0.02
0.0037	1.35	0.74	0.51	0.4	-1.37	0.09
0.0027	1.49	-0.22	0.25	0.42	0.78	1.5
0.0019	0.24	0.05	0.12	0.3	0.77	1.96
0.0014	0.58	-0.33	-0.4	2.11	1.1	3.08
0.001	-0.1	-0.79	-0.47	0.76	1.5	2.82

KEWLS-CV vs SUKF	θ_{path} = 1					
0.1	131.2	86.63	10.77	2.24	1.11	-0.38
0.072	135.5	50.3	8.82	2.35	1.12	-0.22
0.0518	128.8	21.45	0.74	1.98	0.37	-0.38
0.0373	86.16	9.67	4.13	0.55	1.28	0.25
0.0268	33.94	2.97	2.13	0.93	0.2	-0.31
0.0193	13.61	3.9	1.79	0.45	-2.84	-0.63
0.0139	5.21	2.43	0.88	0.36	-0.02	-0.12
0.01	5.77	2.75	1.58	1.02	0.52	-1.68
0.0072	2.64	0.86	0.3	0.3	-0.06	0.03
0.0052	1.97	2.66	-0.3	1.43	1.91	-0.34
0.0037	3.3	2.64	2.42	2.32	-3.76	0.48
0.0027	3.46	-1.09	0.45	0.65	0.95	2.61
0.0019	0.03	-0.18	-0.17	0.1	0.01	3.79
0.0014	1.32	-0.9	-1.14	4.71	0.19	5.54
0.001	-0.06	-2.96	-2.41	0.76	1.3	4.54

0.001 0.0046 0.0215 0.1 0.4642 1

13 Appendix E: Tabulated Data Comparison of Proposed KELS-CA and KEWLS-CA vs SUKF Under Asynchronous Sampling

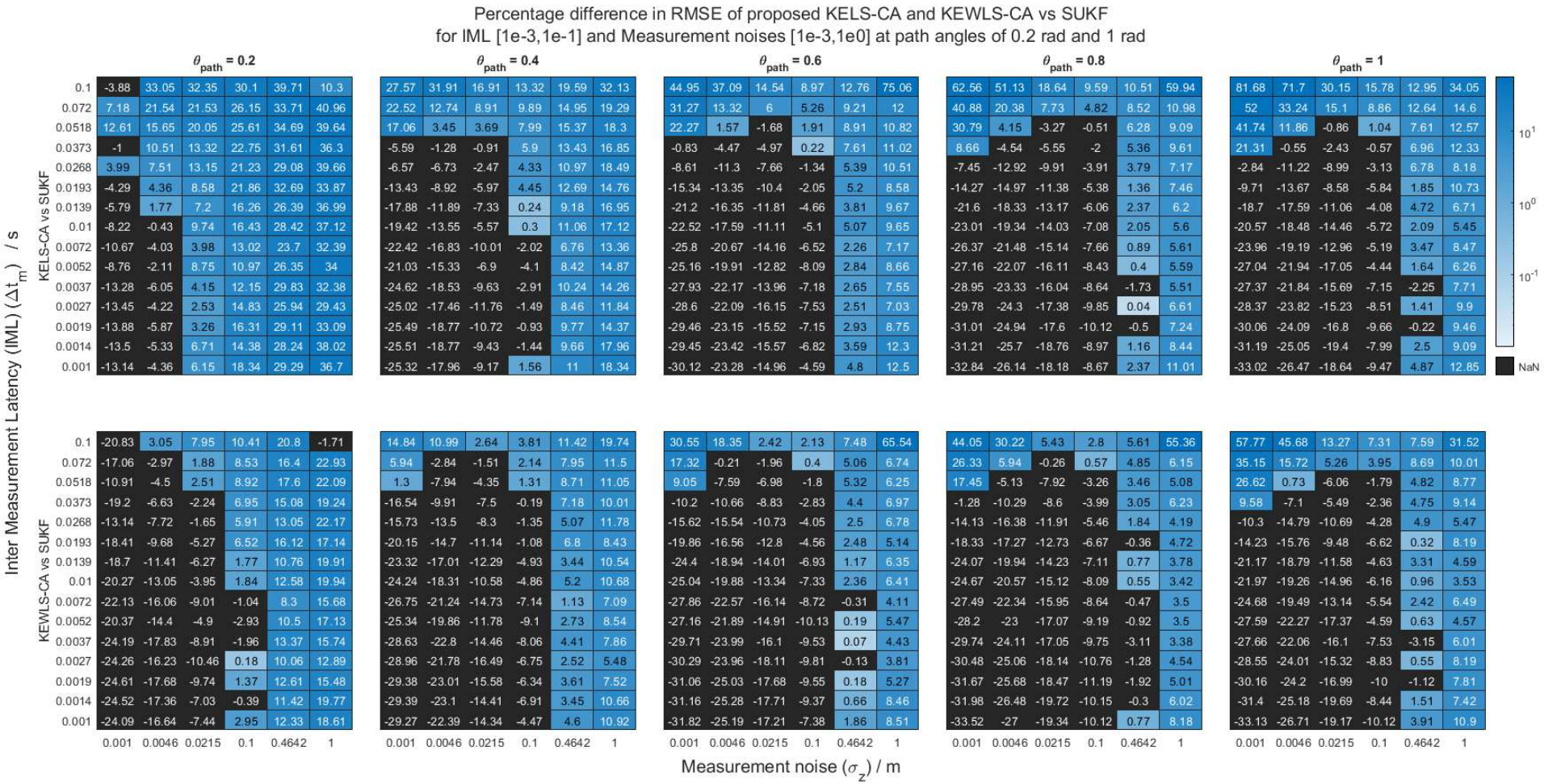

KELS-CA vs SUKF	θ_{path} = 0.2					
0.1	-3.88	33.05	32.35	30.1	39.71	10.3
0.072	7.18	21.54	21.53	26.15	33.71	40.96
0.0518	12.61	15.65	20.05	25.61	34.69	39.64
0.0373	-1	10.51	13.32	22.75	31.61	36.3
0.0268	3.99	7.51	13.15	21.23	29.08	39.66
0.0193	-4.29	4.36	8.58	21.86	32.69	33.87
0.0139	-5.79	1.77	7.2	16.26	26.39	36.99
0.01	-8.22	-0.43	9.74	16.43	28.42	37.12
0.0072	-10.67	-4.03	3.98	13.02	23.7	32.39
0.0052	-8.76	-2.11	8.75	10.97	26.35	34
0.0037	-13.28	-6.05	4.15	12.15	29.83	32.38
0.0027	-13.45	-4.22	2.53	14.83	25.94	29.43
0.0019	-13.88	-5.87	3.26	16.31	29.11	33.09
0.0014	-13.5	-5.33	6.71	14.38	28.24	38.02
0.001	-13.14	-4.36	6.15	18.34	29.29	36.7

KELS-CA vs SUKF	θ_{path} = 0.4					
0.1	27.57	31.91	16.91	13.32	19.59	32.13
0.072	22.52	12.74	8.91	9.89	14.95	19.29
0.0518	17.06	3.45	3.69	7.99	15.37	18.3
0.0373	-5.59	-1.28	-0.91	5.9	13.43	16.85
0.0268	-6.57	-6.73	-2.47	4.33	10.97	18.49
0.0193	-13.43	-8.92	-5.97	4.45	12.69	14.76
0.0139	-17.88	-11.89	-7.33	0.24	9.18	16.95
0.01	-19.42	-13.55	-5.57	0.3	11.06	17.12
0.0072	-22.42	-16.83	-10.01	-2.02	6.76	13.36
0.0052	-21.03	-15.33	-6.9	-4.1	8.42	14.87
0.0037	-24.62	-18.53	-9.63	-2.91	10.24	14.26
0.0027	-25.02	-17.46	-11.76	-1.49	8.46	11.84
0.0019	-25.49	-18.77	-10.72	-0.93	9.77	14.37
0.0014	-25.51	-18.77	-9.43	-1.44	9.66	17.96
0.001	-25.32	-17.96	-9.17	1.56	11	18.34

KELS-CA vs SUKF	θ_{path} = 0.6					
0.1	44.95	37.09	14.54	8.97	12.76	75.06
0.072	31.27	13.32	6	5.26	9.21	12
0.0518	22.27	1.57	-1.68	1.91	8.91	10.82
0.0373	-0.83	-4.47	-4.97	0.22	7.61	11.02
0.0268	-8.61	-11.3	-7.66	-1.34	5.39	10.51
0.0193	-15.34	-13.35	-10.4	-2.05	5.2	8.58
0.0139	-21.2	-16.35	-11.81	-4.66	3.81	9.67
0.01	-22.52	-17.59	-11.11	-5.1	5.07	9.65
0.0072	-25.8	-20.67	-14.16	-6.52	2.26	7.17
0.0052	-25.16	-19.91	-12.82	-8.09	2.84	8.66
0.0037	-27.93	-22.17	-13.96	-7.18	2.65	7.55
0.0027	-28.6	-22.09	-16.15	-7.53	2.51	7.03
0.0019	-29.46	-23.15	-15.52	-7.15	2.93	8.75
0.0014	-29.45	-23.42	-15.57	-6.82	3.59	12.3
0.001	-30.12	-23.28	-14.96	-4.59	4.8	12.5

KELS-CA vs SUKF	θ_{path} = 0.8					
0.1	62.56	51.13	18.64	9.59	10.51	59.94
0.072	40.88	20.38	7.73	4.82	8.52	10.98
0.0518	30.79	4.15	-3.27	-0.51	6.28	9.09
0.0373	8.66	-4.54	-5.55	-2	5.36	9.61
0.0268	-7.45	-12.92	-9.91	-3.91	3.79	7.17
0.0193	-14.27	-14.97	-11.38	-5.38	1.36	7.46
0.0139	-21.6	-18.33	-13.17	-6.06	2.37	6.2
0.01	-23.01	-19.34	-14.03	-7.08	2.05	5.6
0.0072	-26.37	-21.48	-15.14	-7.66	0.89	5.61
0.0052	-27.16	-22.07	-16.11	-8.43	0.4	5.59
0.0037	-28.95	-23.33	-16.04	-8.64	-1.73	5.51
0.0027	-29.78	-24.3	-17.38	-9.85	0.04	6.61
0.0019	-31.01	-24.94	-17.6	-10.12	-0.5	7.24
0.0014	-31.21	-25.7	-18.76	-8.97	1.16	8.44
0.001	-32.84	-26.14	-18.18	-8.67	2.37	11.01

KELS-CA vs SUKF	θ_{path} = 1					
0.1	81.68	71.7	30.15	15.78	12.95	34.05
0.072	52	33.24	15.1	8.86	12.64	14.6
0.0518	41.74	11.86	-0.86	1.04	7.61	12.57
0.0373	21.31	-0.55	-2.43	-0.57	6.96	12.33
0.0268	-2.84	-11.22	-8.99	-3.13	6.78	8.18
0.0193	-9.71	-13.67	-8.58	-5.84	1.85	10.73
0.0139	-18.7	-17.59	-11.06	-4.08	4.72	6.71
0.01	-20.57	-18.48	-14.46	-5.72	2.09	5.45
0.0072	-23.96	-19.19	-12.96	-5.19	3.47	8.47
0.0052	-27.04	-21.94	-17.05	-4.44	1.64	6.26
0.0037	-27.37	-21.84	-15.69	-7.15	-2.25	7.71
0.0027	-28.37	-23.82	-15.23	-8.51	1.41	9.9
0.0019	-30.06	-24.09	-16.8	-9.66	-0.22	9.46
0.0014	-31.19	-25.05	-19.4	-7.99	2.5	9.09
0.001	-33.02	-26.47	-18.64	-9.47	4.87	12.85

KEWLS-CA vs SUKF	θ_{path} = 0.2					
0.1	-20.83	3.05	7.95	10.41	20.8	-1.71
0.072	-17.06	-2.97	1.88	8.53	16.4	22.93
0.0518	-10.91	-4.5	2.51	8.92	17.6	22.09
0.0373	-19.2	-6.63	-2.24	6.95	15.08	19.24
0.0268	-13.14	-7.72	-1.65	5.91	13.05	22.17
0.0193	-18.41	-9.68	-5.27	6.52	16.12	17.14
0.0139	-18.7	-11.41	-6.27	1.77	10.76	19.91
0.01	-20.27	-13.05	-3.95	1.84	12.58	19.94
0.0072	-22.13	-16.06	-9.01	-1.04	8.3	15.68
0.0052	-20.37	-14.4	-4.9	-2.93	10.5	17.13
0.0037	-24.19	-17.83	-8.91	-1.96	13.37	15.74
0.0027	-24.26	-16.23	-10.46	0.18	10.06	12.89
0.0019	-24.61	-17.68	-9.74	1.37	12.61	15.48
0.0014	-24.52	-17.36	-7.03	-0.39	11.42	19.77
0.001	-24.09	-16.64	-7.44	2.95	12.33	18.61

KEWLS-CA vs SUKF	θ_{path} = 0.4					
0.1	14.84	10.99	2.64	3.81	11.42	19.74
0.072	5.94	-2.84	-1.51	2.14	7.95	11.5
0.0518	1.3	-7.94	-4.35	1.31	8.71	11.05
0.0373	-16.54	-9.91	-7.5	-0.19	7.18	10.01
0.0268	-15.73	-13.5	-8.3	-1.35	5.07	11.78
0.0193	-20.15	-14.7	-11.14	-1.08	6.8	8.43
0.0139	-23.32	-17.01	-12.29	-4.93	3.44	10.54
0.01	-24.24	-18.31	-10.58	-4.86	5.2	10.68
0.0072	-26.75	-21.24	-14.73	-7.14	1.13	7.09
0.0052	-25.34	-19.86	-11.78	-9.1	2.73	8.54
0.0037	-28.63	-22.8	-14.46	-8.06	4.41	7.86
0.0027	-28.96	-21.78	-16.49	-6.75	2.52	5.48
0.0019	-29.38	-23.01	-15.58	-6.34	3.61	7.52
0.0014	-29.39	-23.1	-14.41	-6.91	3.45	10.66
0.001	-29.27	-22.39	-14.34	-4.47	4.6	10.92

KEWLS-CA vs SUKF	θ_{path} = 0.6					
0.1	30.55	18.35	2.42	2.13	7.48	65.54
0.072	17.32	-0.21	-1.96	0.4	5.06	6.74
0.0518	9.05	-7.59	-6.98	-1.8	5.32	6.25
0.0373	-10.2	-10.66	-8.83	-2.83	4.4	6.97
0.0268	-15.62	-15.54	-10.73	-4.05	2.5	6.78
0.0193	-19.86	-16.56	-12.8	-4.56	2.48	5.14
0.0139	-24.4	-18.94	-14.01	-6.93	1.17	6.35
0.01	-25.04	-19.88	-13.34	-7.33	2.36	6.41
0.0072	-27.86	-22.57	-16.14	-8.72	-0.31	4.11
0.0052	-27.16	-21.89	-14.91	-10.13	0.19	5.47
0.0037	-29.71	-23.99	-16.1	-9.53	0.07	4.43
0.0027	-30.29	-23.96	-18.11	-9.81	-0.13	3.81
0.0019	-31.06	-25.03	-17.68	-9.55	0.18	5.27
0.0014	-31.16	-25.28	-17.71	-9.37	0.66	8.46
0.001	-31.82	-25.19	-17.21	-7.38	1.86	8.51

KEWLS-CA vs SUKF	θ_{path} = 0.8					
0.1	44.05	30.22	5.43	2.8	5.61	55.36
0.072	26.33	5.94	-0.26	0.57	4.85	6.15
0.0518	17.45	-5.13	-7.92	-3.26	3.46	5.08
0.0373	-1.28	-10.29	-8.6	-3.99	3.05	6.23
0.0268	-14.13	-16.38	-11.91	-5.46	1.84	4.19
0.0193	-18.33	-17.27	-12.73	-6.67	-0.36	4.72
0.0139	-24.07	-19.94	-14.23	-7.11	0.77	3.78
0.01	-24.67	-20.57	-15.12	-8.09	0.55	3.42
0.0072	-27.49	-22.34	-15.95	-8.64	-0.47	3.5
0.0052	-28.2	-23	-17.07	-9.19	-0.92	3.5
0.0037	-29.74	-24.11	-17.05	-9.75	-3.11	3.38
0.0027	-30.48	-25.06	-18.14	-10.76	-1.28	4.54
0.0019	-31.67	-25.68	-18.47	-11.19	-1.92	5.01
0.0014	-31.98	-26.48	-19.72	-10.15	-0.3	6.02
0.001	-33.52	-27	-19.34	-10.12	0.77	8.18

KEWLS-CA vs SUKF	θ_{path} = 1					
0.1	57.77	45.68	13.27	7.31	7.59	31.52
0.072	35.15	15.72	5.26	3.95	8.69	10.01
0.0518	26.62	0.73	-6.06	-1.79	4.82	8.77
0.0373	9.58	-7.1	-5.49	-2.36	4.75	9.14
0.0268	-10.3	-14.79	-10.69	-4.28	4.9	5.47
0.0193	-14.23	-15.76	-9.48	-6.62	0.32	8.19
0.0139	-21.17	-18.79	-11.58	-4.63	3.31	4.59
0.01	-21.97	-19.26	-14.96	-6.16	0.96	3.53
0.0072	-24.68	-19.49	-13.14	-5.54	2.42	6.49
0.0052	-27.59	-22.27	-17.37	-4.59	0.63	4.57
0.0037	-27.66	-22.06	-16.1	-7.53	-3.15	6.01
0.0027	-28.55	-24.01	-15.32	-8.83	0.55	8.19
0.0019	-30.16	-24.2	-16.99	-10	-1.12	7.81
0.0014	-31.4	-25.18	-19.69	-8.44	1.51	7.42
0.001	-33.13	-26.71	-19.17	-10.12	3.91	10.9

	0.001	0.0046	0.0215	0.1	0.4642	1

Measurement noise (σ_z) / m